MULTISCALE CLUTCH MODELS FOR CELL MECHANICS

Chiara Venturini

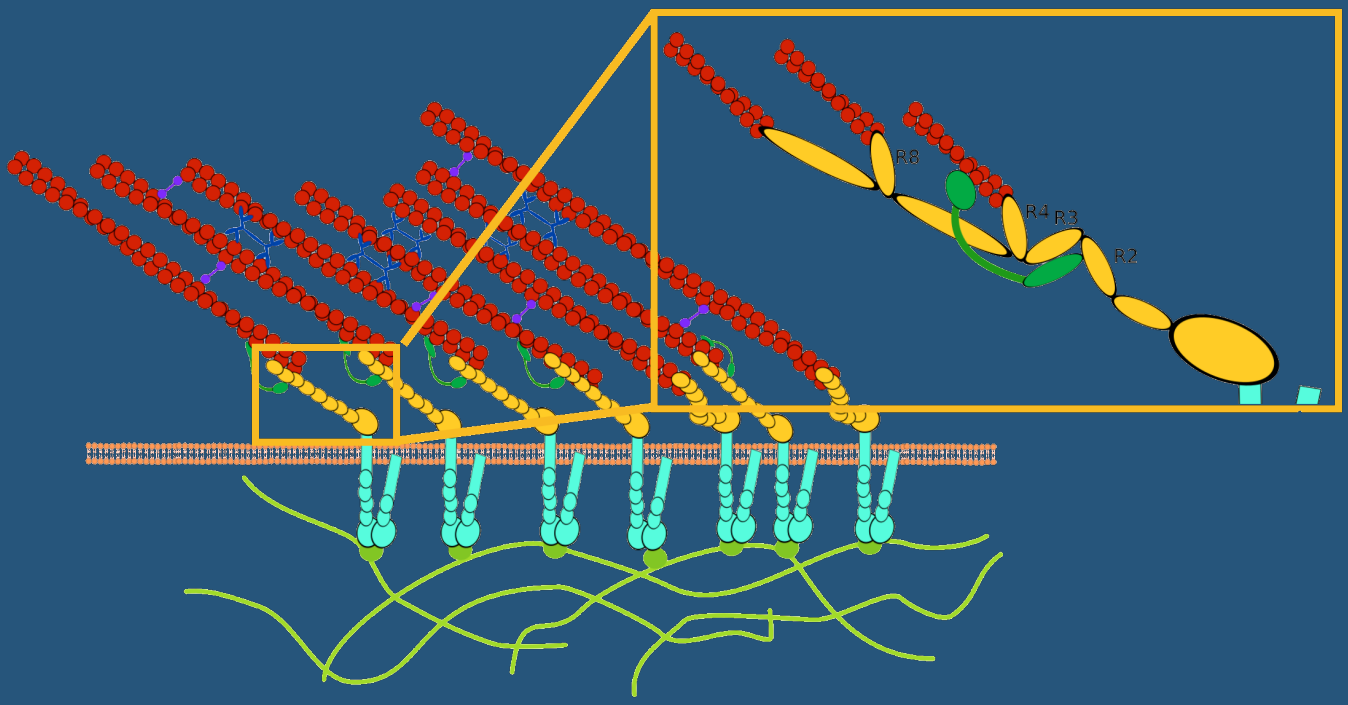

Doctoral Thesis
Barcelona, June 2022

MULTISCALE CLUTCH MODELS FOR CELL MECHANICS

Chiara Venturini

Doctoral Thesis
Advisor: Pablo Sáez
Barcelona, June 2022

School of Mathematics and Statistics
Doctoral Degree in Applied Mathematics
Universitat Politècnica de Catalunya

UNIVERSITAT POLITÈCNICA DE CATALUNYA
BARCELONATECH
Facultat de Matemàtiques i Estadística

Doctoral Degree in Applied Mathematics
School of Mathematics and Statistics
Universitat Politècnica de Catalunya

Multiscale clutch models for cell mechanics

by

Chiara Venturini

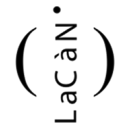

LaCàN: Laboratory of Mathematical and Computational Modeling

Advisor: Pablo Sáez
Barcelona, June 12, 2022

Abstract

Multiscale clutch models for cell mechanics

Chiara Venturini

Integrin-based cell adhesion is a key mechanism in fundamental biological processes such as cell migration, embryogenesis and wound healing, and in diseases like osteoporosis and cancer. For example, during migration, cells form adhesion complexes as they move, exerting tractions on the extracellular matrix (ECM), which enable the formation of protrusions. Cell migration is involved in phenomena like tissue formation or cancer invasion. So far experimental research has demonstrated the role of ligand spacing and substrate rigidity in adhesion dynamics. Moreover, some mathematical models have provided a fundamental understanding of cell adhesion. Specifically, the Clutch Model has been very successful in explaining how cells can sense force and consequently, how they respond to substrate rigidity. To exploit its potential, we have used it to address single cell durotaxis, the migration of a cell due to a stiffness gradient in the substrate.

We provide a mechanistic rationale for durotaxis by integrating continuum models of cell migration with the stochastic clutch model for cell adhesion. We show that a gradient in the ECM stiffness activates an asymmetric intracellular retrograde flow during the initial cell spreading. The competition between this flow and the polymerization velocity at the cell membrane creates a polarized state that establishes cell migration directionality. Our theoretical framework not only confirms previous experimental observations, but also rationalizes why some cell types follow positive stiffness gradients while others move toward softer regions based on an asymmetric distribution of the adhesion forces. The model also provides a conceptual framework to test specific pathways on how mechanical cues control cell migration.

Unfortunately, current clutch models also present some limitations. Adhesion complexes present a number of different adaptor proteins, and are able to link the actomyosin cortex in the interior of the cell to the ECM. The study of their composition and function has shown that the integrin-talin-actin chain serves as a mechanosensor and mechanotransducer of the external and internal forces. Current models simplify the composition and organization of the adhesion complex and use a phenomenological approach to reproduce cell scale variables, such as the retrograde flow velocity or the cell traction. However, they fail in modelling the sub-scale molecular behaviour. These simplifications have limited our mechanistic understanding of cell adhesion.

Therefore, we propose a multiscale clutch model that, from the physical and biological laws of the cell components, reproduces the mechanics of an adhesion complex as well as the dynamics of the subcellular molecules. We include a space-dependent ligand distribution and compute the displacement of the substrate point-wise thanks to Green's functions. We also implement a detailed description of the talin rod, where 13 domains can stretch, unfold and refold under force. Given the importance of the recruitment of adaptor proteins in an adhesion complex, we implement the presence of 11 vinculin binding sites (VBSs) and 3 actin binding sites (ABSs) in the talin rod. Our results nicely reproduce previous cell scale variables but also reproduce the behavior of single adhesion molecules within the adhesion complex. Moreover, our results suggest that cell traction is mostly dependent on ligand density rather than the complex adhesion size. Our computational framework also allows us to easily manipulate VBSs and ABSs and analyze the effect of their depletion in cell adhesion mechanics. Our computational results reproduce experimental data of mouse embryonic fibroblasts, both with full-length talin and with different combinations of talin domains depletion, showing how the traction force changes with respect to the talin configuration.
We believe that our detailed multiscale clutch model represents an important step forward in the understanding of cell adhesion, which can be further extended to account for other adhesion molecules and, e.g., for the study of adhesion maturation. The multiscale durotaxis model can be also used in a wider biological context, to engineer better biomimetic tissue constructs or to propose strategies for arresting tumor invasion.

Acknowledgments

Muchas cosas se han puesto de acuerdo para hacerme llegar hasta aquí.
Quiero agradecer a Pablo, porque sin su trabajo y su ayuda esto no habría sido posible. Quiero agradecer a todos mis amigos el tiempo pasado juntos, y el soporte que me han dado, también sin darse cuenta. Esta tesis es el resultado no solo de mucha investigación, sino también de todas las experiencias que me han hecho crecer en este capítulo de mi vida.
A mi familia que se acuerda de mí. A Aria, que desde lejos me da energía nueva.
A Carles, que ha vivido conmigo lo mejor de estos años.

I gratefully acknowledge the financial support from H2020 FET-Proactive programme (MECHANO-CONTROL, 731957) and the doctoral scholarship FI AGAUR 2018.

Contents

List of Figures

List of Tables

Acronyms

ECM	Extra-cellular matrix
ERM	Ezrin-adixin-moesin
ATP	Adenosine tri-phosphate
CMR	Cyclic mechanical reinforcement
AC	Adhesion complex
FA	Focal adhesion
MC	Monte Carlo
ABS	Actin binding site
VBS	Vinculin binding site
MEF	Mouse embryonic fibroblast
CAM	Cell adhesion molecules
SUPG	Stream-Upwind Pretrov Galerkin
WLC	Worm-like chain
FJC	Free joint chain
NM II	Non-muscle myosin II
DD	Dimerization domain
FL	Full length
HBMC	Human breast myoepithelial cell
IBS	Integrin binding site

Chapter 1

Introduction

Cell adhesion is the ability of a cell to adhere to another cell or the extracellular matrix (ECM). Cell adhesion controls fundamental biological processes such as cell division, cell differentiation, cell communication and signalling, cell regulation, cell migration, embryonic development and wound healing (Chothia and Jones, 1997, Gumbiner, 1996). Changes in cell adhesion dynamics can bust essential cellular processes and cause diseases, including cancer, arthritis, osteoporosis, atherosclerosis and neurological diseases (Etzioni, 1996, Fields, 1998, Hillis and Flapan, 1998).
There are numerous examples of the implication of adhesion in cell and tissue function. For parasites such as certain bacteria and *Plasmodium* species, adhesion to host cells is the most important step of an infection. Thanks to adhesion, intracellular bacteria, such as *Salmonella* and *Brucella* species, manage to invade other cells and enter the cytoplasm where they obtain nutrition and multiply (Detilleux *et al.*, 1990). Other cells, such as blood platelets, are non-adhesive in order to circulate in the blood, but when wounding occurs, they become adhesive to coagulate the blood and prevent bleeding. Therefore cells also possess mechanisms for regulating their adhesiveness (Ruggeri and Mendolicchio, 2007).
In multicellular organisms, how cells interact with each other and coordinate their behaviour regulates the development and maintenance of tissue structure and function. Multicellular organisms are able to self-repair: epithelial cells follow a collective migration towards the center of the wound, extrude ablated cells and heal the tissue (Brugués *et al.*, 2014). During the process, cells remain connected to their neighbours through cell-cell adhesions, and cell crawling is possible thanks to cell-ECM adhesions. In the embryonic brain, neurons extend axons along specific pathways, following a chemical and mechanical regulation. The stiffness of the adhering substrate plays an important role in determining the direction of growth, indeed for example retinal

ganglion cell axons are found to grow toward a softer tissue (Koser *et al.*, 2016).
Cell adhesion also plays a major role in diseases. Metastasis, one of the major causes of mortality in cancer, is a complex cascade process (Bogenrieder and Herlyn, 2003): tumor cells start from their primary site of growth, penetrate blood vessels or lymphatic channels and enter the circulation, survive and finally undergo extravasation in selective organs far from the original tumor site, ending with establishing growing metastatic lesions. Specific adhesive interactions between tumor cells and host cells or the ECM play a fundamental role in the tumor dissemination, leading to a preferential organ colonization (Bendas and Borsig, 2012, Saiki, 1997). Therefore, the inhibition of these interactions represents a useful target for the development of antimetastatic therapies (Janiszewska *et al.*, 2020).
Cell adhesion is also key in biomedical engineering (Bhadriraju *et al.*, 2006, Hickey and Pelling, 2019, Lotfi *et al.*, 2013), for example in the design of biomaterials interacting with blood, like those in artificial heart valves or blood vessels, which are required not to be adherent to cells or plasma proteins, in order to avoid thrombosis and embolism (Devillard and Marquette, 2021). Materials used in scaffolds for tissue generation are needed to act as a substrate to promote cell adhesion and proliferation (Bačáková *et al.*, 2004).
In this thesis, we focus on cell-ECM adhesion. To do so, we look into the intracellular components controlling cell-ECM adhesion and, specifically, into the behavior of the cell adhesion complexes. Adhesion complexes connect the actomyosin network to the extracellular matrix, which also plays a fundamental role in adhesion dynamics. Adhesion complexes are essential components of the adhesion mechanism, serving as mechanosensors and mechanotransducers of the external and internal forces of the cell.

1.1 Intracellular mechanisms towards cell adhesion

Cells are continuously subjected to a variety of forces. These forces are sensed and transduced by the cell through cell adhesion complexes, and converted into biochemical signals that produce specific cellular responses. Such responses may be diverse and include activation of signalling pathways and changes in gene transcription that result in long-term cellular mutations (Burridge *et al.*, 2019).
The actomyosin network is the main source of force generation inside the cell (Parsons *et al.*, 2010). The force generated by the actomyosin network is transmitted first to adaptor proteins, and then to transmembrane proteins that link the cell to the extracellular matrix. Therefore, these two main constituents of the cell, the actomyosin

network and the adhesion complexes, are fundamental to understand the cell adhesion behavior. However, how exactly they interact with each other to control cell adhesion, and what is the specific role of each constituent involved in the adhesion process, are still under active research. Next, we give an overview of the main cell components involved in cell adhesion mechanics, from the interior to the exterior of the cell.

1.1.1 Structure and function of the actomyosin network

The cell cortex and a variety of actin bundles, called stress fibres, are actomyosin networks with different organization and composition (Koenderink and Paluch, 2018, Murrell *et al.*, 2015) (Figure 3.2). The cell cortex is a layer of cross-linked actin filaments lying just beneath the plasma membrane of animal cells (Bray and White, 1988). The filaments form a network parallel to the membrane, with mesh sizes from 20 to 250 nm (Salbreux *et al.*, 2012). Inside the cortex we find crosslinking proteins (α-actinin, filamin, fimbrin), proteins involved in contractility (myosins, tropomyosin, tropomodulin) and linker proteins (proteins of the ezrin - radixin - moesin [ERM] family, filamin) (Burridge and Wittchen, 2013, Geiger *et al.*, 2009, Pellegrin and Mellor, 2007, Tojkander *et al.*, 2012). The cell cortex goes through a dynamic remodeling, with a continuous turnover of actin monomers (G-actin), by polymerization and depolymerization of the filaments, and binding and unbinding of crosslinking proteins (Mogilner, 2002, Pollard and Cooper, 2009a). The time of full turnover is approximately 1 minute, but actin crosslinkers and myosin motors turnover 5-10 times faster than actin. At timescales smaller than the turnover time, the cortex behaves as an elastic network, while at larger timescales the dynamic remodeling of the cortex results in a fluid-like viscous behavior (Tan *et al.*, 2018).
Stress fibres are composed of 10-30 actin filaments, non-muscle myosin II, and crosslinking proteins such as α-actinin, fascin, espin and filamin, building a highly organized structure (Kassianidou and Kumar, 2015). In non-motile cells, they are thick and quite stable, while in motile cells they are fewer, thinner and more dynamic. Stress fibres play an important role in cellular contractility, providing force for cell adhesion, migration and morphogenesis. They are fundamental for the formation and function of cell-cell and cell-ECM adhesions (Pellegrin and Mellor, 2007). Stress fibres can be classified into four categories, based on their protein compositions and association with focal adhesions, the connections between the ECM and the actin cytoskeleton (Lehtimäki *et al.*, 2021, Tojkander *et al.*, 2012). Depending on their positions inside the cell, they are named dorsal and ventral stress fibres, and transverse arcs (Figure 1.2). Dorsal stress fibres are attached to focal adhesions at their distal ends. As they do

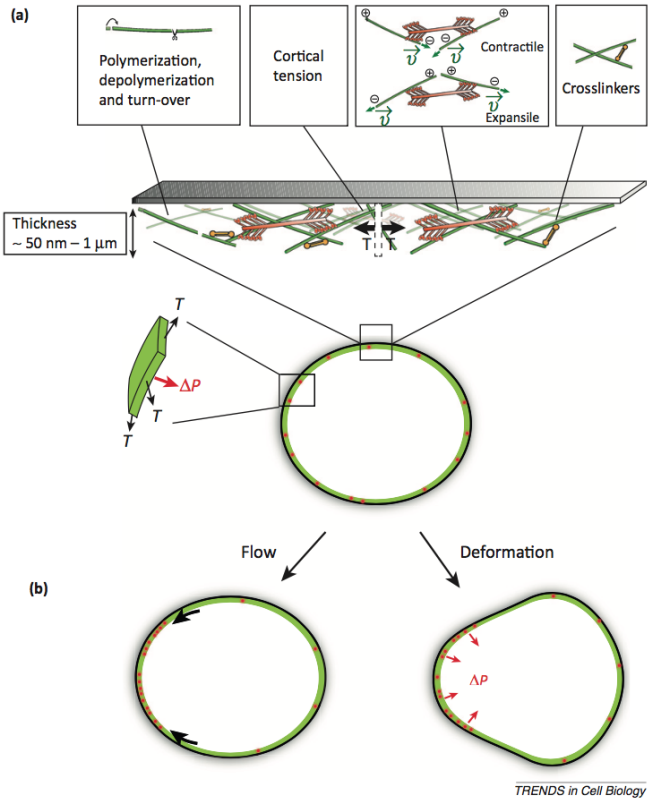

Figure 1.1: (a) Inside the cell cortex, myosin motors connect actin filaments. By consuming chemical energy in the form of ATP, they generate contractile stresses, which produce, together with crosslinks, a cortical tension T. Cortical tension can vary from 30 pN/µm to thousand pN/µm, depending on the cell type. (b) Thanks to the curvature of the cell, cortical tension produces a hydrostatic pressure in the interior of the cell (Salbreux *et al.*, 2012).

not typically contain myosin II, these bundles cannot exert contraction. Ventral stress fibres are contractile actomyosin bundles, attached to focal adhesions at both ends, and they represent the major contractile structure (Hotulainen and Lappalainen, 2006). They are often located at the rear of the cell, promoting contraction and facilitating cell movement. Transverse arcs, on the other hand, are thin, curved actin filament bundles, with a periodic α-actinin–myosin pattern that provides contractility. Arcs do not attach to focal adhesions, but they are connected with dorsal stress fibres, thus they convey the contractile force to the surrounding environment. In migrating cells, transverse arcs can flow from the leading cell edge towards the cell center, producing the actin retrograde flow.

In migrating cells, another specific actin network appears in the front of the cell, as a flat and protruding structure. It is made of two regions: the lamellipodium and

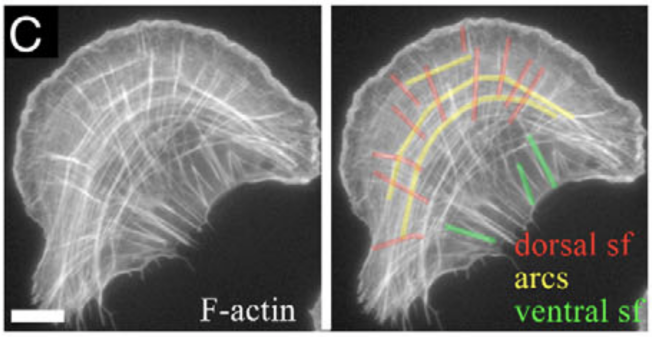

Figure 1.2: Stress fibres inside a non-muscle cell. They can be classified into: dorsal (red) and ventral (green) stress fibres, and transversal arcs (yellow) (Pellegrin and Mellor, 2007).

the lamellum (Hirata *et al.*, 2014a, Ponti *et al.*, 2004a) (Figure 1.3). Lamellipodium is a thin, sheet-like membrane protrusion that spreads 2-4 µm from the leading edge of motile cells. It is composed of a dense and dynamic network of actin filaments. Here the polymerization of G-actin takes place pushing the cell membrane forward in the direction of migration. If the cell is spatially confined, the lamellipodial actin has a faster retrograde flow as a result of the pushing of the actin filaments (F-actin) backwards, from the cell membrane towards the cell centre. The lamellum localizes behind the lamellipodium and is the widest structure, about 10-15 µm wide. Lamellum contains a more stable actin network, and also myosin II.

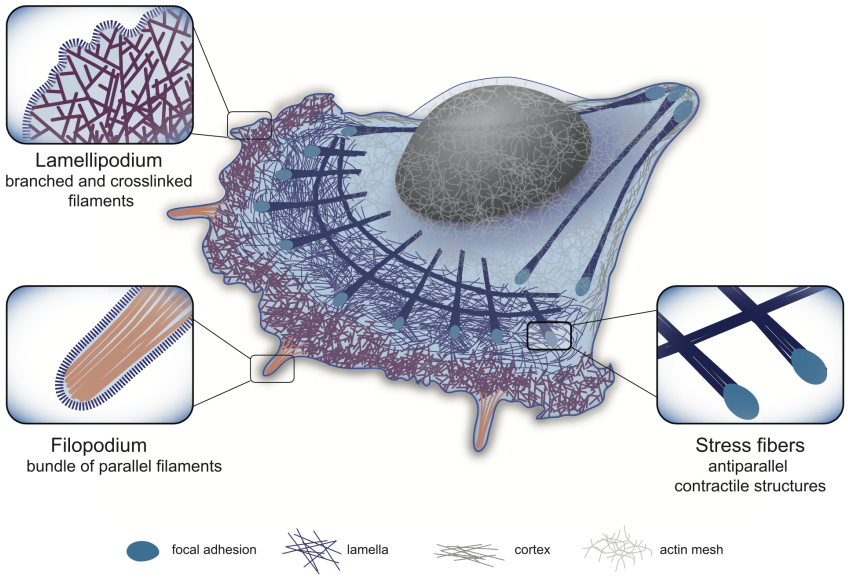

Figure 1.3: Schematic representation of a migrating cell, with filopodia, lamellipodium, lamellum and stress fibres highlighted (Letort *et al.*, 2015).

In all previous actin structures, myosin motors are responsible for pulling two actin fibres along each other. The speed at which myosin II contracts actin filaments is about

120 nm/s if its action is unopposed by force (Chan and Odde, 2008). However, the contraction speed will decrease with force until stalling when the force applied coincides with the maximum force that a myosin motor can apply (2 pN) (Molloy *et al.*, 1995). Non-muscle myosin II has two heads, hydrolyzing ATP and transforming chemical energy into mechanical force, pulling on actin filaments and generating an active tension (Vicente-Manzanares *et al.*, 2009a). This active tension generates flows and drives shape changes (Keren *et al.*, 2008) and motility (Barnhart *et al.*, 2015). For example, the effect of myosin II contraction increases the speed of the retrograde flow (Wilson *et al.*, 2010). Myosin induced tension is also implicated in the maturation (Geiger *et al.*, 2009, Wolfenson *et al.*, 2011), stability (Choi *et al.*, 2008, Vicente-Manzanares *et al.*, 2009a) and disassembly (Geiger *et al.*, 2009, Wolfenson *et al.*, 2011) of adhesion complexes.

1.1.2 Structure and function of cell-ECM adhesion complexes

Cell-ECM adhesion complexes are dynamic structures that contain hundreds of different molecules. The main constituents are ECM ligands, transmembrane integrins, cytoplasmatic proteins and a network of actomyosin filaments (Figure 1.4). Most of these intracellular and transmembrane components have been identified and assigned specific functions in cell adhesion. The vinculin-talin-integrin chain is considered the determining link in adhesion complexes (ACs) (Chothia and Jones, 1997, Geiger *et al.*, 2001). Over the last decades, the ever-improving experimental techniques allowed an increasingly clearer understanding of the AC structure and function.
The first hypotheses on the hierarchical composition of the adhesion chain were made clear by analyzing the kinematics of each molecule through fluorescence speckle microscopy (Hu *et al.*, 2007). Integrins were shown to have a very low correlation with the actin flow, indicating that they should be attached to the fixed ECM. On the other hand, α-actinin was fully correlated with the retrograde flow, proving its full connection within the actomyosin network. Talin and vinculin showed a partial coupling to the actin flow, which indicated that they connect the actomyosin network with the immobile extracellular binding sites. These results demonstrated a stratified organization of the main adhesion molecules and its relation with the retrograde flow. Then, 3D super-resolution fluorescence microscopy confirmed previous results and provided a more precise description of the nanoscale architecture of adhesion complexes (Kanchanawong *et al.*, 2010). They showed that integrins and actin are separated vertically ≈40nm by a first signaling layer consisting of the integrin cytoplasmatic tails, a second layer of talin and vinculin, oriented at 15 degrees with respect to the plasma membrane (Liu *et al.*, 2015b), and an actin regulatory layer containing zyxin and α-actinin, among others, that connect talin with the actin network.

Integrins are membrane-spanning receptor proteins which function as heterodimers

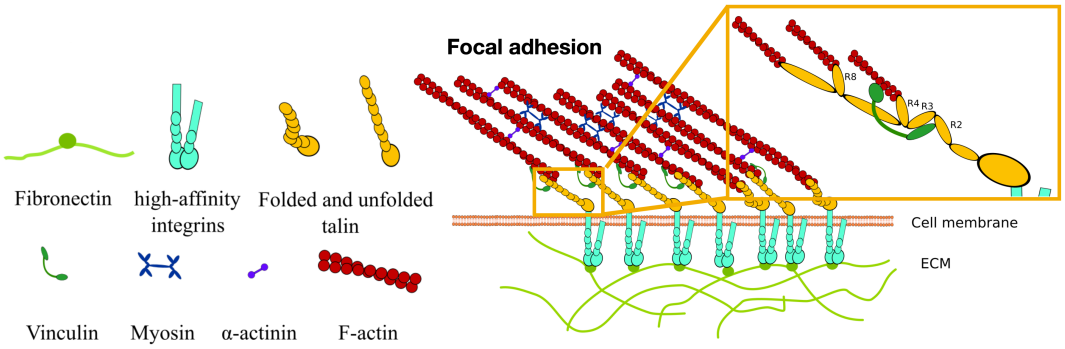

Figure 1.4: Structure of a cell-ECM adhesion complex in migrating cells. Starting from the bottom, fibronectin molecules inside the ECM are linked to integrins, which are transmembrane proteins. Integrins bind to talin, which is made of 13 domains, that can be folded or unfolded and allow the binding of vinculin. Finally, the talin rod is bound to actin filaments, connected to each other through myosin motors and crosslinking proteins.

of α- and β-subunits and bind to ECM proteins as fibronectin (Sun *et al.*, 2016). Force estimations at single integrins during cell adhesion have been measured in the range of 2-100 pN (Sun *et al.*, 2016). However, most of these measures were averaged values across the entire adhesion plaque, which cannot provide precise magnitudes of the forces experienced by single integrins. FRET-based molecular sensors established the single integrin force in 1-5 pN (Morimatsu *et al.*, 2013), which matches the values reported for mechanosensation events in vinculin (Grashoff *et al.*, 2010). The response of integrins to force can have different behaviours. They can be in a bent or extended configuration, which in turn can be closed or open, and they can also bind and unbind following different rates, depending on the force applied to them. *Talin* is a large protein recruited from the cytosol to the adhesion site, which localizes along the long axis of the adhesion complex and interacts with both integrin and actin. The talin head, which binds β-integrin cytoplasmic tails, co-localizes with paxillin and focal adhesion kinase (FAK) near the plasma membrane, whereas the talin tail binds actin, and is extended rearward in the direction of F-actin flow (Critchley, 2009, Goult *et al.*, 2018). The force exerted by the actomyosin fibres induces talin deformation and further conformational changes (del Rio *et al.*, 2009, Yao *et al.*, 2016, Zhang *et al.*, 2008). Upon unfolding of talin rod domains, which expose vinculin binding sites, *vinculin* binds talin, allowing more connections to the actin filaments (Bois *et al.*, 2006). This event eventually induces the clustering of integrins and further maturation and reinforcement of the AC (Elosegui-Artola *et al.*, 2014, Rosowski *et al.*, 2018).

1.1.3 Maturation of adhesion complexes

Adhesion complexes undergo a maturation process, changing in size, shape, location, and proteins composition (Henning Stumpf *et al.*, 2020, Vicente-Manzanares and Horwitz, 2011). As a result, the transmitted traction also evolves in space and time within the cell-ECM interface (Figure 1.5). The maturation time is regulated by different

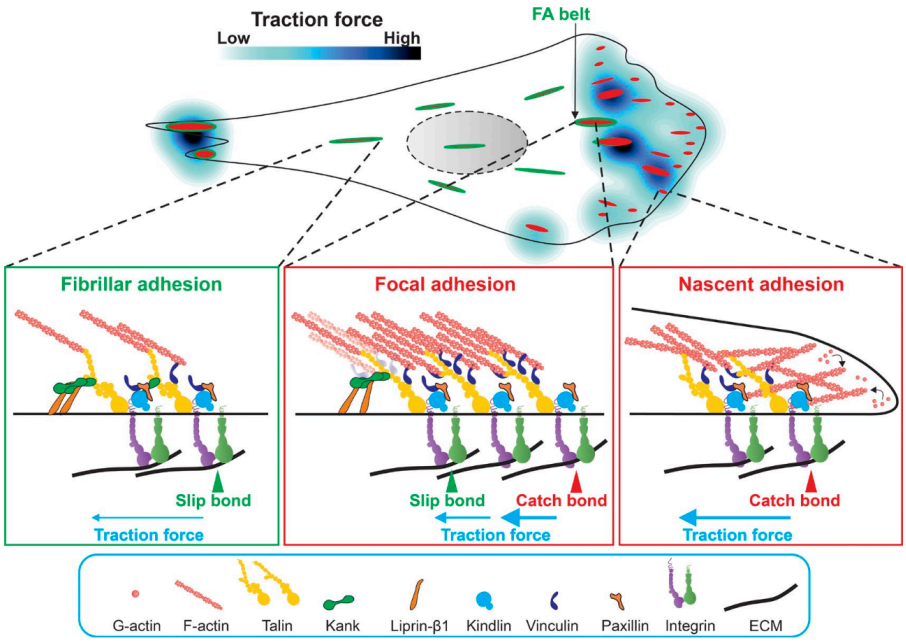

Figure 1.5: Nascent adhesions appear at the leading edge of the cell. A small number matures into focal adhesions, which finally evolve into fibrillar adhesions, close to the cell nucleus. The different protein compositions, shapes and traction intensities are shown. The highest traction is transmitted by focal adhesions (Sun *et al.*, 2016).

factors, including actomyosin contraction (Geiger *et al.*, 2009, Ren *et al.*, 2000), talin unfolding (Lee *et al.*, 2007), integrin activation (Lee *et al.*, 2013) and integrin cyclic mechanical reinforcement (CMR) (Kong *et al.*, 2013).
Adhesion complexes are usually categorized with respect to their evolution in time: nascent, focal and fibrillar adhesions. *Nascent adhesions* are 100 nm clusters of ~50 integrins, which assemble independently of substrate rigidity or cell contractility (Changede *et al.*, 2015). Initial integrins turnover is due to cycles of free-diffusion

within the adhesion plaque, until when integrins become immobilized upon force-induced activation (Rossier *et al.*, 2012). Integrin activation is the most important factor in the assembly of early adhesions (Sun *et al.*, 2019): the application of forces up to tens of pN produces changes in the conformation of the integrin molecule, increasing its affinity for ECM ligands (Li and Springer, 2017, Sun *et al.*, 2016). In their low-affinity state the molecules appear bent and closed. While bent, their length is found to be 11 nm (Sun *et al.*, 2019) or 13 nm (Eng *et al.*, 2011). Low-affinity integrins can be activated by talin, not attached to actin: talin binds to integrins and activates them, making them pass to an extended and closed state. These integrins are now in the intermediate affinity state. After that, actin binds to talin, creating the adhesion chain, and integrins change again their structure passing to an extended and open state, called high-affinity state. The length of extended integrins is found to be 18 – 20 nm (Dai *et al.*, 2015), 20 nm (Liu *et al.*, 2015a), or 23 nm (Eng *et al.*, 2011). The extended state is further stabilized by the force-dependent formation of catch bonds (Kong *et al.*, 2009). Activation fosters integrins attachment to talin, which allows the connection to actin filaments. Then, force transmission allows integrins to cluster in the adhesion patch, reduces their diffusivity outside of the patch, and, eventually, leads to the formation of nascent adhesions (Calderwood, 2004). The CMR of integrins strengthens the fibronectin-integrin bond, increasing the lifetime of the bond when integrins undergo many loading/unloading cycles or loading cycles with high force peaks. In the CMR, integrins start in a short-lived state and evolve to intermediate- and long-lived states. Bonds that undergo CMR stay long-lived also after force removal. During the formation of nascent adhesions, key molecules, e.g. paxillin, kindlin, and FAK, are recruited into the adhesion complex. At this stage of the process, actin filaments are polymerized at the nascent adhesions and elongated towards the cell body, in the direction of the retrograde flow. Then the filaments are crosslinked by α-actinin and myosin II to form short bundles.

Thanks to this force-induced actin aggregation, a subset of the nascent adhesions formed in the lamellipodium stabilize and undergo maturation and elongation at the border between lamellipodium and lamellum, becoming *focal adhesions (FAs)* (Case and Waterman, 2015). At the same time, talin has a significant contribution: it undergoes conformational changes following force application, managing to expose cryptic binding sites for vinculin and actin. Therefore vinculin molecules and actin filaments bind talin, inducing integrins and actin recruitment to the AC. Afterwards in the maturation process, behind the lamellum, the mechanical linkage between FAs and the contractile actomyosin bundles is released or relaxed, leading to FA disassembly or the translocation into *fibrillar adhesions* (Short, 2012).

1.2 Role of the extracellular mechanics in adhesion dynamics and cell function

Mechanotransduction at the AC is bidirectional, with forces not only transmitted from the adhesion complex to various ECM ligands, but also being converted from the ECM to the adhesion complex. For example, fibronectin molecules stretch because of tension originating from ACs, reveal cryptic binding sites and increase their affinity for integrin receptors and other fibronectin and ECM molecules, thereby promoting matrix assembly (Klotzsch *et al.*, 2009, Oberhauser *et al.*, 2002). The ECM stiffness has a fundamental mechanosensing role in cell adhesion. Cells sense substrates of different rigidities and respond to the mechanical cues by regulating cellular activities. At a macro scale level, an outcome of the importance of substrate rigidity is stem cell differentiation: when adhering to soft surfaces they become neuronal cells, on intermediate surfaces they transform into muscle cells, and on stiff surfaces they become bone cells (Kothapalli *et al.*, 2020). Moreover, motile cells are influenced by the stiffness gradient of their adhering substrate, which can determine their direction of migration, in a process called durotaxis (Charras and Sahai, 2014, Shellard and Mayor, 2021, Sunyer and Trepat, 2020). The substrate rigidity has important effects at a molecular level. Substrate stiffness controls the loading rate, i.e. the speed at which force builds at the molecules inside the adhesion complexes (Elosegui-Artola *et al.*, 2018) (Figure 1.6). In rigid substrates there is frictional slippage: as soon as a ligand binds, the force

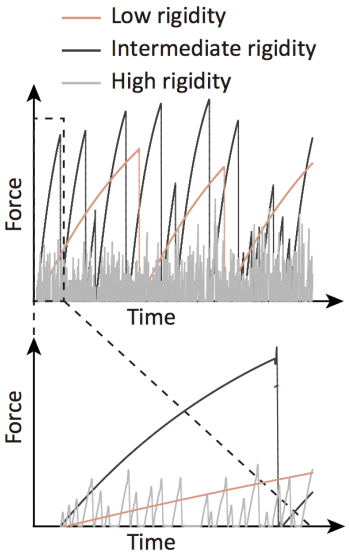

Figure 1.6: Transmitted force during time for binders on low, intermediate, and high rigidity substrates. For high substrate rigidity (grey), there is frictional slippage: the clutches disengage very quickly without reaching high force values. With optimal rigidity (black), the highest values of transmitted force are reached. At low rigidity (red), force loading is the slowest and the force values are lower than the optimal ones (Elosegui-Artola *et al.*, 2018).

created by the myosin contraction builds very quickly through the adhesion chain. If unbinding rates are faster than binding rates, ligands disengage before other ligands have time to bind, lowering the traction on the substrate and increasing the actin retrograde flow velocity (Swaminathan and Waterman, 2016). In soft substrates, the force loading rate decreases because the stretching of the deformable substrate allows time for the engagement of many bonds before they reach the breaking limit. As ligands keep binding, myosin contractility deforms the substrate, building force on the substrate and each bound clutch, and reducing the retrograde flow. At some point, the limit rupture force of the bonds is reached, all clutches disengage, and the cycle starts over again. This is usually called the "load and fail cycle".
Another determining factor for cell-ECM adhesion is the spacing of specific ligands. In low ligand spacing substrates, the maturation of adhesion complexes in rigid substrates is highly compromised, with few maturing into stable focal adhesion, while in soft substrates focal complexes always mature into long-lived complexes (Changede *et al.*, 2015). However, when ligands are put apart by more than 200 nm, focal adhesion formation is impaired (Arnold *et al.*, 2004, Cavalcanti-Adam *et al.*, 2007, 2006), probably due to a restriction in integrin clustering. A detailed study of the combined influence of ECM rigidity and ligand spacing (Oria *et al.*, 2017) found that for soft substrates the bigger the distance between the ligands the bigger the ACs become, while on more stiff substrates, increasing the distance between ligands leads to AC collapse.
However, how specifically cell adhesion responds to the rigidity of the ECM and spacing of ligands is still under active investigation. More importantly, how it determines the dynamics of the adhesion complex at the molecular level is not well known.

1.3 Mathematical modelling of cell adhesion

Different physical models have been proposed in the literature to assist current experimental work in the rationalization of the main mechanisms that govern cell adhesion. Continuum models have been used to describe clustering and growth of adhesion complexes (Deshpande *et al.*, 2008, Ronan *et al.*, 2014, Wang and Gao, 2008, Yuan and Gao, 2012) and cell contractility (Deshpande *et al.*, 2008, Ronan *et al.*, 2014) in adhesion mechanics.
Other approaches have used Monte Carlo (MC) simulations to analyze through discrete stochastic models the role of the ECM in adhesion mechanics (Gao *et al.*, 2011, Qian and Gao, 2010).
Among the Monte Carlo-based models, the Molecular Clutch model focuses on the

specific binding/unbinding events of individual molecular chains, providing a simple rationalization of the most relevant features of cell adhesion as a function of the stiffness of the substrate (Chan and Odde, 2008, Elosegui-Artola *et al.*, 2014). The clutch hypothesis, stating that filopodia protrusion is due to the link between the actomyosin network and the underlying substrate through engaged molecular clutches, was first described while studying axons growth in nerve cells (Mitchison and Kirschner, 1988). The physical model was originally introduced to explain growth cone adhesion (Chan and Odde, 2008) and has been further exploited since then (Bangasser *et al.*, 2013, Bangasser and Odde, 2013, Bangasser *et al.*, 2017, Bennett *et al.*, 2018, Case and Waterman, 2015, Cheng *et al.*, 2016, 2020, Craig *et al.*, 2015, Elosegui-Artola *et al.*, 2016, Oria *et al.*, 2017). More recent and specific models, based on the clutch model, have been developed to focus on integrin clustering dynamics (Cheng *et al.*, 2020).
The specific mechanics of each adhesion protein involved in cell-ECM adhesion has been also investigated in detail. The phenomenon of integrin activation, binding to ECM ligands and clustering has been modelled (Welf *et al.*, 2012). The CMR of $\alpha_5\beta_1$ integrins has been modelled (Li *et al.*, 2016), a few years after its experimental discovery (Kong *et al.*, 2013). The specific myosin II motors force production has been object of modelization (Stam *et al.*, 2015). A complete model for the stochastic folding and unfolding of talin rod domains has been also developed (Yao *et al.*, 2016).
Moreover, mathematical and computational models have been used to rationalize the mechanics of the actin flow coupled with the adhesion to a substrate. A spatial-dependent discrete model for the actin cytoskeleton, coupled with an adhesion model has been proposed (Walcott and Sun, 2010). Other discrete models with spatial dependence (Borau *et al.*, 2012, Coughlin and Stamenović, 2003, Paul *et al.*, 2008) idealize the actin cytoskeleton as a network of elastic rods connected by rigid nodes, considering that some filaments are attached to the substrate as a boundary condition. On the other hand, in continuous models stress fibres and integrins are measured through their concentrations. Cells placed on substrates with micro-patterned ligand patches have been studied, in order to investigate the effect of ligand pattern shape on the cytoskeletal arrangement and the AC distribution (Pathak *et al.*, 2008), managing to capture experimental observations.
In this thesis we focus on the stochastic approach in the study of cell-ECM adhesion mechanics, therefore in the following we provide an explanation of its mathematical ingredients.

1.3.1 Bell's model

The understanding of both cell-ECM and cell-cell adhesion requires a proper characterisation of a single bond. Modelling molecular bonds as elastic springs gives a good approximation for the mechanical behaviour of the adhesion molecules. Adhesions do not break at fixed thresholds, but follow a stochastic behaviour. Using the framework of the elastic-spring model, binders are described as elastic springs which interact via a reversible chemical process to form bond complexes.
In 1978, Bell proposed in a seminal theoretical paper (Bell, 1978), a phenomenological model for the off-rate of slip bonds, which became the basis of state-of-the-art models for cell adhesion. The model extends the transition state theory for reactions in gases. It states that the off-rate of receptor-ligand interactions depends exponentially on the force on the linkage. This law is commonly called Bell's law in the literature and exposes the significant role of mechanical forces in biological chemistry.
A stochastic version of deterministic Bell's model is used to study the stability of adhesion clusters of constant size, with constant loading (Schwarz and Safran, 2013). An adhesion cluster with applied force F is shown in Figure 1.7. The adhesion cluster

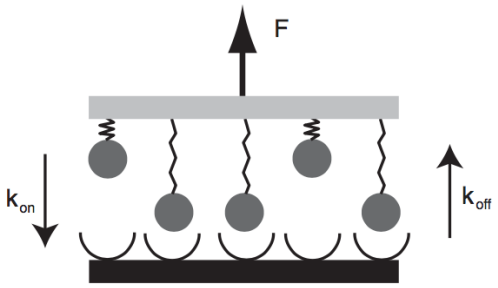

Figure 1.7: Model for an adhesion cluster, under uniform force F, with k_{on} and k_{off} the binding and unbinding rates of each binder (Schwarz and Safran, 2013).

contains N_t molecules, of which $N(t)$ are bound and $N_t - N(t)$ are unbound, at time t. Each bond can bind with binding rate k_{on}, independent of force as in Bell assumption, and unbind with rate k_{off}. Unbinding increases with force, following the so called Bell's law

$$k_{off} = k_0 e^{F/F_b}, \tag{1.1}$$

where F is the uniform force, k_0 is the spontaneous unbinding rate and $F_b = k_B T/x_b$ is a molecular-scale force, with k_B the Boltzmann constant, T the absolute temperature, and x_b the position of a transition state barrier. By defining the dimensionless time $\tau = k_0 t$, the force $f = F/F_b$ and the rebinding rate $\gamma = k_{on}/k_0$, the dimensionless rate

equation reads:

$$\frac{dN}{d\tau} = -Ne^{f/N} + \gamma(N_t - N). \tag{1.2}$$

The first term on the right-hand side is non-linear in the number of bonds N and represents the unbinding process, while the second term is linear in N and represents rebinding. A bifurcation analysis of the steady state behaviour shows that it is unstable when the force exceeds the saddle-node bifurcation value

$$f_c = N_t pln\left(\frac{\gamma}{e}\right), \tag{1.3}$$

where $pln(a)$ solves $xe^x = a$ (Bell, 1978). This shows that a cluster with a finite number of bound binders is only stable up to a critical force f_c.
However, Eq. (1.2) does not include the biological fluctuation effects, so the original work of Bell can be extended to a one-step master equation (Erdmann and Schwarz, 2004). Calling i the number of bound molecules, with $0 \leq i \leq N_t$, the probability $p_i(t)$ that i bonds are present at time t follows:

$$\frac{dp_i}{dt} = r(i+1)p_{i+1} + g(i-1)p_{i-1} - [r(i) + g(i)]p_i, \tag{1.4}$$

with

$$r(i) = ie^{f/i}, \qquad g(i) = \gamma(N_t - i), \tag{1.5}$$

the unbinding and binding rates, respectively. The first two terms in the right-hand side of Eq. (1.4) stay for the increase of bonds in state i, because of the unbinding of a bond in state $i+1$ and the binding of a bond in state $i-1$, respectively. The last two terms represent the decrease of the bonds in state i: the unbinding of bonds in state i contributes to state $i-1$, and the binding of bonds in state i contributes to state $i+1$. While the deterministic equation, Eq. (1.2), predicts infinite cluster lifetimes for forces below a given threshold, the stochastic model, Eq. (1.4), gives finite lifetimes for whatever force. The average lifetime of a cluster with $i = N_t$ bonds at time $t = 0$ can be calculated as the mean time T to evolve to the state with no bound molecules ($i = 0$) (van Kampen, 1992):

$$T = \sum_{i=1}^{N_t} \frac{1}{r(i)} + \sum_{i=1}^{N_t-1} \sum_{j=i+1}^{N_t} \frac{\prod_{k=j-i}^{j-1} g(k)}{\prod_{k=j-i}^{j} r(k)}. \tag{1.6}$$

We reproduce how the average lifetime of the cluster evolves, as a function of f/N_t, for different values of N_t (Figure 1.8).

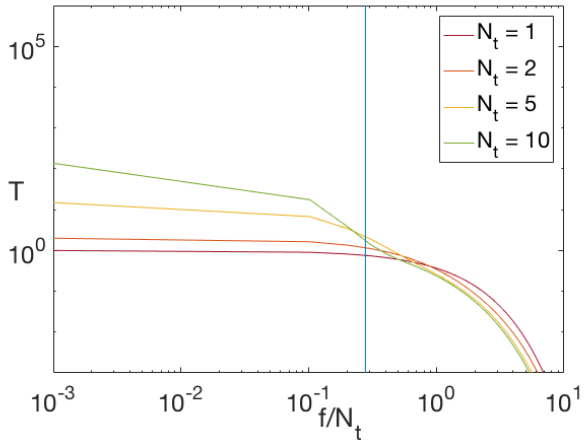

Figure 1.8: Average cluster lifetime T for $N_t = 1, 2, 5, 10$, as a function of f/N_t, for $\gamma = 1$. The vertical line corresponds to the critical force f_c.

1.3.1.1 Slip and catch bond behaviour

Depending on the molecular bond, its lifetime can behave differently while applying a force. The slip behaviour of a bond is the mechanism in which the higher the applied force, the faster the bond will break (Eq. (1.1)). On the contrary, in a catch bond the lifetime increases with the applied force (Evans, 2001, Evans and Ritchie, 1997, Sarangapani *et al.*, 2011, Thomas, 2008). Inspired on Bell's work, the so-called two-pathway model rationalizes the catch-binding behaviour (Pereverzev *et al.*, 2005). The force modifies the receptor structure and produces changes in the ligand-binding location. Mathematically, the dissociation rate constant $k(F)$ depends on the force F applied on a single molecule as:

$$k(F) = k_s^0 \exp\left[\frac{x_s F}{k_B T}\right] + k_c^0 \exp\left[\frac{-x_c F}{k_B T}\right], \tag{1.7}$$

where k_s^0 and k_c^0 are the dissociation rates via the slip and catch pathways respectively in absence of force, x_s and x_c are the distances from the minimum to the corresponding maxima of the energy, k_B is the Boltzmann constant and T the Kelvin temperature. In this equation we assume that the minimum of the energy landscape corresponding to the bound state has two pathways to escape. They correspond to the slip and catch mechanisms of dissociation: at each increase of the force, the bond will break faster via the slip pathway, but it will live longer through the catch pathway. The average lifetime of a single molecule can be computed, in both the slip and catch cases, as the

inverse of the dissociation rate:

$$\tau(F) = \frac{1}{k(F)}. \tag{1.8}$$

The slip and catch bond behaviours are shown in Figure 1.9.

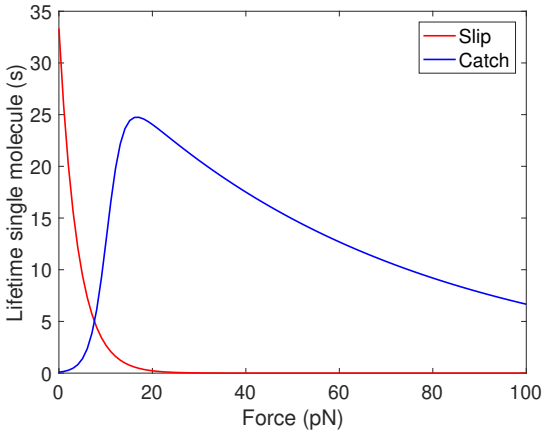

Figure 1.9: Average lifetime of a binder/ligand bond as a function of the force, for slip (red) and catch (blue) behaviour. The lifetime of the slip bond decreases exponentially with force while the catch bond lifetime reaches a maximum and for higher forces exhibits a slip bond behaviour.

1.3.2 Monte Carlo method

The stochastic models currently used to study cell adhesion are based on the Monte Carlo method. This mathematical technique manages to describe the dynamic behaviour of the AC, taking into account the probabilistic nature of the events.
The Monte Carlo (MC) method was developed during the Manhattan Project in 1942 by John von Neumann and Stanislaw Ulam (Metropolis and Ulam, 1949). It is named after the city Monte Carlo in Monaco, known for its casinos. It can model real-life systems, such as a telecommunications network, a production line, the transport of neutrons, or the evolution of the stock market (Kroese *et al.*, 2014).
The Monte Carlo method is used to model the probability of different outcomes in a process, that cannot easily be determined due to the interference of random variables. Indeed, it can reduce complex models to a set of basic events and interactions, opening the possibility to encode the model behaviour through a set of rules which can be implemented on a computer.
A MC simulation is a computational algorithm that relies on the process of repeated random sampling to obtain numerical estimations of the variables of interest. The idea is to repeat the experiment many times. The final variables are computed as the average of the same variables obtained through several equally likely MC simulations. From a mathematical point of view, the average value that a random variable X would

take if the experiment that produced it were carried out infinitely many times, can be defined as the expected value of X, $\mathbb{E}(X)$. Calling f the probability density function (pdf) of X, the expected value can be written as:

$$\mathbb{E}(X) = \int xf(x)dx, \tag{1.9}$$

where the integral covers the entire range of values that X can assume (Johansen *et al.*, 2010). For discrete random variables, the integral is replaced by a summation. Here, for simplicity, we assume random variables to be continuous, but a similar argument can be carried out for discrete ones.
The law of large numbers states that if $X_1, X_2, \ldots$ are an infinite collection of independent and identically distributed (iid) random variables with common pdf f, and $\varphi : E \longrightarrow \mathbb{R}$ is a function with finite expectation, then:

$$\lim_{n\to\infty} \frac{1}{n} \sum_{i=1}^{\infty} \varphi(X_i) = \mathbb{E}(\varphi(X)), \tag{1.10}$$

where convergence holds.
The central limit theorem affirms that if also $\mathbb{E}(\varphi(X)^2) < \infty$, then:

$$\lim_{n\to\infty} \sqrt{n}\left(\frac{1}{n} \sum_{i=1}^{\infty} \varphi(X_i) - \mathbb{E}(\varphi(X))\right) \Longrightarrow \mathcal{N}(0, \sigma^2), \tag{1.11}$$

where $\Longrightarrow$ means convergence in distribution. That is, $\sqrt{n}$ times the sample mean converges in distribution to a normal random variable with mean zero and variance σ^2.
Therefore the Monte Carlo method can be justified using these two theorems. If X is a random variable with probability density function f from which we can obtain samples, in order to estimate its expectation $\mathbb{E}(\varphi(X))$ we can use the empirical mean of φ obtained from a large sample. Given a collection of iid random variables $X_1, X_2, \ldots, X_n$ which have common distribution f, the Monte Carlo estimator of $\mathbb{E}(\varphi(X))$ is:

$$\frac{1}{n} \sum_{i=1}^{\infty} \varphi(X_i). \tag{1.12}$$

The theory of the law of large numbers requires a simulation to be repeated many times to have an accurate estimate. The number of simulations considered sufficient for a stable solution depends on the number of random components in our problem, and the ranges specified for them.

The Monte Carlo method involves three basic steps:

- Set up the predictive model, identifying both the dependent variables to be predicted and the independent input variables that will drive the prediction. Specify the probability distributions of the independent variables: use experimental/historical data to define a range of likely values and assign them probability weights. For each simulation, which can be considered a realization of the system, each independent variable is sampled, i.e. a single random value is selected from the specified distribution and assigned to that variable.

- The system is then simulated through time, and the resulting outcome from that sample is recorded. A large number of simulations are run repeatedly, generating random values of the independent variables at each run. The large number of trials is needed to make up a representative sample of the near-infinite number of possible combinations.

- This provides an extensive number of separate and independent results, each representing a possible "future" for the system, i.e. one possible path that the system may follow through time. The results of the independent system realizations are assembled into probability distributions of possible outcomes.

1.3.2.1 Gillespie algorithm

The Gillespie algorithm makes use of the Monte Carlo method, and it is characterised by a variable time step, determined by the reaction times. Here we describe the general formulation, while later it will be adapted to the specific reactions of our model.
The Gillespie algorithm was developed and published by Dan Gillespie in 1977 to simulate chemical or biochemical systems of reactions efficiently and accurately by using limited computational power (Gillespie, 1976, 1977, 2007). As computers have become faster, the algorithm has been used to simulate increasingly complex systems in chemistry and biology.
We write down the Gillespie algorithm as:

- Initialization of the system:
  In the context of reaction kinetics, it consists in setting up the chemical concentrations in the system, the reaction constants, and the random number generators.

- Monte Carlo Step:
  Generate random numbers to determine the type of reaction to occur, as well as the time interval until the next reaction.

- Update:
  Select an event, and update the state of the system by updating the molecule count based on the reaction that occurred, and increasing the time step by the correspondent generated time.

- Iterate:
  Run the simulation multiple times until some stopping criteria are met, then compute the averages of the variables.

1.4 Goals and structure of the thesis

The main goal of this thesis is to investigate the effect of ECM rigidity in cell adhesion mechanics at two scales of the cell. At a cell scale, we study the behaviour of a motile cell adhering to a substrate with a rigidity gradient. Revealing precise methods to control cell migration represents a fundamental problem in biology, as it is involved in numerous processes of life, including embryogenesis, wound healing and tumor growth. We aim at understanding the preferring moving direction of the cell. In the context of cancer, this knowledge would allow us to design strategies for arresting cell invasion.
At a subcellular scale, we study the adhesion mechanics inside a single FA, for different rigidities of the adhering substrates. All the models described in Section 1.3 capture the behaviour of the complex process of cell adhesion, but they have limited information on how specifically the main molecules control the adhesion complex dynamics. Instead, our objective is to create a multiscale model for the mechanics of a FA that, integrating the physical laws that govern the main components of the adhesion complex, naturally leads to a full description of cell-ECM adhesion mechanics. Therefore, we model the internal organization of FAs in detail, which allows us not only to study the molecular level, but also its implications in the whole complex dynamics. Our goal is to provide new insights on how ACs work by means of a computational physical model and to rationalize key experimental observations.
In Chapter 2 we first describe the clutch model: we study both the original clutch model (Chan and Odde, 2008), and the case of talin reinforcement (Elosegui-Artola *et al.*, 2014). We study the two cases of slip and catch bond behaviour for the off-rate of the binder/ligand bonds. For all case combinations, we analyze the time evolution and the behaviour while changing the rigidity of the substrate. We do a parametric analysis to understand the role of the model parameters in the cell adhesion mechanics.
In Chapter 3 we study the mechanics of a cell seeded on a substrate with a rigidity gradient to understand how positive and negative durotaxis work. We integrate a

Finite Elements model of cell migration with the stochastic clutch model for cell adhesion.
In Chapter 4 we present a multiscale clutch model. Our goal is to reproduce the biological behaviour of the main cell-ECM adhesion components, while reproducing the behavior at the adhesion complex level. We use models of individual adhesion components. We introduce spatial dependence in the substrate displacement: we model the ECM mechanics by means of Green's functions solved at each ligand position. In the clutch model, each adhesion binder made of integrin, talin, vinculin and many other adaptor proteins was modelled as a unique linear spring. Here, we derive an upgraded model of the FA structure. The talin rod is modelled with its 13 domains which can unfold and refold, depending on force in a non-linear way. Specific vinculin binding sites (VBSs) and actin binding sites (ABSs) on talin are implemented. The importance of each talin domain, with its VBSs and ABSs, has been experimentally studied by depleting some domains of the talin rod. We model computationally these depletions and reproduce experimental results. We also propose future experiments of interest.
In Chapter 5 we gather the conclusions of the thesis and propose avenues for future research in this field.

1.5 List of publications

This manuscript gathers most of the published and unpublished (to this date) original research done by the author during his PhD. The following list organizes the original contributions of this manuscript's author.

- J. Betorz, G. R. Bokil, S. M. Deshpande, S. Kulkarni, D. Rolando, C. Venturini, and P. Sáez. A full computational model of cell motility: Early spreading, cell migration and competing taxis. *International Journal of Engineering Science (Submitted)*
- A multi-scale clutch model for focal adhesion mechanics. *In Preparation*
- Adhesion dynamics explains durotaxis across cell types. *In Preparation*

1.6 Conference proceedings

During the PhD thesis, the research done has been presented at a number of international conferences. The presentations delivered by the PhD candidate are listed below.

- ***C. Venturini*** *and P. Sáez.* Coupling of cell adhesion and actin cortex mechanics. *Theoretical and Computational Modelling in Mechanobiology. Barcelona, ES (2018).*
- ***C. Venturini****, M. Arroyo and P. Sáez.* Coupling of cell adhesion and actin cortex mechanics. *CISM-AIMETA Advanced School on Cell Mechanobiology: Theory and Experiments on the Mechanics of Life. Udine, IT (2018).*
- ***C. Venturini****, M. Arroyo and P. Sáez.* A generalized clutch model to explain cell adhesion mechanics. *EMBL-IBEC Winter Conference, Engineering multicellular systems. Barcelona, ES (2020).*
- ***C. Venturini*** *and P. Sáez.* Improved clutch model for cell adhesion mechanics. *14th World Congress on Computational Mechanics and 8th European Congress on Computational Methods in Applied Sciences and Engineering (WCCM XIV, ECCOMAS2020). Virtual congress (2021).*
- ***C. Venturini****, P. Roca-Cusachs and P. Sáez.* Talin manipulation in cell adhesion through an improved clutch model. *American Physical Society March Meeting 2021. Virtual congress (2021).*

Chapter 2

Review of the clutch model

The original clutch model was first proposed to rationalize experimental data of traction forces in embryonic chick forebrain neurons (Chan and Odde, 2008). Since then, it has been further developed to include, for example, the reinforcement produced by vinculin binding to talin observed in mouse embryonic fibroblasts (MEFs) (Elosegui-Artola *et al.*, 2016).
In Section 2.1 we present the original clutch model (Chan and Odde, 2008), and in Section 2.2 we present the model extension of talin-based reinforcement (Elosegui-Artola *et al.*, 2014), to which we will refer as the improved clutch model. The goal is to closely study the model to, later, exploit or enrich it, depending on its strengths and weaknesses. We analyze in detail all model variables and parameters against the substrate stiffness. Finally, we summarize the main results of these models and critically analyze them against data in the literature.

2.1 The original clutch model

Two decades after the introduction of the clutch hypothesis (Mitchison and Kirschner, 1988), the original "motor-clutch" model (Chan and Odde, 2008) used a stochastic approach to analyze the effect of substrate stiffness in the tractions exerted by the cell. This conceptual framework includes some of the most important mechanisms in cell adhesion (see Figure 2.1).
Actin polymerization at the leading edge of the cell, together with the pulling forces of myosin motors inside the actin network, induce an F-actin retrograde flow. Actin filaments flow from the cell leading edge where adhesions form towards the cell center. The clutch model relates the velocity of the retrograde flow with the ECM and the

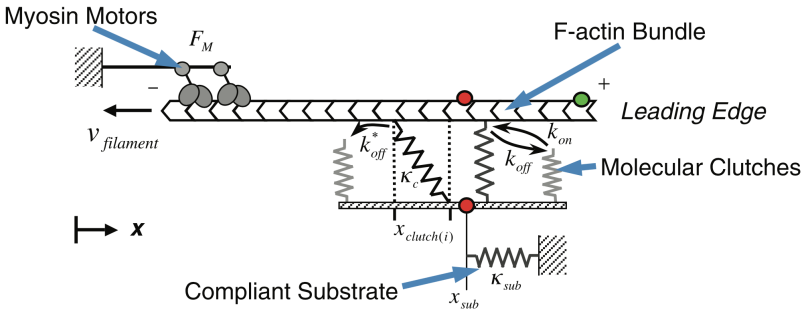

Figure 2.1: Schematic of a motor-clutch model: myosin motors pull an actin filament with force F_M, at velocity $v_{filament}$. Clutches can bind and unbind actin with rates k_{on} and k^*_{off}. The bound clutches have a displacement $x_{clutch(i)}$, the substrate has a displacement x_{sub} and κ_c, κ_{sub} are respectively the stiffness of the clutches and the substrate (Chan and Odde, 2008).

adhesion molecules mechanics. Inside an AC, the molecular clutches link the actin filaments with the ECM, and are allowed to bind and unbind. The molecular clutches are made of several adaptor proteins, among which the most important are vinculin, talin, integrin and fibronectin. Vinculin binds to talin. Talin links the actin filaments at the top, to the integrin at the bottom. Finally, the transmembrane protein integrin, connects to a ligand in the ECM, like fibronectin. In this model, only one type of bond is considered, which is assumed to be the "weakest link" in the adhesion chain. Bound binders deform and transmit force to the underlying substrate. The retrograde flow is inversely correlated to the transmitted force, thus it is slowed down when the traction force increases. The stiffness of the substrate controls the force loading rate, i.e. the speed at which force is built in bound clutches, thus influencing the resulting cell traction and retrograde flow.
The model is based on Monte Carlo simulations, with fixed time step. Inside each MC simulation, at each time step, the molecular clutches are first allowed to bind to the F-actin bundle with binding rate k_{on}:

$$k_{on} = k_{ont} d_{int}, \tag{2.1}$$

where k_{ont} is the constant binding rate and d_{int} is the density of integrins on the membrane.
Then, the bound clutches can unbind following their dissociation rate k^*_{off}. Binders following a slip behaviour have an unbinding rate which increases exponentially with

force according to Bell's Model:

$$k_{off}^{*} = k_{off,slip} e^{\left(\frac{F_c}{F_{b,slip}}\right)}, \tag{2.2}$$

where $k_{off,slip}$ is the dissociation rate in absence of force, $F_{b,slip}$ is the characteristic bond rupture force, and F_c is the force inside one binder:

$$F_{c(i)} = \kappa_c (x_{c(i)} - x_{sub}). \tag{2.3}$$

κ_c is the stiffness of the clutch, $x_{c(i)}$ is the displacement of the molecular clutch i and x_{sub} is the displacement of the substrate. In the catch bonds, the k_{off}^{*} becomes:

$$k_{off}^{*} = k_{off,slip} e^{\left(\frac{F_c}{F_{b,slip}}\right)} + k_{off,catch} e^{\left(\frac{-F_c}{F_{b,catch}}\right)}, \tag{2.4}$$

where $k_{off,slip}$ and $k_{off,catch}$ are the dissociation rates in absence of force via the slip and catch pathway respectively. $F_{b,slip}$ and $F_{b,catch}$ are the characteristic bond rupture forces via the slip and catch pathway, respectively. We will refer to the model of a cell expressing slip or catch bonds without talin reinforcement as slip and catch cases, respectively. All binders behave independently of the others, and the time at which one event happens is computed, e.g. for the binding event, as:

$$\tau_i = \frac{-\ln \xi_i}{k_{on(i)}}, \tag{2.5}$$

where ξ_i, $i = 1 \dots n_c$, are independent random numbers uniformly distributed over $[0, 1]$, and n_c is the total number of binders. The time of all possible events is computed and only the events happening before a fixed time step Δt are executed.
After all the binding and unbinding events have been updated, the bound probability P_b is calculated as:

$$P_b = \frac{n_{eng}}{n_c}, \tag{2.6}$$

where n_{eng} is the number of engaged binders. The clutches and the substrate are treated as simple Hookean springs, i.e. the applied force scales linearly with respect

to the displacement. Thus the force on the substrate F_{sub} is:

$$F_{sub} = \kappa_{sub} x_{sub}. \tag{2.7}$$

The actin velocity v_f is inversely related to the substrate force F_{sub}, as a loaded substrate will decrease the movement of the actin filaments. The force-velocity relation is given by:

$$v_f = v_u \left(1 - \frac{F_{sub}}{F_{stall}} \right), \tag{2.8}$$

where v_u is the unloaded velocity of myosin and F_{stall} is the total myosin motors stall force, defined as:

$$F_{stall} = n_m F_m. \tag{2.9}$$

F_m is the stall force of one myosin motor and n_m is the number of motors. Once the state of the cluster with free and bound clutches is found, the F-actin velocity is calculated using the value of F_{sub}, and bound clutches are displaced by $\Delta x = v_f \Delta t$. The new displacements of all clutches $x_{c(i)}$ are computed, and the new displacement of the substrate becomes:

$$x_{sub} = \frac{\kappa_c \sum_{i=1}^{n_{eng}} x_{c(i)}}{\kappa_{sub} + n_{eng} \kappa_c}. \tag{2.10}$$

From the displacement of the substrate, the force against which the myosin motors are working, F_{sub}, is determined and is used to get the actin velocity for the following time step. Also the force along each molecular clutch is obtained and is used to compute the rate k^*_{off} for the next step.
The Young's modulus E of the substrate is related to the substrate stiffness κ_{sub} through the relation (Ghibaudo *et al.*, 2008):

$$\kappa_{sub} = \frac{E 4 \pi a}{9}, \tag{2.11}$$

where a is the radius of the AC. Moreover, the cell traction P applied to the substrate is computed as:

$$P = \frac{F_{sub}}{\pi a^2}, \tag{2.12}$$

where πa^2 is the area occupied by the n_c molecular clutches considered in the AC.

2.2 The clutch model with talin reinforcement

The clutch model was extended in order to consider the effect of talin unfolding and vinculin binding in the adhesion behaviour (Elosegui-Artola *et al.*, 2014). Here, the binding and unbinding rates exactly refer to the integrin-fibronectin bond, which is considered to behave as a catch bond. Talin unfolding is a mechanosensing event triggered by force: the actin-integrin adaptor protein talin unfolds under force and exposes binding sites to vinculin. Talin unfolding follows a slip bond behaviour, i.e. when a force is applied, the unfolding time decreases exponentially with force. For low forces, integrin unbinding is faster than talin unfolding (the binder breaks and the force goes to zero), whereas for high forces, talin unfolding is faster (Figure 2.2). Therefore, above a stiffness threshold, talin unfolds revealing cryptic vinculin binding

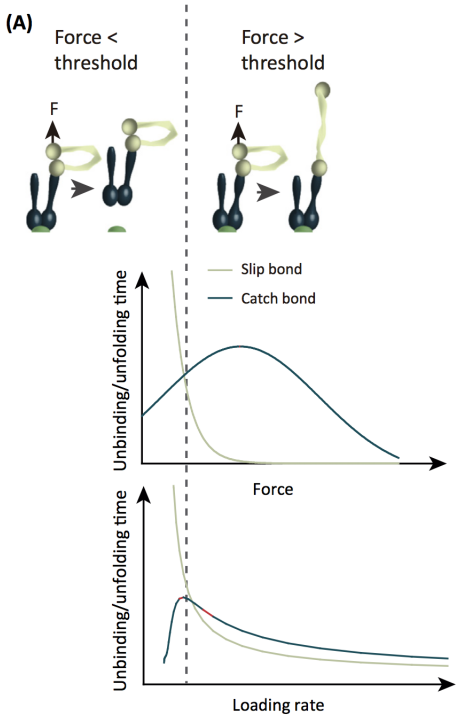

Figure 2.2: Top: if the applied force is below the threshold, integrin unbinds before talin can unfold; if the force is above the threshold, talin unfolds and the clutch remains bound. Bottom: effect of force or loading rate on the unbinding time of integrin-fibronectin bond (catch) and unfolding time of talin (slip) (Elosegui-Artola *et al.*, 2018).

sites, and vinculin binds leading to integrin recruitment and adhesion reinforcement. Below that stiffness threshold, integrins unbind before talin can unfold, so no more integrins are recruited.

As talin is not modelled as a protein with its proper spatial position, though its unfolding mechanics is taken into account, we consider the binder chain spatially made of substrate and integrin, directly bound to actin, so we define the displacement of the integrin as $x_{int(i)} = x_{c(i)} - x_{sub}$.

Now the binding rate k_{on} in Eq. 2.1 evolves during time, as the density of integrins d_{int} can change. At each time step, the unbinding rate $k^*_{off}(F)$ for the integrin-fibronectin catch bond and the unfolding rate $k_{unf}(F)$ for the talin slip bond, are computed for each bound clutch. Unbinding and unfolding times are determined stochastically according to k^*_{off} and k_{unf}. If unfolding happens before unbinding, then either vinculin can bind to talin with a force-independent rate k_{onv}, or talin can refold with rate $k_{fold}(F)$. If vinculin binding occurs, there is adhesion reinforcement and the integrin density, d_{int}, is increased by int_{add} integrins/μm^2. If vinculin binding does not occur, then integrin density is decreased by int_{add}, reflecting that adhesions shrink if force application is decreased (Balaban *et al.*, 2001) (Riveline *et al.*, 2001). However integrin density is never allowed to go below the initial value, nor above the maximum integrin density, m_r, as integrins cannot be closer than a minimum distance. We call d^0_{int} the initial density of integrins.

This model with talin reinforcement has been able to explain the experimental results in Mouse Embryonic Fibroblasts (MEFs) (Elosegui-Artola *et al.*, 2016) (Figure 2.3). Traction forces in embryonic chick forebrain neurons (Chan and Odde, 2008) are

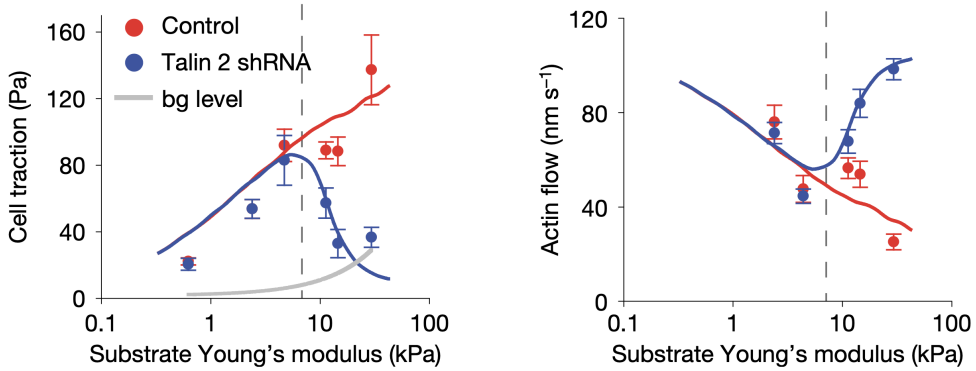

Figure 2.3: Experiments and improved clutch model results for cell traction P and actin velocity v for MEFs with talin (red), and with talin depletion (blue) (Elosegui-Artola *et al.*, 2016).

different than in MEFs as a result of different adhesion mechanics.

2.3 Results

Here in Sections 2.3.1 and 2.3.2, we present the computational results for the clutch model without and with talin reinforcement, respectively. We run MC simulations with constant time step $\Delta t = 0.005$ s. We take as final time $t_f = 100$ s and we let the simulation run, so that we go through many loops in which the adhesion complex is completely disengaged, i.e. P_b goes to zero. Every time that $P_b = 0$, all the model variables reach their initial values, so we can consider that the MC simulation ends and starts again. Therefore fixing the final time t_f, the number of concatenated MC simulations changes depending on the model parameters. The results are values of the variables averaged over several MC simulations.
The codes used here and in the entire thesis are run in MATLAB. The simulations of the clutch models in this chapter, with the parameters in Tables 2.1 and 2.2, can be run on a standard laptop in a few minutes.

2.3.1 Clutch model with slip and catch bonds

In this section we present the results for the slip and catch cases detailed in Section 2.1. We compare these two cases to analyse how a different unbinding rate influences the model variables. We compute the slip and catch cases of cell adhesion for a set of material parameters that we consider the control case (Table 2.1). For the Young's modulus of the substrate we take 16 values with exponential distribution inside the range 0.1 – 100 kPa, as it is the usual range for experimental data in the literature, covering the stiffnesses from brain tissue to bones (Engler *et al.*, 2006). All the parameters for the slip (Chan and Odde, 2008) and catch (Elosegui-Artola *et al.*, 2016) cases are taken from literature. As in the catch case the radius of adhesion a and the number of ligands n_c are given, considering a round adhesion we get that ligands are equispaced with distance $d \approx 100$ nm. In order to have ligands spaced with the same distance and get comparable cases, we set $a = 447$ nm in the slip case. In the catch case, the parameters inside the k^*_{off} are obtained fitting the curve of the lifetime for $\alpha_5\beta_1$ integrins (Kong *et al.*, 2009), which are the main integrins present in MEFs from previous experimental data (Elosegui-Artola *et al.*, 2016). Moreover, k^*_{off} is increased at very low forces (< 1 pN) to take into account that integrins not submitted to CMR have a shorter lifetime. The lifetime τ, computed as the inverse of the unbinding rate k^*_{off}, with the parameters used in the model, is shown in Figure 2.4. We decide to compare slip and catch with these sets of parameters because these lifetimes give comparable values for the cell traction P (Figure 2.5).

Parameters	Slip (Chan and Odde, 2008)	Catch (Elosegui-Artola *et al.*, 2016)
E (kPa)	0.1 - 100	0.1 - 100
a (nm)	447	1700
n_c	75	1200
κ_c (pN/nm)	5	1000
k_{ont} ($\mu m^2/s$)	1	2.11×10^{-4}
d_{int} (int /μm^2)	1	300
$k_{off,slip}$ (s^{-1})	0.1	-
$F_{b,slip}$ (pN)	2	-
F_m (pN)	2	2
n_m	75	800
v_u (nm/s)	120	110

Table 2.1: For the slip and catch cases, values for the parameters used in the plot against substrate stiffness in Figure 2.5, and in the time evolution plots in Figures 2.6, 2.7. For the catch case, the unbinding rate with CMR is $k^*_{off} = 0.00079938\ e^{(F_c/8.16)} + 10.14\ e^{(-F_c/6.24)} + 900\ e^{(-F_c/0.01)}$.

In order to visualize the influence of substrate rigidity, we plot the model variables

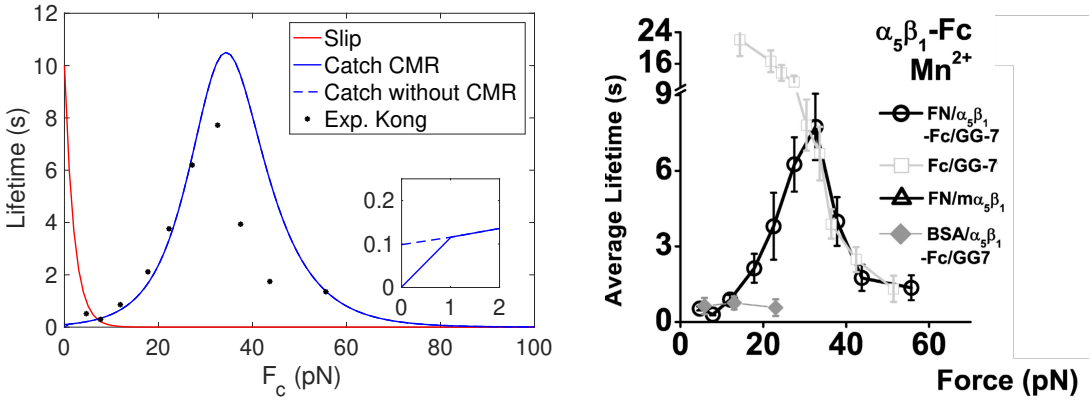

Figure 2.4: Left: Lifetime of the weakest link for slip (red) and catch with CMR (solid blue) cases, as used in Figures 2.5, 2.6, 2.7, and dots (black) for the experimental data of the catch case. Zoom of the lifetime for small forces: catch case with CMR (solid blue) and original fitting of the data (dashed blue). Right: Experimental data for the lifetime of integrin $\alpha_5\beta_1$ in their maximum activation state, in presence of ions of Mn^{2+} (Kong *et al.*, 2009).

against the Young's modulus of the substrate E (Figure 2.5). The clutch model with slip behaviour explains the biphasic relationship between substrate rigidity and actin

retrograde flow, first experimentally found in embryonic chick forebrain neurons (Chan and Odde, 2008).
By averaging over time, we observe that the slip and catch cases follow different trends. In the slip case, the stiffer the substrate the fewer bound binders are present in the

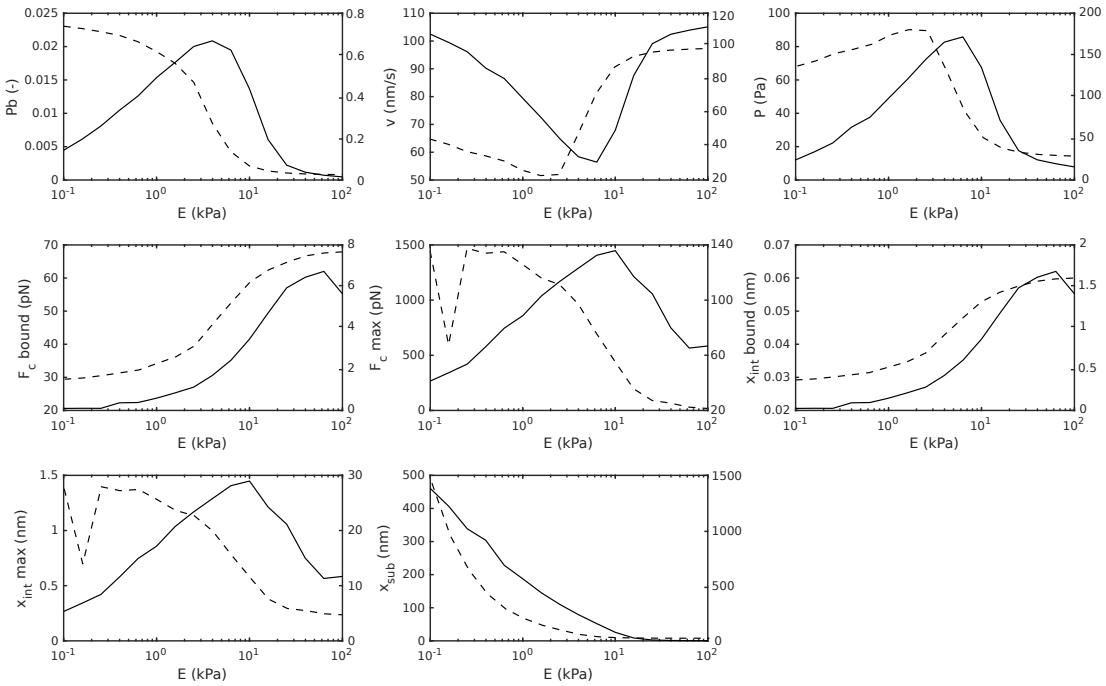

Figure 2.5: Slip (dashed line, with corresponding y-axis on the right) and catch (solid line, with corresponding y-axis on the left) cases comparison. Plot against Young's modulus of the substrate E of the variables P_b, v, P, F_c over bound binders, F_c^{max}, x_{int} over bound binders, x_{int}^{max} and x_{sub}. The parameters are taken from Table 2.1.

cluster, while in the catch case the number of bound binders first increases and then decreases with stiffness. The slip lifetime explains why the P_b is maximum for the softest substrate. Indeed the slip lifetime is maximum for the minimum force, and the minimum force F_c over bound binders is reached for the softest substrate. In the catch case, the two-phase graphs of bound probability P_b, cell traction P, maximum force F_c^{max} and maximum displacement x_{int}^{max} can be justified by the lifetime of catch bonds. As the average force F_c over bound binders increases for stiffer substrates, forces in the middle of the range correspond to the longest lifetimes. Longer lifetimes mean more bound binders, higher maximum forces and higher maximum displacements.
For both slip and catch cases, the cell traction P is maximum for a specific substrate rigidity, called optimal stiffness (Figure 2.5). Above this rigidity value there is frictional

slippage, as can be seen in the time evolution graphs for the stiffest substrate (Figures 2.6, 2.7). The average displacements of the integrins and the substrate follow a similar trend in the slip and catch cases. Indeed the substrate displacement decreases for stiffer substrates, as more rigid springs allow less deformation. Consequently, the integrins, connected in series to the substrate, can deform more in rigid substrates.
In order to better understand the dynamics, in Figures 2.6 and 2.7 we plot the time evolution of the model variables, for the slip and catch case respectively, for $E = 1\,\text{kPa}$ and $E = 10\,\text{kPa}$. The variables analyzed are the probability for binders of being bound P_b, the actin velocity v, the cell traction P, the maximum and the average force over the bound binders F_c^{max} and $F_{c,bound}$, the maximum and the average displacement for bound binders x_{int}^{max} and $x_{int,bound}$, and the displacement of the substrate x_{sub}. When there are no bound binders, all the variables go to their initial values: the actin velocity takes its maximum unloaded value, and forces and displacements go to zero. In the slip case, the cluster passes from being 80% to 20% bound while moving to stiffer substrates, while in the catch case it has a similar probability for all stiffnesses, around 1-2%. As anticipated, because of frictional slippage the lifetime of adhesion complexes becomes shorter for stiffer substrates. More precisely, in the slip case the average load-and-fail cycle for $E = 1\,\text{kPa}$ lasts 7.27 s and for $E = 10\,\text{kPa}$ it lasts 0.215 s. In the catch case, for $E = 1\,\text{kPa}$ it is 4.25 s and for $E = 10\,\text{kPa}$ it is 0.344 s. The results of the model are not in agreement with the experimental FA lifetime of $\approx$ 55 minutes (Stricker *et al.*, 2013).
To understand how many MC simulations are enough to give a stable solution, we run the case where MC simulations are the longest, for a bigger final time t_f: slip case, for $E = 0.1\,\text{kPa}$, and with $t_f = 1000\,\text{s}$. As the MC simulations are concatenated, in order to do the average over MCs we average the variable over time. For $t_f = 1000\,\text{s}$, the average of the cell traction is $P \approx 138\,\text{Pa}$, while for $t_f = 100\,\text{s}$ the average is $P \approx 132\,\text{Pa}$ (Figure 2.8). As the two values are similar, we consider that the number of MCs taking place before the smallest final time is enough to get a stable solution. In this chapter, we decide to use MC simulations as we can show that MC and Gillespie simulations provide similar results, both for the time evolution and the behaviour against the stiffness of the substrate (Figure 2.9).
A parametric analysis of the clutch model for the slip and catch cases has been carried out (Appendix A.1) in order to understand the influence of each parameter on the model variables.

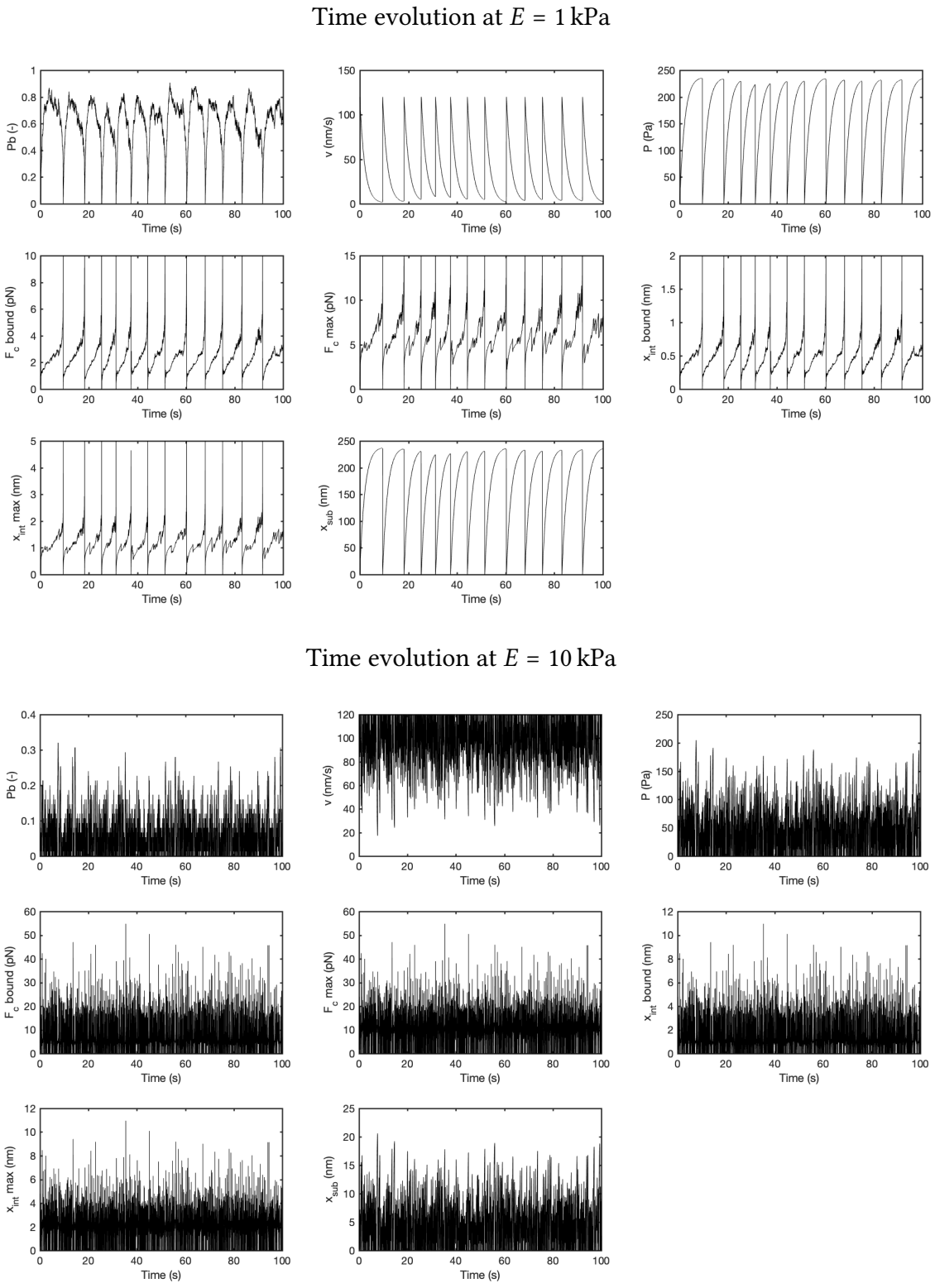

Figure 2.6: For the slip case, time evolution for the variables P_b, v, P, F_c over bound binders, F_c^{max}, x_{int} over bound binders, x_{int}^{max} and x_{sub}, for two different values of the Young's modulus of the substrate E. The parameters are taken from Table 2.1. The MC loops to get a cluster completely made of free binders are considerably shorter for stiffer substrates.

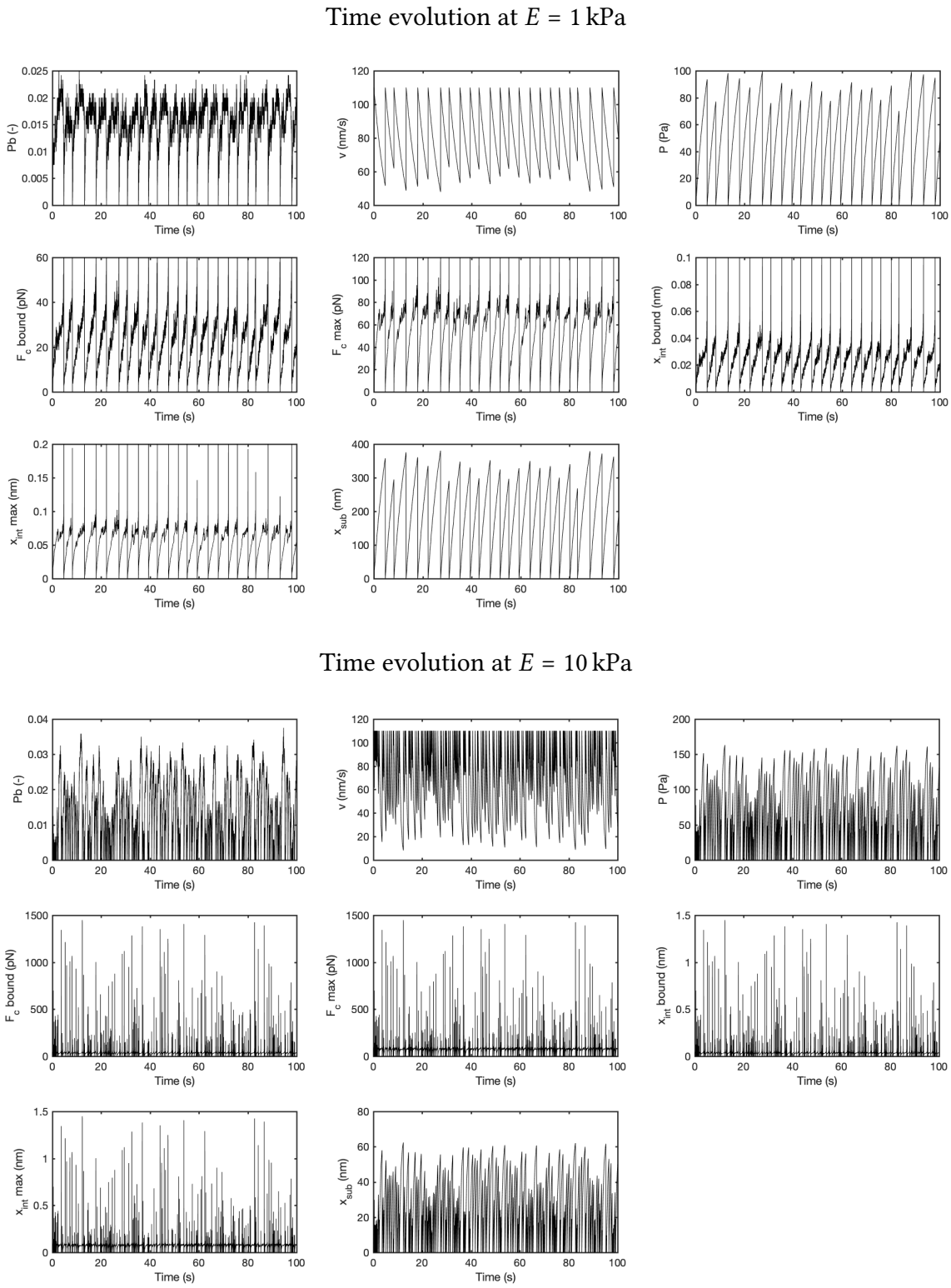

Figure 2.7: For the catch case, time evolution for the variables P_b, v, P, F_c over bound binders, F_c^{max}, x_{int} over bound binders, x_{int}^{max} and x_{sub}, for two different values of the Young's modulus of the substrate E. The parameters are taken from Table 2.1. The MC loops to get a cluster completely made of free binders are considerably shorter for stiffer substrates.

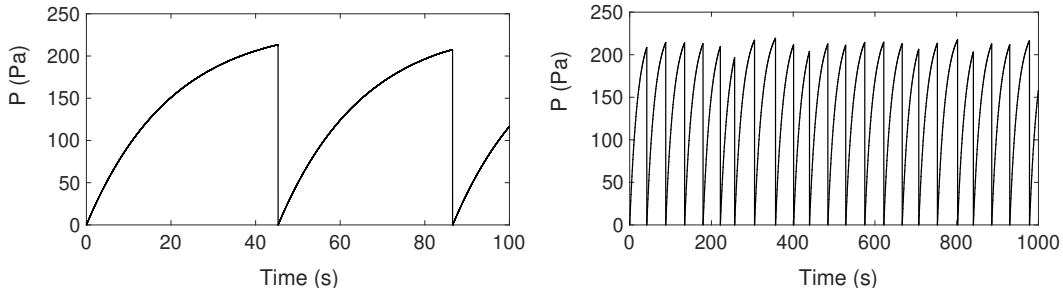

Figure 2.8: For the slip case, fixing the Young's modulus of the substrate $E = 0.1$ kPa, comparison of the number of MC simulations for two different final times $t_f = 100$ s and $t_f = 1000$ s.

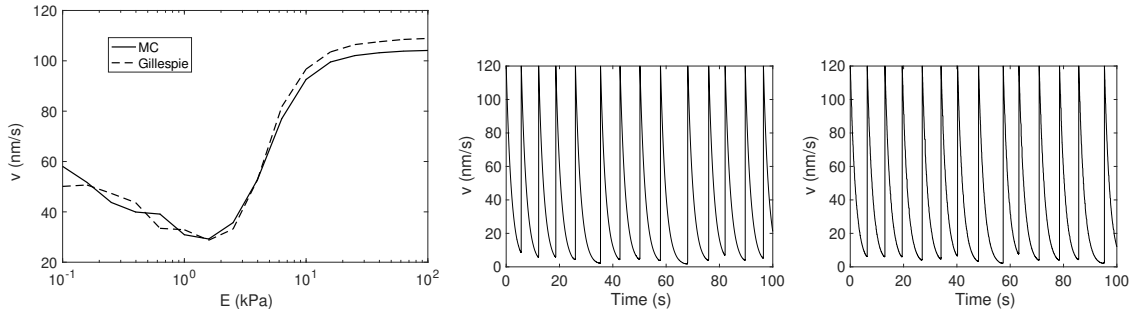

Figure 2.9: For the slip case in Table 2.1. Left: Actin velocity v against the Young's modulus of the substrate E. Comparison between MC (solid line) and Gillespie (dashed line) simulations. Right: Time evolution of the actin velocity v, fixing the Young's modulus of the substrate $E = 1$ kPa. Comparison between MC (left) and Gillespie (right) simulations.

2.3.2 Talin unfolding induces adhesion reinforcement

In this section, we present the results for the case of talin reinforcement (Section 2.2). We consider that the fibronectin-integrin bond follows a catch bond behaviour. We aim at analysing this case, as well as comparing its behaviour with the catch case without talin reinforcement.

The material parameters are taken from literature (Table 2.2) (Elosegui-Artola *et al.*, 2016). The unbinding rate k^*_{off} for $\alpha_5\beta_1$ integrins is considered with CMR as in the catch case without talin reinforcement. The new parameters k_{onv}, int_{add} and m_r are adjusted, without experimental reference.

In order to understand the influence of substrate rigidity, we plot the variables against the Young's modulus of the substrate E (Figure 2.10). The bound probability P_b, the

Parameters	**Catch** (Elosegui-Artola *et al.*, 2016)
E (kPa)	0.1 - 100
a (nm)	1700
n_c	1200
κ_c (pN/nm)	1000
k_{ont} (µm^2/s)	2.11×10^{-4}
d^0_{int} (int /µm^2)	300
F_m (pN)	2
n_m	800
v_u (nm/s)	110
k_{onv} (s^{-1})	1×10^8
int_{add} (int /µm^2)	24
m_r (int /µm^2)	15000

Table 2.2: For the model with talin reinforcement, values for the parameters used in the plot against substrate stiffness in Figure 2.10. The unbinding rate with CMR is k^*_{off} = 0.00079938 $e^{(F_c/8.16)}$ + 10.14 $e^{(-F_c/6.24)}$ + 900 $e^{(-F_c/0.01)}$.

actin velocity v and the cell traction P are not biphasic as in the catch case without talin reinforcement (Figure 2.5). Except in a small interval for the stiffest substrates, the probability P_b and the cell traction P are monotonically increasing, while the actin velocity v is monotonically decreasing. These trends can be explained by the vinculin-talin reinforcement. Indeed, the stiffer the substrate, the more talins unfold and allow vinculin to bind, giving an increasing number of binders with vinculin (Figure 2.10). More vinculins bound produce more integrins recruitment, thus increasing the integrin density d_{int}. Following Eq. 2.1, the binding rate increases, and so do the probability, the force and the cell traction P. The velocity v has a behaviour complementary to the cell traction, as more cell traction means less capacity for the actin filaments to follow their retrograde flow. Contrarily, in the catch case without the vinculin-talin reinforcement, the constant density of integrins gives a constant binding rate, resulting in probability and cell traction that reproduce the catch lifetime shape, as previously mentioned. The model with and without talin reinforcement reproduce previous results (Elosegui-Artola *et al.*, 2016).

We conclude by showing how the average force F_c over bound binders, together with its standard deviation, behaves while varying the Young's modulus of the substrate E and the number of ligands n_c (Figure 2.11). We consider three values for the Young's modulus of the substrate (E = 0.1, 1, 10 kPa) and three values for the number of fibronectin

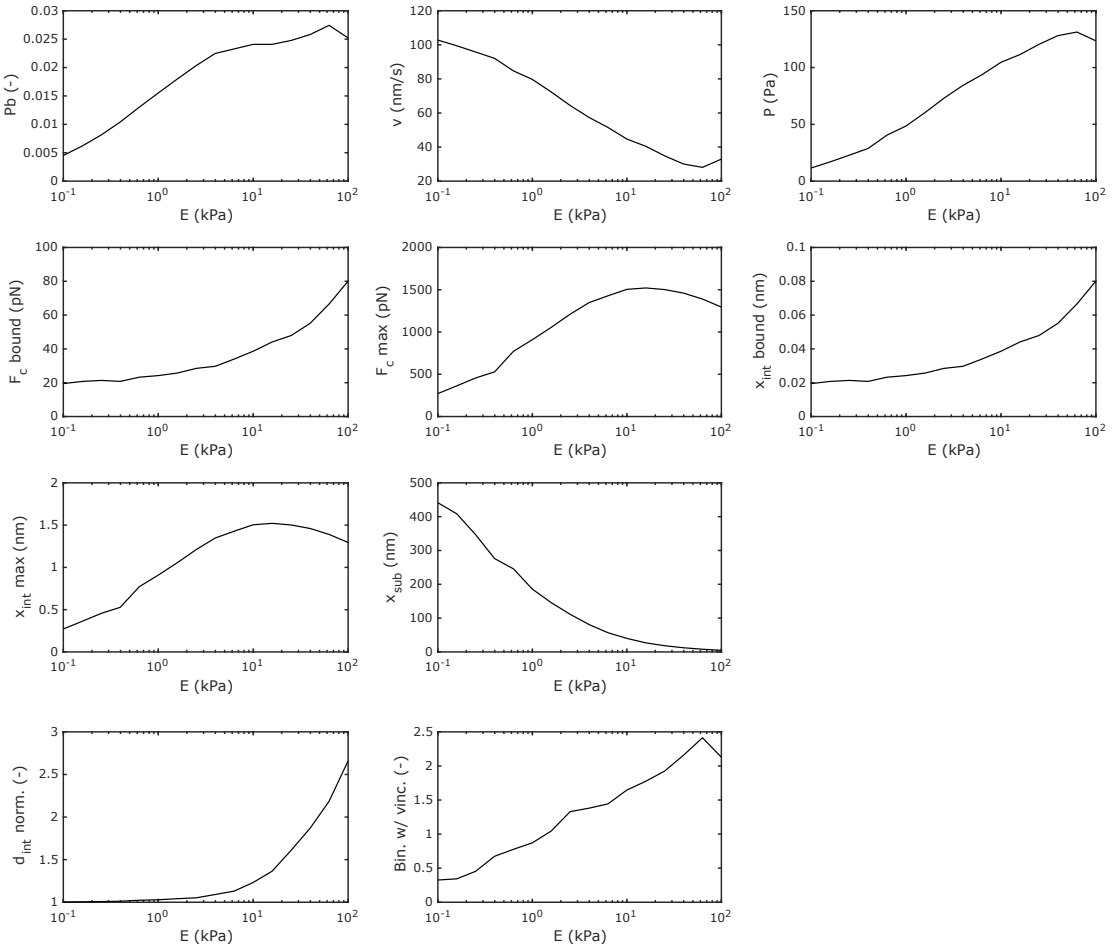

Figure 2.10: For the model with talin reinforcement, plot against Young's modulus of the substrate E of the variables P_b, v, P, F_c over bound binders, F_c^{max}, x_{int} over bound binders, x_{int}^{max}, x_{sub}, $d_{int,norm}$ and # binders with vinculin. The parameters are taken from Table 2.2.

binders, kept equal to the number of myosin motors ($n_c = n_m = 75, 1200, 2000$). The rest of parameters are from Table 2.2. For visualization purposes, the final time is kept fixed to $t_f = 25$ s and the y-limit for the force is set to $F_c = 100$ pN. This y-limit does not show the force peaks up to 300 pN. The higher the Young's modulus of the substrate E, the sooner the MC simulations end. Indeed, for higher substrate rigidity the binders break more easily and the load-and-fail cycle is shorter. The fewer the fibronectin molecules n_c, the sooner the MC simulations end, because fewer binders unbind faster. A parametric analysis of the clutch model with talin reinforcement has been carried out (Appendix A.2).

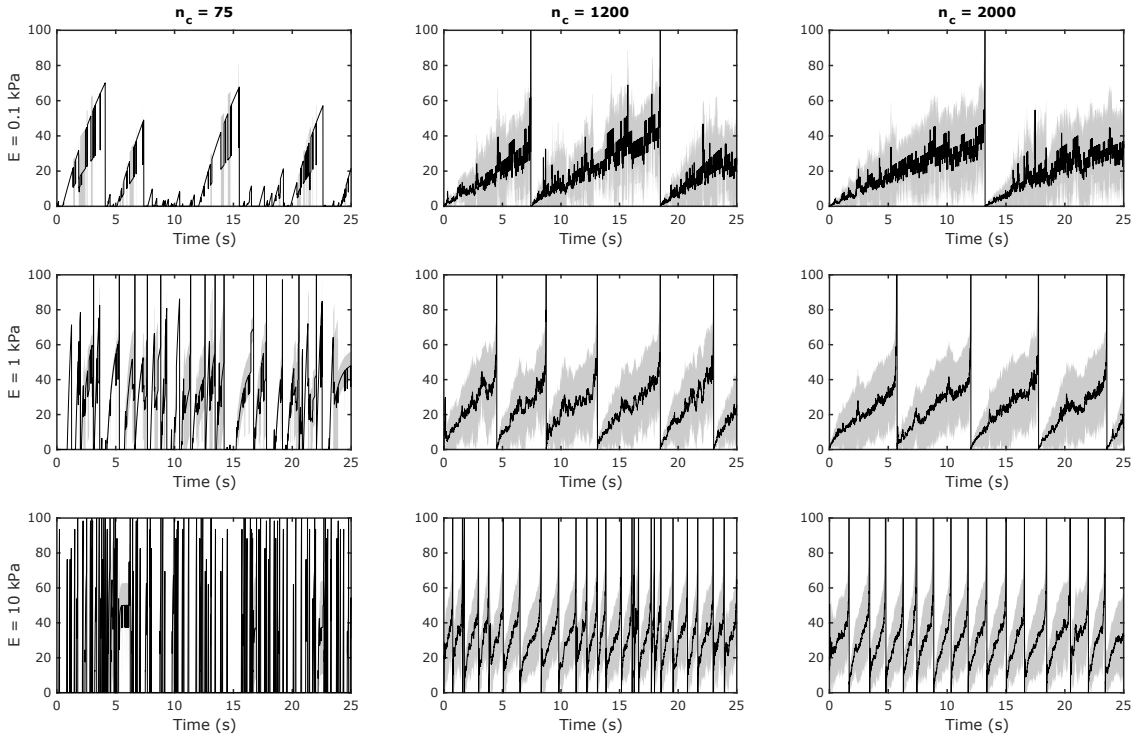

Figure 2.11: For the model with talin reinforcement, plot of the average force F_c over bound binders during time, for three different Young's modulus E (rows) and three different numbers of ligands n_c (columns). The standard deviation is shown in the light grey shade. The rest of parameters are taken from Table 2.2.

2.4 Discussion

The molecular clutch model has been very successful in reproducing the adhesion behaviour at the cell scale. The model reproduces the cell traction P and the actin velocity v for different cell types. Therefore, it represents an excellent option when we aim at studying the behaviour of an entire cell. However, due to a number of simplifications introduced in the modelling of the adhesion mechanism, some variables of the model contradict previous experimental evidence. In the following we outline some of these limitations. When specifically mentioning data, we refer to the full model with talin reinforcement (Elosegui-Artola *et al.*, 2014) (Sections 2.2, 2.3.2), but these conclusions also apply to the original clutch model (Chan and Odde, 2008) (Sections 2.1, 2.3.1).

- The clutch models consider **a single linear spring for the substrate**. The spring has displacement x_{sub} and stiffness κ_{sub}, and is connected in series to a number n_c of linear springs accounting for the binders (Figure 2.1). Modelling the substrate with a single spring gives one single substrate displacement. The modelling could be improved by taking into account that the substrate displacement changes point-wise, depending on the locations of the bound binders.

- As we discussed above, experimental data show that the adaptor proteins building an adhesion chain have different z-position (Shtengel *et al.*, 2009) and different velocities (Hu *et al.*, 2007). The clutch models **simplify the adhesion chain**, modelling it as a unique linear spring accounting for integrin, talin and vinculin. An enhancement could be the modelling of each protein separately, to take into account their mechanical behavior. Although the mechanosensing of talin has been included in the improved clutch model through an unfolding event that fosters vinculin binding and adhesion reinforcement, the actual mechanical response of the talin rod (Yao *et al.*, 2016) has not been studied in the context of cell adhesion.

- The displacement of the entire adhesion chain cannot accommodate the displacements for all the adhesion molecules that it represents. $\alpha_5\beta_1$ integrins can reach a displacement of 50 nm from their extended length, which is the high affinity state from which integrins can bind and create focal adhesions (Figure 2.13). Talin can be found in two different isoforms: talin1 is present in cell adhesion in muscle and nonmuscle cells, while talin2 is present only in muscle cells. Talin2 is 74% identical and it has a similar size to talin1 (Gough and Goult, 2018). Talin1 length in its closed autoinhibited state is $\approx$ 15 nm, while in its open, fully folded state, it measures $\approx$ 60 –80 nm (Dedden *et al.*, 2019, Goult *et al.*, 2013a, Liu *et al.*, 2015a). In its fully unfolded state, its end-to-end length reaches $\approx$ 770 nm (Yao *et al.*, 2016). Therefore talin can have a displacement of $\approx$ 700 nm.
  In the improved clutch model, the displacement of the adhesion binder is $x_c - x_{sub} = 2$ nm (Figure 2.10). This displacement should be up to 50+700 = 750 nm, giving a mismatch between the real displacements of the adhesion chain and the model results.

- Moreover, the forces at each molecular clutch are higher than previous experimental data. Force estimations at single integrins during cell adhesion have been measured in the range 1 – 100 pN (Kechagia *et al.*, 2019, Sun *et al.*, 2016). More precisely, FRET-based molecular sensors pinpointed the single integrin force in 1 – 5 pN (Morimatsu *et al.*, 2013, 2015), which matches the 2 pN rupture

force of chain bonds (Jiang *et al.*, 2003), the mean force 2.5 pN sensed by vinculin (Grashoff *et al.*, 2010), and the force 7 – 10 pN sensed by talin (Austen *et al.*, 2015). DNA-based sensors established an higher range: 33 – 43 pN (Wang and Ha, 2013) in $\alpha_V\beta_3$ integrins, one of the most ubiquitous type of integrins across cell types. The lifetime both for $\alpha_5\beta_1$ integrins (Kong *et al.*, 2009) and $\alpha_V\beta_3$ integrins (Elosegui-Artola *et al.*, 2016) vanishes for forces larger than 60 pN. By estimating the number of bound integrins per unit area (Galior *et al.*, 2016), a force value of 1 – 2 pN in each integrin was found in adhered fibroblasts. In the improved clutch model, the force reaches high peak values, out of the biological range (Figure 2.11), at the time step just before the complete disengagement of the entire cluster. This computational issue can not be avoided running a Gillespie simulation (Figure 2.12). In Figure 2.10, for example, the average in

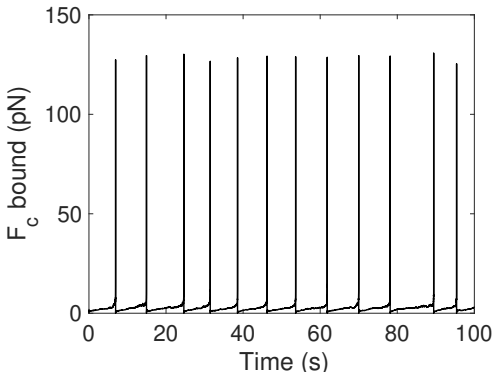

Figure 2.12: Gillespie simulation for the average force over bound binders F_c, fixing the Young's modulus of the substrate $E = 1$ kPa, for the slip case in Table 2.1.

time includes these peaks and, therefore, the maximum force on the binders reaches $F_c^{max} = 1500$ pN. In order not to include the peaks, we check the values from the time evolution plots. Excluding these peak values, the maximum force on an integrin is $F_c^{max} = 100$ pN. This result is still higher than the range found experimentally. As regards the average force on an integrin, the computational results give a range 0 – 60 pN (Figure 2.11), higher than the few picoNewtons value found experimentally along the molecular chain.

- Computational results give a FAs lifetime shorter than previous experimental data. In the improved clutch model, the longest FA lifetime obtained is 6.52 s, found for the softest substrate, $E = 0.1$ kPa. However, previous experimental data show that the time after which the focal adhesion cluster becomes completely free, the FA lifetime, is on average 55 minutes (Stricker *et al.*, 2013). Using the standard integrin lifetime, the FA enters a steady-state where binding and unbinding rates are equilibrated. Therefore, the CMR modification of integrins lifetime for low forces is the reason for the short FA lifetimes. The FA disassembly

can be modelled after understanding its real causes, which are the presence of particular proteins and ions, as we will see later on.

- We also observe that the results of the improved clutch model for the maximum vinculin/talin ratio, found for the stiffest substrate (Figure 2.10) for a total of $n_c = 1200$ binders and a bound probability $P_b = 0.025$, i.e. 30 bound binders, give 2.5/30 = 0.083 vinculins for each talin. Experimental results show vinculin/talin ratios of 1.4 (Atherton *et al.*, 2015) and 2.2 (Rahikainen *et al.*, 2019). As the model results are not in agreement with previous data, perhaps more than one single vinculin binding site on the talin rod should be considered.

- The model includes some **free parameters**, that could be obtained from previous experimental data.

  - Experimental values for adhesion length have been reported in the range 500 – 1500 nm (Oria *et al.*, 2017), being it the length of the major axis of the elliptical FA. Other data reported FA areas that, if we consider them circular, give us a radius of $a = 422\,\text{nm}$ (Horzum *et al.*, 2014). To reproduce experimental traction values, the radius of a FA has to be fixed to $a = 1700\,\text{nm}$, which is larger than the mentioned experimental data.

  - The stiffness of the linear spring modelling the binder $\kappa_c = 1000\,\text{pN/nm}$ does not have experimental evidence. If we analyze the stiffness of $\alpha_5\beta_1$ integrins as the force/displacement ratio (Figure 2.13), it results in $\kappa_c = 0.4 - 1$ pN/nm (Kong *et al.*, 2013, 2009). For $\alpha_V\beta_3$ integrins, a stiffness of $\kappa_c = 0.4 - 0.7$ pN/nm has been also found experimentally (Chen *et al.*, 2017). Therefore, the binder stiffness used in the model is higher than experimental values.

  - The force-dependent unbinding rate for integrins $\alpha_5\beta_1$ taken from experimental data (Kong *et al.*, 2009) is modified in the improved clutch model in order to take into account the CMR, by increasing the rate for forces lower than 1 pN. We consider that the lifetime should be increased for high forces instead of being reduced for the small ones. Indeed integrins with low forces have been bound for a small period of time, while integrins bearing high forces have been bound for a longer time, living cycles of mechanical reinforcement and therefore increasing the lifetime of their bonds.

  - In the improved clutch model, the binding rate of vinculin to talin $k_{onv} = 1 \times 10^8\ \text{s}^{-1}$ was probably adjusted to fit the experimental data. The binding

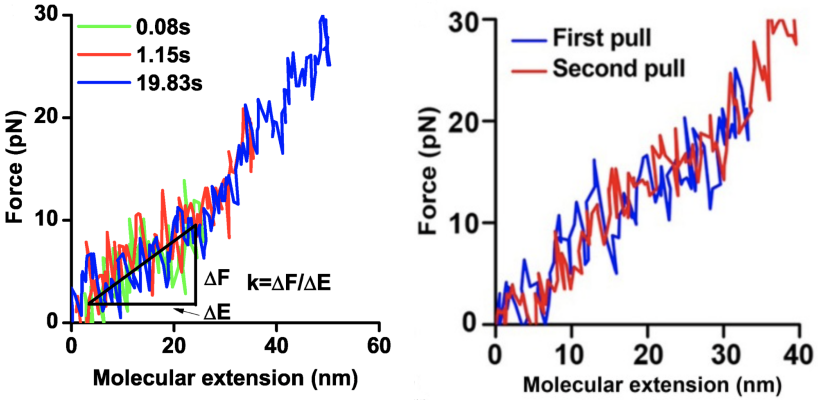

Figure 2.13: Force-extension curve for integrin $\alpha_5\beta_1$, giving a value for its stiffness (Kong *et al.*, 2013, 2009).

rate of vinculin has been measured to be $k_{onv} = 0.2\,s^{-1}$ (Hu *et al.*, 2016, Tapia-Rojo *et al.*, 2020). Therefore, we believe that the high value was needed as the model considers one of the 11 vinculin binding sites on talin, one of the two actin binding sites on talin, and adopts a talin unfolding rate k_{unf} not based on experiments.

Chapter 3

Adhesion mechanics explains durotaxis across cell types

Cells migration is critical in numerous processes of life, including embryogenesis, wound healing or tumor growth. Revealing precise methods to control cell migration represents a fundamental problem in biological science and tissue engineering. Durotaxis, the ability of cells to follow mechanical signals, has been shown ubiquitous across cell types. Even so, certain cell types follow positive stiffness gradients while others move toward softer regions. Unfortunately, the complexity of tackling durotaxis in-vivo and in-vitro and the poor understanding of how the physical mechanisms involved in cell migration cooperate to follow mechanical cues, have hindered durotaxis. Here, we provide a mechanistic rationale for durotaxis by integrating continuum models of cell migration with stochastic clutch models for cell adhesion.

3.1 Introduction

Cell migration is central to life (Friedl and Gilmour, 2009b, Mayor and Etienne-Manneville, 2016, Van Helvert *et al.*, 2018). It determines fundamental processes such as embryonic development, regeneration, wound healing or tumour invasion, among many other biological processes. Cells move guided by exogenous chemical (Kay *et al.*, 2008, Van Haastert and Devreotes, 2004), electrical (Cortese *et al.*, 2014, McCaig *et al.*, 2005) and mechanical signals in-vivo and in-vitro (Charras and Sahai, 2014, Shellard and Mayor, 2021, Sunyer and Trepat, 2020). For decades, there have been tremendous efforts to understand how cells organize themselves and with others to follow these stimuli. There is also an increasing interest in controlling cell migration through external cues. Controlling cell migration may allow us not only to propose

strategies to arrest tumour progression (Butcher *et al.*, 2009, Friedl and Wolf, 2003, Yamaguchi *et al.*, 2005) or boost regeneration of tissues, but also to precisely design novel tissue constructs (Langer and Tirrell, 2004, Wegst *et al.*, 2014).
Among other migration cues, such as chemotaxis (Van Haastert and Devreotes, 2004) or electrotaxis (Cortese *et al.*, 2014), durotaxis (Espina *et al.*, 2021, Shellard and Mayor, 2021, Sunyer and Trepat, 2020) represents a universal mode of directed cell migration across cell types. Fibroblasts (Lo *et al.*, 2000), smooth muscle cells (Wong *et al.*, 2003), neurons (Koser *et al.*, 2016) or cancer cells (DuChez *et al.*, 2019, McKenzie *et al.*, 2018, Ulrich *et al.*, 2009), among others, express durotaxis. Durotaxis has been also proved during development (Flanagan *et al.*, 2002, Koser *et al.*, 2016). A stiffness gradient exposes migrating cells to a differential rigidity that they sense, transduce and integrate into intracellular responses. Experimental evidences show dependences on the stiffness gradient (Isenberg *et al.*, 2009, Koser *et al.*, 2016, Sunyer *et al.*, 2016) and on the absolute stiffness value in which cells migrate (DuChez *et al.*, 2019, Sunyer *et al.*, 2016). Still, there is a lack of physical models that rationalize durotaxis by integrating its main ingredients at different cell scales. Among other insights, this could allow us to understand why some cells durotac toward positive gradients while others migrate down the gradient.

3.1.1 Physical forces in cell motility

To model and reveal the mechanisms that enable durotaxis, we need first to understand the fundamental physical forces that control every step in cell motility, from the early cell spreading (Wolfenson *et al.*, 2014), to signalling polarization (Huttenlocher, 2005, Ridley *et al.*, 2003) and the subsequent cell migration (Friedl and Gilmour, 2009a). Cells migrate following distinct physical modes of locomotion, which can be generally categorized as ameboid and mesenchymal cell migration (see (Bear and Haugh, 2014, Yamada and Sixt, 2019) for a review). Here, we focus on mesenchymal cell migration. Mesenchymal cell motility is driven by the competition of two internal mechanisms (Fig. 3.1): a continuous polymerization of actin filaments at the leading edge of the cell, that protrudes the cell membrane forward (Footer *et al.*, 2007, Schreiber *et al.*, 2010), and the contractile forces that myosin motors exert on the actin network, which generate active forces that create a continuous flow of actin (Pantaloni *et al.*, 2001, Pollard and Borisy, 2003). This actomyosin flow is usually referred to as retrograde flow. Balancing these two forces, mesenchymal cell migration is also characterized by strong adhesions (Bear and Haugh, 2014, Yamada and Sixt, 2019) that establish the attachment between cells and their surroundings through a large number of cell adhesion molecules (CAMs) (Parsons *et al.*, 2010, Vicente-Manzanares *et al.*, 2009b).

Actin is unarguably a fundamental element in cell motility (Mitchison and Cramer,

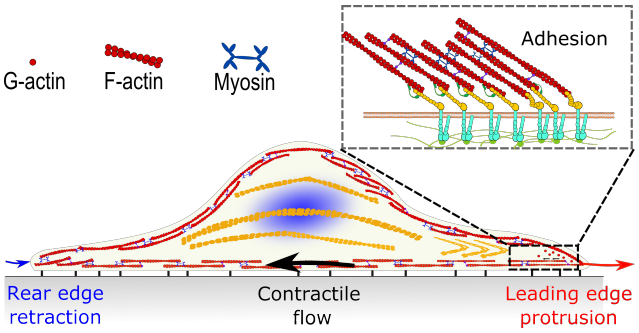

Figure 3.1: Sketch of the main forces acting in the process of cell polarization: a contractile actomyosin flow (black), protrusive forces at the leading edge of the cell (red), and retraction forces at the back of the cell (blue) compete to advance or retract both cell fronts. At the cell-ECM interface, a friction-like force appears as a result of the formation of ACs.

1996, Pollard and Borisy, 2003, Pollard and Cooper, 2009b). Actin determines the protrusion of the leading edge and the dynamics of the retrograde flow (Ponti *et al.*, 2004b). In short, actin undergoes cycles of polymerization and depolymerization which exchange monomeric (G-actin) and filamentous (F-actin) forms of actin. This process occurs at the different actin-based structures of the cell (see, e.g., the actin cycle at the cell front in Fig. 3.2). The actin cycle at different spatial and temporal scales of the cell is now well understood (Pollard and Cooper, 2009b, Raz-Ben Aroush *et al.*, 2017). There are dozen, if not a hundred, proteins involved in this process (Carlier *et al.*, 1997, Pollard, 2016). However, mechanistically, F-actin (von der Ecken *et al.*, 2015) is the most important actin structure for cell motility (Carlier *et al.*, 1997, Pollard and Borisy, 2003).

To create the active retrograde flow that is required for cell motility (Lin *et al.*, 1996, Svitkina *et al.*, 1997, Wilson *et al.*, 2010), myosin motors exert contractile forces on the F-actin filaments. The motor domain of myosins, a superfamily of ATP-dependent motor proteins, binds to F-actin and generates force via ATP hydrolysis, to move along the filament towards the barbed end (Honda *et al.*, 1986). Overall, the actomyosin network is responsible for breaking the cell symmetry and inducing further cell motility (Yam *et al.*, 2007). The force generated by the myosin motors is also implicated in cell adhesion dynamics (Vicente-Manzanares *et al.*, 2009a). Therefore, the actomyosin network is not only responsible for the active movement of the F-actin network, and therefore for the generation of a motile force, but it also controls cell adhesion dynamics, as we discussed in Chapter 1.

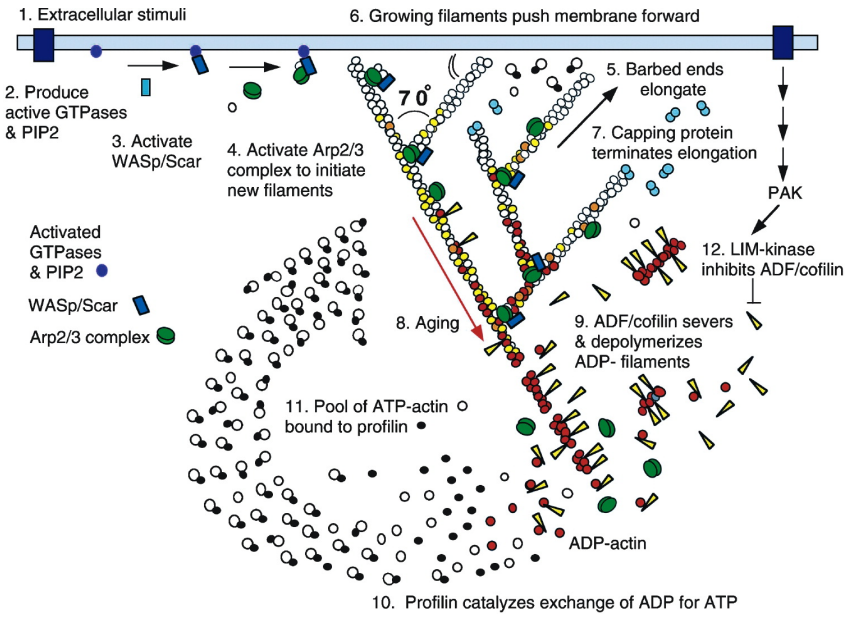

Figure 3.2: Sketch of the actin transformation during the turnover cycle. Actin monomers nucleate, promoted by formin, profilin and cofilin (Ghosh *et al.*, 2004, Lew, 2002), and polymerize rapidly after a period of slow nucleation (Campellone and Welch, 2010, Pollard and Cooper, 2009b). Arp2/3 activates and promotes the formation of new branches of actin filaments along the barbed ends of the actin filaments (Amann and Pollard, 2001). F-actin dissociates, mediated by ADP and cofilin, producing ADP-actin dissociations. Then, profilin promotes the ATP replacement of ADP, providing a pool of new actin monomers ready to bind the barbed ends (Campellone and Welch, 2010, Pollard and Borisy, 2003).

3.1.2 Effect of substrate rigidity in cell spreading

One of the very first phases in cell motility is cell spreading (Wolfenson *et al.*, 2014), an expanding, flattening process during which cells acquire their polarization and motile features. Cell spreading, as a form of cell motility, is coordinated by the active actomyosin network (Mogilner and Manhart, 2018, Pollard *et al.*, 2000), the membrane tension (Batchelder *et al.*, 2011, Keren, 2011, Raucher and Sheetz, 2000) and the cell adhesion mechanisms (Kechagia *et al.*, 2019, Pontes *et al.*, 2017, Vicente-Manzanares *et al.*, 2009b). Therefore, cell spreading is also determined by the rigidity of the substrate (Li *et al.*, 2014, Tee *et al.*, 2011, Yeung *et al.*, 2005). The symmetric cell spreading, the one that occurs prior to the cell polarization, consists of three main stages (Wolfenson *et al.*, 2014) within 10-20 minutes after the cell has been seeded on the substrate. In the first phase, the cell attaches weakly to the ECM, due to the integrin clustering in nascent adhesions at the cell periphery (Gauthier *et al.*, 2011, Ibata and Terentjev, 2020, Pontes *et al.*, 2017). Then, a fast spreading phase driven by the actin

polymerization against the cell membrane starts. Moreover, after the transient nascent adhesions formation, they either disintegrate or grow into mature focal adhesions (Changede *et al.*, 2015, Sun *et al.*, 2019, Vicente-manzanares and Horwitz, 2011), increasing the adhesion and friction of the cell with the substrate. During this fast spreading phase, the cell membrane is capable of increasing its area via endocytosis and by progressively depleting the membrane reservoirs (Gauthier *et al.*, 2012). As the membrane reservoirs deplete, the membrane tension starts to increase and the fast spreading phase decelerates. Although not fully understood, it is believed that biochemical signals, prompted by physical forces imposed by the plasma membrane (Diz-Muñoz *et al.*, 2013, Gauthier *et al.*, 2011, 2012, Keren, 2011), induce changes in actin polymerization, activate exocytosis (Diz-Muñoz *et al.*, 2013, Gauthier *et al.*, 2012) and myosin activity. The differential adhesion of the cell with the substrate may also induce asymmetric forces that the cell may use to polarize and, consequently, to direct its migration (Yam *et al.*, 2007).
When a cell is placed on a substrate, it spreads to balance the active contractile and viscous forces with the friction. The spreading area and rate vary when cells are cultured on substrates of varying rigidity (Li *et al.*, 2014, Tee *et al.*, 2011, Yeung *et al.*, 2005) because cells form larger FAs and adhere more strongly on stiffer substrates, exerting larger traction forces on the substrate (Elosegui-Artola *et al.*, 2016, Oria *et al.*, 2017). The size of FAs increases during cell spreading (Fouchard *et al.*, 2014), but also when cells are seeded on substrates of varying rigidity (Chaudhuri *et al.*, 2015, Han *et al.*, 2012, Vertelov *et al.*, 2016).

3.1.3 Cellular mechanisms toward durotaxis

To break the cell symmetry and create a directed cell migration, an external mechanical cue, in the form of a stiffness gradient of the ECM, can polarize the cell in a process known as durotaxis (Espina *et al.*, 2021, Shellard and Mayor, 2021, Sunyer and Trepat, 2020). If a stiffness gradient in the substrate controls the cell migration direction, durotaxis must then be activated during the first stage of cell spreading. Unpolarized cells read external stiffness signals through cell protrusions and cell ACs (Kechagia *et al.*, 2019, Parsons *et al.*, 2010, Pontes *et al.*, 2017, Vicente-Manzanares *et al.*, 2009b). At some point, the formation of a cell front orients the lamellipodia toward the stiffness gradient. How exactly this front forms, either by direct mechanical feedback or indirectly by downstream signals, is still unclear.
Nascent adhesions can already feel and transduce intracellularly the extracellular rigidity at the time of formation. The feedback that the cell receives from the ECM causes nascent adhesions to disintegrate or to mature into focal adhesions (Kawano

and Kidoaki, 2011, Wong *et al.*, 2014). This dynamic process is mediated by the pulling forces from the actomyosin network at the ACs (Giannone *et al.*, 2009, Vicente-Manzanares *et al.*, 2009a) that we discussed in Chapter 1. Regions of the cell where strong ACs form, may also serve as anchored points for actin polymerization against the cell membrane, which is further enhanced by Arp2/3- and Rac1 (Wong *et al.*, 2014). The contractility of stress fibers also modifies durotaxis (Trichet *et al.*, 2012). Durotaxis arrests if the vinculin and paxillin interaction is inhibited (Plotnikov *et al.*, 2012, Wang *et al.*, 2001) because the traction forces on the ECM are reduced. In summary, ACs positioned at locations of different ECM stiffness may serve as sensors of local ECM mechanics.

The protrusive forces of the actin polymerization against the cell membrane induce changes in the membrane tension that may also play a role in durotaxis. Indeed, membrane tension is directly involved in the polarization of signaling cues (Houk *et al.*, 2012) and, consequently, in actin polymerization (Diz-Muñoz *et al.*, 2013, Gauthier *et al.*, 2012, Keren, 2011). By creating a gradient in membrane tension, lower at the rear than at the front of the cell, cells may activate signaling events, mainly GTPases, to orient cell migration (Houk *et al.*, 2012). GTPases are critical not only for cell migration but also for durotaxis. For example, if Cdc42 and Rac activity is inhibited from the leading edge, the asymmetry that is established by a differential traction force is lost and, consequently, durotaxis is cancelled (Wormer *et al.*, 2014). Moreover, the membrane tension may induce the opening of mechanosensitive ion channels (Koser *et al.*, 2016) allowing changes in the electrochemistry balance of the cell and, eventually, changes in the actin activity (Ridley *et al.*, 2003). On the other side of the cell, disassembling of nascent adhesions inhibits actin protrusion while the myosin-mediated retrograde flow at the rear of the cell increases at the same time (Pelham and Wang, 1997, Wong *et al.*, 2014), which may also be involved in enabling durotaxis (Chao *et al.*, 2014, Raab *et al.*, 2012). Caveolae have been also shown to increase at the rear of the cell (Hetmanski *et al.*, 2019), activating downstream signals for RhoA which, in turn, enhance actomyosin contractility and cell retraction. All these asymmetric responses to ECM rigidity may be the first mechanotransduction events that boost durotaxis. Rac1 is also involved in durotaxis, due to a positive feedback loop that enhances the cell front protrusion (Wong *et al.*, 2014, Wormer *et al.*, 2014).

Durotaxis seems to be favoured in matrices with increasing strength of the stiffness gradients (Isenberg *et al.*, 2009, Koser *et al.*, 2016, Sunyer *et al.*, 2016), but seems to be less dependent on the absolute stiffness modulus (Hadden *et al.*, 2017, Isenberg *et al.*, 2009, Joaquin *et al.*, 2016). Nevertheless, some cell types express durotaxis similarly strong on shallow stiffness gradients (Evans *et al.*, 2018). In any case, both

stiffness gradient and stiffness value seem to influence cell migration, although it may be cell-type dependent. What is more intriguing, and still unknown, is why most cells express positive durotaxis while others, such as neurons (Koser *et al.*, 2016) and human fibrosarcoma cells (Singh *et al.*, 2014) migrate toward negative gradients of the ECM.

3.1.4 Goal of this chapter

How all these physical-based mechanisms cooperate to enable durotaxis across cell types, remains unclear. Different models have been proposed to explain the physical principles of durotaxis. There are three main lines of action (see, e.g., the review in (Shellard and Mayor, 2021)). Persistent random walk models, where cycles of polarization and migration make cells to continuously change direction, have been used to address durotaxis (Novikova *et al.*, 2017, Yu *et al.*, 2017). These models suggest an inefficient migration because cells would move around to sense stiffness gradients. Secondly, standard migration models explain durotaxis by the effect of an asymmetric adhesion strength (Barnhart *et al.*, 2015). Through this type of models, an optimum adhesion strength, at intermediate stiffnesses, has been suggested during durotaxis, which was confirmed experimentally (Goodman *et al.*, 1989). This type of models still lacks a deep insight into the adhesion dynamics, which has fundamental implications in durotaxis. The third type of models are based on the clutch hypothesis (Chan and Odde, 2008, Mitchison and Kirschner, 1988), summarized in Chapter 1. These models predict the movement of the cell toward positive stiffness gradients (Bollmann *et al.*, 2015, Chaudhuri *et al.*, 2015, Sunyer *et al.*, 2016), because the cell fronts located at the soft and stiff regions are deformed differently. These models include information on the molecular behavior (Bangasser *et al.*, 2013, 2017, Elosegui-Artola *et al.*, 2016), but lack a close insight into how all intracellular motile mechanisms cooperate during durotaxis. Moreover, why some cell types migrate toward positive gradients while others move toward negative ones is still an open question in cell motility and for these biophysical models.

We hypothesize that the striking durotactic modes found across cell types are due to a differential expression of the adhesion dynamics across the cell length, that polarizes the propelling forces in the cell. To rationalize durotaxis and answer these questions, we explore a mechanistic model of cell motility to reveal the intracellular forces that rule single cell durotaxis. Because cell adhesion is the most determining and directly involved unit of the cell, capable of detecting and responding to changes in the stiffness of the ECM (Chen *et al.*, 2015a, Chen and Lee, 2004, Parsons *et al.*, 2010), we assume that durotaxis is determined by the intracellular motility forces described above and the

cell adhesion dynamics. To analyze the effect of cell adhesion dynamics in durotaxis, we couple the clutch models described in the previous chapter with an active gel model that reproduces the intracellular forces in cell migration.

3.2 Minimal model for cell motility

We consider a model that integrates the main ingredients for cell motility (Danuser *et al.*, 2013, Mogilner, 2009) in a 1D domain Ω (see Fig. 3.1) with moving coordinates $x(t) \in [l_r(t), l_f(t)]$. $l_r(t)$ and $l_f(t)$ represent the rear and front boundaries of the cell and, therefore, the length of the cell is determined as $L(t) = l_f(t) - l_r(t)$. The subindexes r and f indicate the rear and front of the cell. The boundaries move with velocity $\dot{l}_r(t)$ and $\dot{l}_f(t)$ respectively. We model the mechanics of the actomyosin network as a viscous network that shows contractility forces due to the pulling forces exerted by myosin motors (Barnhart *et al.*, 2015, Putelat *et al.*, 2018, Rubinstein *et al.*, 2009). The friction with the substrate is obtained by solving clutch models (see Chapter 2) at every position in Ω. We also consider the transport of myosin motors and the F-actin network, to describe how they localize in the cell body along time. Then, we include a model of cell membrane protrusion driven by actin polymerization at both sides of the cell (Mogilner and Oster, 2003), which in turn depends on the cell membrane tension (Diz-Muñoz *et al.*, 2013, Keren, 2011). In the following sections, we provide details on these models and the numerical solution of the problem.

3.2.1 Mechanical model of the actomyosin network

We consider an active, viscous segment in contact with the ECM to model the retrograde flow (Mogilner and Manhart, 2018, Prost *et al.*, 2015, Putelat *et al.*, 2018). We assume that viscous forces dominate the elastic forces and that inertial forces are negligible (Rubinstein *et al.*, 2009). In this framework, the balance of linear momentum for the actin network is

$$\partial_x \sigma^F = \eta v^F \quad \text{in} \quad \Omega, \tag{3.1}$$

where v^F is the velocity of the F-actin network, commonly referred to as retrograde flow.
The constitutive relation of the F-actin network stress is

$$\sigma^F = \mu^F \partial_x v^F + \zeta \rho^F \rho^M, \tag{3.2}$$

that accounts for the viscosity of the actin network and the myosin contractility, respectively. μ^F is the shear viscosity, ζ the active contraction exerted by the myosin motors and ρ^F and ρ^M are the densities of F-actin and myosin motors, respectively (see details below). The r.h.s term represents the friction between the actin flow and the extracellular space, with friction parameter η. In the next section, we will address the cellular friction with the ECM as a function of the substrate rigidity.
Neumann boundary conditions for the F-actin network allow us to compute the resulting velocity field and, consequently, the migration velocity (see Section 3.2.2 for details). Specifically, we impose that $\sigma^F = 0$ on $\Gamma^N_{r,f}$ so that there are no pushing or pulling forces on the boundary of the F-actin network. The superindex N indicates Neumann boundary conditions.

3.2.2 Effect of membrane tension in protrusion velocity and moving velocity of the cell membrane

Besides the retrograde flow of the actomyosin network, a second differentiated actin network polymerizes at the cell periphery and protrudes the membrane tension outwards (Pollard and Borisy, 2003, Ponti *et al.*, 2004b). This actin branching depends on the G-actin availability, as well as the promoting factors for the F-actin nucleation (Pollard, 2016, Pollard and Borisy, 2003).
When actin pushes against the cell membrane, it increases its tension. Membrane tension has been well characterized experimentally and theoretically in the past (Gauthier *et al.*, 2012, Popescu *et al.*, 2006, Sitarska and Diz-Muñoz, 2020), and there is a clear relationship between actin polymerization velocity and membrane tension (Footer *et al.*, 2007, Schreiber *et al.*, 2010). We follow here a previous model of actin filament polymerization against the cell membrane (Mogilner and Oster, 2003). Filaments grow freely with velocity $v_0^p = k_{on}\delta$ if there is no opposing force to it. k_{on} is the rate of actin assembly and δ is the size of one single monomer at the tip of the filament. We assume here that there is always a large pool of actin monomers available for polymerization (see discussion in Section 3.2.4). The actin network polymerizes and pushes against the cell membrane, which further builds membrane tension (Kozlov and Mogilner, 2007, Mogilner and Oster, 2003). If membrane tension increases, the actin polymerization decreases. Previous theoretical models have shown that the actual velocity of actin polymerization at the cell membrane decreases with respect to the free polymerization velocity as (Keren *et al.*, 2008)

$$v^p = v_0^p \left[1 - \frac{\tau(L(t))}{\tau_{stall}}\right]^z \tag{3.3}$$

where τ_{stall} is a tension required to stall the polymerization of the actin network and z is a model parameter that controls the velocity decay. To model the membrane tension τ, we use a simple Hookean spring such that $\tau(L(t)) = k(L(t) - L_b)$, where k is the spring constant and $L_b = L_0 + L_r$ accounts for the resting length, L_0, and the buffer membrane area, L_r, in reservoirs and foldings of the cell membrane. Therefore, the membrane tension starts to increase once all reservoirs and membrane folds have flattened, i.e $L(t) > L_b$. We assume zero compressive stresses when $L(t) < L_b$.
Finally, the protruding velocity of both sides of the cell is $\dot{l}_{r,f(t)} = v^p_{r,f} - v^F|_{l_{r,f(t)}}$ so that the outward polymerization velocity against the cell membrane, $v^p_{r,f}$, competes with the inward retrograde flow velocity $v^F|_{l_{r,f(t)}}$ to expand or retract the cell boundary. Once the moving velocities of both ends are obtained, we compute the migration velocity of the cell as $v = (\dot{l}_r(t) + \dot{l}_f(t))/2$.

3.2.3 Cell adhesion behaviour

To compute the friction that opposes the retrograde flow, we make use of clutch models (see Chapter 2 for details). We take a slightly different interpretation of the clutch hypothesis. We consider that the clutch model reproduces the behaviour of those actin networks directly attached to the substrate, mainly stress fibers, instead of the retrograde flow. The velocity $\hat{v}$ and traction P that result from the clutch models represent the velocity and traction force of these actin networks. As we described previously, the velocity $\hat{v}$ allows us to compute the displacement of the engaged molecular clutches and, therefore, the force acting on each clutch. The reaction force at the substrate, F_{sub}, and the area occupied by the AC, πa^2, give us the total traction force on the substrate P. Then, we compute an effective friction parameter $\hat{\eta} = P/\hat{v}$ that, added to a baseline friction of the retrograde flow with the surrounding cytoskeletal structures, $\eta_0 = 0.05 kPa \cdot s/\mu m^2$, results in a total friction $\eta = \eta_0 + \hat{\eta}$.

We recall the adhesion behavior of slip and reinforced cases, i.e. cells expressing mostly slip bonds (Chan and Odde, 2008) and catch bonds with talin reinforcement (Elosegui-Artola *et al.*, 2016), respectively (see Chapter 2). We show the velocity and traction results for each of these adhesion cases as a function of the ECM stiffness in Fig. 3.3 (a). The results, in agreement with previous experimental work (Chan and Odde, 2008, Elosegui-Artola *et al.*, 2016) (see also Chapter 2, Sections 2.3.1, 2.3.2, for details), show that the slip case has an optimal rigidity, from where the reinforced case diverges and keeps increasing as the stiffness of the substrate increases. Below the optimal stiffness of the slip case, the traction force increases with an increasing substrate rigidity, while above the optimal stiffness, the traction force decreases with an increasing stiffness. The resulting friction behaves similarly to the tractions (Fig. 3.3

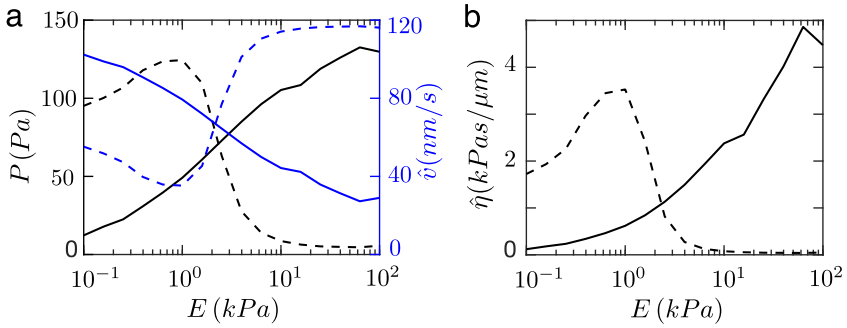

Figure 3.3: Results of computational clutch models for cells expressing slip (slip case) and reinforced catch bonds (reinforced case) for values of the substrate rigidity in 0.1-100 kPa. (a) Traction (black) and velocity (blue) for slip case (dash) and reinforced case (solid). (b) Effective friction for the slip case (dash) and reinforced case (solid). Similarly to the traction forces, friction increases monotonically for increasing values of the substrate rigidity in the reinforced case, while it presents a hill shape with a maximum at $\approx 1kPa$, where the optimal rigidity localizes, in the slip case.

(b)). For the slip case, we see a maximum friction of $\approx 3.75\ kPa{\cdot}s/\mu m^2$ at the value of the optimal rigidity. The friction is $\approx 2kPa$ at 0.1 kPa and vanishes for substrate rigidities larger than 10 kPa. Friction increases monotonically from zero to $\approx 4.5\ kPa \cdot s/\mu m^2$ in the reinforced case. We believe that these differences in the cell adhesion behavior could explain the opposite durotactic responses across cell types.

3.2.4 Transport of the actomyosin network

To model the distribution of the F-actin density, $\rho_F(x,t)$, in time and space, we consider the advection-diffusion reaction equation

$$\partial_t \rho_F + \partial_x \left(w\rho_F - D_F \partial_x \rho_F \right) = k_p \rho_G - k_d \rho_F \quad \text{in} \quad \Omega \text{ x } (0,\text{T}), \tag{3.4}$$

where the right hand side includes the polymerization and depolymerization terms, with their associated rates k_p and k_d, respectively. D_F is the diffusive parameter of the F-actin. We write the transport equations in the cell frame and, accordingly, we define the velocity of the F-actin network in the cell frame as $w = v^F - v$. We impose zero fluxes on the boundaries, to reflect that no F-actin can enter or leave the cell domain:

$$w\rho_F - D_F \partial_x \rho_F = 0 \text{ on } \Gamma^N_{r,f}. \tag{3.5}$$

This single-specie model of the actin turnover is a simplification of the actual actin dynamics (see Section 3.1.1 for a discussion). Although more complete actin turnover

models have been proposed (Kollepara *et al.*, 2018, Raz-Ben Aroush *et al.*, 2017), considering only the dynamics of the F-actin network is a good approximation to model the role of actin in cell motility (Mitchison and Cramer, 1996, Pollard and Borisy, 2003, Pollard and Cooper, 2009b). Many other models also focused on a single transient advection-diffusion problem with first order kinetics to model the F-actin network (Larripa and Mogilner, 2006, Putelat *et al.*, 2018, Raz-Ben Aroush *et al.*, 2017), which showed good predictions for cell migration. This approach assumes that the concentration of G-actin is constant in space due to a fast diffusion process (Larripa and Mogilner, 2006, Raz-Ben Aroush *et al.*, 2017), but changes in time as $\rho_G L(t) = 1 - \int_0^{L(t)} \rho_F dx$.

To describe the distribution in time and space of the myosin density, we also consider a single-specie model of myosin motors, ρ^M, bound to the F-actin network (Putelat *et al.*, 2018, Rubinstein *et al.*, 2009). Myosin motors unbind from the F-actin network, diffuse in the cytoplasm and bind again to the F-actin (Svitkina, 2018). If we assume that the binding-unbinding process is fast, i.e. $k_{u_M}/k_{b_M} << 1$ (Putelat *et al.*, 2018), we can model the effective transport of bound myosin motors bound, ρ^M, through a transient advection-diffusion problem (Barnhart *et al.*, 2011, Putelat *et al.*, 2018, Rubinstein *et al.*, 2009), that advects the bound myosin motors with velocity w as

$$\partial_t \rho^M + \partial_x(w\rho^M - D\partial_x \rho^M) = 0 \quad \text{in } \Omega \text{ x } (0,T). \tag{3.6}$$

$D = k_{u_M}/k_{b_M} D_M + D_m$ is the effective diffusion parameter (Barnhart *et al.*, 2011, Putelat *et al.*, 2018) and D_M and D_m are the diffusion parameters of the bound and unbound species, respectively. The myosin species have also to obey zero flux boundary conditions at both cell ends, to describe that no bound myosin motor can enter or leave the cell:

$$w\rho^M - D\partial_x \rho^M = 0 \qquad \text{on} \quad \Gamma^N_{r,f}. \tag{3.7}$$

3.2.5 Numerical solution of the system of equations and model parameters

We solve computationally the system of Eqs 3.1-3.6 in a staggered approach. We use the finite element method to discretize the system in space, and an implicit second-order Crank-Nicholson method to discretize the parabolic equations in time (Jean Donea and Huerta, 2003, Zienkiewicz and Taylor, 2000).

The numerical solution of the parabolic equations (Eqs. 3.4 and 3.6) can present undesired oscillations if the problem becomes convective dominant, i.e. $Pe > 1$. The

Parameters		
μ^F [kPa·s]	10	(Larripa and Mogilner, 2006, Putelat *et al.*, 2018)
η_0 [kPa·s/μm]	0.05	(Bergert *et al.*, 2015, Larripa and Mogilner, 2006, Putelat *et al.*, 2018)
ζ [kPa]	0.05	(Larripa and Mogilner, 2006, Rubinstein *et al.*, 2009)
k	0.1	(Putelat *et al.*, 2018)
D_F [μm/s]	0.2	(Barnhart *et al.*, 2011, Larripa and Mogilner, 2006)
D [μm/s]	0.4	(Barnhart *et al.*, 2011, Larripa and Mogilner, 2006)
k_d	0.1	(Raz-Ben Aroush *et al.*, 2017, Wilson *et al.*, 2010)
k_p	0.1	(Raz-Ben Aroush *et al.*, 2017, Wilson *et al.*, 2010)
δ [nm]	2.2	(Mogilner and Oster, 2003)
k_{on} [s^{-1}]	250	(Mogilner and Oster, 2003)
L_0 [μm]	10	*
L_b [μm]	0.3*L_0	*
τ_{stall} [nN/μm]	0.4	*

Table 3.1: Model parameters, values adopted and references to publications where they were obtained. * indicates values used in this work.

Peclet numbers for the actin and myosin transport problems are $Pe_F = hw/2D_F$ and $Pe_M = hw/2D$ respectively, where h is the size of the finite elements. As the convective velocity is the solution of Eq. 3.1, we cannot guarantee a priori that the problem will remain in the limit case of $Pe < 1$. We use finite elements of constant size $h = l_f(t)/N$, where N is the number of elements. Because we want to keep the number of elements of our domain constant, and avoid remeshing strategies in the case that the element size needs to be decreased to keep $Pe < 1$, we include the Stream-Upwind Pretrov Galerkin (SUPG) stabilization term to overcome possible numerical oscillations in our solution (Codina, 2000, Jean Donea and Huerta, 2003). The complete finite element and time discretization procedure is presented in Appendix B. The model parameters presented in this section are summarized in Table 3.1.

3.3 Results

3.3.1 Cell spreading

First, we analyze the symmetric cell spreading, an early phase of cell motility. Because there is not yet a cell rear and front established (see Section 3.1.2 for details), $l_r(t)$ and $l_f(t)$ represent now the left and right sides of the cell (Fig. 3.4 (a)). We analyze cells crowded by slip bonds and catch bonds with talin reinforcement, i.e. the slip and reinforced cases (see Chapter 2). We place these cells in substrates of 4 different rigidities, E=0.1, 1, 10 and 100 kPa.

We analyze the cell length, the membrane tension, the retrograde flow velocity

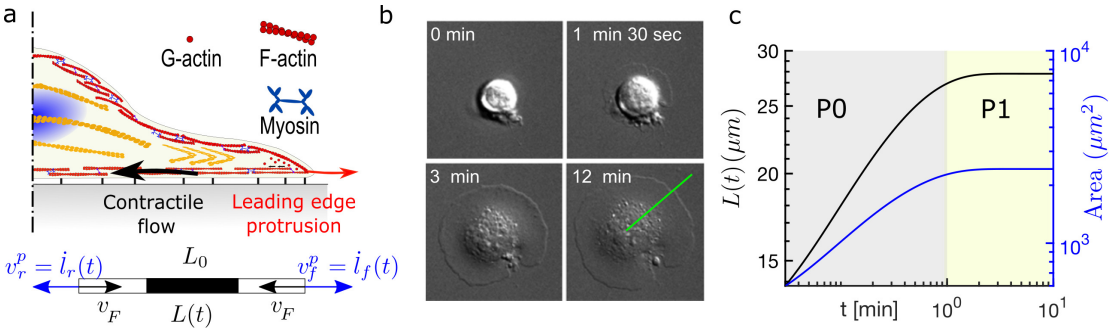

Figure 3.4: (a) Sketch of the main forces acting in the cell spreading process: an active and contractile actomyosin flow (black) and protrusive forces at the leading edge of the cell (red). At the cell-ECM interface, a friction-like force appears as a result of adhesion mechanisms. (b) Cell spreading process in time. Images adapted from (Gauthier *et al.*, 2011). (c) Radius and area evolution of the spreading process. Results reproduce previous experimental data (Dubin-Thaler *et al.*, 2008, Gauthier *et al.*, 2011). Grey region shows the time period in which P0 takes place, up to ≈ 3 min. Yellow region shows the time period in which P1 occurs. P1 spans from ≈ 3 to 10 min.

and the actin and myosin densities as a function of the substrate stiffness at steady-state (Fig. 3.5). All variables show the same tendency, resembling the response of the slip and reinforced cases. In the slip case, all variables remain approximately constant for substrates of E=0.1, 10 and 100 kPa. However, in substrates of E=1kPa, the cell length (L=30 μm) and the membrane tension ($\tau = 70nN/\mu m$) are maximum, while the velocities ($v_f^F \approx 0$) and densities ($\rho_F \approx 1.01$, $\rho^M = 1.02$) reach a minimum value. In the reinforced case, the cell length and, consequently, the membrane tension, increase with increasing stiffness of the substrate, from ≈ 26 to $30\mu m$ and from ≈ 50 to $70nN/\mu m$, respectively. The network velocities and, therefore, myosin and actin densities decrease from ≈ 4 to $1nm/s$, ≈ 1.4 to 1, and 1.07 to 1, respectively.

We also analyze the cell radius (Fig. 3.4 (b-c)) in time, for the slip case at E=1 kPa. All other cases follow the same behavior with different values at steady-state. The radius of the cell shows a first phase of fast spreading that lasts ≈ 3 min, where it increases ≈ 3-fold (P0). Then, the spreading rate decreases until steady-state, which occurs at ≈ 10 min (P1). These results closely recapitulate previous results on the kinetics of cell spreading (Cuvelier *et al.*, 2007, Dubin-Thaler *et al.*, 2008, Fouchard *et al.*, 2014, Gauthier *et al.*, 2011, Lam Hui *et al.*, 2012), where the initial stages of cell spreading show systematically a power-law for the cell radius.

For the same case, the slip case at E=1 kPa, we then analyze all model variables to

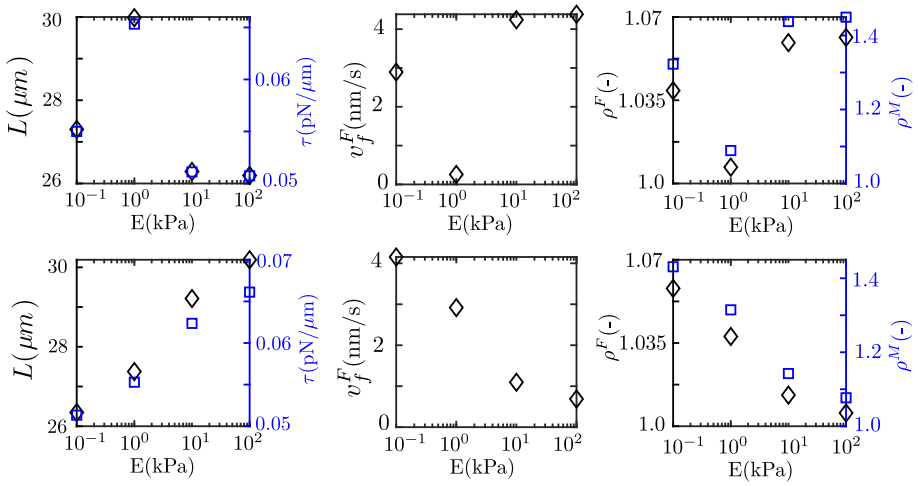

Figure 3.5: Results of cell spreading at steady-state, for cells expressing slip (top) and reinforced catch bonds (bottom) for values of the substrate rigidity in 0.1-100 kPa. Similarly to the traction forces, the cell length and the membrane tension increase monotonically for increasing values of the substrate rigidity in the reinforced case, while they present a hill shape with a maximum at $\approx 1kPa$ in the slip case. The densities of actin and myosin follow the same behaviour of the retrograde flow.

rationalize through physical terms the spreading process. We show the evolution in space and time of the myosin and actin densities, the network velocities and stress, the cell radius and the membrane tension (Fig. 3.6 (a-d)). The density of actin and myosin at both sides of the cell are equal, which indicates a symmetric distribution of the intracellular components (Fig. 3.6 (a,d)). The protrusion velocity of actin flow at the cell fronts starts at the free velocity, when there is no membrane tension resisting the F-actin polymerization at the cell front (Fig. 3.6 (c)), and it evolves symmetrically (Fig. 3.6 (b)) in time. A quick increase in membrane tension (Fig. 3.6 (c)) up to 0.05 $nN/\mu m$ decreases the actin polymerization velocity at the cell fronts (Fig. 3.6 (b)). The membrane tension is in close agreement with previous experimental results (Shi *et al.*, 2018). The polymerization and retrograde velocities equal at $\approx$ 3 min, at the end of P0 (Fig. 3.6 (b)), when the spreading process quickly reaches the steady-state, i.e. $\dot{l}_{r,f(t)} = 0$, at $\approx$ 10 min. We also show the kymographs of the actin and myosin velocities, as well as of the retrograde flow (Fig. 3.6 (d)). The results also indicate that the quick spreading of the cell during P0 restricts the actomyosin network to the center of the cell during the first 3 min of the spreading process. That accumulation of contractile myosin motors in the cell center is responsible for the acceleration of the retrograde flow (Fig. 3.6 (b)). Then, the myosin and actin concentrations evolve to a less but still polarized state because of diffusion and turnover.

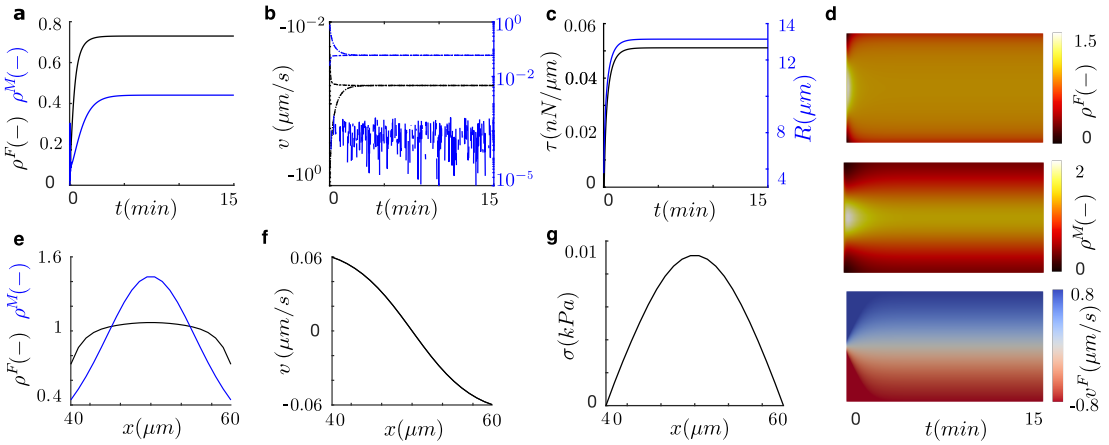

Figure 3.6: Time and space evolution of cell spreading. (a) Actin (black) and myosin (blue) densities at the left (dash) and right (solid) fronts of the cell. Left and right variables are superimposed as a result of their symmetric distributions. (b) At the front and rear of the cell: polymerization velocity (dot-dash) and retrograde velocity at the cell membrane (dash). Total velocity of protrusion (solid). Negative velocities are in black, positive velocities are in blue. (c) Membrane tension (black) and cell radius (blue). (d) Kymographs of the actin density (top), myosin density (center) and retrograde flow velocity (bottom). At steady-state, along the cell length, (e) actin (black) and myosin (blue) densities, (f) retrograde flow at the cell (blue) and lab frame (black) and (g) tension of the actin network.

3.3.2 Durotaxis

Then, we focus on single cell durotaxis. At some point during the symmetric spreading process, cells read external cues that they use to, directly or indirectly, mediate the motile forces of the cells. During durotaxis, cells are exposed to exogenous stimuli in the form of a shallow or a highly localized mechanical signal that they use to orientate themselves towards a target direction. To reproduce the effect of a stiffness gradient in the ECM, we take a range of stiffnesses between 0.1 and 100 kPa (Elosegui-Artola *et al.*, 2016) (Fig. 3.3). To change the stiffness gradient of the substrate, we use samples of varying lengths (1000, 500 and 200 μm) with the same stiffness range. To study how the absolute value of the substrate stiffness, and not only its gradient, may regulate the durotactic response, we also consider three initial locations at the sides and centre of the sample, where cells are initially seeded. As in the previous spreading analysis, we study cells crowded by slip bonds and catch bonds with talin reinforcement.
We first analyze the velocity and direction of the motile cells. We study the process

during the first 20 minutes, as it already allows us to analyze the durotactic response. We consider that cells undergo durotaxis if the migration velocity is higher than $v = 1nm/s$, otherwise we assume that they remain in the spreading phase. In the reinforced case (Fig. 3.7, bottom), we obtain positive velocities in all cases, i.e. cells migrate toward the positive stiffness gradient of the substrate. We call this behavior positive durotaxis. In the three samples (L_s=1000, 500 and 200 μm), the strongest durotactic response, that is cells with the largest migrating velocity, is obtained for cells located at the center of the sample (E = 1-10 kPa), closely followed by those at stiffer (E = 10-100 kPa) and softer sides (E = 0.1-1 kPa) of the sample, respectively. For the time analyzed, we see that cells seeded in the L_s=1000 μm do not leave the spreading phase. However, there is a strong durotactic response in those cells located at the 200 μm-length sample. Cells seeded at the L_s=500 μm length sample also undergo durotaxis but at a lower migration velocity. These results indicate that cells need a strong stiffness gradient to express durotaxis and that they prefer intermediate stiffnesses rather than soft or stiff substrates, which confirms previous experimental results (Hadden *et al.*, 2017, Isenberg *et al.*, 2009, Joaquin *et al.*, 2016, Koser *et al.*, 2016, Sunyer *et al.*, 2016).

For the slip case, we see opposite migration velocities. Cells located at the softest region (E = 0.1-1 kPa) of the samples undergo positive durotaxis. Cells located at the stiffest region of the samples, above 10 kPa, show a weak durotactic response and stay mostly at the spreading phase. However, cells located at the middle of the sample, between 1 and 10 kPa, move with negative velocities and, therefore, migrate toward negative gradients of the substrate rigidity. We define this behavior as negative durotaxis. In other words, cells located at the left of the optimal rigidity, migrate toward positive gradients of the stiffness gradients, while cells at the right of the optimal rigidity migrate toward negative stiffness gradients. The migration velocity is maximum in cells starting the migration at the middle of the sample. In the strongest durotactic sample, of length L_s=200 μm, the migration velocity is $\approx 8nm/s$ for cell seeded at intermediate stiffnesses. For cells initiating the migration in the softest location, the migration velocity is $\approx 4.5nm/s$. However, cells seeded at the stiffest locations of the samples show a weak durotactic response (Fig. 3.7, points *iii*). Our results show that migration in cells expressing slip bonds is also favoured in matrices with steep stiffness gradients and intermediate stiffnesses (E = 1-10 kPa).

As we described in the introduction of this chapter, most cell types express positive durotaxis. This is the case of fibroblasts (Lo *et al.*, 2000) or smooth muscle cells (Wong *et al.*, 2003). However, there are other cell types, such as neurons (Koser *et al.*, 2016) and human fibrosarcoma cells (Singh *et al.*, 2014), that present negative durotaxis. It

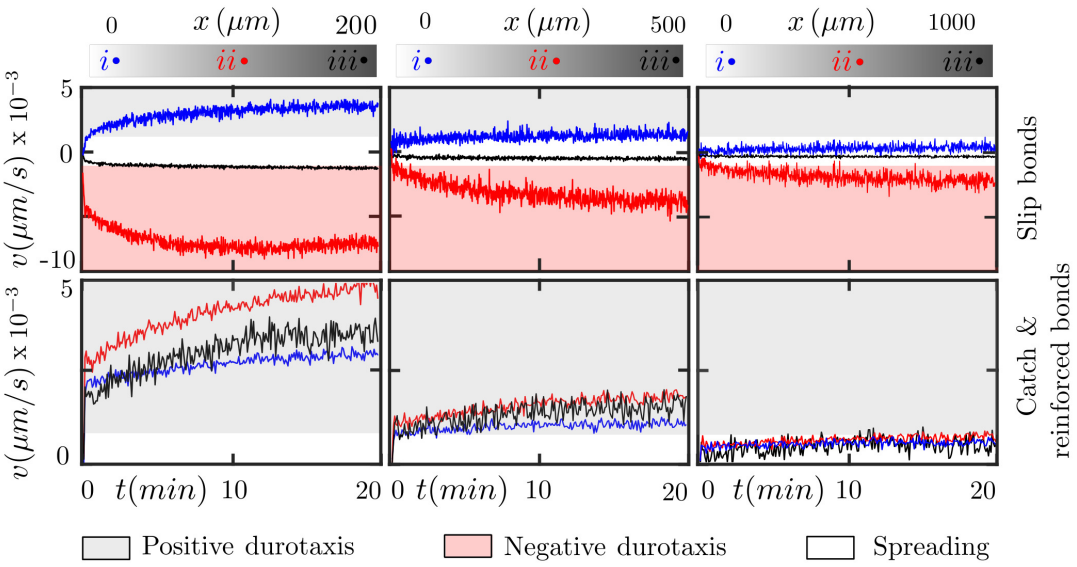

Figure 3.7: Migration velocities for cells expressing slip bonds (top) and catch bonds with talin reinforcement (bottom). Cells are followed for 20 min. The substrate stiffness goes from 100 kPa, at the right of the sample, to 0.1 kPa, at the left. Points i (blue), ii (red) and iii (black) represent the locations where the cells are initially seeded. In the sample of 200μm in length, i=33 μm, ii=100μm, iii=166 μm. In the sample of 500 μm in length, i=83 μm, ii=250 μm, iii=416 μm. In the sample of 1000 μm in length, i=150 μm, ii=500 μm, iii=850 μm. Grey shadow shows regions of positive durotaxis, red shadow represents negative durotaxis and white represents regions of spreading.

is worth noting that those cells that follow positive durotaxis seem to express the reinforced case of adhesion (Elosegui-Artola *et al.*, 2016), while those that present negative durotaxis are known to present a slip case of adhesion (Chan and Odde, 2008). Therefore, our results explain positive and negative durotaxis by the adhesion behavior of the cells.

To further understand and rationalize the physical mechanisms behind this behavior, we analyze all variables of the model at specific locations. We choose the slip case and the sample with the largest stiffness gradient (L_s=200 μm). We also choose the soft and intermediate locations, which strongly express positive and negative durotaxis (Fig. 3.7, points *i* and *ii*, respectively). In both cases, we see a response of all model variables similar in magnitude but with opposed polarization. We show a polarization of the actomyosin network (Fig. 3.8-3.9 (a,e,h)), which induces an asymmetric retrograde flow (Fig. 3.8-3.9 (b,f,h)). The increased retrograde flow at one cell side establishes

the cell rear, while the reduced retrograde flow at the other end establishes the cell front, where a higher protruding velocity moves the cell front forward (Fig. 3.8-3.9 (b,f)). Cells elongate 4-fold and the cell membrane reaches a tension of $\approx 60 pN/nm$, similar to previous experimental data (Shi *et al.*, 2018). As cells migrate, they travel through regions of different stiffnesses (Fig. 3.8-3.9 (d)) and, therefore, the friction computed through the clutch model also changes in space and time (Fig. 3.8-3.9 (h)). This asymmetric distribution of the adhesive forces is responsible for the initial durotactic response. The stress of the actomyosin network is mostly symmetric with a maximum at the cell center of 50 Pa (Fig. 3.8-3.9 (g)). This result indicates that the stress of the actomyosin network imposes a traction on the nuclear region of the cell, which is in agreement with previous results on the mechanosensitivity of the cell nucleus (Elosegui-Artola *et al.*, 2017). All cases with durotactic responses show similar results, with a smaller or larger polarization of the model variables. All cases with spreading signatures (see above) show results similar to the spreading cases above (Fig. 3.6).

We then analyze the effect of the migration velocity as cells travel along the sample and until they reach a steady-state. We focus on the three cases that showed the strongest durotactic responses for all locations and sample lengths of the slip and reinforced cases (Fig. 3.7). We analyse the two slip cases expressing durotaxis, i.e. cells initially seeded at soft and intermediate stiffness locations of the 200 μm length sample, and reinforced case with cells seeded on the stiff side of the 200 μm length sample, i.e. E $\approx$ 30 kPa. To allow cells to travel along the entire domain, we increase the final time of the simulation until steady-state, which in all three cases occurs when cells stop and no longer migrate (Fig. 3.10). As we discussed above, cells seeded on the soft part of the sample and cells with reinforced bonds migrate toward positive stiffness gradients, while cells with slip bonds seeded at intermediate stiffnesses express negative durotaxis. As we also discussed above, cells located at the left of the optimal rigidity, migrate toward positive gradients of the stiffness, while cells to the right migrate toward negative stiffness gradients (Fig. 3.10 (a)). We also observe that cells migrate toward the optimal rigidity location and stop when they reach it, which occurs at E $\approx$ 1-2 kPa (see Fig. 3.3 and Fig. 3.10 (b-c)). Cells stall at this location because they reach a symmetric distribution of the adhesion forces, which reverses the durotactic mode into the symmetric spreading phase. In the slip case, the non-motile steady-state is reached at $\approx$ 1 hr for cells with negative durotaxis and at $\approx$ 4 hr for the cells with positive durotaxis (Fig. 3.10). Of course, this time would change depending on the distance from the optimal stiffness to the initial location of the cell. For the reinforced case, cells also reach a steady-state at $\approx$ 4 hr, when they reach a stiffness of

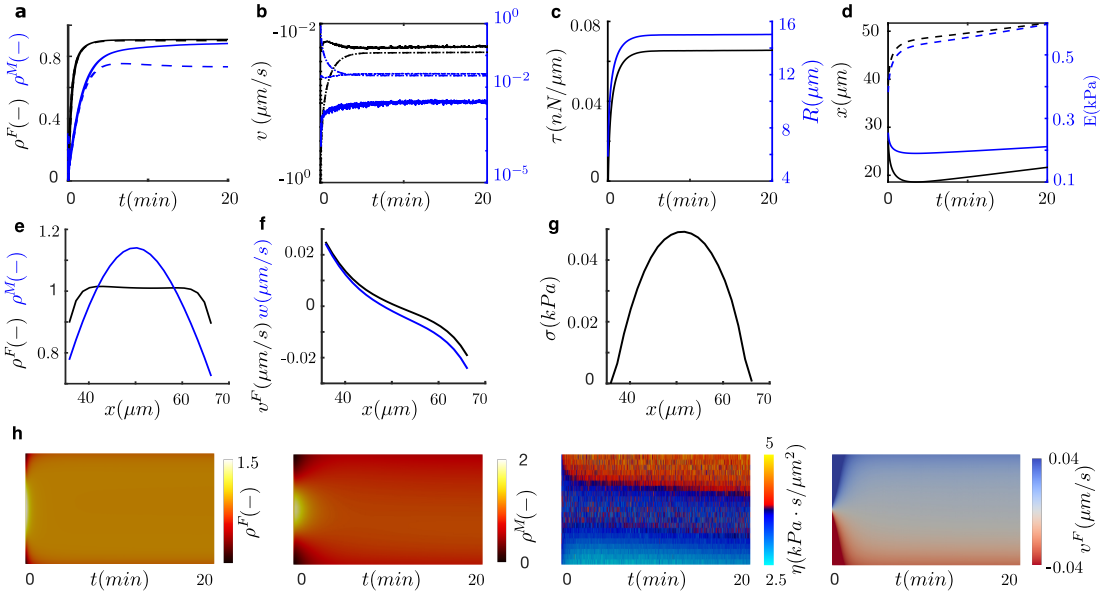

Figure 3.8: Positive durotaxis of single cells in a sample of 200 μm in length for cell expressing slip bonds and seeded at E ≈ 0.3 kPa. (a) Actin (black) and myosin (blue) densities at the rear (dash) and front (solid) of the cell. (b) At the front and rear of the cell: polymerization velocity (dot-dash) and retrograde velocity at the cell membrane (dash). Total velocity of protrusion (solid). Negative velocities are in black, positive velocities are in blue. (c) Membrane tension (black) and cell radius (blue). (d) Position (black) of the cell front (solid) and rear (dash) and stiffness (blue) seen by the cell front and rear. At steady-state, (e) actin (black) and myosin (blue) densities, (f) retrograde flow in the lab (black) and cell (blue) frame and (g) tension of the actomyosin network. (h) Kymographs of the actin density, myosin density, adhesion friction and retrograde flow velocity.

≈ 60 kPa. Here, cells stop because the friction is large enough to significantly reduce the retrograde flow, which reduces the difference between the inward flow and the outward actin polymerization velocity between the rear and front and, consequently, cells also get into a spreading-like phase. These results indicate that cells migrate toward the optimal rigidity location, when it exists, or up to a location of friction large enough to stall the retrograde flow.

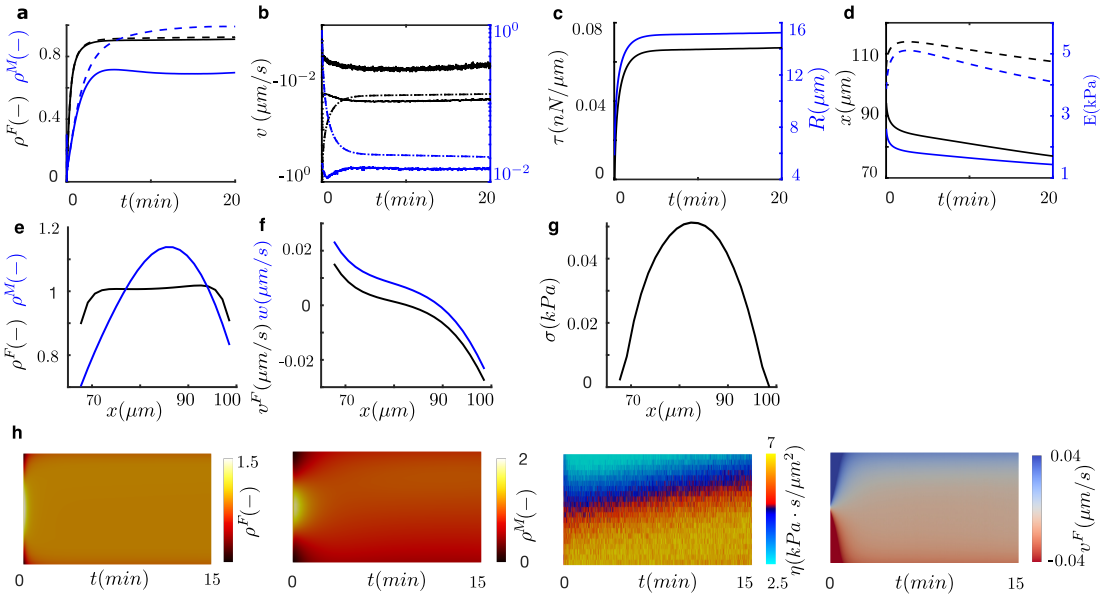

Figure 3.9: Negative durotaxis of single cells in a sample of 200 μm in length for cell expressing slip bonds and seeded at E ≈ 3 kPa. (a) Actin (black) and myosin (blue) densities at the front (dash) and rear (solid) of the cell. (b) At the front and rear of the cell: polymerization velocity (dot-dash) and retrograde velocity at the cell membrane (dash). Total velocity of protrusion (solid). Negative velocities are in black, positive velocities are in blue. (c) Membrane tension (black) and cell radius (blue). (d) Position (black) of the cell rear (solid) and front (dash) and stiffness (blue) seen by the cell front and rear. At steady-state, (e) actin (black) and myosin (blue) densities, (f) retrograde flow in the lab (black) and cell (blue) frame and (g) tension of the actomyosin network. (h) Kymographs of the actin density, myosin density, adhesion friction and retrograde flow velocity.

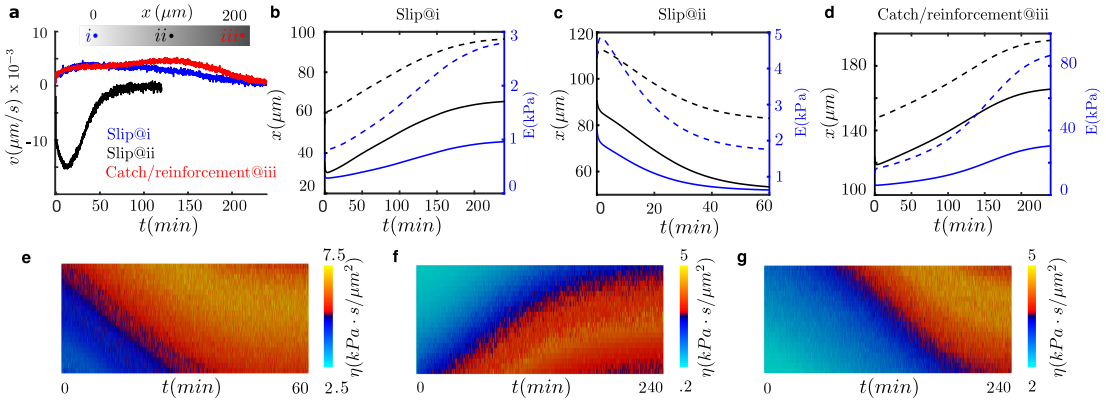

Figure 3.10: Analysis of durotaxis until steady-state. All cells are in a sample of 200 μm in length, which shows the strongest durotactic expression. For the slip cases (b-c), cells are located at soft (a, point i) and intermediate stiffness (a, point ii) locations. For the reinforced case, cells are seeded at stiff stiffness (a, point iii) locations. (a) Migration velocity of the cell. (b-d) Position (black) of the cell front (solid) and rear (dash) and stiffness (blue) seen by the cell front and rear for the three durotactic cases analyzed. (e-g) Kymographs of the cell friction for the three durotactic cases analyzed.

3.3.3 Durotaxis response to talin plasmids: switching to negative durotaxis

Then, we wonder about how we could reverse positive durotaxis. We look into the effect of talin knockdown because we know that it changes the cell adhesion behavior remarkably (Elosegui-Artola *et al.*, 2016) and, therefore, it could reverse positive durotaxis. By depleting talin, talin reinforcement is cancelled and, therefore, the adhesion behaves as a pure catch bond (see Chapter 2 and Fig. 3.11). Talin depletion results in a decrease in cell traction above a substrate rigidity threshold (see Chapter 2 and Fig. 3.11 (a)). By computing the equivalent friction, as we described above, we see that an optimal rigidity is now obtained at E≈7 kPa. In short, talin knockdown induces a drastic reduction in the traction force of the cell at substrate rigidities above ≈7 kPa and so it does for the friction of the cell with the ECM (white region, Fig. 3.11 (b)).

Therefore, we wonder whether this cell manipulation may change the durotactic

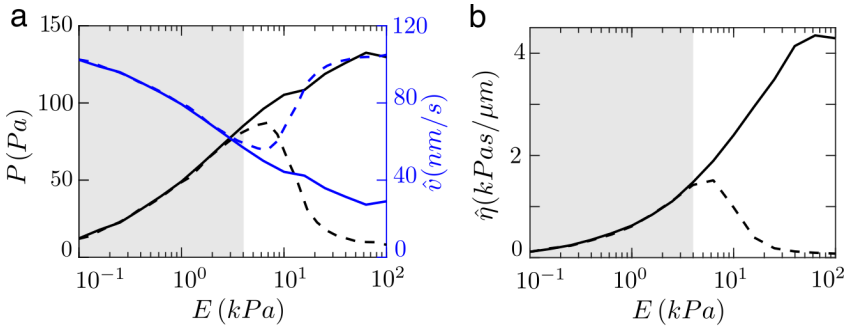

Figure 3.11: Results of computational clutch models for cells expressing catch (catch case) and reinforced catch bonds (reinforced case) for values of the substrate rigidity between 0.1-100 kPa. (a) Traction (black) and velocity (blue) for catch case (dash) and reinforced case (solid). (b) Effective friction for the catch case (dash) and reinforced case (solid). Similarly to the traction forces, friction increases monotonically for increasing values of the substrate rigidity in the reinforced case, while in the catch case it presents a hill shape with a maximum at ≈ $1kPa$.

behavior of the cell. To analyze this scenario, we use again a sample of 200 μm in length and we seed cells at E ≈ 30 kPa. We choose this location to analyze substrate regions where the catch and the talin reinforced cases differ (white region, Fig. 3.11). Our results show that by a talin knockdown, we are able to shift the direction of durotaxis (Fig. 3.12 (b-c)). Furthermore, the motility of the cell is enhanced and the maximum migration velocity doubles in the knockdown case to ≈ $8nm/s$. These cells reach the goal location at the optimal rigidity in ≈ 1.5 hr (Fig. 3.12 (b)). At this location, as happens in the slip cases, the cell reaches a state of symmetric friction at the optimal rigidity, which makes it unpolarize and stall. The talin knockdown allows us to tune

the location where the motility of the cell stalls. Therefore, we could design matrices to precisely control the goal location of cell migration.

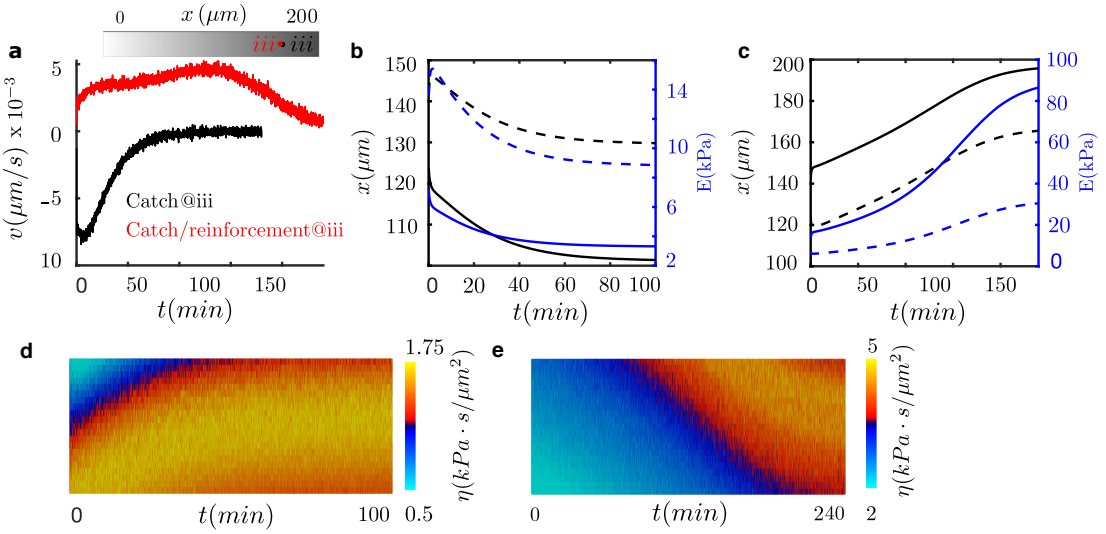

Figure 3.12: Durotaxis for catch and reinforced cases until steady-state. All cells are in a sample of 200 μm in length. Cells are located at the stiff side of the sample (a, point iii), where their behaviors differ. For the catch (b) and reinforced case (c), position (black) of the cell front (solid) and rear (dash), and stiffness (blue) seen by the cell front and rear. For the catch (d) and reinforced case (e), kymographs of the cell friction.

3.3.4 Engineering durotaxis

Finally, we further explore possibilities for engineering durotaxis other than establishing the matrix regions where cells are seeded. To do so, we performed a parametric analysis of the different adhesion models (see details in Appendix A). For all the adhesion models, we focus on the activity of myosin motors through the forces F_m, the number of binders n_c, the binding rate k_{ont}, and the slip part of the off-rate in all the unbinding models $k_{off,slip}$. For the catch case, we also analyze the catch part of the unbinding rate, $k_{off,catch}$. This is also analyzed for the reinforced case, in addition to the number of integrins added to the system int_{add} and the rate of vinculin attachment k_{onv}. Our results above indicate that cell adhesion determines durotaxis. Therefore, we specifically choose these parameters because they clearly induce changes in the adhesion properties of the AC. Moreover, they also represent physical quantities prone to be controlled or manipulated in-vitro and in-vivo. We show in Fig. 3.13 the specific

values of the physical parameters and the resulting traction.

We are interested in changes of these physical quantities that may enhance, arrest or

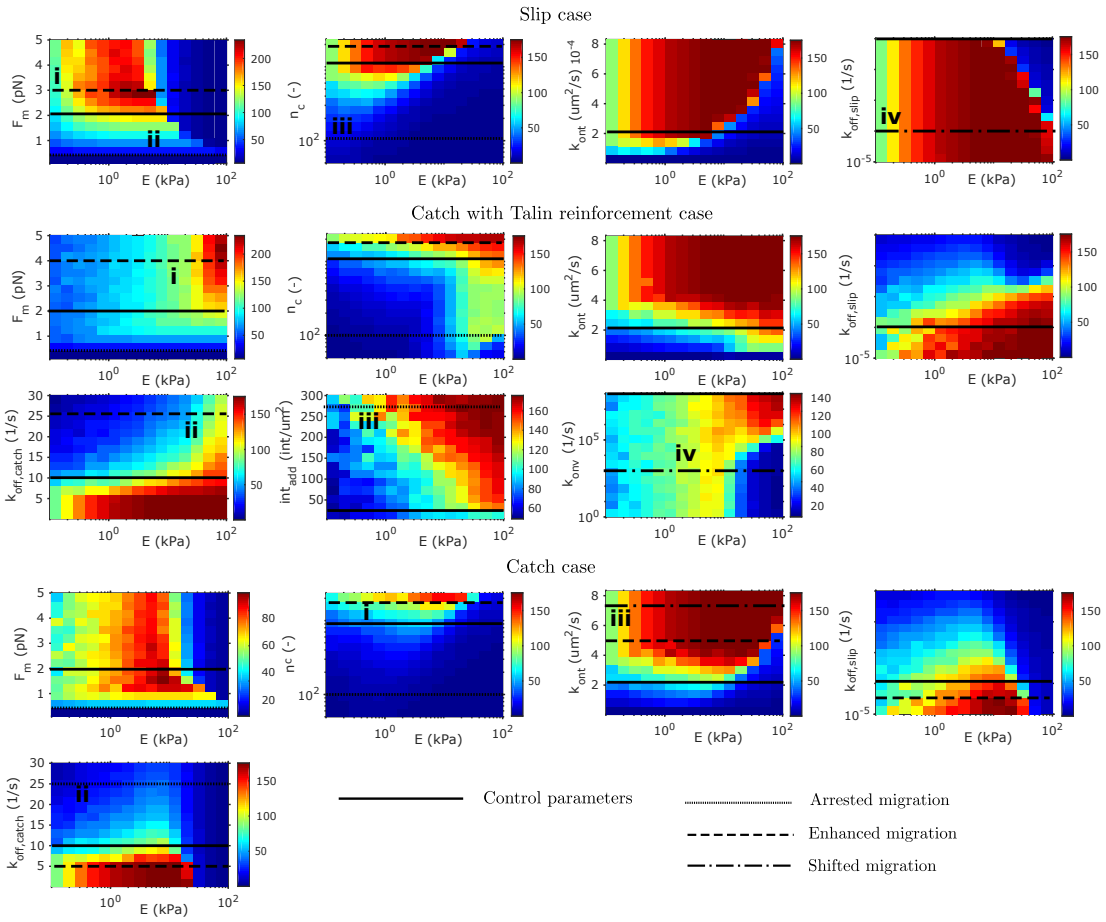

Figure 3.13: Results of computational clutch models for the traction force of cells expressing slip (slip case), reinforced catch bonds (reinforced case) and pure catch bonds (catch case) for values of the substrate rigidity in 0.1-100 kPa. The activity of myosin motors through the forces F_m, the number of binders n_c, the binding rate k_{ont} and the slip part of the off-rate in all the unbinding models $k_{off,slip}$, the catch part of the unbinding rate $k_{off,catch}$, the number of integrins added to the system int_{add}, and the rate of vinculin attachment k_{onv} are analyzed (see details in Appendix A).

shift durotaxis (Fig. 3.13). From our previous results, where we discuss that durotaxis can be explained through the asymmetric distribution of the adhesion strength, we can hypothesize what we have to manipulate the cell adhesion behavior to induce these changes. In short, we should arrest durotaxis when the traction force vanishes, enhance it when the stiffness gradient increases, in combination with placing cells in

specific stiffnesses, and shift the durotactic direction if the stiffness gradient changes sign. In the slip case, cells are initially seeded at the middle of the sample, E≈ 3 kPa. For the catch and reinforced case, cells are initially seeded at the stiff part of the sample, E≈ 30 kPa. To test these hypotheses, we start the analysis for cells expressing slip bonds (Fig. 3.14 (a)). The maximum velocity at the control case is ≈ 7nm/s. We can arrest durotaxis by decreasing the myosin activity and ligand density (Fig. 3.14 (a) and Fig. 3.13, slip, ii-iii), which reduces the migration velocity to less than 2 nm/s. We can foster durotaxis by increasing the myosin activity (Fig. 3.14 (a) and Fig. 3.13, slip, i). When we induce a durotactic enhancement, the maximum migration velocity rises to 12 nm/s. These qualitative results are obtained in all adhesion cases. Moreover, reducing the off-rate of the integrins, i.e. making them more persistent, shifts the direction of migration to stiff substrates (Fig. 3.14 (a) and Fig. 3.13, slip, iv).
We can operate similarly with cells crowded with bonds expressing a pure catch behavior, or with talin reinforcement. In the pure catch case, we can arrest and enhance durotaxis by increasing and decreasing the off-rate of the catch bond, respectively (Fig. 3.13, catch). We show that for these two scenarios, the maximum migration velocity in the control case, ≈ 5 nm/s, reduces to less than 0.5 nm/s and increases to 12 nm/s (Fig. 3.14 (b)). We also show a shift in the migration direction when the rate of integrin binding increases. Similarly, for the reinforced case (Fig. 3.14 (c)), we can foster durotaxis by increasing the off-rate of the catch part of the bond. We can also foster durotaxis for cells seeded in the soft part of the sample by increasing the recruitment of integrins to the AC. From a maximum migration velocity of ≈ 5 nm/s, we induce an increase to ≈ 7 nm/s and 9 nm/s, respectively. However, this same change for cells initially seeded at the stiff part of the sample arrests durotaxis. We can also shift the durotaxis direction, with a remarkable enhancement in the migration velocity of 12 nm/s, by reducing the on-rate of vinculin to talin.

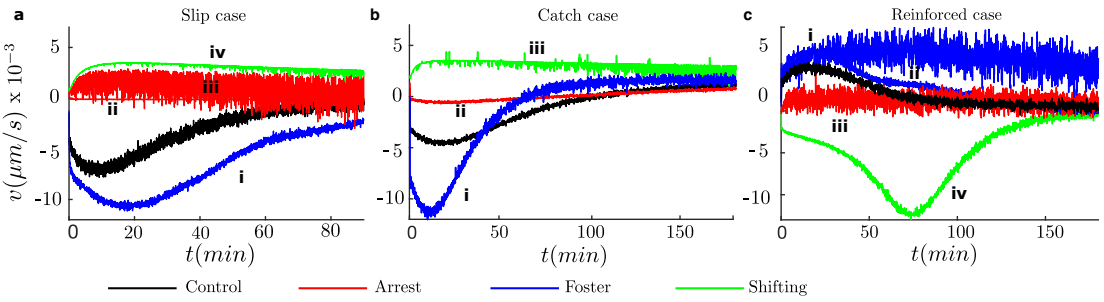

Figure 3.14: Migration velocity during durotaxis simulated until steady-state for slip, catch and reinforced cases of cell adhesion. All cells are in a sample of 200 μm in length. The control cases are plotted in black. We show cases of arrested (red) and enhanced (blue) migration, and shifted migration direction (green).

3.4 Discussion

In this chapter, we have taken advantage of the potential of the clutch models to analyze durotaxis in single cells. Durotaxis was first proved in fibroblasts (Lo *et al.*, 2000) although previous evidences of the matrix stiffness as signalling cue were based on the changes observed in the actin network (Choquet *et al.*, 1997). Based on this argument, we hypothesized that, if adhesion strength becomes asymmetric, the transmission of the motile forces of the cell polarizes and, therefore, enables durotaxis. To address the study of durotaxis, we have coupled classical active gel models (Mogilner and Manhart, 2018, Prost *et al.*, 2015, Putelat *et al.*, 2018) with the friction that we obtained from clutch models in Chapter 2 (Chan and Odde, 2008, Elosegui-Artola *et al.*, 2016). Our results reproduce the idea that most cells express positive durotaxis, the one that makes cells migrate toward positive gradients of the ECM. This type of durotactic behavior has been shown in different cell types, e.g. fibroblasts (Lo *et al.*, 2000) or smooth muscle cells (Wong *et al.*, 2003), that express cell adhesion with catch bonds and talin reinforcement (Elosegui-Artola *et al.*, 2016). However, our results show that cells expressing adhesion dynamics of slip type undergo negative durotaxis when placed at stiffer locations than the optimal stiffness. This behavior is expressed, for example, in neurons (Koser *et al.*, 2016) and human fibrosarcoma cells (Singh *et al.*, 2014). Our model suggests that these two opposing durotactic responses emerge due to an asymmetric strength adhesion, which polarizes the motile forces of the cell. Indeed, we show that cells migrate toward the optimal stiffness, where they stall. We show that this inhibition of cell motility is because cells reach a state of symmetric and high adhesion strength.

Our results also show that durotaxis is mostly dependent on the stiffness gradient

of the matrix, which confirms previous experimental results (Hadden *et al.*, 2017, Isenberg *et al.*, 2009, Koser *et al.*, 2016, Sunyer *et al.*, 2016). Furthermore, our results show that durotaxis also depends on the absolute stiffness, although less noticeable than the stiffness gradient. Indeed, cells located at intermediate stiffnesses, E = 1-10 kPa, express the largest motility. These results also confirm previous experimental data (Hadden *et al.*, 2017, Isenberg *et al.*, 2009, Joaquin *et al.*, 2016).

We also demonstrate that we can manipulate the cell to arrest, enhance and reverse the direction of durotaxis. Specifically, we demonstrate that by inhibiting talin reinforcement and, consequently, making the cell express pure catch bonds, we can shift from positive to negative durotaxis at stiff substrate rigidities, above E ≈ 7 kPa. We also show different cell manipulations, including the activity of myosin motors, ligand density and integrin behavior, that can induce these three forms of durotactic control. In our opinion, this is an important result because it may allow to engineering cell responses to specific matrix stiffnesses, to further control the fate of cell migration and the specific location toward which cells migrate. This may have important implications in designing better biomimetic materials in tissue engineering (Langer and Tirrell, 2004, Wegst *et al.*, 2014), and also in designing new therapies for arresting cancer cells invasion (Butcher *et al.*, 2009, Friedl and Wolf, 2003, Yamaguchi *et al.*, 2005).

Recently, an interesting model of negative durotaxis has been developed (Isomursu *et al.*, 2020). It shares some similarities with our work, as we both explain positive and negative durotaxis, also including the talin knockdown switching of directionality. The model of cell-ECM adhesion is similar as we both make use of a clutch model, but we include the study of a slip or catch behaviour of the bond. The migration model is different as we make use of an active gel model.

Nevertheless, our model still presents some limitations and simplifications. First, we have not considered the effect of the polarization of signaling cues. Polarization of signaling cues produces downstream changes in the actomyosin network, that control the directed cell migration (Huttenlocher, 2005, Ridley *et al.*, 2003). Among others, the members of the Rho GTPases family are particularly relevant (Fukata *et al.*, 2003, MacHacek *et al.*, 2009, Ridley, 2015, Ridley *et al.*, 2003). Upstream, phosphatidylinositol 3,4,5-trisphosphate (PIP3) and GTPase exchange factors (GEFs) (Katsumi *et al.*, 2002) control Rho GTPases activity, including the Cdc42 (Etienne-Manneville and Hall, 2001, Martin, 2015, Wedlich-Soldner *et al.*, 2003, Woods and Lew, 2019), Rac (Katsumi *et al.*, 2002) and RhoA (Lessey *et al.*, 2012), which are directly involved in cell polarization and cell motility. For example, actin polymerization is regulated by Cdc42 and Rac1 (Edelstein-Keshet *et al.*, 2013, Katsumi *et al.*, 2002, MacHacek *et al.*, 2009, Ridley, 2001, Ridley *et al.*, 2003) and RhoA regulates myosin activity. In short,

GTPases directly establish and enhance the formation of the front and back of the cell. We have preliminarily shown this effect in a single cell migration model. By considering the so called wave-pinning model, which describes essential features of cell polarization of a single GTPase in its active and inactive form (Mori *et al.*, 2008), we induced a signalling-based migration (Fig. 3.15). Without these signals, and not considering stiffness gradients, cells would just spread as described in Section 3.3.1. We modified the constitutive relation of the F-actin mechanics as $\sigma^F = \mu^F \partial_x v^F + \zeta \rho^F \rho^M \rho^{\hat{R}}$, to activate the myosin contractility just in regions where GTP-RhoA, defined by the quantity $\rho^{\hat{R}}$, is accumulated and the free polymerization velocity as $v_0^p = k_{on} \rho^R \delta$, to increase actin polymerization velocity at the cell front. ρ^R is the density of the active form of signalling proteins, that we associate to the active GTPases responsible for actin polymerization, and ρ^S is the density of the inactive form. Future work should include the coupling of cell signaling in durotaxis.

Furthermore, membrane tension at the cell front opens mechanosensitive channels

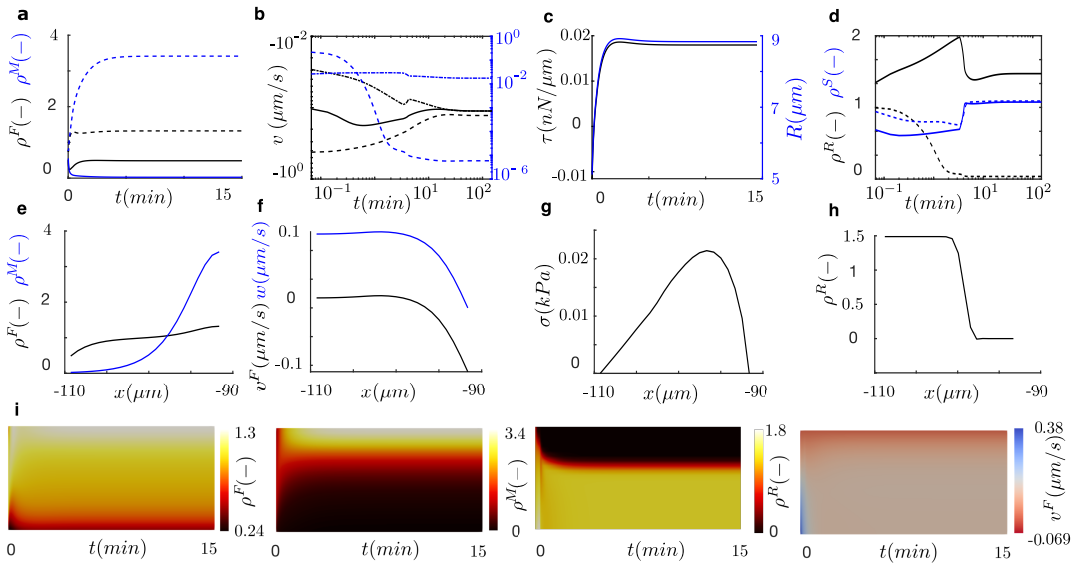

Figure 3.15: Mesenchymal cell migration. (a) Actin (black) and myosin (blue) densities at the center (dash) and front (solid) of the cell. (b) At the front and rear of the cell: polymerization velocity (dot-dash) and retrograde velocity at the cell membrane (dash). Total velocity of protrusion (solid). Negative velocities are in black, positive velocities are in blue. (c) Membrane tension. (d) ρ^R (black) and ρ^S (blue) in the front (solid) and rear (dash) of the cell. At steady-state, (e) actin (black) and myosin (blue) densities, (f) retrograde flow in the lab (black) and cell (blue) frame, (g) tension of the actin network and (h) density of the active signals along the cell length. (i) Kymographs of the actin density, myosin density, ρ^R and retrograde flow velocity.

and fosters ion fluxes (Koser *et al.*, 2016), including calcium, which may remodel the cytoskeletal organization and membrane protrusion (Wei and Chen, 2012). These protrusions are enhanced at the cell front toward the stiffness gradient (Wong *et al.*, 2014). Actually, negative durotaxis has been explained based on the capacity of the cell membrane to transduce mechanical signals. By blocking Piezo1, a mechanosensitive ion channel, axonal growth is mostly impaired (Koser *et al.*, 2016). Therefore, cell migration is mechanochemically regulated by the membrane tension at the front, which we have not included but, of course, should be the next step in our modeling of durotaxis.

Second, we have focused on single cell migration. Collective cell migration, and specifically durotaxis, is more persistent for most cell types, which suggests that the collective motility is more efficient than in single cells (Friedl and Gilmour, 2009a, Ladoux and Mège, 2017, Mayor and Etienne-Manneville, 2016, Sunyer *et al.*, 2016). The general reasoning is that cell clusters feel larger differences in the matrix stiffness when the cluster covers a larger portion of substrate rigidities. We have shown that cells placed in steep gradients migrate more effectively than those in shallow gradients, in agreement with that argument. Therefore, this explains not only collective durotaxis, but also single cell durotaxis. Previous works suggested that a cell cluster probes the matrix rigidity at edges and transmits the reaction forces at the front and rear through supracellular actin fibers (Sunyer *et al.*, 2016). This is also the case of single cells, which transmit forces along the cell fronts through intercellular actin networks. However, Should a hypothetical cell of a given size and a cell cluster of the same size, i.e. made of cells of smaller size, have the same motility features? Single cells polarize the actomyosin network and the actin protrusion in one single domain. Clusters, on the other hand, present a weaker polarization as a system, because each cell should polarize weaker as they feel a smaller stiffness gradient than the whole, single cell. Even the proximity of cells in a cluster should diminish cell migration by contact inhibition. However, this argument does not reproduce the higher migration efficiency of clusters compared to single cells. Therefore, the extension of our current single cell model to a cluster of cells could shed some light on the collective migration problem.

Chapter 4

A multiscale clutch model for adhesion complex dynamics

In this chapter we focus on the modelling of a single focal adhesion, and we investigate its dynamics for different rigidities of the ECM.
In Chapter 2 we summarised some limitations of the clutch model with talin reinforcement (Elosegui-Artola *et al.*, 2016). Here we overcome these modelling issues by extending the complexity of the adhesion chain and by computing the deformation at the nano-scale of the adhesion patch at each ligand position. This allows us to model more accurately mechanosensing events such as vinculin and actin binding to different domains of the talin rod. Finally, given the role of talin mechanosensitivity in diseases like cancer (Azizi *et al.*, 2021), we study how the depletion of some talin domains influences force transmission and integrin recruitment.

4.1 Model

4.1.1 Substrate displacement with Green's function

First, we focus on computing the substrate displacement point-wise in the whole FA area. We use Green's functions (Weinberger *et al.*, 2021) to compute the substrate displacement $x_{sub(s)}$ in whatever position inside the FA, starting from the forces $F_{c(b)}$ of the bound binders.
In a 3D elastic medium, the balance of linear momentum is:

$$\nabla \cdot \boldsymbol{\sigma} = \boldsymbol{b} \qquad \text{with} \qquad \boldsymbol{\sigma} = \mathbb{C} \cdot \nabla \boldsymbol{u}, \tag{4.1}$$

where $\boldsymbol{\sigma}$ is the Cauchy stress and $\boldsymbol{b}$ the body force density. The solution of this equation is the displacement field $\boldsymbol{u}$ under external forces and boundary loads.
To solve our problem of a FA, we consider a domain in which n_c extracellular adhesion sites exert forces on the substrate.
We use the Green's function of a semi-infinite, isotropic and homogeneous medium to compute the force-displacement relation in all points within a radius R, where a subset of N ligands, $N < n_c$, are engaged. The elastic Green's function $G_{ij}(\boldsymbol{x}, \boldsymbol{x}')$ represents the displacement at $\boldsymbol{x}$ in the direction i due to a punctual force at $\boldsymbol{x}'$ in the direction j. Here $\boldsymbol{x}$ and $\boldsymbol{x}'$ are points in a 3D environment, with coordinates (x, y, z) and (x', y', z'). The Green's function is the displacement solution of Eq. 4.1 under point body force such that $b_k(\boldsymbol{x}) = \delta_{jk}\delta(\boldsymbol{x} - \boldsymbol{x}')$.
As the Green's function $G_{ij}(\boldsymbol{x}, \boldsymbol{x}')$ only depends on the displacement between the material points, we can rewrite it as:

$$G_{ij}(\boldsymbol{x}, \boldsymbol{x}') = G_{ij}(\boldsymbol{x} - \boldsymbol{x}'). \tag{4.2}$$

Consider a constant point force $\boldsymbol{F}$ acting at $\boldsymbol{x}'$ within an infinite elastic body. The volume V is any arbitrary finite volume enclosed by a surface S with an outward normal $\boldsymbol{n}$. The displacement field in the direction i, due to the point force acting in the direction j, is given by:

$$u_i(\boldsymbol{x}) = G_{ij}(\boldsymbol{x} - \boldsymbol{x}')F_j. \tag{4.3}$$

Taking the gradient of this displacement expression and plugging it into Eq. 4.1 we obtain:

$$\boldsymbol{\sigma}(\boldsymbol{x}) = \mathbb{C}\nabla G_{ij}(\boldsymbol{x} - \boldsymbol{x}')F_j. \tag{4.4}$$

If the volume V encloses the point $\boldsymbol{x}'$, then the external body force $\boldsymbol{F}$ must balance the traction acting on the domain's surface S, which can be expressed as:

$$\boldsymbol{F} + \int_S \boldsymbol{\sigma}(\boldsymbol{x}) \cdot \boldsymbol{n}\, dS(\boldsymbol{x}) = 0 \tag{4.5}$$

$$\boldsymbol{F} + \int_S \mathbb{C}\nabla G_{ij}(\boldsymbol{x} - \boldsymbol{x}')F_j \cdot \boldsymbol{n}\, dS(\boldsymbol{x}) = 0. \tag{4.6}$$

Applying the Divergence theorem and noting that the body forces can be described by a 3D Dirac delta function, we can rewrite it as:

$$\int_V \left[\mathbb{C}\nabla G_{ij}(\boldsymbol{x}-\boldsymbol{x}')F_j + \boldsymbol{F}\delta(\boldsymbol{x}-\boldsymbol{x}')\right] dV(\boldsymbol{x}) = 0. \tag{4.7}$$

This expression must hold for any arbitrary volume V containing the point $\boldsymbol{x}'$ and any arbitrary constant force $\boldsymbol{F}$, thus it must hold point-wise, resulting in the equilibrium condition:

$$\mathbb{C}\nabla G_{ij}(\boldsymbol{x}-\boldsymbol{x}') + \boldsymbol{\delta}\delta(\boldsymbol{x}-\boldsymbol{x}') = 0. \tag{4.8}$$

This is the equilibrium equation satisfied by the Green's function in an infinite elastic medium. Eq. 4.8 is equivalent to Eq. 4.1 when the body force is a delta function, $b_k = \delta_{jk}\delta(\boldsymbol{x}-\boldsymbol{x}')$.
In order to reach the expression for the Green's function, we solve Eq. 4.8 using Fourier transforms. Defining the Fourier transform of the elastic Green's function as $g_{ij}(\boldsymbol{k})$, they are related as follows:

$$g_{ij}(\boldsymbol{k}) = \int_{-\infty}^{\infty} \exp(i\boldsymbol{k}\cdot\boldsymbol{x})G_{ij}(\boldsymbol{x})d\boldsymbol{x} \tag{4.9}$$

$$G_{ij}(\boldsymbol{x}) = \frac{1}{(2\pi)^3}\int_{-\infty}^{\infty} \exp(-i\boldsymbol{k}\cdot\boldsymbol{x})g_{ij}(\boldsymbol{k})d\boldsymbol{k}. \tag{4.10}$$

After some mathematical manipulation, and defining $\boldsymbol{\zeta} = \dfrac{\boldsymbol{k}}{|\boldsymbol{k}|}$, we get:

$$g_{ij}(\boldsymbol{k}) = \frac{1}{\zeta_{ij}k^2}. \tag{4.11}$$

Substituting the solution found for $g_{ij}(\boldsymbol{k})$ into Eq. 4.10, we get:

$$G_{ij}(\boldsymbol{x}) = \frac{1}{(2\pi)^3}\int_{-\infty}^{\infty} \exp(-i\boldsymbol{k}\cdot\boldsymbol{x})\frac{1}{\zeta_{ij}k^2}d\boldsymbol{k}, \tag{4.12}$$

which, after changing from cartesian to spherical coordinates, becomes:

$$G_{ij}(\boldsymbol{x}) = \frac{1}{8\pi^2 x}\int_0^{2\pi} \zeta_{ij}^{-1}\, d\theta|_{\boldsymbol{x}\cdot\boldsymbol{\zeta}=0}. \tag{4.13}$$

This is the expression of the Green's function for an infinite medium for general anisotropic materials. It can be particularised by assuming the medium isotropic, which

results in $\zeta_{ij} = z_p z_q \mathbb{C}_{ipjq}$. Defining $R = |\boldsymbol{x}|$ and after some mathematical operations we end up with:

$$G_{ij} = \frac{1}{8\pi\mu}\left[\delta_{ij}R_{kk} - \frac{1}{2(1-\nu)R_{ij}}\right], \tag{4.14}$$

where μ is the shear modulus and ν the Poisson's ratio of the medium. This expression of G_{ij} for the displacement in the direction i, due to a force applied in the direction j, refers to a 3D environment.
In our problem, we consider a substrate in 2D on the XY-plane, so our engagement points have coordinates $\boldsymbol{x} = (x, y)$, being $z = 0$. The angle $\theta = 15°$ between the adhesion chains and the substrate (Liu *et al.*, 2015b) gives forces in the same direction and results in a substrate displacement with non-zero components in the three dimensions. However, we introduce an approximation and consider horizontal forces and substrate displacements, both laying in the XY-plane. More specifically, as we consider just a FA and not an entire cell, all bound binders bear forces with the same direction as all actin filaments can be considered parallel among them. Therefore our substrate displacements will have only one dimension.
In 1D, calling i the only dimension, the expression for the displacement of the substrate due to the force $F_{c,i}$, becomes:

$$x_{sub,i} = G_{ii}F_{c,i}, \tag{4.15}$$

where G_{ii} is the Green's function referring to the only dimension i.
From now on we consider implicit the notation of the direction i, and we define $\hat{G} = G_{ii}$. We call $\boldsymbol{x}_{sub}$ the vector of one-dimensional displacements $x_{sub(s)}$ in all the points s inside the FA, and we call $\boldsymbol{F_c}$ the vector of forces $F_{c(b)}$ in the ligand points $b = 1, \dots, n_c$. Therefore, after each balance of forces giving the new forces, the displacement of the substrate becomes $\boldsymbol{x}_{sub} = \hat{\boldsymbol{G}} \cdot \boldsymbol{F_c}$.
As the Green's function is singular at the point where the binder is bound and the force is applied, the displacement is computed at a distance of 5 nm from the binder.

4.1.2 Talin mechanics

Talin is one of the most important intracellular proteins for mechanosensing and mechanotransduction in cell-ECM adhesion. It is made of 18 structured domains: the FERM domain in the talin head including F0, F1, F2 and F3, connected via an 80 amino-acid linker to the talin rod, made of 13 helical bundles, R1 - R13, as can

be seen in Figure 4.1. Talin is recruited from the cytosol and binds its head to the

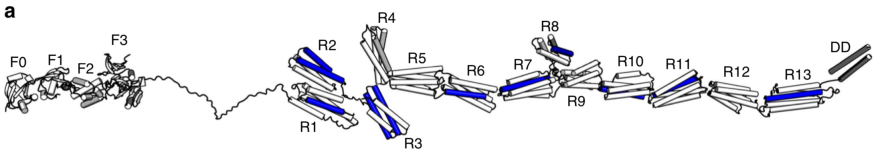

Figure 4.1: Talin structure with head, neck and 13 rod domains (Yao *et al.*, 2016).

β-integrin units and its tail to the actin cytoskeleton (Klapholz and Brown, 2017). The 13 rod domains undergo conformational changes under the force exerted by the actomyosin, allowing different interactions with other adaptor proteins. R3 is considered the weakest domain as it unfolds with a force of ≈ 5 pN (Yao *et al.*, 2016), exposing two cryptic binding sites to vinculin. However, in the whole talin protein, there are 11 vinculin binding sites (VBSs) and three actin binding sites (ABSs). One peculiarity is that the domain R8 is inserted inside two helices of R7, which makes the unfolding of R8 only possible when R7 is unfolded (Yao *et al.*, 2016).
The actual mechanics of this molecule has never been integrated within the clutch hypothesis. Here we couple the improved clutch model in Chapter 2 with a full-length model of the talin rod (Yao *et al.*, 2016), where its 13 domains have specific unfolding and refolding rates depending on force, and the molecule displacement follows non-linear laws under mechanical loads.
We define the end-to-end length of a domain as the minimum distance between the two ends of the domain. We call x_{trans} the end-to-end distance of a folded domain and x_{unf} the end-to-end distance of an unfolded domain. For an unfolded domain we call L its contour length, i.e. the maximum possible length for that domain (Figure 4.2).
For all the domains, the unfolding kinetic parameters were determined by fitting

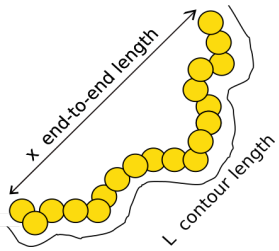

Figure 4.2: For both folded and unfolded domains: x is the end-to-end length, i.e. the minimum distance between the two ends of the domain. Only for unfolded domains, L is the contour length, i.e. the maximum possible length of the domain.

experimental data to the force probability of Bell's model. The unfolding rates of all domains directly follow Bell's model for slip bonds:

$$k_u(F) = k_u^0 \exp\left(\frac{\Delta x_u F}{k_B T}\right), \tag{4.16}$$

where k_u^0 is the unfolding rate at zero force and Δx_u is the transition distance from the folded state to the transition state.
For all the domains, the folding rates are fitted using the Arrhenius relation (Chen *et al.*, 2015b):

$$k_f(F) = k_f^0 \exp \int_0^F \Delta x_f(F')dF', \tag{4.17}$$

where k_f^0 is the refolding rate at zero force and $\Delta x_f(F) = x_{trans}(F) - x_{unf}(F)$ is the force-dependent refolding transition distance, that can be computed knowing the transition state $x_{trans}(F)$ and the unfolded state $x_{unf}(F)$.
The transition state, which is like a partially folded state, behaves as a freely-jointed chain (FJC), so the end-to-end distance of the folded domain x_{trans} follows:

$$x_{trans}(F) = L_0 \coth\left(\frac{FL_0}{k_B T}\right) - \frac{k_B T}{F}, \tag{4.18}$$

where L_0 is the rigid body size of the folded domain, i.e. the maximum length that a folded domain can reach. The unfolded domain and the talin neck behave as a worm-like chain (WLC):

$$\frac{FA}{k_B T} = \frac{1}{4(1 - x_{unf}/L)^2} - \frac{1}{4} + \frac{x_{unf}}{L}, \tag{4.19}$$

where x_{unf} is the end-to-end length of the unfolded domain, A is the persistence length and L the contour length.
We implement one VBS in the domain R3 of talin, which is exposed when the domain unfolds. Vinculin can bind with a binding rate k_{onv}. While vinculin is bound, the domain can not refold (Yao *et al.*, 2014), and we consider that vinculin unbinds only when the binder becomes free. If vinculin binds to talin, it induces integrins recruitment and reinforcement of the focal adhesion.
In the improved clutch model, a binder bound and unfolded could only become free, but could not refold and remain bound. Here we allow the refolding of each of the talin

domains, following their particular force-dependent folding rate $k_f(F)$. Only in the case in which a vinculin molecule is bound to R3, the domain is locked in an unfolded conformation.

We give references for the parameters related to talin mechanics. Talin head behaves stiff and has a length $offset = 10\,\text{nm}$ (Yao *et al.*, 2016). Talin neck follows a WLC law as in Eq. 4.19, with contour length $L = 40\,\text{nm}$ (Yao *et al.*, 2016). For all folded domains, we take as rigid body size inside the FJC Equation 4.18 $L_0 = 5\,\text{nm}$ (Yao *et al.*, 2016). For all unfolded domains, we take as persistence length inside the WLC Equation 4.19 $A = 0.8\,\text{nm}$ (Yao *et al.*, 2016). For the product of Boltzmann constant and absolute temperature, we take $k_B T = 4.1\,\text{pN} \cdot \text{nm}$ (Yao *et al.*, 2016).

For the rest of parameters, we refer to Table 4.1. The domain size in the first row refers

Domain	**1**	**2**	**3**	**4**	**5**	**6**	**7-8**	**9**	**10**	**11**	**12**
L (nm)	69.2	52.4	49.6	52.4	64	60.4	118.4	66.8	63.2	66.4	62.8
$k_{u,0}$ (s^{-1})	4.2×10^{-6}	1.7×10^{-8}	0.018	4.2×10^{-6}	2.5×10^{-5}	2.5×10^{-5}	4.2×10^{-6}	4.2×10^{-6}	2.5×10^{-5}	2.5×10^{-5}	1.7×10^{-8}
Δx_u (nm)	3.1	3.4	5.7	3.1	4.1	4.1	3.1	3.1	4.1	4.1	3.4
$k_{f,0}$ (s^{-1})	0.11	0.019	22.2	0.46	1	1	0.39	0.93	0.93	0.93	0.93
Δx_f (nm)	18.2	12.5	15.5	4.4	15.7	15.7	13.3	14.5	14.5	14.5	14.5

Table 4.1: Parameters from experiments for talin rod domains R1-R12 (Yao *et al.*, 2016).

to the contour length L for unfolded domains as in the WLC Equation 4.19. $k_{u,0}$ in the second row is the unfolding rate at zero force inside the unfolding rate in Eq. 4.16. Δx_u in the third row is the transition distance from folded to transition state inside the unfolding rate in Eq. 4.16. $k_{f,0}$ in the fourth row is the refolding rate at zero force inside the refolding rate in Eq. 4.17.

Because of hysteresis, when talin domains refold after having been in the unfolded state, they start following a new FJC law, with a bigger rigid-body size $L_0 > 5\,\text{nm}$. These values of L_0 are in the last row of Table 4.1, with the name Δx_f. We consider these new rigid body size values L_0 inside the computation of $x_{trans}(F)$ in the force-dependent refolding transition distance $\Delta x_f(F) = x_{trans}(F) - x_{unf}(F)$ inside the integral of the refolding rate $k_f(F)$ in Eq. 4.17. Being the refolding events not so frequent, elsewhere, as in the computation of the displacements, we consider that all the folded domains follow a FJC law with rigid body size $L_0 = 5\,\text{nm}$, without checking their history (Yao *et al.*, 2016).

This set of parameters for talin mechanics is used from now on.

4.1.3 Use of Gillespie's algorithm in adhesion complex dynamics

We introduce in the model the use of the Gillespie's algorithm (Gillespie, 1976, 1977) instead of the MC algorithm. We use a variable timestep, determined by the reaction times. Instead of updating the state of all the binders whose reaction time is smaller than the fixed Δt, in the Gillespie's algorithm we update just the state of one binder at each timestep.
In Chapter 2 we already showed that MC and Gillespie give similar results. Here we adopt Gillespie's algorithm, as it updates only the state of one binder at a time, which gives a better control over the simulation running.
Depending on its initial state, the possible events for each binder are binding, unbinding, unfolding of one talin domain, refolding of one talin domain and vinculin binding to talin. As in MC, all binders behave independently of the others. The time at which one event happens is computed, for example for the binding event we have:

$$\tau_i = \frac{-\ln \xi_i}{k_{on(i)}}, \tag{4.20}$$

for all binders $i = 1 \dots n_c$, where ξ_i are independent random numbers uniformly distributed over $[0, 1]$. After computing the time of all possible events, we choose the minimum $\tau_\nu = \min_i(\tau_i)$ and we update only the corresponding event in the binder ν.
In the improved clutch model, we had a fixed final time t_f and several MC simulations happening one after the other. As a result, we averaged the variables in time, getting also the average over the MC simulations.
Here in the multiscale clutch model, we let the Gillespie simulation run until a fixed final time t_f. Depending on the choice of parameters, we can have a certain number of loops of full unbinding of the cluster, i.e. $P_b = 0$, but we can also reach the final time t_f without ever getting a free cluster. Hence, depending on the computational cost of each case, we run 10 or 100 Gillespie simulations all starting at time $t_0 = 0\,\mathrm{s}$ and finishing at t_f, in order to get stable results. Having a variable timestep, when averaging over Gillespie simulations, we choose a small enough fixed timestep, and we interpolate the values of the variables previously obtained. For the graphs against Young's modulus, we first compute the weighted average in time for each Gillespie simulation, and then we calculate the average over the Gillespie simulations, to get one value for each Young's modulus E.

4.2 Results

In this section, we make use of the multiscale clutch model to understand how FAs behave when crowded with either $\alpha_5\beta_1$ or $\alpha_V\beta_3$ integrins. We then analyze FA dynamics while varying the type of integrin, as each integrin owns characteristic binding and unbinding rates. Finally, we investigate the influence of ligand spacing in FA dynamics. Twelve domains of talin are modelled, excluding R13. Regarding vinculin binding sites, only the VBS in R3 is considered, being R3 the first domain in unfolding. As regards actin binding sites, only ABS3 in R13 is implemented. Actin velocity is applied to R13 and it is treated as a scalar variable.
Additionally, here the integrin density is incremented as in the improved clutch model in Chapter 2: when a binder becomes free, the integrin density is updated, being incremented by int_{add} if a vinculin was bound to that binder, and decreased by int_{add} if vinculin was not bound.
We average over 10 Gillespie simulations, each run until the final time $t_f = 30$ s.

4.2.1 $\alpha_5\beta_1$- and $\alpha_V\beta_3$-based focal adhesions

$\alpha_5\beta_1$ and $\alpha_V\beta_3$ are considered the most relevant integrins in cell-ECM adhesion. Here we compare two FAs, each fully crowded with one type of integrins, in order to understand their characteristic behaviour.
In Table 4.2 we report the values for the model parameters. To define the parameters of the integrin dynamics, we look into experimental values for integrin $\alpha_{IIb}\beta_3$ (Barsegov, 2012). In its high activation state, in presence of Mn^{2+} ions, $\alpha_{IIb}\beta_3$ exists in two states, with zero force off-rates $k_{off,1} = 2.42\,\mathrm{s}^{-1}$ and $k_{off,2} = 0.6\,\mathrm{s}^{-1}$ respectively. The dissociation constants are $K_{d,1} = 5 \times 10^4\ \mu\mathrm{m}^{-2}$ and $K_{d,2} = 0.3 \times 10^3\ \mu\mathrm{m}^{-2}$ respectively. Being $K_d = k_{off}/k_{ont}$, we get $k_{ont,1} = 4.84 \times 10^{-5}\ \mu\mathrm{m}^2\mathrm{s}^{-1}$ and $k_{ont,2} = 0.002\,\mu\mathrm{m}^2\mathrm{s}^{-1}$. Considering the same order of magnitude of experimental values for integrin $\alpha_{IIb}\beta_3$, we take the binding rates $k_{ont} = 0.005\,\mu\mathrm{m}^2\mathrm{s}^{-1}$ for integrin $\alpha_5\beta_1$, and $k_{ont} = 1 \times 10^{-4}\ \mu\mathrm{m}^2\mathrm{s}^{-1}$ for integrin $\alpha_V\beta_3$.
As $\alpha_5\beta_1$ integrins undergo CMR (Kong *et al.*, 2013), we modify their characteristic lifetime. Keeping the original shape, we increase the lifetime for forces in the middle of the range. This modification reflects the fact that integrins that have been subjected to loading and unloading cycles with high force peaks have a longer lifetime. As our model is not storing information about the history of each integrin, we do not take into account that the number of loading and unloading cycles is also increasing the lifetime. We remove the modification of the lifetime for low forces, introduced in the improved clutch model. We consider $\alpha_V\beta_3$ integrins with their characteristic unbinding rate, as

Parameters	$\alpha_5\beta_1$	$\alpha_V\beta_3$
k_{ont} (μm^2/s)	0.005	1×10^{-4}
$k_{off,slip}$ (s^{-1})	3.68×10^{-4}	4.173×10^{-4}
$F_{b,slip}$ (pN)	7.168	5.4825
$k_{off,catch}$ (s^{-1})	2	0.4012
$F_{b,catch}$ (pN)	7.168	28.67
E (kPa)	0.1 - 100	
a (nm)	708	
d (nm)	100	
n_c	158	
κ_c (pN/nm)	10	
d^0_{int} (int /μm^2)	300	
F_m (pN)	2	
n_m	158	
v_u (nm/s)	110	
k_{onv} (s^{-1})	1×10^8	
int_{add} (int /μm^2)	24	
m_r (int /μm^2)	15000	

Table 4.2: For a FA with $\alpha_5\beta_1$ or $\alpha_V\beta_3$ integrins, parameters used in Figures 4.4, 4.5, 4.6 and 4.7, for the multiscale clutch model with ABS3 and 1 VBS.

CMR has not been proved for this type of integrins. For both integrins we use the catch formulation of k^*_{off} in Eq. 2.4, and we get the parameters $k_{off,slip}$, $F_{b,slip}$, $k_{off,catch}$, $F_{b,catch}$ in Table 4.2. In Figure 4.3 we plot the two lifetime curves, together with the experimental data (Elosegui-Artola *et al.*, 2016, Kong *et al.*, 2009).

For the Young's modulus of the substrate, we take 16 values with exponential distribution in the range $E = 0.1 - 100$ kPa. We take a fixed radius of the FA, $a = 708$ nm (Oria *et al.*, 2017). We choose a FA with equispaced ligands at distance $d = 100$ nm, a realistic value for distances between binders. The number of equispaced ligands n_c is computed given the radius a of the circular FA and the distance d at which ligands are kept. For the stiffness of the linear spring modelling the integrin we take $\kappa_c = 10$ pN/nm, but a more biological value should be $\kappa_c = 0.8$ pN/nm (Figure 2.13) (Kong *et al.*, 2013, 2009). For the initial density of integrins we choose $d^0_{int} = 300$ int/μm^2, of the same order of experimentally measured values: $d^0_{int} = 488$ int/μm^2 for $\alpha_5\beta_1$ integrins and $d^0_{int} = 2513$ int/μm^2 for $\alpha_V\beta_6$ integrins (Elosegui-Artola *et al.*, 2014). For the stall force of a single myosin motor we take $F_m = 2$ pN (Molloy *et al.*, 1995). We take a number of myosin motors equal to the number of ligands, $n_m = n_c = 158$. As for the unloaded actin velocity v_u, we review several sources. In a recent computational model for myosin

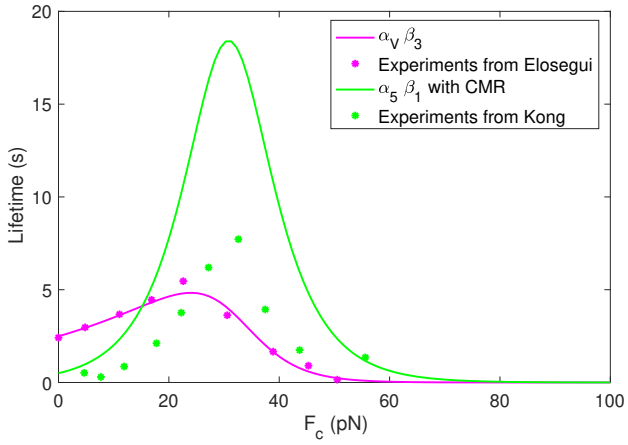

Figure 4.3: Lifetime for $\alpha_5\beta_1$ integrins with CMR and for $\alpha_V\beta_3$ integrins: fitting (line) and experimental data (dots) (Elosegui-Artola *et al.*, 2016, Kong *et al.*, 2009). The parameters obtained for k^*_{off} are reported in Table 4.2.

activity based on experimentally validated parameters, unloaded velocity values are obtained: for NM IIA the unloaded velocity is $v_u \approx 42 - 70$ nm/s (Stam *et al.*, 2015). Unloaded velocity values have also been obtained through the gliding filament assay (Kron and Spudich, 1986), where the movement of fluorescently labeled filaments moving on motors attached to a coverslip is recorded (O'Connell *et al.*, 2007). At maximum motor density, for NM IIA the unloaded velocity is $v_u = 300$ nm/s (Wang *et al.*, 2000) and for NM IIB it is $v_u = 92$ nm/s (Pato *et al.*, 1996). Experiments for nonmuscle phosphorylated platelet myosin give unloaded velocity values $v_u = 82 - 113$ nm/s (Cuda *et al.*, 1997). In light of these findings for the different types of nonmuscle myosin II, and reminding that focal adhesions present a percentage of both NM IIA and NM IIB, for our model we choose $v_u = 110$ nm/s. For the binding rate of vinculin we take $k_{onv} = 1 \times 10^8$ s^{-1} (Elosegui-Artola *et al.*, 2016). For the value of the increment of integrin density int_{add} at each reinforcement event we choose $int_{add} = 24$ int/μm^2 (Elosegui-Artola *et al.*, 2016), and for the maximum integrin density we take $m_r = 15000$ int/μm^2 (Elosegui-Artola *et al.*, 2016).
We show the time evolution of the main variables for a FA of $\alpha_5\beta_1$ integrins (Figure 4.4) and for a FA of $\alpha_V\beta_3$ integrins (Figure 4.5). We fix the Young's modulus of the substrate $E = 2.51$ kPa, and we run one Gillespie simulation until $t_f = 30$ s. In the FA crowded with $\alpha_5\beta_1$, after a short period of ~ 2 s of transition from the initial fully free state, the adhesion enters a quasi-static phase in which the number of bound binders stabilizes to ~ 50%, as the binding and unbinding rates equal (Figure 4.4). The response of a FA

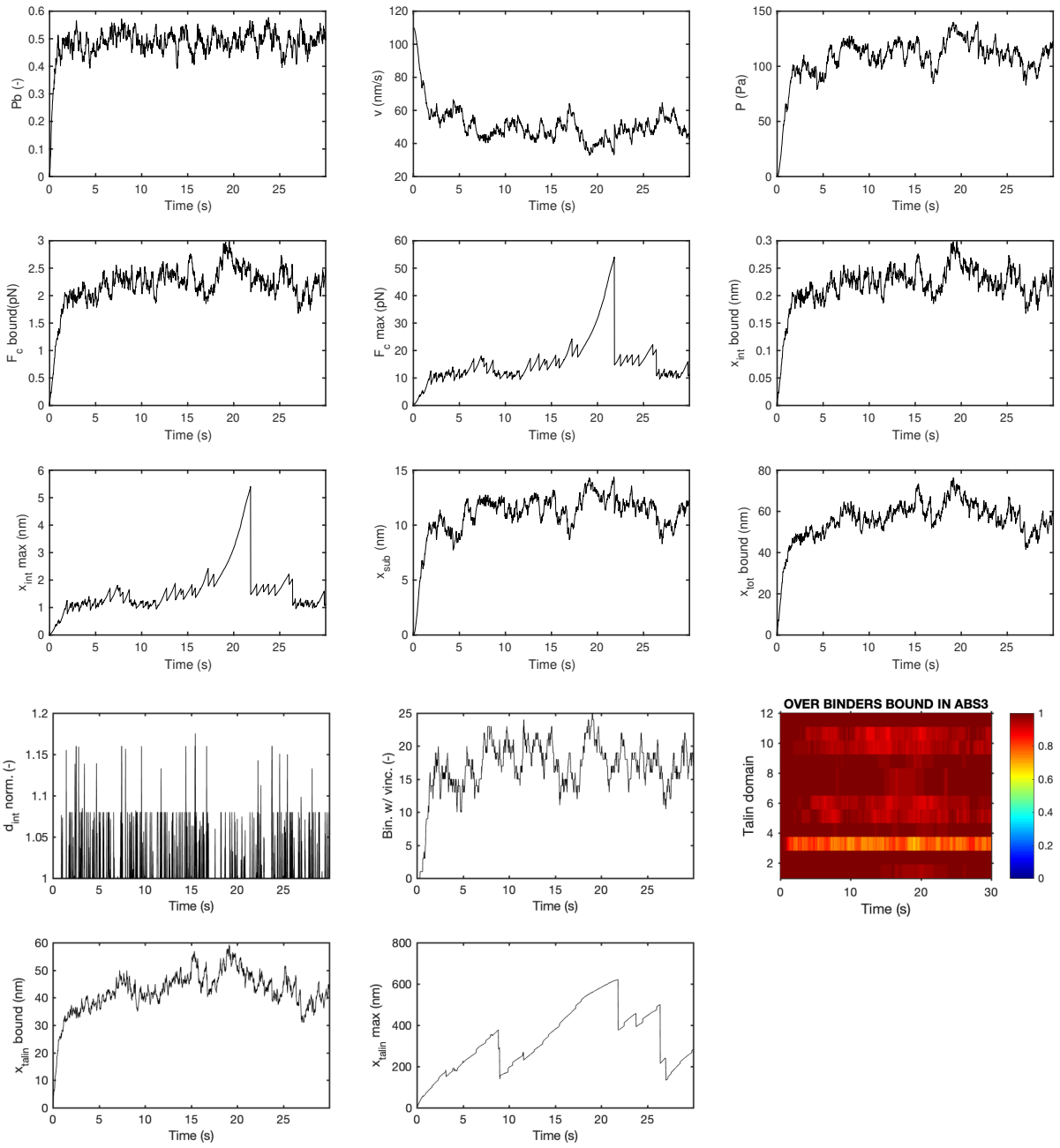

Figure 4.4: For one Gillespie simulation, time evolution of the main variables fixing $E = 2.51$ kPa, for a FA with $\alpha_5\beta_1$ integrins. The parameters are taken from Table 4.2 and Table 4.1.

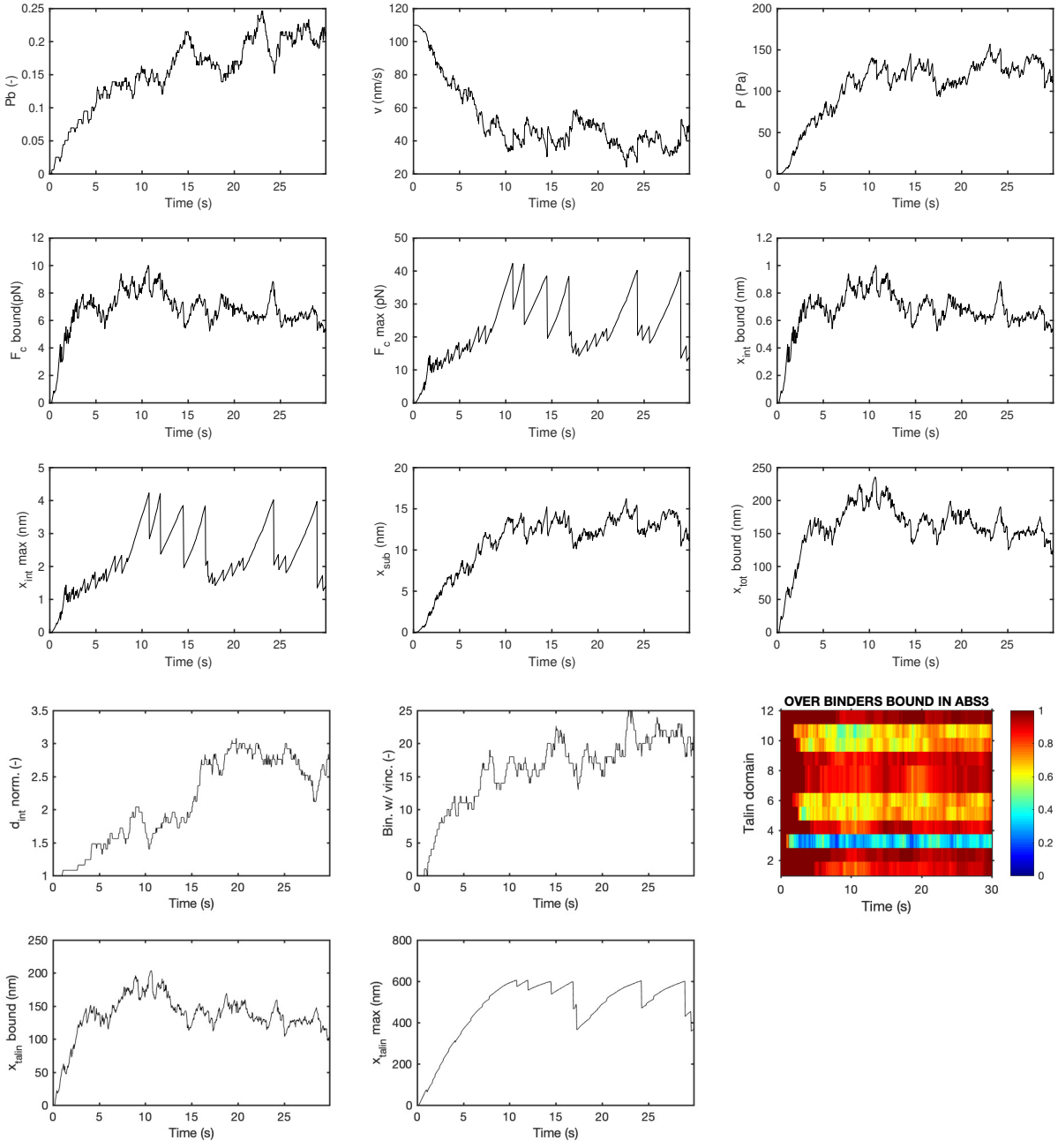

Figure 4.5: For one Gillespie simulation, time evolution of the main variables fixing $E = 2.51\,\text{kPa}$, for a FA with $\alpha_V\beta_3$ integrins. The parameters are taken from Table 4.2 and Table 4.1.

crowded with $\alpha_V\beta_3$ follows a similar behaviour, with a longer transition phase between the free state and the quasi-static state, of ~ 15 s (Figure 4.5). At this state, we observe a smaller amount of bound binders, around 25%. It is important to note that for both integrins our model reaches a quasi-steady state that does not capture the collapse of the FA before the chosen final time. We propose that FA disassembly happens because of a specific mechano-chemical signalling of external proteins, and cannot be explained only by the force transmission inside the actin-talin-integrin-fibronectin chain.

All model variables averaged over bound binders follow the same steady-state tendency. For both integrins, the velocity of the actin fibres decreases to ~ 40 – 50 nm/s and the traction at the adhesion patch increases up to ~ 125 – 150 Pa.

As regards the force, we do not have peaks out of the biological range. Indeed, it reaches a maximum among all binders of $F_c \approx 50$ pN, in agreement with experimental force values in $\alpha_V\beta_3$ integrins (Elosegui-Artola *et al.*, 2016, Wang and Ha, 2013).

In the plot in colour we show the time evolution of the folded/unfolded state of each domain of the talin rod, averaging over the bound binders. At the beginning, all talin domains are folded (red), and during time most of them unfold (blue). For both integrins, domain R3 is the first in unfolding, while R2 and R12 are the least likely to unfold. The $\alpha_V\beta_3$-based FA presents a larger amount of unfolding events, specifically in domains R3, R5, R6, R10 and R11. Indeed, the average force over bound binders F_c is higher for $\alpha_V\beta_3$ integrins, giving more deformation in the binders and therefore allowing more unfoldings of talin domains.

To conclude the analysis, we show the variables against the Young's modulus of the substrate for $\alpha_5\beta_1$ integrins (Figure 4.6) and $\alpha_V\beta_3$ integrins (Figure 4.7). Thanks to the introduction of an accurate modelling of talin mechanics, now talin displacement reaches a maximum $x_{talin} \approx 450$ nm, coherent with the previous experimental result ≈ 770 nm (Yao *et al.*, 2016).

The substrate displacement is maximum for softer substrates, and it reaches $x_{sub} \approx 100$ nm, coherent with the maximum displacement of fibronectin ≈ 120 nm (Erickson *et al.*, 1981, Guthold *et al.*, 2007). However the ECM contains more proteins involved in cell adhesion, therefore a higher displacement resulting from the model would still reflect biological behaviours.

From the talin domains plot, we observe that domains are more likely to be unfolded for stiffer substrates, with domain R3 the most unfolded on average. Therefore, for stiffer substrates, the VBS in R3 is revealed, and the number of vinculins bound increases. As integrins are recruited every time that a new vinculin binds talin, the integrin density d_{int} also increases, resulting in a higher integrin binding rate, and a

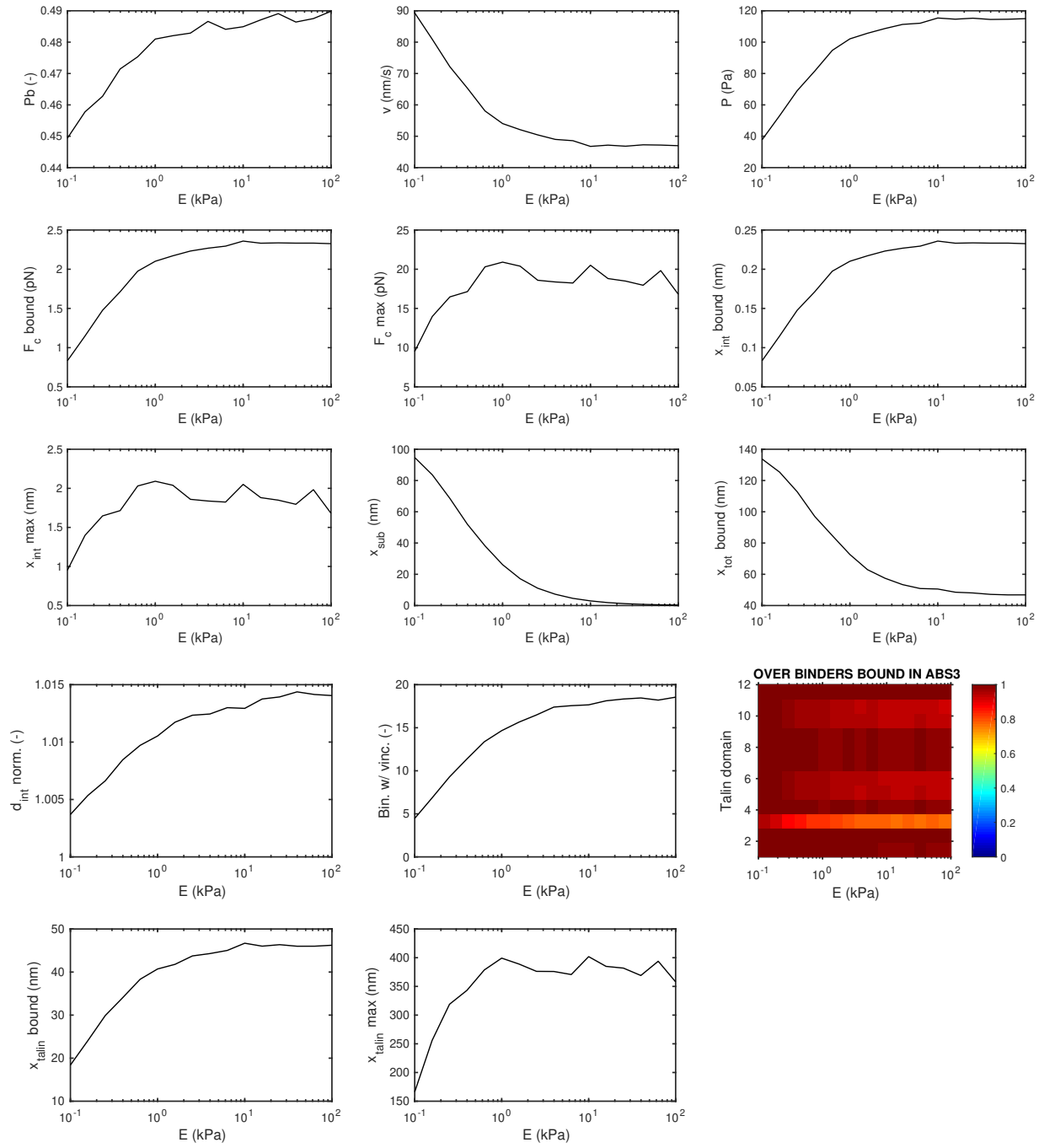

Figure 4.6: Plot of the main variables against Young's modulus of the substrate E for a FA with $\alpha_5\beta_1$ integrins, averaging 10 Gillespie simulations. The plot showing the folded/unfolded state of talin domains is obtained for one Gillespie simulation, averaging over the bound binders. The parameters are taken from Table 4.2 and Table 4.1.

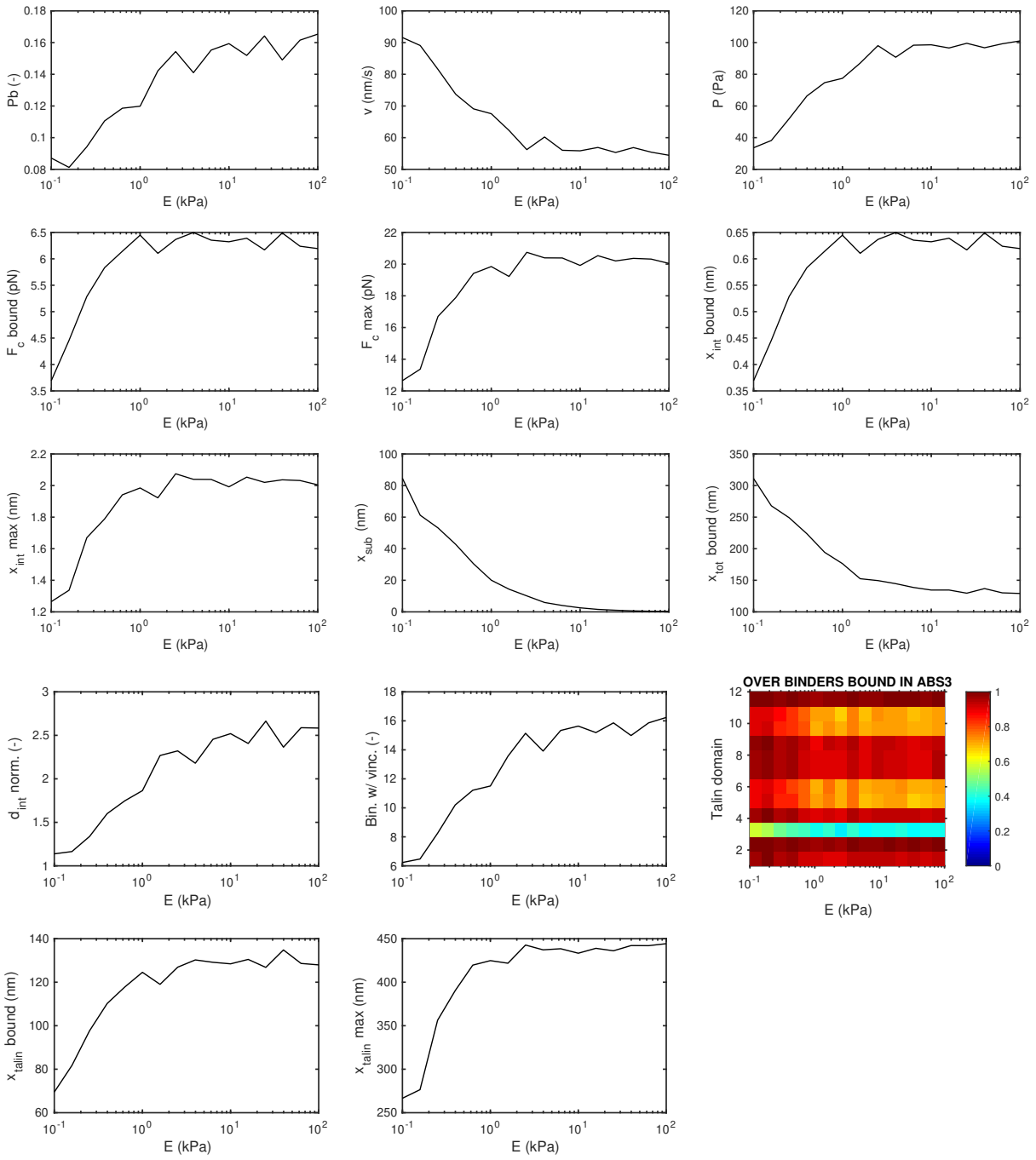

Figure 4.7: Plot of the main variables against Young's modulus of the substrate E for a FA with $\alpha_V\beta_3$ integrins, averaging 10 Gillespie simulations. The parameters are taken from Table 4.2 and Table 4.1.

bound probability which increases for stiffer substrates (Figures 4.6, 4.7).
For both integrins, the percentage of bound binders increases for stiffer substrates, reaching as maximum values 49% for $\alpha_5\beta_1$ and 16% for $\alpha_V\beta_3$. Similarly, the cell traction increases as the ECM stiffness increases, reaching a higher maximum for the $\alpha_5\beta_1$-based integrins. The interesting fact is that the two types of integrin can reach very similar cell tractions, with two very different patch situations. The $\alpha_5\beta_1$-based FA has many binders bound, each with an average force of 1 – 3 pN, while the $\alpha_V\beta_3$-based FA has fewer binders bound, but with a higher average force, 3 – 7 pN. Indeed, as mentioned, in the FA of $\alpha_V\beta_3$ the higher forces determine the higher number of talin unfoldings, reaching as many bound vinculins as in the FA of $\alpha_5\beta_1$.

4.2.2 Role of ECM rigidity in adhesion dynamics for all types of integrins

In this section, we enlarge the view to all types of integrins. Apart from the most common $\alpha_5\beta_1$ and $\alpha_V\beta_3$ already analyzed, other integrins can bind fibronectin, such as $\alpha_4\beta_1$, $\alpha_{IIb}\beta_3$, $\alpha_V\beta_6$ and $\alpha_V\beta_8$. A particular type of cell can present a majority of specific integrins or a combination of many. Also, the maturation state of the adhesion, from nascent to focal to fibrillar adhesion, is related to a majority of specific integrins. Finally, the unbinding rate of an integrin is influenced by its activation state, which depends on the presence of different ions (Kong *et al.*, 2009), and can be influenced by the CMR (Kong *et al.*, 2013). In light of these findings, we carry out a parametric analysis of the multiscale clutch model. Specifically, we focus on the characteristic parameters of each integrin type, i.e. the binding and unbinding rates, as the remaining model parameters are already better established in literature. We analyse the effect of their variation while changing the ECM rigidity.
The values for the parameters k_{ont}, $k_{off,slip}$, $F_{b,slip}$, $k_{off,catch}$ and $F_{b,catch}$ are presented in Table 4.3. Nine values are taken inside each range, with the default in the middle of the range. For $k_{off,slip}$ and $k_{off,catch}$ an exponential distribution is chosen, as their range covers many orders of magnitude, while for the rest of parameters we take a linear distribution.
The range of the binding rate k_{ont} takes into account the experimental values for integrin $\alpha_{IIb}\beta_3$ (Barsegov, 2012). The range of the unbinding rate k^*_{off} takes into account the experimental data for the lifetime of $\alpha_5\beta_1$, $\alpha_V\beta_3$ (Figure 4.3), and $\alpha_L\beta_2$ (Chen *et al.*, 2010). In Figure 4.8 we plot the lifetimes obtained using the values at the extremes of the ranges for $F_{b,slip} = F_{b,catch}$, $k_{off,catch}$ and $k_{off,slip}$, together with the experimental

Parameters	Default	Min	Max
k_{ont} ($\mu m^2/s$)	0.002575	1.5×10^{-4}	0.005
$k_{off,slip}$ (s^{-1})	0.002	2×10^{-5}	0.2
$F_{b,slip}$ (pN)	6	2	10
$k_{off,catch}$ (s^{-1})	5	0.5	50
$F_{b,catch}$ (pN)	6	2	10

Table 4.3: Default values and ranges for the parameters in the binding and unbinding rates of integrins, used in Figures 4.9 and 4.10, for the multiscale clutch model with ABS3 and 1 VBS.

data for $\alpha_5\beta_1$ and $\alpha_V\beta_3$. The rest of parameters are from Table 4.2.

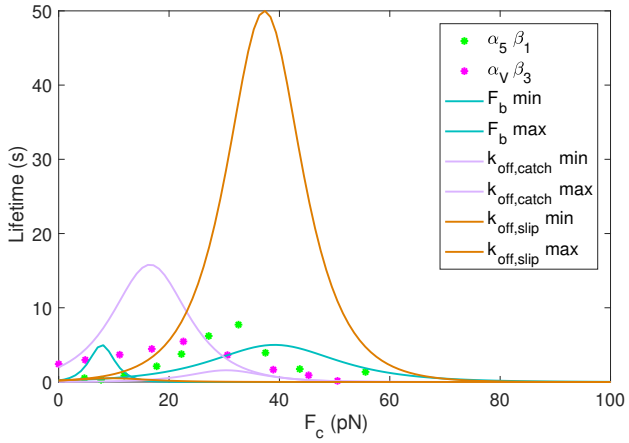

Figure 4.8: Integrin lifetimes obtained with the extremes of the ranges for $F_{b,slip} = F_{b,catch}$, $k_{off,catch}$ and $k_{off,slip}$, as in Table 4.3, together with experimental data for $\alpha_5\beta_1$ (Kong *et al.*, 2009) and $\alpha_V\beta_3$ (Elosegui-Artola *et al.*, 2016).

In Figure 4.9 we present the main model variables against the Young's modulus of the substrate, while varying the parameters k_{ont}, $k_{off,slip}$, $k_{off,catch}$ and $F_{b,slip} = F_{b,catch}$. For all the analyzed parameters, stiffer substrates allow a stronger mechanosensing of talin, with a consequent increase in the amount of bound vinculins. It results in a higher traction force transmitted to the substrate, and a decrease in the retrograde flow. Similarly to the clutch model (Figure A.4), a higher binding rate k_{ont} of integrins results in a higher cell traction, and an increase in the unbinding rates $k_{off,slip}$ or $k_{off,catch}$ results in a lower cell traction. Indeed, a higher binding rate, as well as a lower unbinding rate, produce more bound binders and therefore a higher cell traction, being the aggregation of the forces on the individual binders. We observe that F_b, the

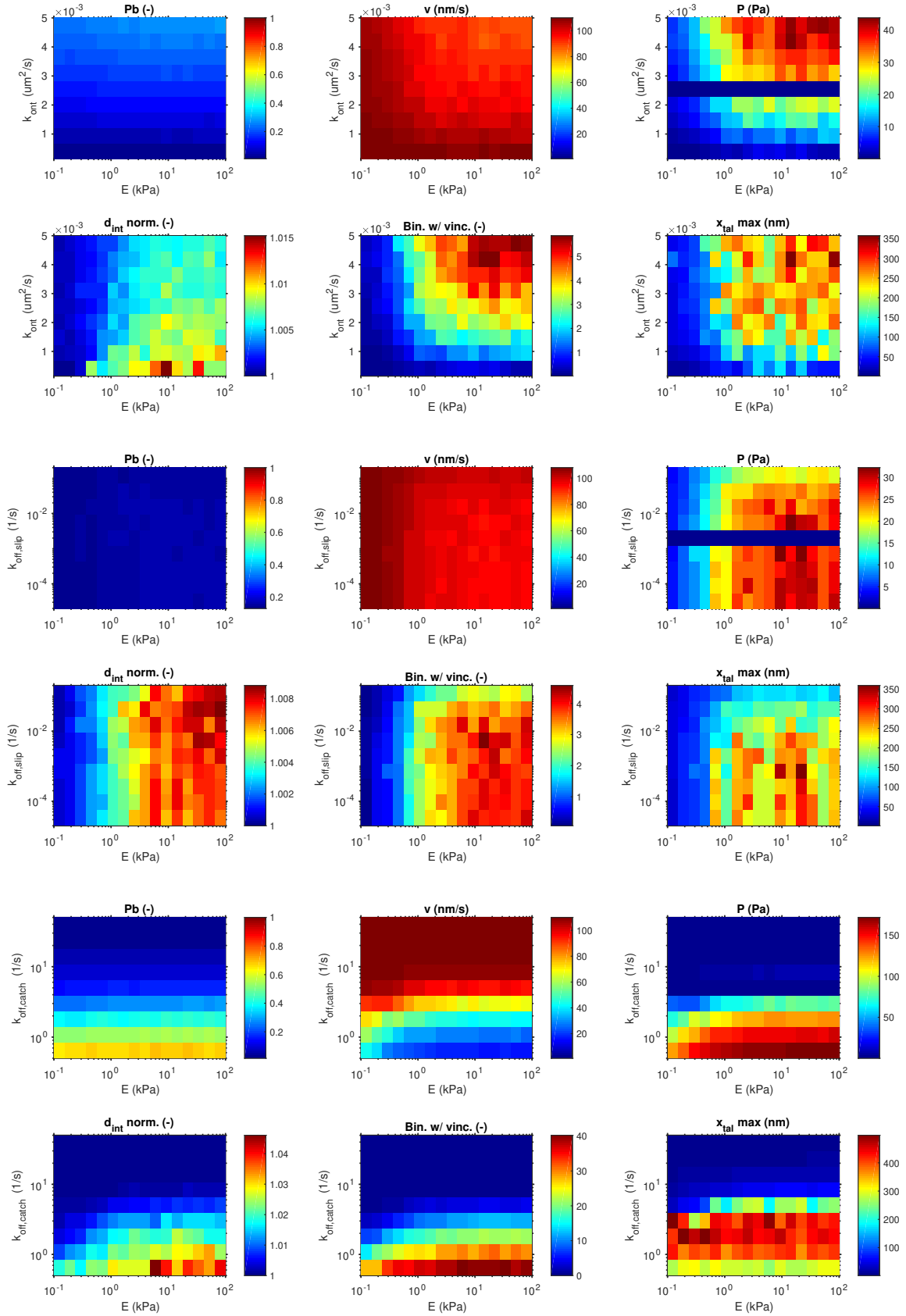
Pb (-)
v (nm/s)
P (Pa)
d_int norm. (-)
Bin. w/ vinc. (-)
x_tal max (nm)
k_ont (um^2/s)
k_off,slip (1/s)
k_off,catch (1/s)
E (kPa)
×10^-3

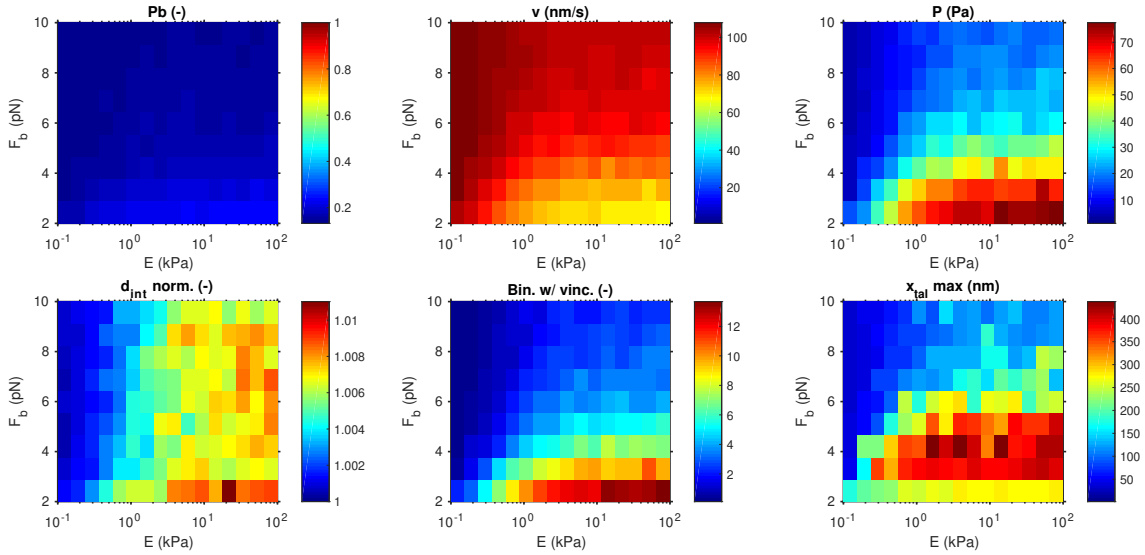

Figure 4.9: Plot of the variables P_b, v, P, $d_{int,norm}$, number of binders with vinculin and x_{tal}^{max} against the Young's modulus of the substrate E, while varying the parameters k_{ont}, $k_{off,slip}$, $k_{off,catch}$ and $F_{b,slip} = F_{b,catch}$ in suitable ranges, as in Table 4.3. We average over 10 Gillespie simulations.

characteristic bond rupture force through both the slip and catch pathways, behaves similarly to $k_{off,catch}$. Indeed, considering negligible the slip pathway because of the order of magnitude of $k_{off,slip}$ compared to $k_{off,catch}$, a variation in the rupture force F_b has the same impact as a variation in $k_{off,catch}$ (Eq. 2.4). A large increase in $k_{off,catch}$ causes few clutches to be bound, resulting in a free-flowing system, as the motors quickly break the bonds.

In Figure 4.10, for $E = 10$ kPa, we perform a parametric analysis by varying simultaneously two of the aforementioned parameters. We do not include the analysis of $k_{off,slip}$, as it does not influence significantly the results (see Figure 4.9). Thanks to the joint variation, we observe that the combination of the highest k_{ont} and the smallest $k_{off,catch}$ gives the highest number of bound vinculins and the highest cell traction, recalling the aforementioned explanation. A similar result can be found for the combination of the highest k_{ont} and the smallest rupture force F_b, recalling the justification of the previous figure.

For some combinations of the parameters, we notice that there is no correspondence between the integrin density and the number of vinculins bound. Using this implementation for integrins recruitment, there is probably a more direct correspondence between the two variables only if the FA becomes completely free before the final time.

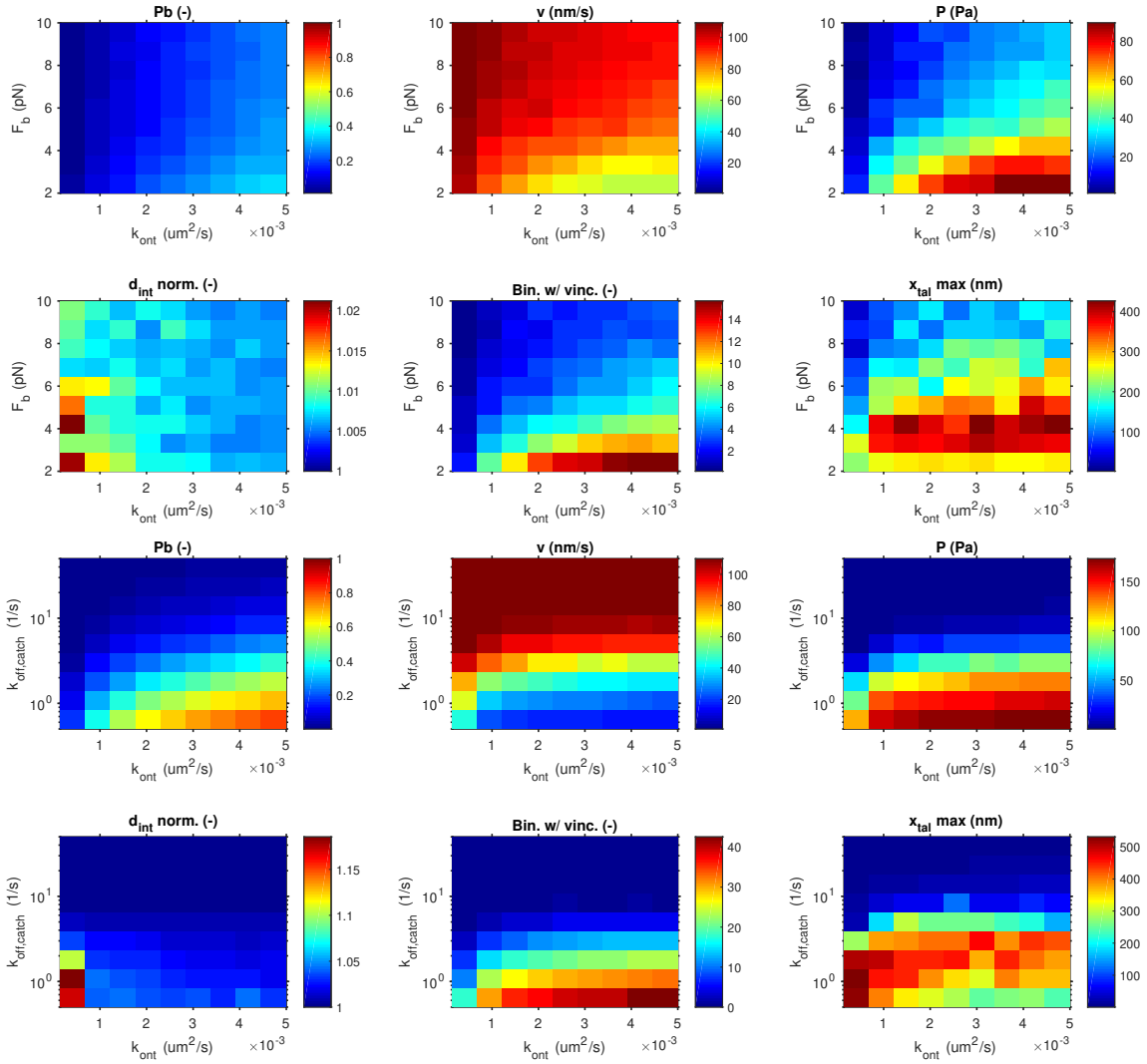

Figure 4.10: Fixing the Young's modulus of the substrate $E = 10\,\text{kPa}$, plot of the main variables varying simultaneously the parameters k_{ont} and $F_{b,slip} = F_{b,catch}$ first, and the parameters k_{ont} and $k_{off,catch}$ later. The ranges for the parameters are in Table 4.3. We average over 10 Gillespie simulations.

However, in order to get always a bijective correspondence between the two variables, later on in the thesis we will correct the implementation of integrins recruitment. Overall, these results of the multiscale clutch model are in agreement with the clutch model (Figure A.4), with the added value that talin displacement reproduces experimental data.

4.2.3 Influence of ligand spacing

FA dynamics depends not only on the rigidity of the ECM, but also on the spacing of the ligands in the ECM (Arnold *et al.*, 2004, Cavalcanti-Adam *et al.*, 2007, 2006, Oria *et al.*, 2017). To analyze this, we focus on $\alpha_5\beta_1$ integrins and we vary the spacing between the fibronectin molecules. We choose three values for the distance between

d (nm)	50	100	200
a (nm)	170-650	160-770	180-1000
$n_c = n_m$	50-736	11-233	5-108

Table 4.4: Parameters for the variation of ligand spacing in $\alpha_5\beta_1$ integrins, used in Figure 4.12 for the multiscale clutch model with ABS3 and 1 VBS.

the equispaced ligands, precisely $d = 50, 100, 200$ nm, and we analyze the evolution of FA dynamics for a Young's modulus of the substrate in 0.1 – 100 kPa. We use experimental data of the adhesion length while varying the substrate stiffness, for each of the three distances (Figure 4.11, dots) (Oria *et al.*, 2017). The adhesion length is the

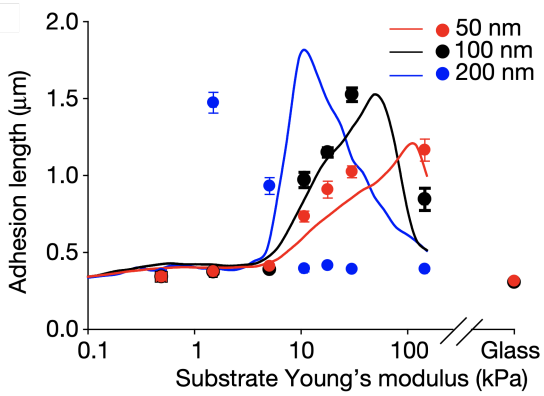

Figure 4.11: Experimental data (dots) of focal adhesion length for integrins $\alpha_5\beta_1$ while varying the substrate rigidity, for three fixed distances among the ligands (Oria *et al.*, 2017).

major axis of the elliptical FA. We approximate the FA to a circle, and we compute the radius a and the number of ligands n_c. The number of myosin motors n_m is kept equal to the number of ligands. We summarize in Table 4.4 the values for the parameters used in the results, referring to Table 4.2 for the fixed ones.
In Figure 4.12 we present the model variables against the Young's modulus of the substrate. We observe an overall similar behaviour for the three distances, except for the variables computing the maximum value or those depending on the number of

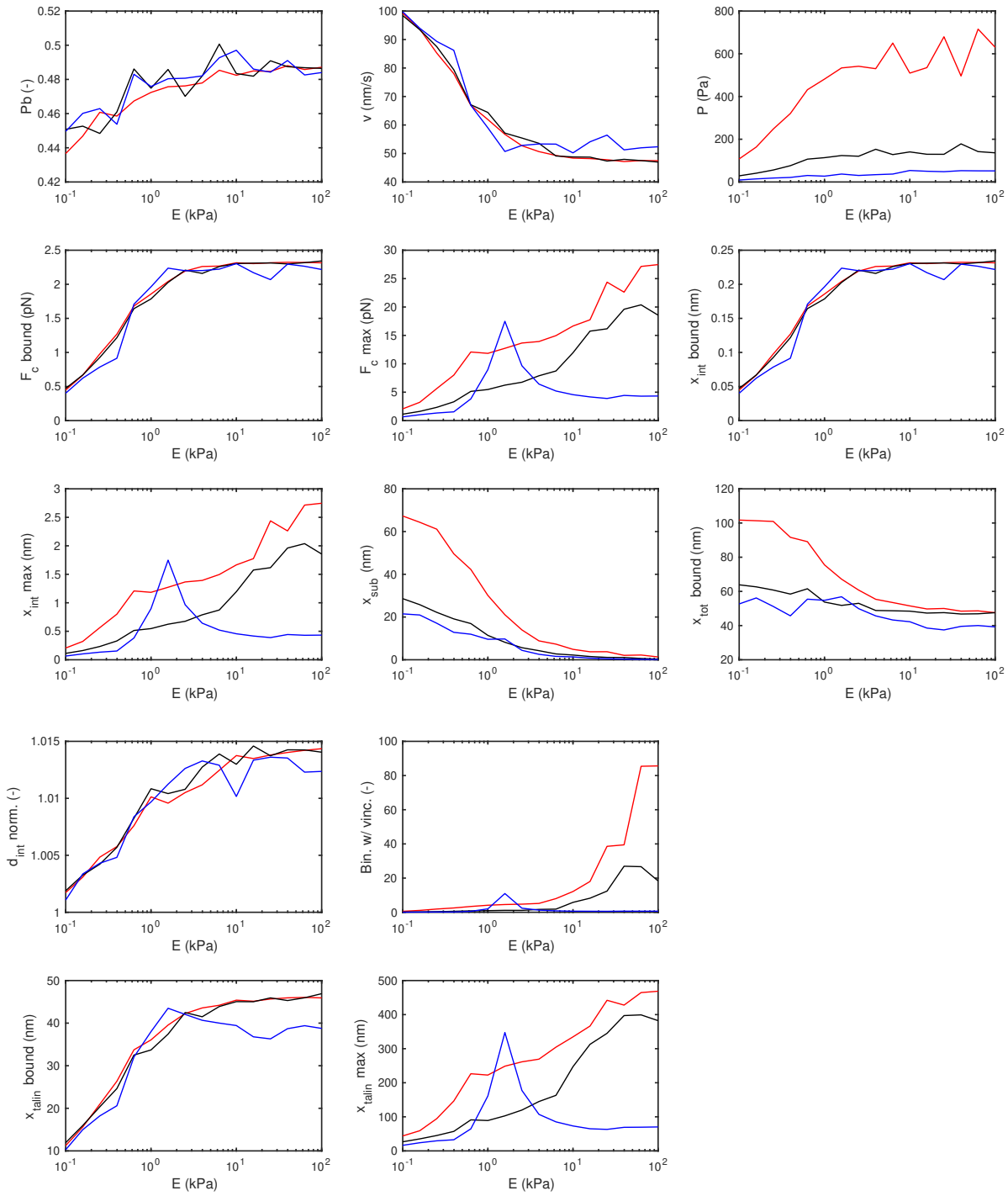

Figure 4.12: Variation of ligand spacing for $\alpha_5\beta_1$ integrins, averaging over 10 Gillespie simulations, for distances $d = 50$ nm (red), $d = 100$ nm (black) and $d = 200$ nm (blue). The parameters are taken from Table 4.4.

ligands n_c. F_c^{max}, x_{int}^{max} and x_{tal}^{max} take values in the same range for the three distances, but have different trends. These trends reproduce the different evolution of the focal adhesion length for the three distances (Figure 4.11, dots). Indeed, looking for example at the maximum force over binders F_c^{max} for a fixed distance, a bigger FA is crowded with more binders bound, resulting in a higher maximum force, while a smaller FA is crowded with fewer binders bound, resulting in a lower maximum force transmitted. The variables depending on the number of ligands n_c are the substrate displacement x_{sub}, and consequently the total displacement x_{tot}, the number of bound vinculins and the cell traction P. The highest substrate displacement, the highest number of bound vinculins and the highest cell traction are reached for $d = 50$ nm, the case with the highest number of ligands n_c (Table 4.4). Indeed, more ligands produce a higher deformation of the substrate and also allow the binding of more vinculin molecules. The cell traction, computed as the sum of the forces in the bound binders divided by the area of the FA (Eq. 2.12), gives very different results for the three distances, as the number of ligands in the three cases is very different. Moreover, the evolution of the cell traction does not resemble that of the FA size. Therefore, our results suggest that cell traction depends more on ligand density than FA size.

Contrarily, experiments with Human breast myoepithelial cells (HBMCs) show similar cell tractions for ligand distances $d = 50$ nm and $d = 100$ nm (Oria *et al.*, 2017). The multiscale clutch model refers to a single FA, while the experiments refer to the entire cell. As an adhesion model of the entire cell would probably lose information at the FA scale, we would need an instrument to relate the FA and the cell length scales, for example by knowing the exact conditions in which experimental data are measured. In order to do a comparison, we propose that the computational results should be multiplied by a curve accounting for the FA density in the cell section in which the traction is measured. For example, a FA density higher for $d = 100$ nm than for $d = 50$ nm would give overlapping curves for the cell traction.

Nevertheless, our results for the actin velocity are very similar when changing the distance among the ligands, and this is coherent with experimental results (Oria *et al.*, 2017). Therefore, probably the experimental technique for measuring the velocity is not involving relevant differences between the two ligand spacing cases.

4.3 Modelling vinculin and actin binding sites on talin

After obtaining these preliminary results, we improve further the model, adding important features. We include the talin R13 domain, we implement more vinculin and actin binding sites on talin, we modify the implementation of integrins recruitment and we adopt a vectorial actin velocity.
For the lack of data about the talin R13 domain, we choose parameters in the same order as the ones experimentally found for the other domains, excluding R3 which has the highest unfolding rate. The parameters for R13 are summarized in Table 4.5.
Talin rod has 11 cryptic vinculin binding sites (VBSs), localized in domains R1, R2

	R13
Domain size L (nm)	63.36
$k_{u,0}$ (s^{-1})	2.0003×10^{-5}
Δx_u (nm)	3.96
$k_{f,0}$ (s^{-1})	0.958
Δx_f (nm)	14.98

Table 4.5: Parameters for R13 talin domain.

(double), R3 (double), R6, R7, R8, R10, R11 and R13 (Gingras *et al.*, 2005). VBSs allow vinculin to bind talin, and consequently to increase integrins density and the binding rate, thus reinforcing the FA. So far, only the VBS in R3 was implemented. Now we implement a total of 7 VBSs, avoiding the double sites of R2 and R3, as their presence would have a similar effect, and the site in R8, as it unfolds cooperatively with R7. We do not implement the VBS in R13. When a talin domain unfolds, vinculin binds with binding rate k_{onv}, considered constant for all VBSs. While vinculin is bound, the domain can not refold, therefore we consider that vinculin unbinds only when the binder becomes free.
We also correct the evolution of the integrin density. Every time that a vinculin binds talin, we increase the integrin density by a quantity int_{add}, and every time that a binder with vinculins becomes free, we decrease the integrin density by the same quantity int_{add} for each of the vinculins bound to that talin. This gives always a one-to-one correspondence between the number of vinculins bound and the actual integrin density.
Talin also presents three important actin binding sites (ABSs). ABS3 covers R13 and the dimerization domain (DD) (Gingras *et al.*, 2008). It was the only actin binding site

included in the model so far. ABS1 is located in the FERM domain in F2-F3, and is usually considered not active as it overlaps with the integrin binding site (Hu *et al.*, 2016). ABS2 is located in the section R4-R8, being the exact position not well identified but most likely in R4 or R8 (Atherton *et al.*, 2015, Kumar *et al.*, 2016). ABS2 has been recently found to be important in force transmission, allowing two actin filaments to be bound to the same talin molecule. It is considered to be activated by the binding of vinculin to the R3 talin domain (Atherton *et al.*, 2015).
Therefore we introduce the presence of ABS2 in our multiscale clutch model. $F_{c,13}$ is the force applied in R13 because of ABS3. We call $F_{c,ABS2}$ the force applied at ABS2, due only to the actin filament bound in ABS2. Then, the total force applied at ABS2, located between R4 and R5, becomes $F_{c,4} = F_{c,13} + F_{c,ABS2}$. The cell traction P is computed considering the sum of all the forces on bound binders, both binders bound only in ABS3 and binders bound in ABS2 and ABS3:

$$P = \frac{\sum_{i=1}^{n_c} F_{c,4(i)}}{\pi a^2}. \tag{4.21}$$

So far the actin velocity was considered as a scalar variable, thus elongating all bound binders with the same magnitude. Here we implement a vectorial velocity, i.e. taking a different value in each binder. Each binder is deformed differently, depending on the force applied in that particular location, giving a more realistic response. This occurs at two different positions in every binder, each one corresponding to an ABS on talin. The vectors for the actin velocity in R13, $\boldsymbol{v}_{13}$, and in R4, $\boldsymbol{v}_4$, follow:

$$\boldsymbol{v}_{13} = v_u\left(1 - \frac{\boldsymbol{F}_{c,13}}{F_{stall}}\right) \tag{4.22}$$

$$\boldsymbol{v}_4 = v_u\left(1 - \frac{\boldsymbol{F}_{c,4}}{2\,F_{stall}}\right), \tag{4.23}$$

where $\boldsymbol{F}_{c,13}$ and $\boldsymbol{F}_{c,4}$ are the vectors of the forces $F_{c,13}$ and $F_{c,4}$ respectively, in all the binders.
So far the number of myosin motors was kept equal to the number of total clutches, $n_m = n_c$. With a scalar velocity, the total number of motors n_m was exerting the same contraction on a single binder bound in the whole adhesion cluster, or on a completely bound FA. With the vectorial velocity, we consider n_m myosin motors for each actin filament, so that only the motors connected to a specific binder exert contraction on it. The binders bound only in ABS3 are elongated with velocity $\boldsymbol{v}_{13}$. At each timestep,

each binder has a total displacement:

$$x_{tot} = x_{tot} + v_{13}\Delta t. \tag{4.24}$$

The binders bound in ABS2 and ABS3 have a total displacement:

$$x_{tot} = x_{tot}^{sub-4} + x_{tot}^{5-13}, \tag{4.25}$$

where x_{tot}^{sub-4} is the displacement of the chain made of substrate, integrin, talin head, talin neck and domains R1 to R4 of the talin rod, and x_{tot}^{5-13} is the displacement of the domains R5 to R13. These binders bound in ABS2 and ABS3 are elongated with two different velocities: at each timestep, for each binder we have

$$x_{tot}^{sub-4} = x_{tot}^{sub-4} + v_4\Delta t \tag{4.26}$$

$$x_{tot}^{5-13} = x_{tot}^{5-13} + (v_{13} - v_4)\Delta t. \tag{4.27}$$

In order to find values for the number of myosin motors n_m attached to an actin fibre and the stall force for a single myosin motor F_m, we look for an experimental value of the total stall force $F_{stall} = n_m\ F_m$. The ensemble stall force can be written as (Stam *et al.*, 2015):

$$F_{stall} = F_{sm}\, N_{heads}\, \rho(F_{sm}), \tag{4.28}$$

where $F_{sm} = K_{x-bridge} d_{step}$ is the stall force for a single motor, N_{heads} is the number of myosin motors and $\rho(F_{sm})$ is the duty ratio of a single motor at stall, which can be computed as:

$$\rho(F_{sm}) = \frac{k_{on}}{k_{on} + k_{off}(F_{sm})}. \tag{4.29}$$

The expression for the myosin off-rate is (Guo and Guilford, 2006):

$$k_{off}(F) = k_{off}(0)\left[\alpha_{catch}\exp\left(\frac{-Fx_{catch}}{k_B T}\right) + \alpha_{slip}\exp\left(\frac{Fx_{slip}}{k_B T}\right)\right]. \tag{4.30}$$

Myosins are a superfamily of motor proteins. Myosin II is responsible for producing muscle contraction in muscle cells in most animals, but it is also found in non-muscle cells inside stress fibres. Hence, it can be further classified into skeletal muscle myosin II, smooth muscle myosin II, and nonmuscle myosin II (NM II) (Stam *et al.*, 2015). More precisely, the myosins having a role in cell adhesion are NM IIA and NM IIB. NM

IIA mediates the initial maturation of FAs, and NM IIB is found in fibrillar adhesions. Adhesions with NM IIA are dynamic, while those with NM IIB are very stable (Vicente-Manzanares and Horwitz, 2011). In the leading edge of the cell, both types are present, while NM IIA characterizes the rear edge and NM IIB is found in the actin close to the nucleus of the cell (Vicente-Manzanares *et al.*, 2009b). It has been demonstrated that 90% of the traction force generated by mouse embryonic fibroblasts (MEFs) on a fibronectin-coated substrate is lost with the removal of NM IIs, and that NM IIA is responsible for ~ 60% of the force, whereas NM IIB accounts for the ~ 30% (Cai *et al.*, 2006, Shutova and Svitkina, 2018). In Sections 4.4.1, 4.4.2 and 4.4.3, we consider MEFs, whose FAs have a percentage of NM IIA and a percentage of NM IIB.

Using Eqs. 4.28, 4.29 and 4.30, with parameters in Table 4.6, we compute the ensemble

Parameters		
$K_{x-bridge}$(pN/nm)	0.7	(Veigel *et al.*, 2003)
d_{step} (nm)	5.5	(Veigel *et al.*, 2003)
N_{heads}	50	(Niederman and Pollard, 1975)
k_{on} (s^{-1})	0.2	(Kovacs *et al.*, 2003), (Wang *et al.*, 2003)
$k_{off}(0)$ NM IIA (s^{-1})	1.71	(Kovacs *et al.*, 2003)
$k_{off}(0)$ NM IIB (s^{-1})	0.35	(Wang *et al.*, 2003)
α_{catch}	0.92	(Guo and Guilford, 2006)
α_{slip}	0.08	(Guo and Guilford, 2006)
x_{catch} (nm)	2.5	(Guo and Guilford, 2006)
x_{slip} (nm)	0.4	(Guo and Guilford, 2006)

Table 4.6: Parameters for myosin motors used inside Eqs. 4.28, 4.29 and 4.30, with experimental references.

stall force F_{stall} for NM IIA and NM IIB. Considering that in our setting there is a percentage of myosin motors of each type, we choose a total stall force in the range $[F_{stall}^{NMIIA}, F_{stall}^{NMIIB}] = [73.34, 143.03]$ pN, and precisely $F_{stall} = 80$ pN. The stall force for a single myosin motor is found to be at least $F_m = 1.7$ pN (Molloy *et al.*, 1995), therefore, following $F_{stall} = n_m\, F_m$, we consider $n_m = 40$ myosin motors, each with a stall force $F_m = 2$ pN.

4.4 Results

In this section, we present the computational results of the multiscale clutch model, considering seven VBSs and two ABSs: ABS3 located in the section R13-DD of talin,

and ABS2 located between the domains R4 and R5, which can be activated when a vinculin binds to the domain R3.
To clearly see the goals reached with our model, in Section 4.4.1 we first show the results for a unique adhesion binder kept always bound. In Sections 4.4.2, 4.4.3 and 4.4.5, we enlarge the view to an entire FA, and analyze cases of depleted talin domains. We give some details on the simulation speed of the complete multiscale clutch model (Section 4.3), as it is more computationally expensive than its simpler version (Section 4.1). More precisely, the case of talin full-length (FL) is more expensive than the talin domains depletion case. For the talin FL case, run for 4 Gillespie simulations until final time $t_f = 30$ s and with parameters in Table 4.8, we notice that the simulation speed highly depends on the Young's modulus of the substrate E. For the softest substrate $E = 0.1$ kPa the simulations ends in a few minutes, while for the stiffest substrate $E = 39.81$ kPa the simulation lasts up to 10 days. The code is run in parallel with 16 cores and with a 4 GB RAM. The simulation time highly depends on the parameters, as for example it increases with a higher number of binders n_c or a higher binding rate k_{on}.

4.4.1 Analysis of one adhesion chain

We start by analyzing one adhesion chain made of substrate, integrin, talin, and an actin filament connected to a number of myosin motors (Figure 4.13). Talin is

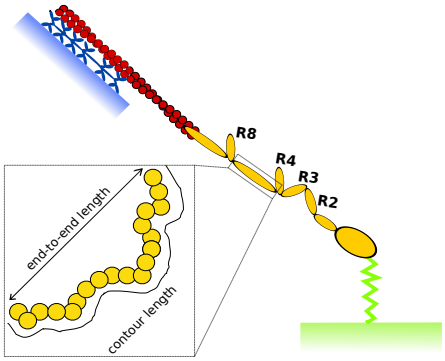

Figure 4.13: Adhesion chain, from bottom to top made of substrate (green), a linear spring accounting for integrin (green), which is bound to talin with its 13 domains (yellow), whose tail is attached to an actin fibre (red), finally connected to a number of myosin motors (blue), anchored to a fixed surface.

considered in its full-length, with head, neck and 13 rod domains.

The model parameters are summarized in Table 4.7. The parameter a has been used

Parameters	
E (kPa)	0.1 - 100
a (nm)	20
n_c	1
κ_c (pN/nm)	0.8
k_{ont} ($\mu m^2/s$)	1×10^4
d^0_{int} (int /μm^2)	300
k_{off} (s^{-1})	0
F_m (pN)	2
n_m	20
v_u (nm/s)	110
k_{onv} (s^{-1})	0.2
int_{add} (int /μm^2)	24
m_r (int /μm^2)	15000

Table 4.7: For one adhesion chain kept bound, parameters of the multiscale clutch model used in Figures 4.14 and 4.16.

until now as the radius of the FA. Here, we consider an area of influence of the unique binder, with radius $a = 20$ nm (Oria *et al.*, 2017). The stiffness of the linear spring modelling the integrin is $\kappa_c = 0.8$ pN/nm (Figure 2.13) (Kong *et al.*, 2013, 2009). We remind that for a binder inside a FA we consider $n_m = 40$ myosin motors exerting contraction on it. Nevertheless, myosin motors are always linking two actin filaments together. In this ideal case of a unique binder, there is only one actin filament bound to R13, not linked to other actin filaments, therefore we consider half of the myosin motors previously calculated, $n_m = 20$. For all VBSs we choose the vinculin binding rate $k_{onv} = 0.2\,s^{-1}$ (Hu *et al.*, 2016, Tapia-Rojo *et al.*, 2020). For the parameters E, d^0_{int}, v_u, int_{add} and m_r we take the same values of Section 4.2.1.

In Figure 4.14 we show the time evolution of the main variables, for one adhesion binder kept always bound, fixing the Young's modulus of the substrate $E = 0.1$ kPa. We choose the final time $t_f = 30$ s, as it allows the unfolding of most talin domains. In the graphs, we see the effect of each unfolding on the model variables.

In the plot of talin domains, we show the time evolution of their folded/unfolded state. At the beginning, all talin domains are folded, and during time most of them unfold. Domain R3 is the only one that refolds many times, to finally remain unfolded, and R7 and R8 unfold cooperatively. We show this result for one Gillespie simulation, to see clearly the exact time of each unfolding.

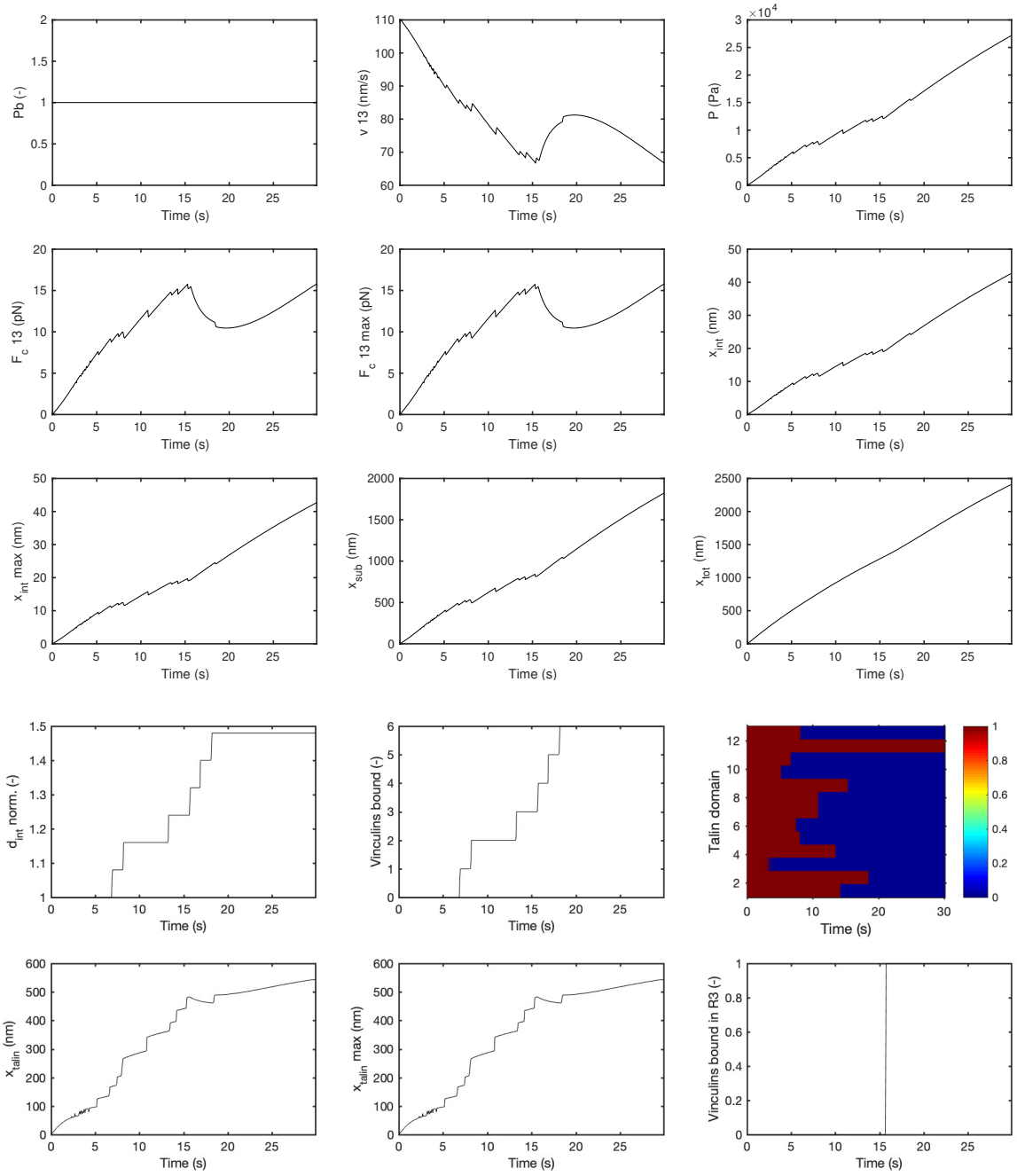
Pb (-)
v 13 (nm/s)
P (Pa)
×10^4
F_c 13 (pN)
F_c 13 max (pN)
x_int (nm)
x_int max (nm)
x_sub (nm)
x_tot (nm)
d_int norm. (-)
Vinculins bound (-)
Talin domain
x_talin (nm)
x_talin max (nm)
Vinculins bound in R3 (-)
Time (s)

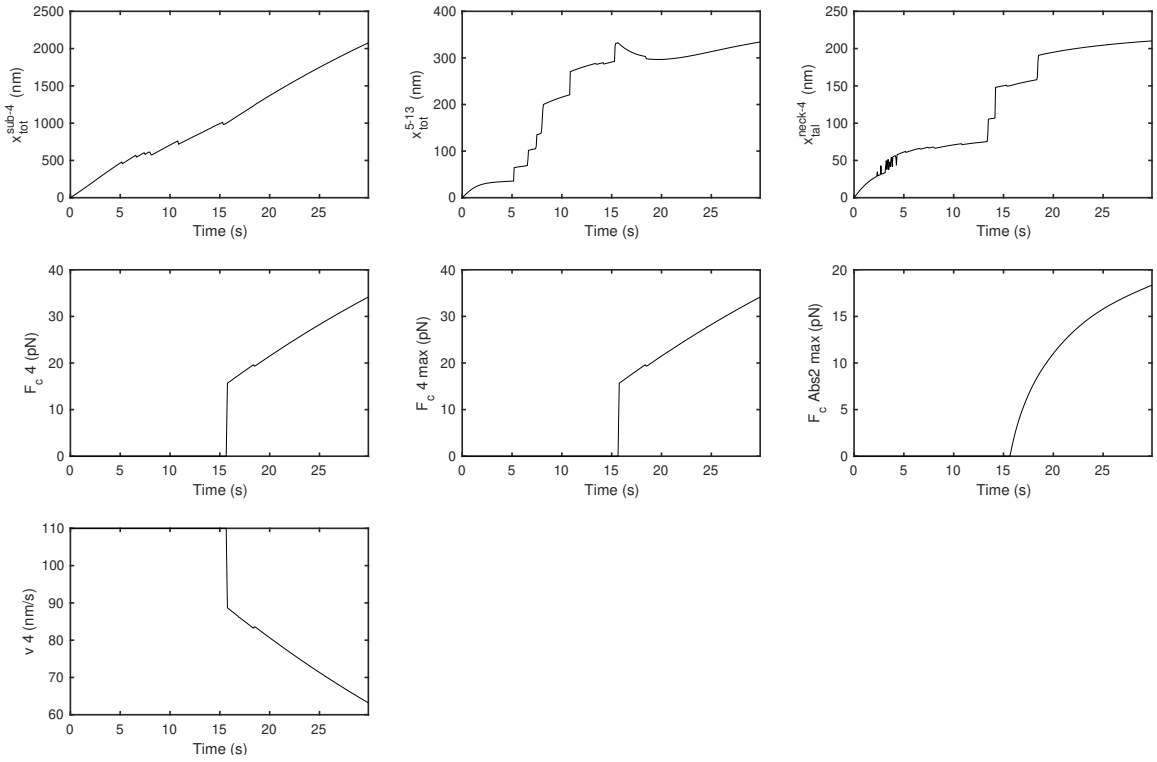

Figure 4.14: For one adhesion chain kept bound, fixing the Young's modulus of the substrate $E = 0.1$ kPa, we run one Gillespie simulation. Time evolution of the variables P_b, v_{13}, P, $F_{c,13}$, x_{int}, x_{sub}, x_{tot}, $d_{int,norm}$, # vinculins bound, x_{talin}, # vinculins bound in R3, x_{tot}^{sub-4}, x_{tot}^{5-13}, x_{tal}^{neck-4}, $F_{c,4}$, $F_{c,ABS2}^{max}$ and v_4. The parameters are taken from Tables 4.7, 4.1 and 4.5.

In the graph of x_{talin}, we notice the displacement jumps corresponding to the unfolding of talin domains. In the graph of x_{tot}^{5-13}, just after time $t = 10$ s, we observe the biggest jump, corresponding to the joint unfolding of R7 and R8. In the graph of x_{tal}^{neck-4}, we recognize in the time interval 0 – 5 s the unfoldings and refoldings of domain R3.
In Figure 4.15, we compare our result of talin displacement with experiments (Yao *et al.*, 2016). The time evolution graph of x_{talin} can be compared to the constant force loading rate experiment, as the forces applied to talin $F_{c,13}$ and $F_{c,4}$ increase almost linearly with time. Besides the similar shape, we notice that the end-to-end length of talin obtained computationally is ≈ 550 nm, and it is coherent with the end-to-end length of ≈ 770 nm in the experimental results. In the model, the ABS2 activation at $t = 15$ s induces a compression in the talin rod with respect to its previously displaced conformation (Figure 4.15, left). Conversely, in the experiments, the talin molecule is kept between two magnetic beads, between the domains R1 and R13, and ABS2 is

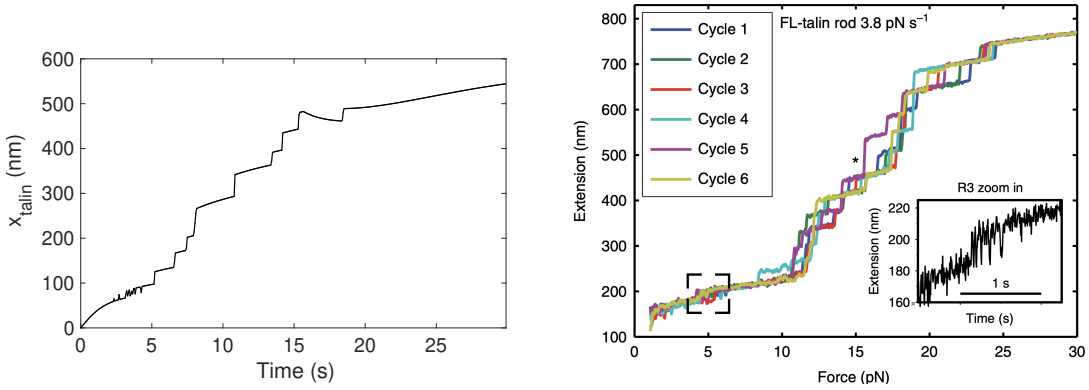

Figure 4.15: Left: Talin displacement x_{talin} during time, as a result of the multiscale clutch model. Right: Force-extension curves of talin unfolding at constant force loading rate, each colour corresponding to a different cycle. Cycles have similar shapes, but they are not identical because of the stochastic nature of unfolding and refolding events (Yao *et al.*, 2016).

not active. Moreover, in our results the unfoldings of R3 happen with a force ≈ 5 pN, matching the experimental data (Yao *et al.*, 2016).
In correspondence to talin unfoldings, the forces $F_{c,13}$ and $F_{c,4}$ decrease (Figure 4.14), so talin acts as a force buffer (Yao *et al.*, 2016), and the same happens to the cell traction P. The actin velocities v_{13} and v_4, being inversely related to forces, increase in correspondence to talin unfoldings. Finally, integrin and substrate displacements decrease in order to compensate talin instantaneous elongation.
Going back to the general behaviour of the adhesion chain, we see that while the binder is kept bound ($P_b = 1$), the forces $F_{c,13}$, $F_{c,4}$, $F_{c,ABS2}$ and the cell traction P increase during time, and the actin velocities v_{13} and v_4 decrease (Figure 4.14), because the actin flow is slowed down when adhesion force is built. The total displacement $x_{tot} = x_{sub} + x_{int} + x_{talin}$ increases linearly with respect to time, as at each timestep the entire chain elongation depends on actin velocity following $x_{tot} = x_{tot} + v_{13}\Delta t$. The displacements of substrate, integrin and talin increase during time, because the binder is kept bound, force is built and each part of the chain elongates in a force-dependent manner. At each talin unfolding, more VBSs become available, and the total number of bound vinculins increases. The density of integrins d_{int} is increased every time that a new vinculin binds talin. In particular, around time $t = 15$ s, a vinculin molecule binds the domain R3, activating ABS2. As a result, a second actin filament binds talin, and the new force $F_{c,ABS2}$ becomes positive. In this location, between R4 and R5, the total force is $F_{c,4} = F_{c,13} + F_{c,ABS2}$. The velocity in ABS2, v_4, starts decreasing. The effect of the activation of ABS2 is that the talin section R5-R13 undergoes a compression

with respect to the previously displaced state, because R5 is elongated with a velocity $v_4 = v_u$, higher than the velocity applied in that moment to R13, $v_{13} \approx 70\,\text{nm/s}$. As a consequence of talin compression, the force $F_{c,13}$ applied in R13 decreases, and the velocity v_{13} in R13 increases.

Now, we show in Figure 4.16 the variables against the Young's modulus of the substrate, obtained averaging 100 Gillespie simulations. In the plot of talin domains, obtained for one Gillespie simulation, we observe that for stiff substrates the domains are more likely to be unfolded, as the final time is fixed for all rigidities. Increasing the stiffness of the substrate, the total displacement starts being shared more by the adhesion proteins integrin and talin than by the substrate, so talin displacement increases faster and the moment of complete talin unfolding happens sooner. The domain R3 is the most likely to unfold and R12 is the least likely to unfold.

As talin unfolding happens sooner in stiffer substrates, the forces $F_{c,13}$ and $F_{c,4}$ reach sooner their maximum value, giving a higher average value in stiffer substrates. As a result, the cell traction P, computed with the total force $F_{c,4}$, increases monotonically while increasing the Young's modulus. Our results for the force $F_{c,13}$ reproduce those obtained through a computational model for the binding and unbinding of the myosin motors to an actin filament bound to an adhesion chain (Stam *et al.*, 2015).

As more force means less capacity for the actin filaments to follow their retrograde flow, the velocities v_{13} and v_4 decrease monotonically while increasing the Young's modulus, as in the improved clutch model (Section 2.3.2). The total displacement x_{tot} decreases while increasing the Young's modulus, as it depends on the velocity v_{13} which is also decreasing (Eq. 4.24).

As in stiff substrates talin is unfolded more often, the number of vinculins bound is higher, and the integrin density d_{int} is also higher, as integrins are recruited every time that a new vinculin binds talin. Consequently, the amount of vinculins bound in R3 is higher in stiffer substrates, with a higher activation of ABS2. However, on average there are 0.7 – 0.8 vinculins bound out of a maximum of 1 vinculin in R3, so in this ideal case of a unique binder always bound, increasing E does not have a large influence on ABS2 activation.

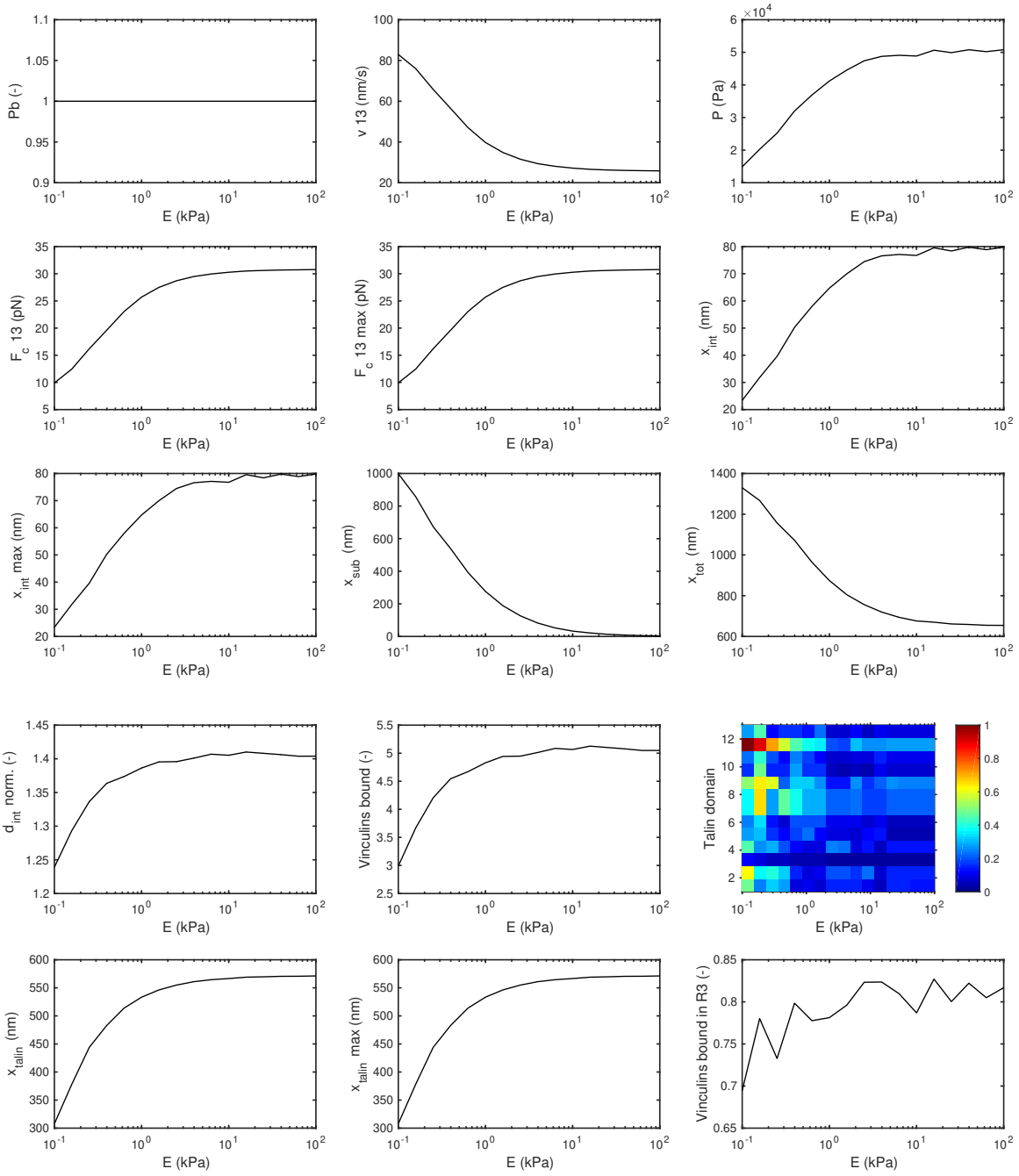
Pb (-)
v 13 (nm/s)
P (Pa)
×10^4
F_c 13 (pN)
F_c 13 max (pN)
x_int (nm)
x_int max (nm)
x_sub (nm)
x_tot (nm)
d_int norm. (-)
Vinculins bound (-)
Talin domain
x_talin (nm)
x_talin max (nm)
Vinculins bound in R3 (-)
E (kPa)

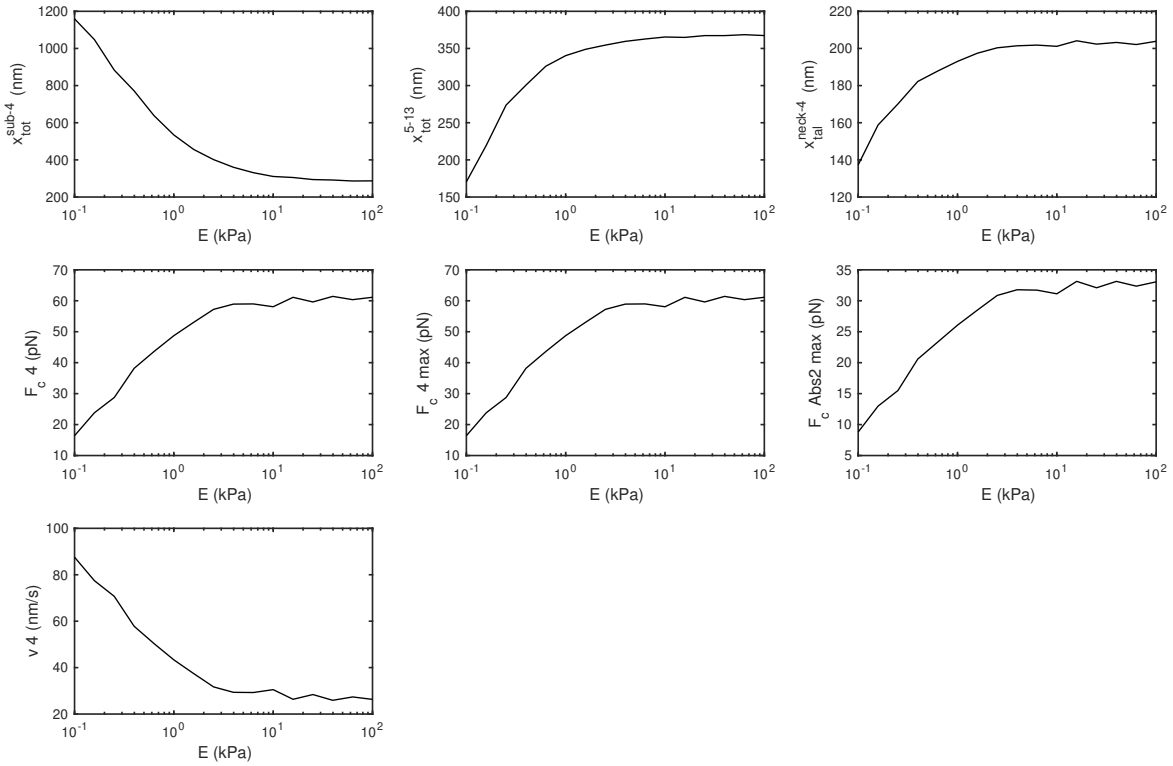

Figure 4.16: For one adhesion chain kept bound, we run 100 Gillespie simulations. Plot against Young's modulus of the substrate E of the variables P_b, v_{13}, P, $F_{c,13}$, x_{int}, x_{sub}, x_{tot}, $d_{int,norm}$, # vinculins bound, x_{talin}, # vinculins bound in R3, x_{tot}^{sub-4}, x_{tot}^{5-13}, x_{tal}^{neck-4}, $F_{c,4}$, $F_{c,ABS2}^{max}$ and v_4. The parameters are taken from Tables 4.7, 4.1 and 4.5.

4.4.2 Focal adhesion with $\alpha_V\beta_3$ integrins

Now, we enlarge the view to an entire FA with a number of equispaced binders. The use of biological parameters will allow us to reproduce experimental results for MEFs, obtained by the group of Pere Roca-Cusachs at IBEC, Barcelona (unpublished work) (see Section 4.4.4). MEFs present talin1, which has high affinity with $\alpha_V\beta_3$ integrins. In the model, we take into account only this type of integrins, but we can not exclude that a small percentage of $\alpha_5\beta_1$ integrins can be present.

The model parameters are reported in Table 4.8. For the Young's modulus of the substrate, we use the experimental range $E = 0.1 - 39.81$ kPa. In the experiments, they do not control for the spacing between fibronectin molecules, but the distance among them results in ≈ 50 nm, therefore we choose a FA with equispaced ligands, fixing this same distance. We take values of the adhesion length obtained experimentally for HBMCs with $\alpha_5\beta_1$ integrins (Figure 4.11, dots, $d = 50$ nm) (Oria *et al.*, 2017) . Although

Parameters	
E (kPa)	0.1 - 39.81
a (nm)	170 - 500
d (nm)	50
n_c	50 - 341
κ_c (pN/nm)	0.8
k_{ont} ($\mu m^2/s$)	7×10^{-5}
d^0_{int} (int /μm^2)	300
$k_{off,slip}$ (s^{-1})	4.173×10^{-4}
$F_{b,slip}$ (pN)	5.4825
$k_{off,catch}$ (s^{-1})	0.4012
$F_{b,catch}$ (pN)	28.67
F_m (pN)	2
n_m	40
v_u (nm/s)	110
k_{onv} (s^{-1})	0.2
int_{add} (int /μm^2)	24
m_r (int /μm^2)	15000

Table 4.8: For a FA of MEFs with $\alpha_V\beta_3$ integrins and talin FL, parameters of the multiscale clutch model used in Figures 4.17, 4.18 and 4.19.

we use a different type of integrin, we consider that the two types follow a similar behaviour while increasing the stiffness of the substrate: the vinculin-driven adhesion reinforcement produces an increase in the size of the FA. As before, we approximate the adhesion length to the diameter of a circular FA. For each Young's modulus of the substrate, we get a fixed number of equispaced ligands n_c in the range 50 – 341, computed given the radius a of the FA and the distance d at which they are kept. Assuming that the binding rate of integrin $\alpha_V\beta_3$ has the same order of magnitude of integrin $\alpha_{IIb}\beta_3$ (Barsegov, 2012), we take $k_{ont} = 7 \times 10^{-5}$ $\mu m^2 s^{-1}$. For the parameters κ_c, d^0_{int}, F_m, v_u, k_{onv}, int_{add} and m_r we refer to Section 4.4.1, and for the unbinding rate parameters $k_{off,slip}$, $F_{b,slip}$, $k_{off,catch}$ and $F_{b,catch}$ for $\alpha_V\beta_3$ integrins, we refer to Section 4.2.1.

First, we show the time evolution of the model variables, fixing $E = 15.84$ kPa, and running one Gillespie simulation (Figure 4.17). The force in R13 reaches a maximum, among all binders, of $F_{c,13} = 50$ pN, and the total force in ABS2 reaches a maximum, over all binders with ABS2 active, of $F_{c,4} = 60$ pN, both in agreement with experimental force ranges in $\alpha_V\beta_3$ integrins (Elosegui-Artola *et al.*, 2016, Wang and Ha, 2013). The integrin displacement reaches as maximum $x_{int} = 80$ nm, in agreement with the

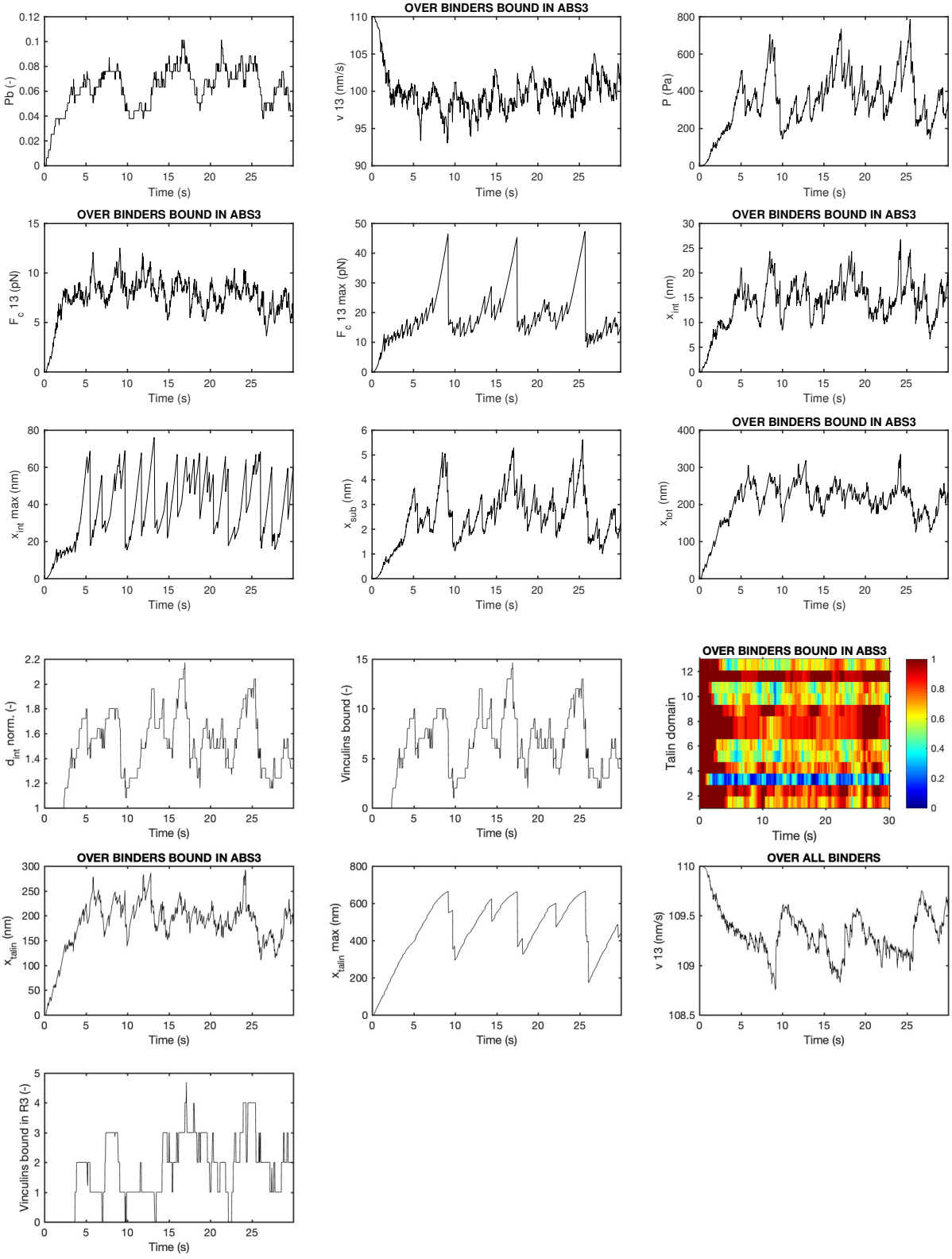
Pb (-)
Time (s)
OVER BINDERS BOUND IN ABS3
v 13 (nm/s)
P (Pa)
F_c 13 (pN)
F_c 13 max (pN)
x_int (nm)
x_int max (nm)
x_sub (nm)
x_tot (nm)
d_int norm. (-)
Vinculins bound (-)
Talin domain
x_talin (nm)
x_talin max (nm)
OVER ALL BINDERS
Vinculins bound in R3 (-)

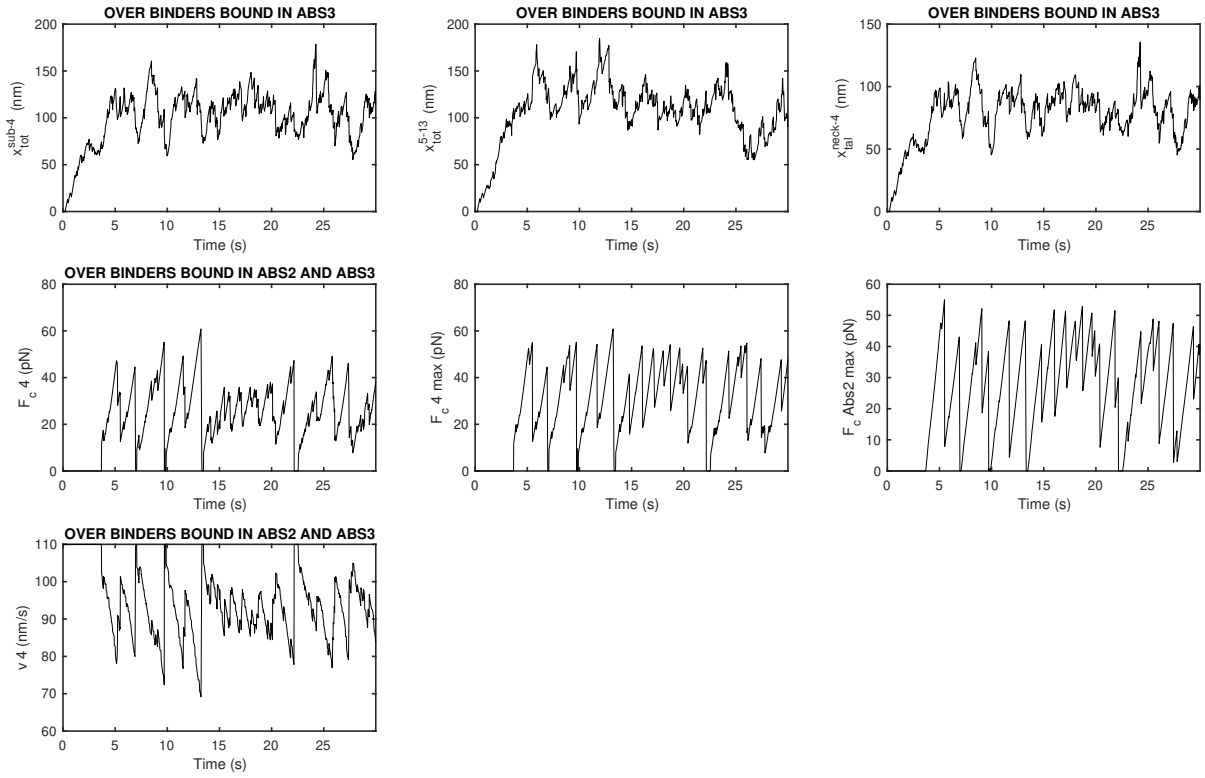

Figure 4.17: For a FA of MEFs with $\alpha_V\beta_3$ integrins and talin FL, fixing the Young's modulus of the substrate $E = 15.84\,\text{kPa}$, we run one Gillespie simulation and plot the time evolution of the main variables. The parameters are taken from Tables 4.8, 4.1 and 4.5.

experimental result $x_{int} \approx 50\,\text{nm}$, for $\alpha_5\beta_1$ integrins (Kong *et al.*, 2013, 2009). Talin displacement reaches a maximum of $x_{talin} \approx 650\,\text{nm}$, coherent with previous experimental result of $\approx 770\,\text{nm}$ (Yao *et al.*, 2016). The amount of vinculins increases when talin domains unfold and activate VBSs, and the density of integrins d_{int} increases according to the number of vinculins. For the first time at $t = 4\,\text{s}$, a vinculin molecule binds the R3 talin domain of one of the bound binders, which activates the ABS2 of that specific binder. Before reaching the final time t_f, at maximum 5 vinculins bind the R3 talin domain, giving 5 active ABS2 in the whole adhesion cluster.
Then, we analyze the variables against the Young's modulus of the substrate, averaging over 4 Gillespie simulations (Figure 4.18). Because of their computational cost, an higher number of simulations can not be run in a reasonable time. The entire FA behaves similarly to the individual adhesion chain kept bound. The total number of vinculins bound to talins increases for stiffer substrates, as talin domains are more likely to be unfolded. For the stiffest substrate, $E = 39.81\,\text{kPa}$, there are on average 20

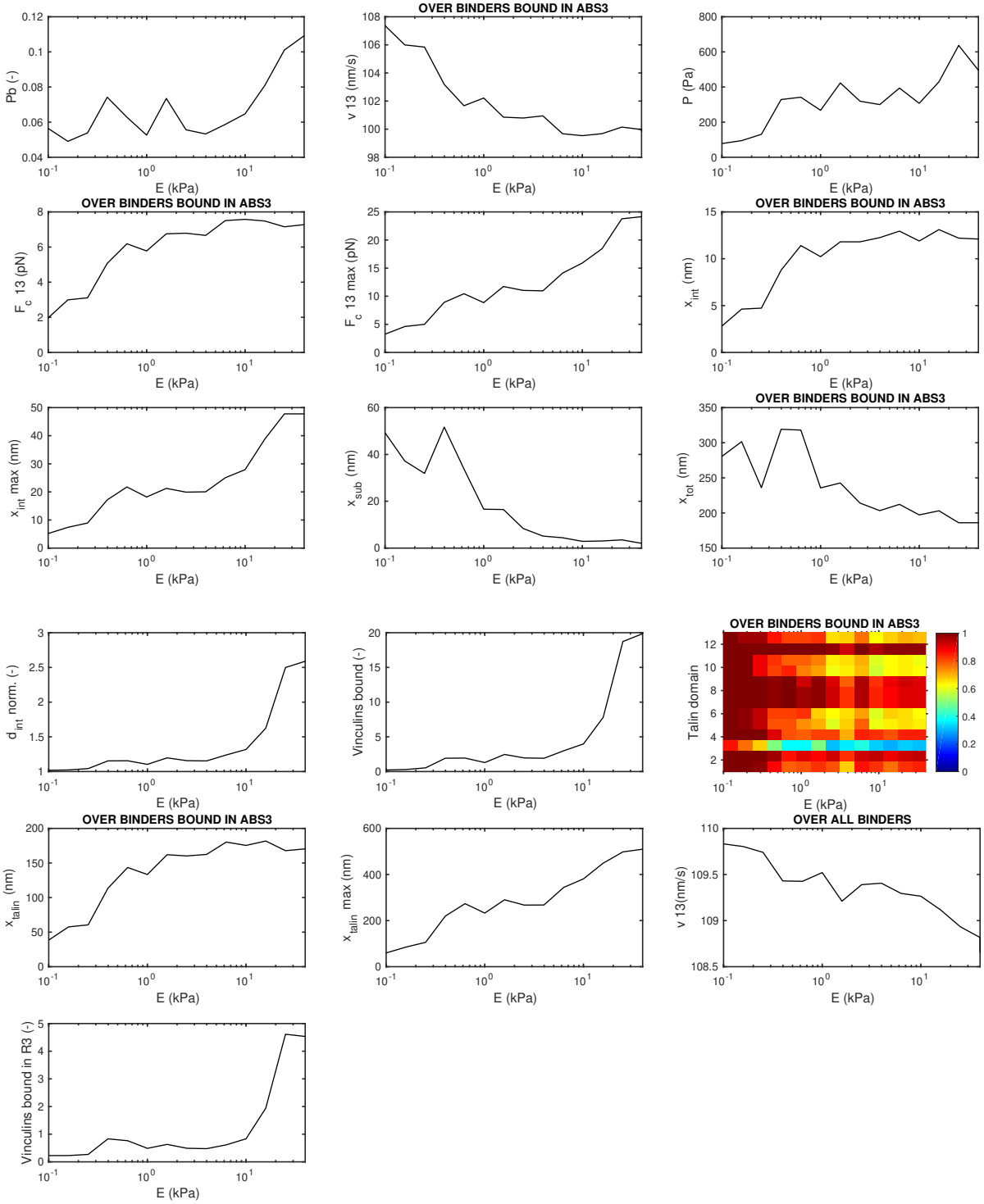
OVER BINDERS BOUND IN ABS3
Pb (-)
v 13 (nm/s)
P (Pa)
F_c 13 (pN)
F_c 13 max (pN)
x_{int} (nm)
x_{int} max (nm)
x_{sub} (nm)
x_{tot} (nm)
d_{int} norm. (-)
Vinculins bound (-)
Talin domain
x_{talin} (nm)
x_{talin} max (nm)
OVER ALL BINDERS
v 13(nm/s)
Vinculins bound in R3 (-)
E (kPa)

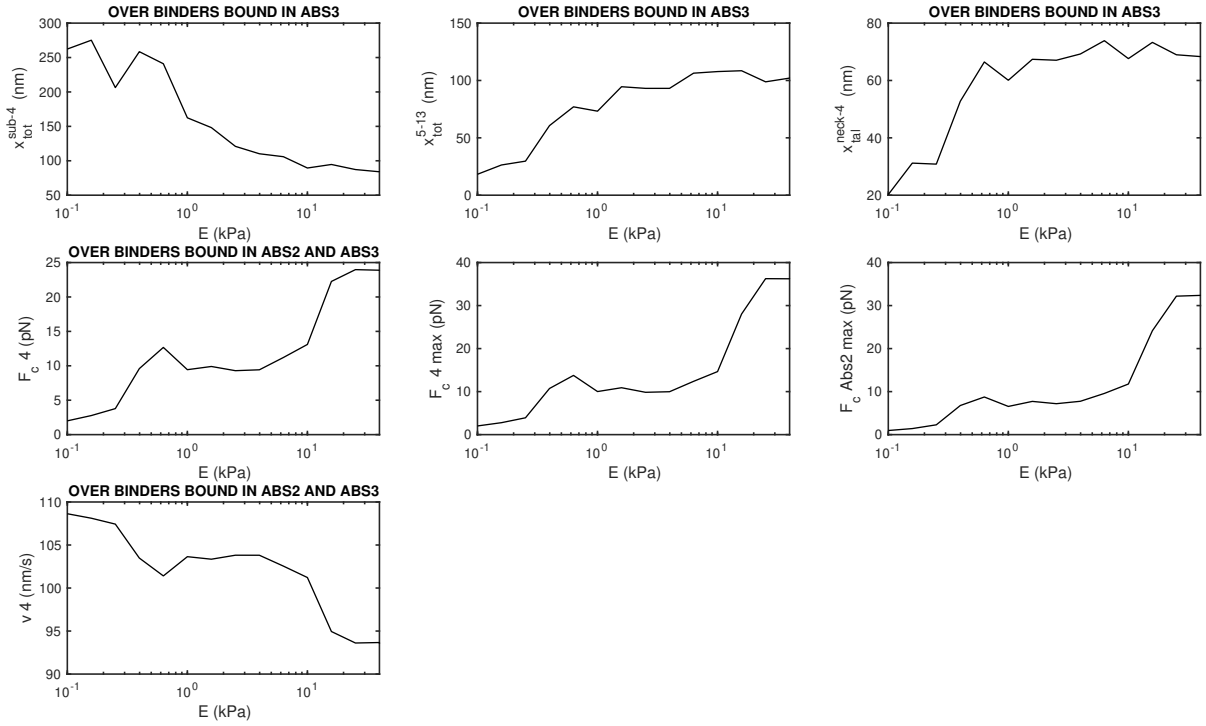

Figure 4.18: For a FA of MEFs with $\alpha_V\beta_3$ integrins and talin FL, we run 4 Gillespie simulations. Plot of the main variables against Young's modulus of the substrate E. The parameters are taken from Tables 4.8, 4.1 and 4.5.

vinculins bound, over a total of ≈ 37 bound binders, which gives a vinculin/talin ratio of ≈ 0.5 vinculin per talin. However for this same Young's modulus, the maximum value reached during time is 50 vinculins bound over a total of ≈ 51 bound binders, which gives ≈ 1 vinculin per talin, in agreement with the experimental vinculin/talin ratio of 1.4 (Atherton *et al.*, 2015). The integrin density d_{int} increases for stiffer substrates, as integrins are recruited according to the number of vinculins bound to talin. Again, the stiffest substrate $E = 39.81$ kPa, presents on average $d_{int,norm} = 2.5$, normalized with respect to the initial integrin density. For the same Young's modulus, the maximum values reached during time is $d_{int,norm} = 5$. The maximum values found experimentally are $d_{int,norm} = 3$ for β_3 integrins (Elosegui-Artola *et al.*, 2016), $d_{int,norm} = 5$ for $\alpha_5\beta_1$, and $d_{int,norm} = 2$ for $\alpha_V\beta_6$ (Elosegui-Artola *et al.*, 2014). Assuming that $\alpha_V\beta_3$ integrins behave similarly to the cited integrins, our results are again in agreement with previous data. Similarly to the total number of vinculins, also the vinculins in R3 increase for stiffer substrates, with a consequent higher activation of ABS2 on talin. For the stiffest substrate, $E = 39.81$ kPa, there are on average 4 binders with vinculin bound in R3 out

of 37 binders bound, i.e. on average 10% of the binders bound have vinculin bound in R3 and ABS2 active.
In Figure 4.19, we show the substrate displacement x_{sub} in a top view of the FA in the xy-plane. One Gillespie simulation is run and the plotted values are obtained

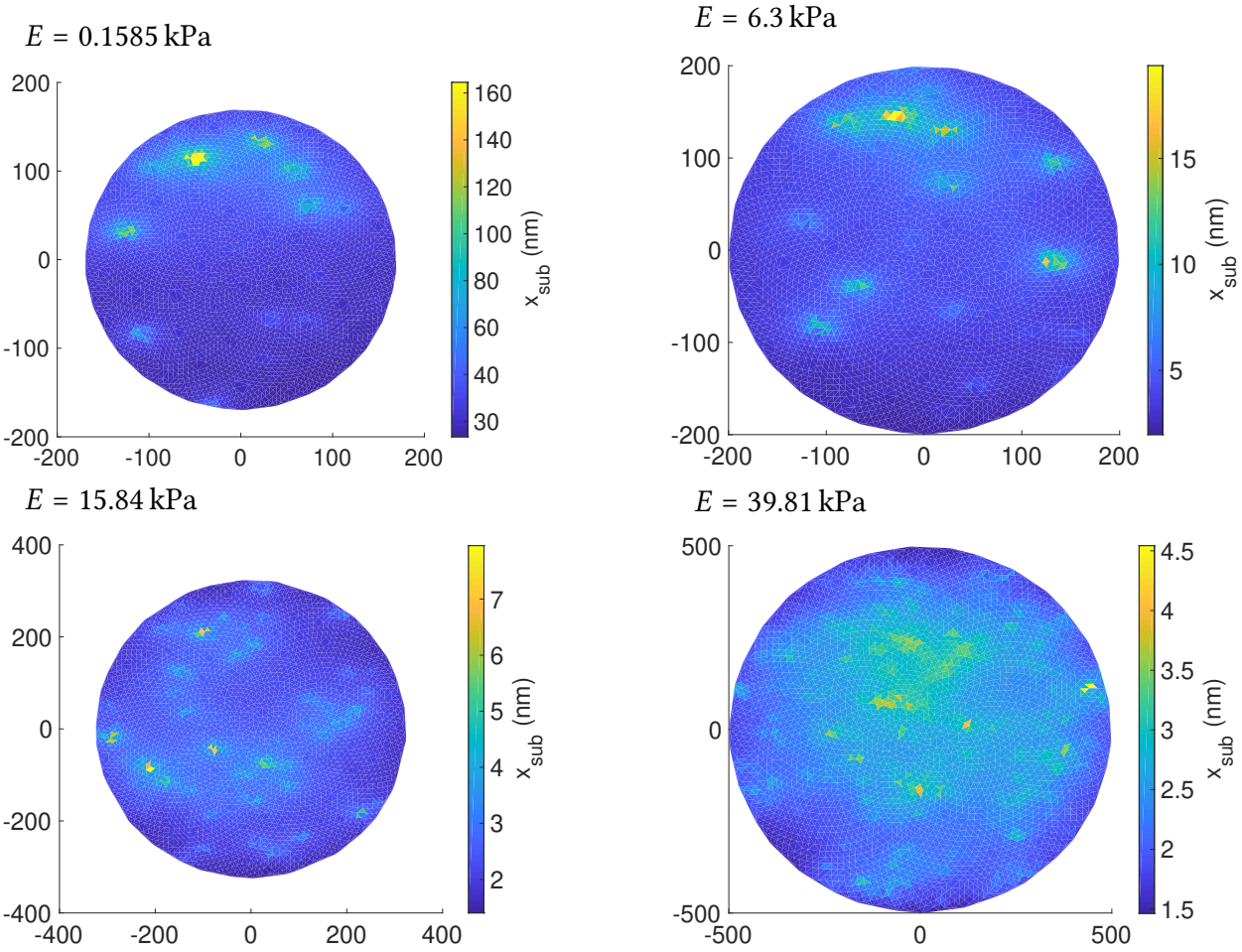

Figure 4.19: Top view of a FA of MEFs with $\alpha_V\beta_3$ integrins and talin FL. We show the substrate displacement x_{sub} for four values of the Young's modulus of the substrate E. The parameters are taken from Tables 4.8, 4.1 and 4.5.

averaging over the time interval. As imposed in the model, while increasing the stiffness of the substrate, the size of the FA increases, together with the number of binders n_c. As the substrate becomes more rigid, the total displacement starts to be shared by the adhesion proteins integrin and talin, giving smaller values for the substrate displacement x_{sub}. Moreover, we clearly notice that the number of bound binders increases while increasing the stiffness of the substrate (see also Figure 4.18, P_b).

4.4.3 Focal adhesion with $\alpha_V\beta_3$ integrins and talin dR(1-12)

The study of cells with talin domains depletion has great importance in biology, e.g. it has been shown that cancer cells present mutations in specific talin domains (Azizi *et al.*, 2021). Therefore, the study of the individual and joint behaviour of talin domains can help in predicting cancer cell functioning and arresting tumour progression.
In order to test the importance of the ABSs and VBSs on talin, which influence force transmission and FA reinforcement, we analyze the case of talin dR(1-12), i.e. the talin molecule where all domains from R1 to R12 have been depleted, so that talin is made of head and neck, directly linked to R13 and DD. Precisely, we study a FA where all talins are of type dR(1-12). Talin dR(1-12) presents ABS3 in the section R13-DD. ABS2, located between the domains R4 and R5, is not present. In Table 4.9 we summarize the values for the model parameters. Unlike the talin FL case, here

Parameters	
E (kPa)	0.1 - 100
a (nm)	562
d (nm)	50
n_c	501
κ_c (pN/nm)	0.8
k_{ont} ($\mu m^2/s$)	7×10^{-5}
d^0_{int} (int /μm^2)	300
$k_{off,slip}$ (s^{-1})	4.173×10^{-4}
$F_{b,slip}$ (pN)	5.4825
$k_{off,catch}$ (s^{-1})	0.4012
$F_{b,catch}$ (pN)	28.67
F_m (pN)	2
n_m	40
v_u (nm/s)	110

Table 4.9: For a FA of MEFs with $\alpha_V\beta_3$ integrins and talin dR(1-12), parameters of the multiscale clutch model used in Figures 4.20 and 4.21.

we take a fixed radius $a = 562\,nm$, in agreement with the FA length $1.2\,\mu m$ obtained in this same experimental work. As in the talin FL case, in the experiments they do not control for the spacing between fibronectin molecules, but the distance among them results in $\approx 50\,nm$, therefore we choose a FA with equispaced ligands, fixing this

same distance. For all Young's modulus of the substrate, we get the same number of equispaced ligands $n_c = 501$. For the parameters κ_c, k_{ont}, d^0_{int}, $k_{off,slip}$, $F_{b,slip}$, $k_{off,catch}$, $F_{b,catch}$, F_m, n_m and v_u we refer to Section 4.4.2.

We show in Figure 4.20 the time evolution of the model variables, fixing $E = 0.63\,\text{kPa}$, for one Gillespie simulation. In the plot of talin domains, the folded/unfolded state of the unique domain R13, averaged over the bound binders, is shown. All binders start free, with domain R13 folded, and after 30 s the domain appears unfolded in the majority of bound binders, thanks to the force transmitted. As in the case of talin FL, the force $F_{c,13}$ and the integrin displacement x_{int} reach maximum values in agreement with experimental results (Elosegui-Artola *et al.*, 2016, Kong *et al.*, 2009, Wang and Ha, 2013). Talin displacement x_{talin} reaches a value of $\approx 85\,\text{nm}$, coherent with the sum of the contour lengths of domain R13, talin neck and talin head. In the model, we consider a completely functioning ABS3 with R13 and DD, but the few-nanometers displacement of DD is neglected. In the talin dR(1-12) FA, the integrin density d_{int} does not increase with respect to the initial value, because the unique VBS in R13 is not considered.

We aim now at comparing the results against the Young's modulus of the substrate, for the FAs of talin FL (Figure 4.18) and talin dR(1-12) (Figure 4.21). In both cases, in stiffer substrates the talin domains are more likely to be unfolded, the force increases, the velocity decreases, the substrate displacement decreases and integrin and talin displacements increase. In particular, we look at the maximum and average forces. For the case of talin FL, binders can be bound only in ABS3 or both in ABS3 and ABS2. The force $F^{max}_{c,13}$ is the maximum force in R13 computed over all bound binders. Because of the presence of ABS2, binders bound also in ABS2 bear a higher force, located in R4, where the second actin filament is bound. Therefore, for the case of talin FL, the maximum force reached, computed over binders bound both in ABS3 and ABS2, is $F^{max}_{c,4} = 37\,\text{pN}$, for $E = 39.81\,\text{kPa}$. For the case of talin dR(1-12), the force is applied only in R13, reaching at maximum $F^{max}_{c,13} = 45\,\text{pN}$, for the same substrate stiffness. We conclude that the maximum force achieved is similar for the two FAs. Concerning the average forces, for $E = 39.81\,\text{kPa}$ the talin FL focal adhesion presents a total of 34 bound binders: 4 binders bound both in ABS2 and ABS3, and 30 binders bound only in ABS3. The 4 binders have average force $F_{c,4} = 24\,\text{pN}$, while the 30 binders have average force $F_{c,13} = 7\,\text{pN}$. In the FA of talin dR(1-12), there are 15 binders bound in ABS3, with average force $F_{c,13} = 18\,\text{pN}$. We find that also the average values are similar, proving that force is not influenced by the number of domains inside the talin rod.

As for the differences between talin FL and talin dR(1-12), we notice that the probability of being bound P_b takes values in the same range, but has a very different behaviour

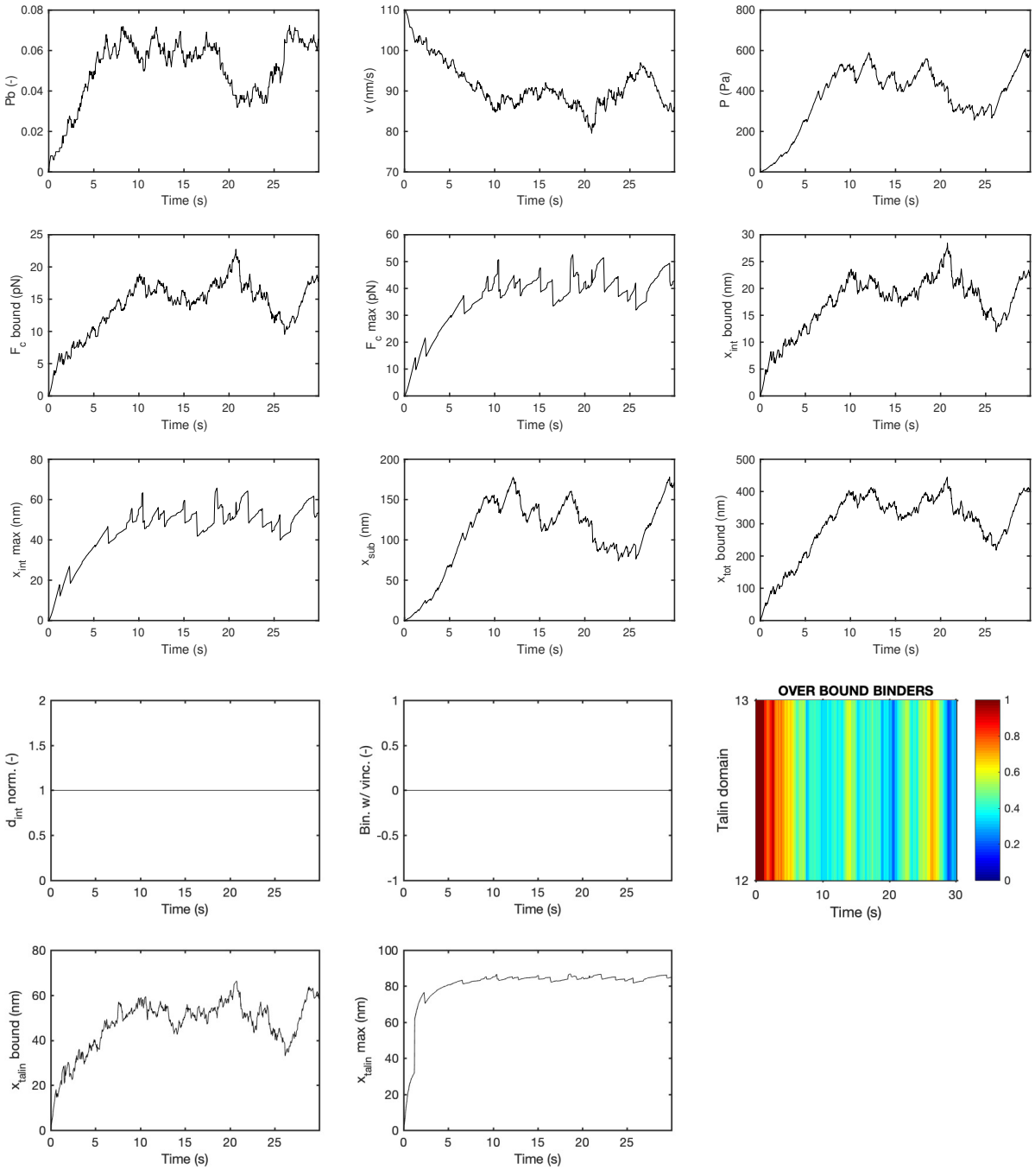

Figure 4.20: For a FA of MEFs with $\alpha_V\beta_3$ integrins and talin dR(1-12), fixing the Young's modulus of the substrate $E = 0.63\,\text{kPa}$, we run one Gillespie simulation and plot the time evolution of the main variables. The parameters are taken from Tables 4.9 and 4.5.

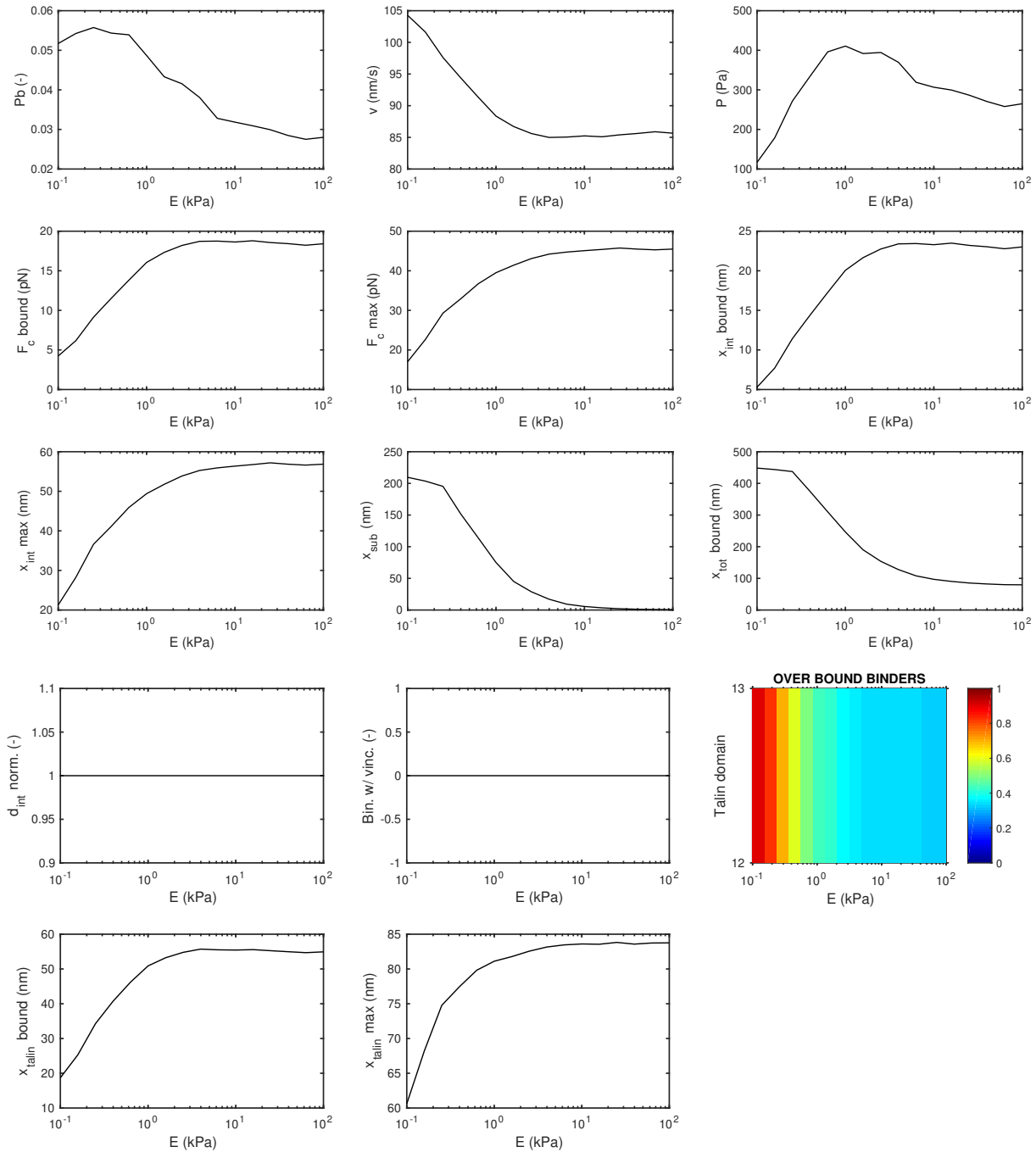

Figure 4.21: For a FA of MEFs with $\alpha_V\beta_3$ integrins and talin dR(1-12), we run 10 Gillespie simulations. Plot of the main variables against Young's modulus of the substrate E. The parameters are taken from Tables 4.9 and 4.5.

while varying the stiffness of the substrate. For talin FL, P_b increases, while for talin dR(1-12) it decreases. This is because in talin FL there are 7 VBSs implemented, and vinculins have a determining role in adhesion reinforcement: they increase the integrin density d_{int}, the binding rate k_{on}, and finally the probability P_b. In talin dR(1-12), no VBSs are implemented, therefore, in absence of vinculin, the integrin binding rate is constant for all substrate stiffnesses, and in stiff substrates fewer binders have time to bind because of the frictional slippage. Also, the cell traction P has a different behaviour in the two talin conformations. As P is computed summing the forces at single binders, it can increase both if the average force in the binders increases and if the number of bound binders increases. In talin FL, the cell traction is increasing for stiffer substrates, as both the average force and the bound probability P_b are increasing. In talin dR(1-12), the cell traction is first increasing and then decreasing while varying the Young's modulus of the substrate. It increases because the average force is increasing, but then starts decreasing because the bound probability decreases, for the absence of vinculin as justified before.

4.4.4 Model validation with experimental results of Mouse Embryonic Fibroblasts

In parallel to the development of the computational model, the group of Pere Roca-Cusachs at IBEC, Barcelona, performed experimental work on MEFs (unpublished work), which express $\alpha_V\beta_3$ integrins and cases of talin in full-length and talin dR(1-12). The computational results for the cell traction P obtained so far do not fit the experimental data of MEFs: our traction results are significantly higher than those obtained in the experiments. Experimental data are obtained by analyzing a cell section that contains a certain density of FAs. However, in our current interpretation of the multiscale clutch model, the traction is obtained within a single FA. Therefore, we hypothesize that the differences in the traction forces are due to differences in the scales of the results.

To analyze this idea, we multiply our computational result of P for a single FA, by a curve for the density of FAs inside the analyzed cell section. The curves for talin FL and talin dR(1-12) are shown in Figure 4.22. The shape of the curve is taken from the phospho-paxillin recruitment data (Suppl. Fig. 3 (a) Oria *et al.* 2017), which can be considered as a measure of the adhesion density in the cell.

For talin FL, we consider that in the experimentally analyzed section there is a percentage of FAs going from 15% in the softest substrate to 55% in the stiffest one. These

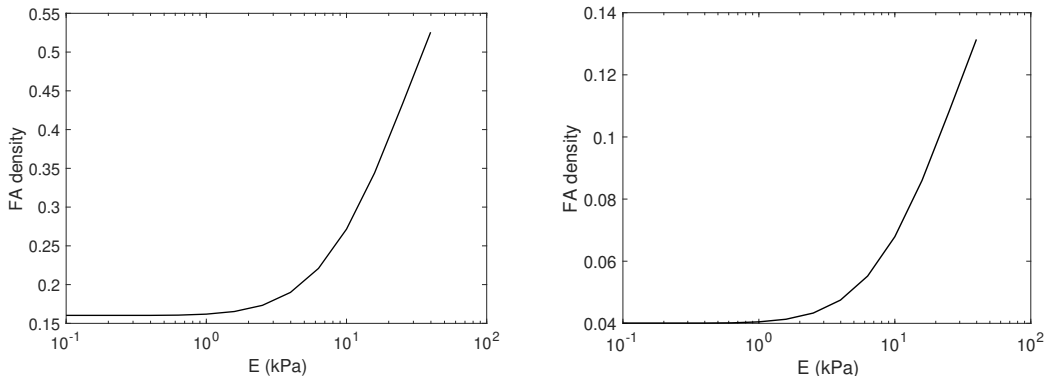

Figure 4.22: For talin FL (left) and talin dR(1-12) (right), FA density inside the experimentally analyzed cell section, varying the Young's modulus of the substrate. The curve is used to adapt the results of the multiscale clutch model for a FA, to the experimental data for P for the whole cell.

values are adjusted, but we consider them consistent with experimental images (Fig. 1 (d), $d = 50$ nm, Oria *et al.* 2017).

For the case of talin dR(1-12), the values are adjusted. Apart from considering the variation in the density of FAs, this curve could also take into account the increase in size of the FA while varying E. Indeed, the size of the adhesion is considered fixed in the model for the lack of more accurate experimental data, but most probably it varies, as it happens for talin FL. As previously seen, increasing the FA size for stiffer substrates results in an increase in the number of binders, which produces an increase in the cell traction P for stiff substrates (behaviour similar to applying the curve in Figure 4.22).

Finally, in Figure 4.23 we present the traction results for talin FL and talin dR(1-12). The cell traction for talin dR(1-12) is significantly lower than talin FL. Indeed, from the microscopic images of the experiments of MEFs (Figure 4.24), we notice that the cell with talin FL presents a long filopodia and a high density of adhesions in the lamellipodium. On the contrary, cells with talin dR(1-12) have a more rounded shape and smaller adhesions.

We summarize the differences between talin FL and talin dR(1-12). Talin FL presents all the 13 domains of the talin rod, while talin dR(1-12) presents only domain R13. Recalling the results of the model (Figures 4.18, 4.21), we guess that the number of talin domains is not influencing the intensity of the forces and the cell traction. We precise that here we just refer to an ideal depletion of the domains, without removing all the VBSs and ABSs. Additionally, talin FL presents 11 VBSs, while talin dR(1-12) presents

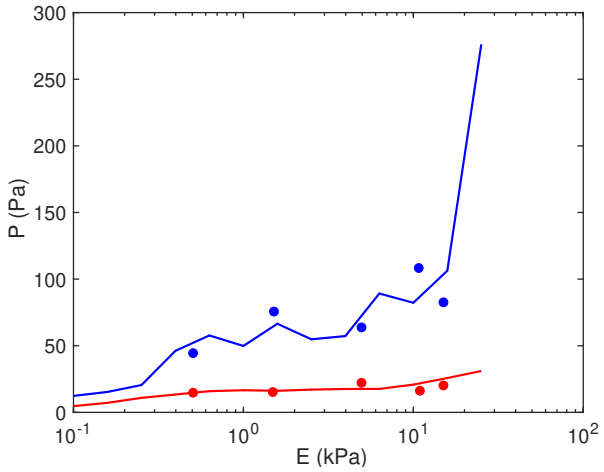

Figure 4.23: Values of the cell traction P for talin FL (blue) and talin dR(1-12) (red). The computational results are obtained with the multiscale clutch model (solid). The unpublished experimental data (dots) are obtained for MEFs with $\alpha_V\beta_3$ integrins by the group of Pere Roca-Cusachs at IBEC, Barcelona (unpublished).

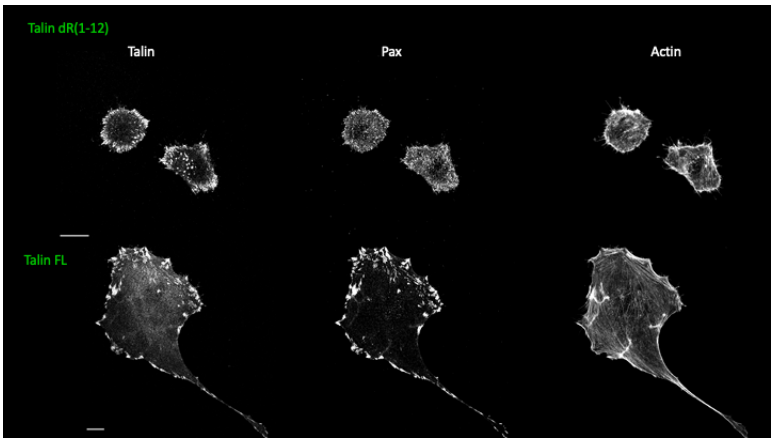

Figure 4.24: Experiments of MEFs with $\alpha_V\beta_3$ integrins: two cells with talin dR(1-12) in the first row, and one cell with talin FL in the second row. In white we see talin, paxillin and actin. From Pere Roca-Cusachs, IBEC (unpublished).

only 1 VBS. This means that the effect of vinculin is way higher in the talin FL case. Vinculin induces integrin recruitment, thus allowing the binding of more adhesion binders, resulting in a higher cell traction. This vinculin effect is better seen for stiff substrates, as talin is more elongated and unfolds many domains, revealing more VBSs. The computational results confirm this observation (Figure 4.18). Finally, talin FL

presents ABS2 and ABS3, while talin dR(1-12) presents only ABS3. The activation of ABS2 is again an outcome of the presence of vinculin, as it is activated by the binding of vinculin to the domain R3. The activation of ABS2 is probably increasing the cell traction, thus becoming another ingredient explaining the gap in the values for the two talin conformations. Also this vinculin effect is better seen for stiff substrates, and it is confirmed by the model results (Figure 4.18).

We propose here some alternative explanations for the discrepancies from the experimental data of the cell traction. Indeed, by using as many experimental parameters as possible, the fitting of the experimental data would result more accurate. A higher vinculin binding rate could be used, as the value $k_{onv} = 0.2\,\mathrm{s}^{-1}$ is obtained from in vitro studies and can be higher in vivo (Hu *et al.*, 2016). This would result in more vinculins bound, more integrin recruitment, higher bound probability and higher cell traction. As the most often unfolded domain R3 is only present in talin FL, a higher k_{onv} would produce a cell traction higher in talin FL than in talin dR(1-12), as in the experiments. The incremental integrin density int_{add} has been adjusted, therefore data on the integrin density behaviour correlated to the number of vinculins bound are needed, in order to reproduce more accurately the adhesion reinforcement process. Moreover, precise data on the FA size and the FA density could explain the results. Additionally, it is proved that $\alpha_5\beta_1$ integrins inside FAs are subjected to CMR, but a complete model for CMR has not been developed yet. To our knowledge, there are no published studies on the CMR of $\alpha_V\beta_3$ integrins. However, it could be possible that these integrins undergo some kind of reinforcement. Also, for the binding rate k_{ont} we take a value in the range of $\alpha_{IIb}\beta_3$ integrins, considering that all integrins behave similarly, but an experimental value for $\alpha_V\beta_3$ is needed. Finally, the VBS in R13 should be implemented, but probably this would not have an important influence on the results, as few vinculins would produce a low integrin recruitment and a low adhesion reinforcement.

The study of talin domains depletion is essential to understand the role of the VBSs, as we have observed that the absence of many VBSs reduces drastically the traction produced by a cell adhering to the ECM. The vinculin/talin ratio is found to be 0.2 for talin dR(1-12) and 2.2 for talin FL (Rahikainen *et al.*, 2019). It is proved that talin dR(1-10) and talin dR(4-12) are able to create more adhesions than talin dR(1-12), but less than talin FL, and more precisely talin dR(4-12) adheres more to the substrate than talin dR(1-10) (Rahikainen *et al.*, 2019). This is explained because talin dR(4-12) is made of head, neck, R1, R2, R3, R13 and DD, so it presents a total of 6 VBSs. Instead, talin dR(1-10) is made of head, neck, R11, R12, R13 and DD, so it presents a total of 2 VBSs. Not only the number of VBSs is influencing the adhesive behaviour, but

also the fact that domain R3 is the first in unfolding and revealing its VBS. A deeper investigation in the field of talin domains depletion could help to predict the outcome of some pathologies related to cell-ECM adhesion.

4.4.5 Focal adhesion with $\alpha_5\beta_1$ integrins and full-length talin

Analogously to Section 4.4.2, here we make use of the multiscale clutch model to reproduce experimental results obtained for Human breast myoepithelial cells (HBMCs) crowded with $\alpha_5\beta_1$ integrins (Oria *et al.*, 2017). We consider a FA with full-length talin. Coherently with the experimental results, we study substrate stiffnesses in $E = 0.1 - 25.12$ kPa. In the FA, equispaced ligands are positioned at distance $d = 100$ nm, as in the experiments (Oria *et al.*, 2017), and experimental values for the adhesion length are taken (Figure 4.11, dots, $d = 100$ nm) (Oria *et al.*, 2017). For each Young's modulus of the substrate, we get a fixed number of binders n_c in the range $11 - 108$, computed given the radius a of the circular FA and the distance d. We take $k_{ont} = 0.001\ \mu m^2 s^{-1}$, considering for integrin $\alpha_5\beta_1$ the same order of magnitude of experimental values for integrin $\alpha_{IIb}\beta_3$ (Barsegov, 2012). For the parameters κ_c, d^0_{int}, F_m, v_u, k_{onv}, int_{add} and m_r we refer to Section 4.4.1. For the unbinding rate parameters $k_{off,slip}$, $F_{b,slip}$, $k_{off,catch}$ and $F_{b,catch}$, for $\alpha_5\beta_1$ integrins with CMR, we refer to Section 4.2.1. In Table 4.10 we summarize the adopted values for the parameters.

Computational results are obtained averaging cell traction values over 10 Gillespie simulations, each run until the final time $t_f = 30$ s. The result for P for a single FA is then multiplied by the curve for the density of FAs inside the analyzed cell section (Figure 4.25, left). Again, the shape of the curve is taken from the phospho-paxillin recruitment data (Suppl. Fig. 3 (a) Oria *et al.* 2017). We consider that in the experimentally analyzed section there is a percentage of FAs going from 15% in the softest substrate to 75% in the stiffest one. These values are adjusted, but we can consider that they reproduce the tendency in the experimental images (Fig. 1 (d), $d = 100$ nm, Oria *et al.* 2017).

In Figure 4.25, we show the final graph for the cell traction P, together with the experimental data. Comparing the cell traction values for two types of cell, MEFs (Figure 4.23) and HBMCs (Figure 4.25), we can state that even with a different type of cell and integrin, the obtained cell tractions are similar.

The experimental data for the cell traction could be better reproduced by using more accurate experimental values for the vinculin binding rate k_{onv}, the incremental integrin density int_{add} and the binding rate k_{ont} of $\alpha_5\beta_1$ integrins. Experimental data for the FA density while varying the substrate stiffness would be also required for a

Parameters	
E (kPa)	0.1 - 25.12
a (nm)	160 - 550
d (nm)	100
n_c	11 - 108
κ_c (pN/nm)	0.8
k_{ont} ($\mu m^2/s$)	0.001
d^0_{int} (int /μm^2)	300
$k_{off,slip}$ (s^{-1})	3.68×10^{-4}
$F_{b,slip}$ (pN)	7.168
$k_{off,catch}$ (s^{-1})	2
$F_{b,catch}$ (pN)	7.168
F_m (pN)	2
n_m	40
v_u (nm/s)	110
k_{onv} (s^{-1})	0.2
int_{add} (int /μm^2)	24
m_r (int /μm^2)	15000

Table 4.10: For a FA of HBMCs with $\alpha_5\beta_1$ integrins and talin FL, parameters of the multiscale clutch model used in Figure 4.25.

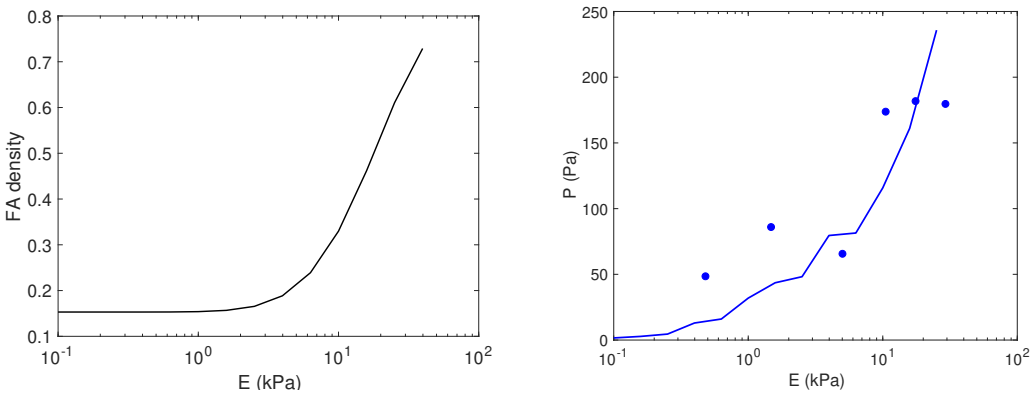

Figure 4.25: Left: FA density inside the experimentally analyzed cell section, varying the Young's modulus of the substrate. The curve is used to adapt the results of the multiscale clutch model for a FA, to the experimental data for P for the whole cell. Right: Multiscale clutch model (solid) reproducing experimental data (dots) of the cell traction P for HBMCs with $\alpha_5\beta_1$ integrins and talin FL (Oria *et al.*, 2017).

more precise analysis. Finally, a complete model for CMR for $\alpha_5\beta_1$ integrins could be developed.

4.5 Discussion

In this chapter we described our main original contributions to the clutch model:

- **Modelling the substrate displacement with Green's functions**
  We introduced spatial dependence in the deformation of the substrate due to the forces borne by the bound binders inside a FA. It is reasonable to argue that the ECM deforms more close to the attached adhesions than elsewhere. The ECM displacement is computed in all the points of the adhesion patch, by means of Green's functions solved at each ligand position.

- **Modelling talin mechanics, implementing VBSs and ABSs**
  Motivated by describing in detail the mechanics, velocities and displacements of the different adhesion proteins, we improved the modelling of the complex adhesion chains building the FA. We included a detailed model of the talin molecule (Yao *et al.*, 2016), to capture the deformation and the conformational changes occurring during cell adhesion. The talin rod is modelled with its 13 domains, which can unfold and refold.
  Essential mechanosensing events are vinculin and actin binding to different domains of the talin rod. We modelled the binding of vinculin in 7 of its 11 VBSs on talin and the binding of actin in 2 of its 3 ABSs on talin. This simplification is good enough, as the second VBS in the same talin domain behaves similarly to the first one, and ABS1 is considered not active. The actin binding site located in domains R4-R8 of talin, ABS2, has an essential role in force transmission (Atherton *et al.*, 2015). Our implementation of this key feature allows two actin filaments to be bound to the same talin rod.
  Some experimental studies depleted some domains of the talin rod, to study the importance of specific VBSs and ABSs in force transmission and FA growth. Our model can solve these depletions in a simpler and faster way than in the experimental work, managing to reproduce experimental results and inform future experiments.

The multiscale clutch model provides very specific data for displacements, forces, and velocities at a molecular level. To our knowledge, the corresponding experimental data are difficult to obtain, but it would be interesting to do the comparison.

Our multiscale clutch model solves some of the limitations of previous clutch models presented at the end of Chapter 2. When specifically mentioning data, we refer to the computational results of MEFs, for talin FL (Section 4.4.2) and talin dR(1-12) (Section 4.4.3), but these conclusions also apply to the results of HBMCs (Section 4.4.5). One of the key aspects of our modelling approach is the **use of model parameters that are directly obtained from previous experimental results**. It allows us not only to define the building blocks of the model, but also to obtain results of the model variables in close agreement with previous experimental data. For the radius of a FA, in the talin FL case we use values changing with the stiffness of the substrate $a = 170 - 500$ nm (Oria *et al.*, 2017), and in the talin dR(1-12) case we use $a = 600$ nm, from the MEFs experiment of Pere Roca-Cusachs. Both for talin FL and talin dR(1-12), we use the distance $d = 50$ nm among the equispaced ligands, as in the experimental setup. For both talin FL and talin dR(1-12), the stiffness of the linear spring modelling integrin is $\kappa_c = 0.8$ pN/nm, in agreement with experiments (Chen *et al.*, 2017, Kong *et al.*, 2013, 2009). The force-dependent unbinding rate for integrins $\alpha_V\beta_3$ is taken from experimental data (Elosegui-Artola *et al.*, 2016) without any modification, as the CMR is not proved for this type of integrins. The unbinding rate for integrin $\alpha_5\beta_1$ is taken from experimental data (Kong *et al.*, 2009). As it is proved that $\alpha_5\beta_1$ integrins undergo CMR (Kong *et al.*, 2013), we introduce a modification of their characteristic lifetime: keeping the original shape, we increase the lifetime for forces in the middle of the range. This modification reflects the fact that integrins bearing high forces have been bound for a longer time, being subjected to loading and unloading cycles with high force peaks, which have increased the lifetime of their bonds. Finally, for the binding rate of vinculin to talin we take $k_{onv} = 0.2\,s^{-1}$, as found experimentally (Hu *et al.*, 2016, Tapia-Rojo *et al.*, 2020).

The **actin velocity is implemented as a vector**, in order to displace every bound binder individually, depending on the force borne by that particular chain. This modelling approach allows to reproduce the biological behaviour of the adhesion proteins. The detail is further increased by introducing two different vectorial velocities in each binder: one corresponding to ABS2, between R4 and R5, and one in the location of ABS3, in the R13 talin domain. The vectorial velocity in R13 gives a more accurate spatial description than a scalar variable, as binders inside a FA stay apart $50 - 200$ nm, which are significant distances for our biological setting. Additionally, considering also binders with ABS2 activated, the presence of two velocities in each binder further increases the spatial biological accuracy. Indeed the domains R4 and R13 can distance from a few nanometers when they are all folded, up to $\approx 60 * 9 = 540$ nm when they are all unfolded, being 60 nm an average contour length of unfolded domains (Table

4.1), and 9 the number of the domains between R4 and R13. In the multiscale clutch model, we consider $n_m = 40$ myosin motors for each actin filament, so that only the motors connected to a specific bound binder exert force on it.
Moreover, in our model **each of the 13 talin rod domains can refold**, with its specific force-dependent folding rate $k_f(F)$. Only in the case in which a vinculin molecule is bound to a talin domain, that domain is locked in an unfolded conformation. Our implementation reproduces biology, as talin domains are always allowed to refold, except in the case in which vinculin is bound (Yao *et al.*, 2014).
Finally, the **integrins recruitment is corrected**: as soon as a vinculin binds talin, the integrin density is incremented by the quantity int_{add}, and as soon as a binder with vinculin becomes free, the integrin density is decreased by the same quantity int_{add} for each of the vinculins bound to that talin. Our implementation can be further refined, to take into account, e. g., the situation in which vinculin unbinds talin, remaining the binder bound, although not many data exist about this phenomenon.
Importantly, the use of biological parameters has allowed us to obtain **substrate and binders displacements in agreement with experiments** and **force values closer to the biological range**.
In the multiscale clutch model, for the substrate displacement we get at maximum $x_{sub} = 120\,\text{nm}$ for talin FL, and $x_{sub} = 300\,\text{nm}$ for talin dR(1-12). From experimental data, we deduce that fibronectin can have a maximum displacement of 120 nm (Erickson *et al.*, 1981, Guthold *et al.*, 2007). Therefore, as in the improved clutch model, our results are coherent with experiments.
Concerning the adhesion binder displacement, we get at maximum $x_{int}^{max} = 80\,\text{nm}$, $x_{tal}^{max} = 700\,\text{nm}$ in the case of talin FL, and $x_{int}^{max} = 80\,\text{nm}$, $x_{tal}^{max} = 90\,\text{nm}$ in the case of talin dR(1-12). These results are again in agreement with previous data: indeed $\alpha_5\beta_1$ integrins can reach a displacement of $\approx 50\,\text{nm}$ (Kong *et al.*, 2013, 2009), and talin can have a displacement of $\approx 700\,\text{nm}$ (Goult *et al.*, 2013a, Liu *et al.*, 2015a, Yao *et al.*, 2016). Talin dR(1-12) presents only talin head, neck and R13, and its maximum displacement is coherent with the contour lengths of the three components.
Concerning the maximum force borne by one adhesion binder, we get $F_{c,4}^{max} = 60\,\text{pN}$ in the case of talin FL, and $F_{c,13}^{max} = 60\,\text{pN}$ in the case of talin dR(1-12). As regards the average force, in the case of talin FL we get $F_{c,4} = 2 - 25\,\text{pN}$ on binders bound in ABS2 and ABS3, and $F_{c,13} = 2 - 8\,\text{pN}$ on binders bound only in ABS3. In the case of talin dR(1-12), we get as average force $F_{c,13} = 5 - 20\,\text{pN}$. DNA-based sensors established a maximum force of 33 – 43 pN (Wang and Ha, 2013) in $\alpha_V\beta_3$ integrins. In adhered fibroblasts, traction force microscopy gave an average force of 1 – 2 pN in each integrin (Galior *et al.*, 2016). Therefore our maximum and average values are slightly higher,

but not far from the biological ranges.
In the multiscale clutch model, the **FA lifetime is longer** than in previous models. In both talin FL and talin dR(1-12) cases, the FA enters a steady-state where binding and unbinding rates are equilibrated. This steady-state is reached sooner for stiffer substrates, and for almost all Young's modulus of the substrate it is reached before the final time $t_f = 30$ s. However, we can not reproduce the FA experimental average lifetime of ≈ 1 hour (Stricker *et al.*, 2013). Our model predicts that the force itself cannot be responsible for FA disassembly. In turn, FA disassembly may be a downstream mechanotransductive effect. It is caused by many phenomena, including the presence of calcium ions, RIAM and other proteins (Coló *et al.*, 2012, D'Souza *et al.*, 2020, Nagano *et al.*, 2012). As our model lacks the modelling of FA disassembly, it is planned as a future work.
Finally, in our model the **vinculin/talin ratio reproduces previous data**. In the case of talin FL, the maximum vinculin/talin ratio 0.98 is in agreement with the experimental values 1.4 (Atherton *et al.*, 2015) and 2.2 (Rahikainen *et al.*, 2019). This is possible thanks to the inclusion of multiple VBSs on the full-length talin, with a biological value of the vinculin binding rate.
Nevertheless, our multiscale clutch model predicts cell traction values that do not fit the experimental data. For that, we took into account the density of FAs in the experimentally analyzed cell section. As the multiscale clutch model studies the mechanics of a single FA, its limitation is **not being able to predict the density of FAs in the cell**.
Moreover, the multiscale clutch model **can not predict the change in size of the FA**, but it should be included by modelling the maturation of adhesion complexes. However our results suggest that cell traction is mostly dependent on ligand density rather than the complex adhesion size.

Chapter 5

Conclusions

We began this thesis by summarising the main biological phenomena involved in cell-ECM adhesion. We also discussed the behaviour of the cell-ECM adhesion complex based on its architecture and the mechanobiological role of its components. Then, we provided a literature review of the most important models developed in the last decades. We focused on the clutch model, as it can reproduce experimental results on cell adhesion, becoming the basis of many of the latest works. We carried out a deep analysis of the previous clutch model, and understood its strengths and limitations. To exploit its capabilities at the whole cell scale, we studied durotaxis through a finite element model coupled to the clutch model. Additionally, in order to overcome the limitations of the clutch model, we developed the multiscale clutch model, which still reproduces the cellular behaviour, but also shows excellent agreement with the behaviour of the molecular mechanisms that control the adhesion complex mechanics. Here we review the work performed in the thesis. Then, we propose precise goals for the future research in this field.

- We performed an extensive study of the clutch model. We showed, confirming previous works (Chan and Odde, 2008, Elosegui-Artola *et al.*, 2016), that it can reproduce adhesion dynamics at the cell scale, especially the velocity of the retrograde flow and the strength of the traction forces. Therefore, we used this computationally light model in the study of durotaxis. We developed a 1D finite element model and solved the clutch variables at the integration point level, which represents the behaviour of the adhesion at the ligand positions. We showed that a gradient in the ECM stiffness creates a polarized signal for the activation of an asymmetric intracellular retrograde flow during the initial cell spreading. The competition between this asymmetric retrograde flow and the polymerization velocity at the cell membrane creates a polarized state that

establishes cell migration directionality. Moreover, we showed that current discrepancies across cell types are explained by cell adhesion dynamics. Specifically, we showed that positive and negative durotaxis, which are prevalent in, e.g., epithelial and neural cells respectively, can be explained by the adhesion behaviour of the cell. Our theoretical framework confirmed previous experimental observations, corroborated the impact of a gradient in the matrix rigidity, rationalized positive and negative durotaxis and provided a conceptual framework to test specific pathways on how mechanical cues control cell migration.

- We identified in previous clutch models a number of inconsistencies with actual experimental observations. Apart from using some adjusted parameters, it includes a modelization of the adhesion chain that over-simplifies its rich mechanosensing features, resulting in unphysiological displacement values and vinculin/talin ratios not in agreement with experiments. Additionally, the reduction of the ECM mechanics to a single linear spring results in a lack of spatial description.

- Based on the aforementioned limitations, we pinpointed and addressed the areas of improvement. We extended the previous models based on the clutch hypothesis, creating a multiscale clutch model that explains the single FA behavior. We used physical and biological laws of the adhesion components at the single molecule level to describe the behavior at the FA level. We increased the complexity in the description of the substrate, through the use of Green's functions, and we introduced talin mechanics, to better characterise the adhesion chain. By integrating detailed models of the FA components, we reduced significantly the uncertainty of model parameters. The model resulted in integrin and talin displacements in agreement with experiments, biological force values and biological vinculin/talin ratios. We also found out that the force itself is not responsible for FA disassembly because, at steady-state, the rate of binding equals the one of unbinding. Therefore, FA disassembling should be the effect of further mechanosensitive mechanisms that, probably, foster changes in specific ions and proteins (Coló *et al.*, 2012, D'Souza *et al.*, 2020, Nagano *et al.*, 2012). We also understood the differences in the behaviour of different integrins and different ligand distances. Thanks to the study of talin domains depletion, we further showed the importance of each talin domain, with its own VBSs and ABSs, in cell adhesion behavior. We proposed that the density of FAs could be a determining factor in explaining the difference in cell tractions in different cell systems. A precise manipulation of cell adhesion components may allow to

foster cell migration during development and tissue repair or arrest it during tumor invasion. In light of these findings, we believe that the work carried out in this thesis took the modelling of cell-ECM adhesion a step forward.

5.1 Future work

Nevertheless, the field of cell adhesion modelling and its connection to the whole cell behavior needs to be object of further research. We summarize here some questions that, in our opinion, are still open from a biological and modelling point of view.

- **Studying CMR and other integrin features**
  Force-induced strengthening of cell-ECM adhesion has been explained with catch bond, integrins recruitment and CMR.
  CMR strengthens the fibronectin-integrin bond when integrins undergo many loading/unloading cycles or loading cycles with high force peaks (Kong *et al.*, 2013). CMR has been modelled first with a 2-state model (Chen *et al.*, 2015b), and later with a 3-state model, considering short-, intermediate- and long-lived states (Li *et al.*, 2016). However, the reaction rates between the three states have not been studied yet. Therefore, an accurate modelling of the CMR of integrins could be included in the multiscale clutch model, which would allow us to understand the evolution of different types of ACs.
  Other integrins features that can be included in the multiscale clutch model are integrin activation, turnover and clustering (Iwamoto and Calderwood, 2015). Integrin activation and clustering have been recently addressed mathematically (Cheng *et al.*, 2020). Finally, more information about the characteristics of different types of integrin is needed, as it would allow us to understand the behaviour of different cell types.

- **Improve the modelling of talin reinforcement, including no-VD1**
  The multiscale clutch model includes a simple modelling of the reinforcement caused by vinculin binding to talin. The recruited integrins just increase the integrin density, while it should be taken into account that they also increase the AC size. Another crucial consequence of vinculin binding to talin is actin recruitment. Actin fibres bind directly to full-length vinculin (Hirata *et al.*, 2014b). Vinculin binds talin through its D1 domain and binds actin through its tail. Therefore, vinculin can bind actin only in its full-length conformation, also called the no-VD1 case. The VD1 case refers to vinculin presenting only its D1 domain, thus allowed to bind talin but not actin. The actin-vinculin catch bond

has been included in some recent studies (Cheng *et al.*, 2020, Huang *et al.*, 2017). The multiscale clutch model is halfway between modelling the VD1 case, the simplest, and the no-VD1 case, the complete one. Indeed, the direct link between vinculin and actin is not taken into account, but integrin recruitment is considered. Integrin recruitment is thought to happen in the no-VD1 case, with full-length vinculin, and probably, in a reduced measure, also in the VD1 case. Previous data showed that in the VD1 case the cell traction is significantly reduced for stiff substrates, compared to the control case of full-length vinculin (Elosegui-Artola *et al.*, 2016). The VD1 case produces almost the same effect of talin depletion. Depleting talin, we do not need to specify the vinculin conformation, as vinculin is completely absent. In light of these results, the open question is if the VD1 case, apart from eliminating actin recruitment, also diminishes or eliminates the integrin recruitment, and if it influences ABS2 activation.
A complete implementation of the no-VD1 case inside the multiscale clutch model will give, from a mechanical point of view, an effect similar to ABS3 and ABS2: instead of two actin fibres bound to the same talin, we will have potentially a total of $2 + 11 = 13$ actin fibres bound to the same talin, considering that 11 actin fibres are bound to the vinculins bound in the 11 VBSs on talin. This would result in forces higher in the first domains of the talin rod than in the last ones, and earlier unfoldings of talin domains.

- **Extend the study of talin domains**
  It is important to extend the study of talin domains, to understand the role of specific VBSs and ABSs. Previous data showed that cancer creates mutations affecting specific talin domains (Azizi *et al.*, 2021). Other experimental studies on talin domains depletion focused on the role of talin domains in signalling, adhesion reinforcement and stability (Rahikainen *et al.*, 2019), and on the force-dependent bond between vinculin and talin (Atherton *et al.*, 2020).
  To our knowledge, we have been the first in addressing these problems from a computational point of view. It will be interesting to compare experimental and computational results for some other specific talin conformations.
  ABS3 is located in section R13-DD of talin, and the dimerization domain DD, apart from allowing the binding of talins between them, has a fundamental role in actin binding (Gingras *et al.*, 2008). The talin-R13 is made of talin head, neck and domain R13. Cells with the talin-R13 are not able to create adhesions to the ECM, giving a cell traction $P \approx 0$ (Roca-Cusachs, unpublished). Only a complete ABS3 made of R13 and DD allows talin to bind actin and transmit force to the ECM. We can study computationally talin-R13, to understand if the dimerization

domain DD, present in the study of talin dR(1-12), is fundamental for ABS3.
In order to study the importance of ABS2 instead, two interesting talin conformations are talin dR(1-3) and talin dR(4-12). In talin dR(1-3), R3 is removed, thus an important amount of vinculin is removed, and ABS2 can not be activated. Talin dR(4-12) presents the full ABS3, with R13 and DD, but does not present ABS2.
Finally, a significant conformation to study the importance of ABS3 is talin dR(13-DD). It presents the entire talin, except for the domains R13 and DD, which together build ABS3. As ABS3 is the first site allowing the talin-actin link, most probably these cells will not present any AC. Altogether, this computational study may allow us to predict the results of the more laborious experimental domains depletion.

- **Modelling other protein-protein bonds**
  In our multiscale clutch model, we only consider the fibronectin-integrin link, which is the "weakest link" of the adhesion chain. We do not include, e.g., the modelling of the actin-talin bond, which follows a slip behaviour (Cheng *et al.*, 2020, Choquet *et al.*, 1997, Srivastava *et al.*, 2008). We also assumed that talin is always bound to integrin, but it has been proved that also this bond can break (Bodescu *et al.*, 2020, Jiang *et al.*, 2003), and it has been included in some recent models (Neumann and Gottschalk, 2016, Yuan *et al.*, 2017). Talin presents two integrin binding sites (IBSs): the usual IBS1 in the domain F3 of talin head, and IBS2, localized in R11-R12. Although IBS2 has been object of different experimental studies (Gingras *et al.*, 2009, Gough and Goult, 2018, Klapholz *et al.*, 2015),its precise function needs to be clarified, before considering its implementation in the model.
  The aforementioned fibronectin-integrin and actin-talin bonds follow different dynamics in different cell types, hence we believe that the specific characteristics of each cell type should be the focus of further investigation.
  The detail of the ACs can be further increased, including other adaptor proteins, such as YAP, FAK, VASP, tensin, paxillin, zyxin, α–actinin and kindlin, with their mechano-chemical roles in cell adhesion. VASP, e. g., plays a mechanical role in Arp2/3-complex-dependent motility by amplifying the elastic modulus of the actin network and by strengthening its cohesion for persistent protrusion (Suei *et al.*, 2011). α–actinin influences the cohesiveness and mechanics of the cytoskeleton by cross-linking actin filaments. It also plays a major role in the maturation of ACs (Choi *et al.*, 2008).

- **Modelling AC maturation and disassembly**
  In this thesis, we make use of the multiscale clutch model to analyse only one type of ACs: focal adhesions. It is well known that the adhesion patch of a cell evolves in time and space. ACs follow a maturation process, from nascent adhesions to focal adhesions, to fibrillar adhesions (Stumpf *et al.*, 2020, Vicente-Manzanares and Horwitz, 2011). Depending on their maturation stage, the ACs are located in different positions of the cell-ECM interface, they increase in size and change in shape. Integrins are recruited thanks to vinculin, and follow different clustering processes. During maturation, the predominant integrin type changes. Indeed there are studies on the role of $\alpha_5\beta_1$ and $\alpha_V\beta_3$ in adhesion assembly, force transmission and cell spreading (Diaz *et al.*, 2020, Roca-Cusachs *et al.*, 2009, Schaufler *et al.*, 2016). Adhesion maturation is also characterized by the presence of specific proteins in each maturation stage. Talin-integrin stoichiometry is shown to be 2:1 in nascent adhesions and 1:1 in focal adhesions. Thanks to the actomyosin force, RIAM bound to talin in NAs is gradually substituted by vinculin in FAs (Goult *et al.*, 2013b, Vigouroux *et al.*, 2020). In the multiscale clutch model, we set an AC size varying with the stiffness of the substrate, but the size variation should arise from the model itself, linking integrin recruitment to the change in the AC size. We believe that a complete model for adhesion maturation should be developed, taking inspiration from some recent works on this subject (Ibata and Terentjev, 2020, Walcott *et al.*, 2011).
  The disassembly of ACs is caused by the activity of calcium (D'Souza *et al.*, 2020), RIAM (Coló *et al.*, 2012), microtubules, kinesin-1, FAK, dynamin, phosphatases and m-calpain (Nagano *et al.*, 2012). We consider that including the process of AC disassembly in the multiscale clutch model will allow us to reach a FA lifetime in agreement with previous data (Stricker *et al.*, 2013).

- **Develop similar models for cell-cell adhesion**
  Cell-cell contacts are key in the development of multicellular organisms, as cells form tissues and need to communicate between them (Casares *et al.*, 2015, Guillot and Lecuit, 2013, Saltzman and Chien, 2007, Suki and Hubmayr, 2014). Both cell-cell adhesions and cell-ECM adhesions integrate the actin cortex with ligands attached to the membrane. The molecular architecture of the cadherin-based cell-cell adhesions reminds of cell-ECM adhesion complexes. Integrins and cadherins are different classes of receptors, but vinculin is located between actin and transmembrane proteins, and its structure is made of an actin-binding tail domain, linked to the head, that can bind to α- or β-catenin, in cadherin

adhesions, or talin, in integrin adhesions.
However, some molecular mechanisms are different: in ACs, talin plays a structural role connecting integrin to actin, while in cell-cell adhesions the cadherin-actin binding is mediated by cadherin/β-catenin/α-catenin, α-catenin/Eplin and β-catenin/vinculin complexes. The number of vinculin molecules is also different. In ACs there are 11 VBSs on talin, while vinculin has a single binding site on α-catenin. The rigidity of the ECM can explain this difference, as it covers several orders of magnitude, so multiple binding sites are needed to adjust the cell mechanosensitivity, while forces between two cells cover a smaller range of rigidity, so fewer vinculin-binding sites could be needed.
Nevertheless, given the similarities with the cell-ECM adhesion, we believe that the models developed in this thesis could be potentially used for the study of cell-cell adhesion.

- **Build a deterministic version of the multiscale clutch model**
  A deterministic version, described by differential equations, of the multiscale clutch model can reduce its computational cost, giving a formulation that can be easily coupled to more comprehensive models. We studied an ODE (Bangasser and Odde, 2013) for the original clutch model (Chan and Odde, 2008). The system of equations reads:

$$
\begin{aligned}
\frac{dP_b}{dt} &= (1 - P_b)k_{on} - P_b\overline{k^*_{off}} \\
\overline{F_c} &= \kappa_c(\overline{x_c} - \overline{x_s}) \\
\overline{x_s} &= \frac{\kappa_c n_c \overline{x_c}}{\kappa_s + n_c\kappa_c} \\
\overline{v_f} &= v_u\left(1 - \frac{\kappa_s\overline{x_s}}{n_m F_m}\right) \\
\frac{d\overline{x_c}}{dt} &= (1 - P_b)\frac{d\overline{x_s}}{dt} + P_b\overline{v_f} \\
\overline{k^*_{off}} &= (1 - P_b)k_{off} + P_b k_{off}\left(1 - \frac{\overline{F_c}}{rP_bF_b}\right)^{-r}
\end{aligned}
\tag{5.1}
$$

where the bar symbol stays for the mean value of the variable over the clutches, and r is the shape parameter of the gamma distribution representing the distribution of forces among the bound clutches. For the original clutch model in the slip case, the ODE reproduces the results obtained with MC simulations (Figure 5.1). In the catch case, we could not recognize a fixed probability distribution

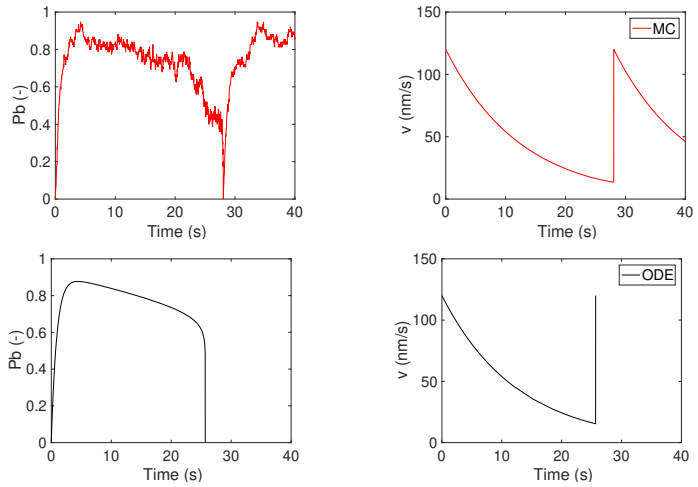

Figure 5.1: For the slip case in Table 2.1 fixing $\kappa_s = 0.1$ pN/nm, comparison between one MC simulation at the top, and the ODE at the bottom.

for the forces among the bound clutches. It would be interesting to reproduce the catch case, and extend the ODE to the latest version of the clutch model.
The model for durotaxis in Chapter 3 makes use of a stochastic clutch model, which is very computationally demanding. Integrating a deterministic version of the adhesion model would speed the simulation remarkably. Because of the computational cost, the study of collective cell durotaxis is not reliable currently.

- **Integrate 3D actomyosin continuum models with the multiscale clutch model**
  Cell function, specifically cell adhesion, is largely affected by the 3D setting found in most physiological conditions. Therefore, a 3D version of a continuum multi-scale clutch model could provide interesting insights. For example, it would allow us to analyze phenomena in 3D environments, including the interaction between neighbouring ACs, and the diffusion and turnover of the different proteins inside the cell.
  Recently very comprehensive models of actin cortex have been developed (Banerjee *et al.*, 2021, Torres-Sánchez *et al.*, 2019), and could be coupled to a continuum version of the clutch models.

Appendices

A Parametric analysis of the clutch model

A.1 Slip and catch cases

For both slip and catch cases, we vary the parameters over suitable ranges, to understand their influence on the main variables of the model. In Table A.1 we give the values used for the parametric analysis of Figures A.2, A.3. The defaults are the fixed values while varying another parameter, and the minima and maxima are the range limits. For all parameters, 16 values are taken inside each range.

The default parameters for the catch case are taken from literature (Elosegui-Artola *et al.*, 2016). k^*_{off} is obtained fitting the curve of the lifetime for $\alpha_5\beta_1$ integrins from experiments (Kong *et al.*, 2009). The k^*_{off} for the slip case is created ad hoc in order to be comparable with catch, giving cell tractions of the same order of magnitude. The rest of default parameters are the same in both cases.

Parameters	**Slip**			**Catch**		
	Default	Min	Max	Default (Elosegui-Artola *et al.*, 2016)	Min	Max
E (kPa)	-	0.1	100	-	0.1	100
a (nm)	1700	-	-	1700	-	-
n_c	1200	50	2320	1200	50	2320
κ_c (pN/nm)	1000	0.01	1000	1000	0.001	1000
k_{ont} ($\mu m^2/s$)	2.11×10^{-4}	3.5×10^{-6}	8.3×10^{-4}	2.11×10^{-4}	3.5×10^{-6}	8.3×10^{-4}
d_{int} (int /μm^2)	300	-	-	300	-	-
$k_{off,slip}$ (s^{-1})	0.1	1×10^{-5}	0.01	7.9938×10^{-4}	1×10^{-5}	0.01
$F_{b,slip}$ (pN)	12	0.1	20	8.1633	0.1	20
$k_{off,catch}$ (s^{-1})	-	-	-	10.143	0.1	30
$F_{b,catch}$ (pN)	-	-	-	6.2461	0.1	20
F_m (pN)	2	0.1	5	2	0.1	5
n_m	800	50	2320	800	50	2320
v_u (nm/s)	110	20	250	110	20	250

Table A.1: For the slip and catch cases, default values and ranges for the parameters used in Figures A.2, A.3. Linear or exponential distribution are adopted inside the ranges. The exponential distribution is chosen for ranges covering many orders of magnitude, in order to get more values in the first half of the range.

We do not vary the integrin density d_{int}, as it appears only inside Eq. 2.1 and we vary the parameter k_{ont}. Similarly, we do not vary the number of myosin motors n_m, as it appears only inside Eq. 2.9 and we vary the stall force of a single myosin motor F_m. We vary the number of ligands n_c in two different ways. First, we vary n_c keeping all the rest of parameters fixed, including the number of motors n_m. Second, we balance the clutch parameter against the motor parameter, setting $n_c = n_m$. Doing so, when all

clutches are engaged, there will be one myosin motor pulling each clutch. We analyse this combination of parameters as, in absence of a clutch-motor equilibrium, two extreme situations can take place. If the motors are too strong, the actin retrograde flow almost coincides with the unloaded velocity for all substrate stiffnesses, and the cell traction is nearly zero. On the other hand, if the clutches are too strong, transmitting high traction, then the actin flow is nearly zero for all substrate stiffnesses (Bangasser and Odde, 2013).

For the number of ligands n_c, we take a range centered in the default value. Indeed, as the radius of the adhesion $a = 1700\,\text{nm}$ is fixed, considering less and more ligands is like enlarging and reducing their distance, originally being around $d = 100\,\text{nm}$, thus covering possible biological distances between ligands as $d = 50\,\text{nm}$ and $d = 200\,\text{nm}$. For the stiffness of the clutch κ_c, the range goes to the left of the default value, as $\kappa_c = 1000\,\text{pN/nm}$ is too rigid and gives displacements smaller than experimental ones (Kong *et al.*, 2013, 2009). For the binding rate k_{ont}, the range covers experimental orders of magnitude (Barsegov, 2012). For the four parameters inside the unbinding rate $k_{off,slip}$, $k_{off,catch}$, $F_{b,slip}$ and $F_{b,catch}$, the ranges include the lifetimes describing the behaviour of integrins as $\alpha_5\beta_1$, $\alpha_V\beta_3$ or others, in all their possible activation states (Elosegui-Artola *et al.*, 2016, Kong *et al.*, 2013). Finally, as F_m and v_u have experimental references (Chan and Odde, 2008, Elosegui-Artola *et al.*, 2016, Molloy *et al.*, 1995), we take a narrow range in the same order of magnitude.

We show for the slip and catch cases the graphs of the cell traction P against Young's modulus, with variations of the parameters (Figures A.2, A.3). We focus on describing the results for the cell traction P, but we studied the effects on all the model variables.

We analyze how the optimal stiffness changes, varying the parameters of the model. Unless specified otherwise, all comments refer to both slip and catch cases.

Any parameter change that strengthens the clutches shifts the optimum towards higher stiffnesses: this is the case of the parameters k_{ont}, $F_{b,slip}$ and n_c. Contrarily, parameter changes that strengthen the motors shift the optimum towards lower stiffnesses: it can be seen by varying the motor parameters F_m and v_u. Moreover, increasing the unloaded off-rate coefficients $k_{off,slip}$, $k_{off,catch}$ or the characteristic bond rupture force via the catch pathway $F_{b,catch}$, shifts the optimum towards lower stiffnesses. This can be explained because an increase in the unbinding rate weakens the clutches.

By increasing k_{ont} we get an increase in the cell traction P corresponding to the optimal stiffness, as increasing the biding rate will give more bound binders and so higher cell traction. A large increase in k_{ont} eventually causes a stalled system because more clutches are bound at any given time, providing too much resistance for the motors to break all the bonds. A large decrease in k_{ont} causes few clutches to be bound,

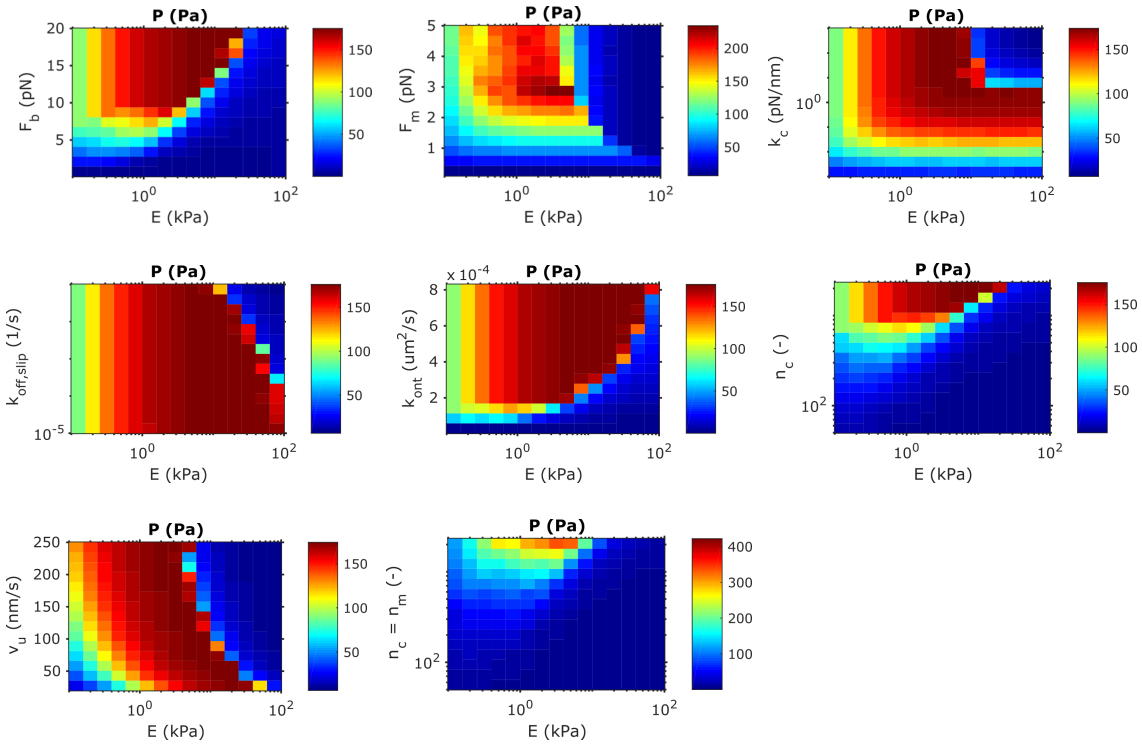

Figure A.2: For the slip case, values of the cell traction P following colormap, against Young's modulus E in the x-axis, varying in a suitable range the parameters F_b, F_m, κ_c, $k_{off,slip}$, k_{ont}, n_c, v_u and n_c kept equal to n_m in the y-axis, as in Table A.1.

resulting in a free-flowing system because the motors quickly break the bonds. On the other hand, by increasing $k_{off,slip}$ or $k_{off,catch}$ we get a decrease in the cell traction P corresponding to the optimal stiffness. In the slip case, it would be visible by choosing a bigger range. Similarly, increasing the off-rate will give less bound binders and so lower cell traction.

By increasing $F_{b,slip}$ we get an increase in the cell traction P corresponding to the optimal stiffness. Indeed, by increasing the characteristic bond rupture force $F_{b,slip}$, the off-rate decreases according to Eqs. 2.2 and 2.4, and it results in more bound binders and therefore higher cell traction. $F_{b,catch}$ follows exactly the opposite behaviour, being the two parameters inside exponentials with opposite signs.

By increasing n_c both independently and by setting $n_c = n_m$, we get an increase in the cell traction P corresponding to the optimal stiffness. By increasing the number of binders, the number of bound binders increases and results in higher cell traction.

Finally, we point out a difference between the slip and catch behaviour. In the slip

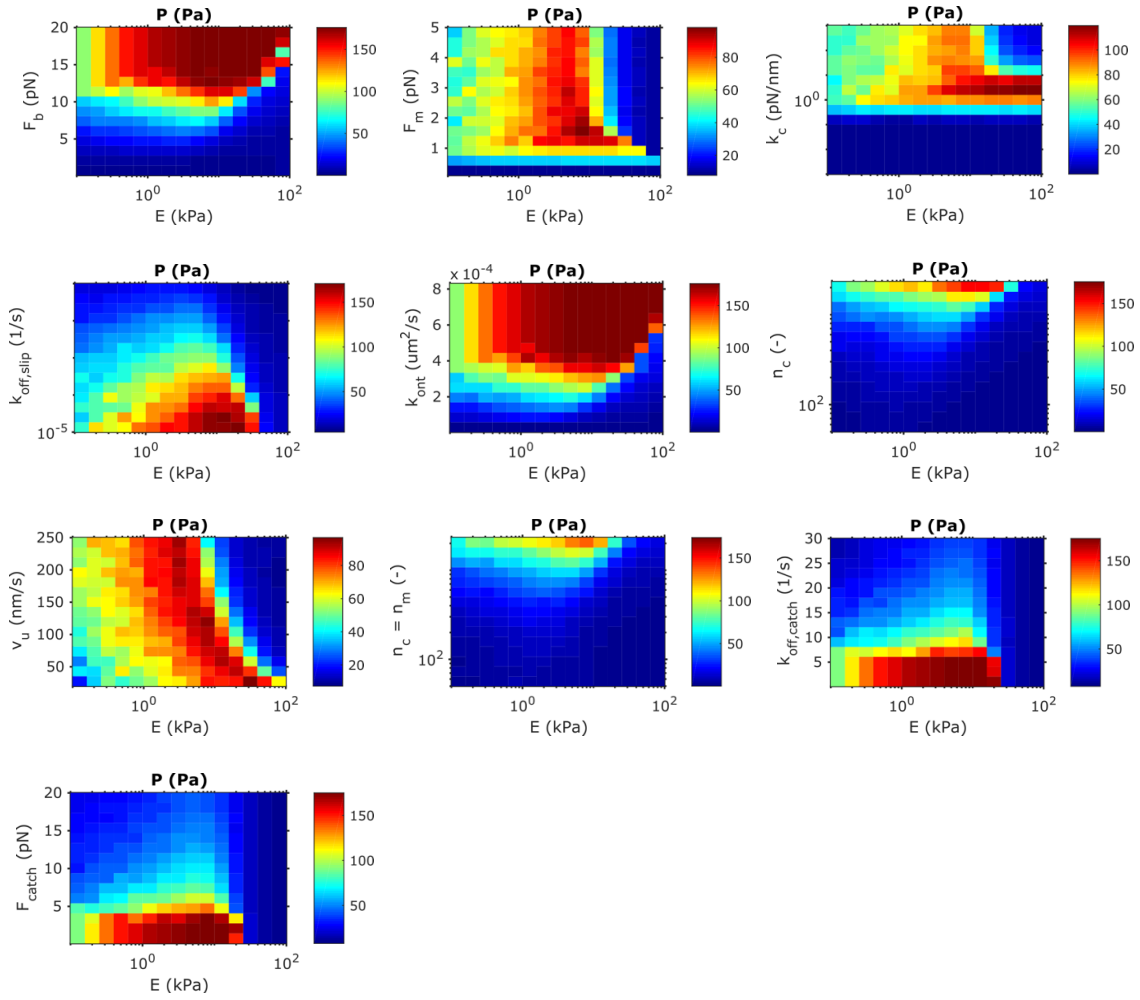

Figure A.3: For the catch case, values of the cell traction P following colormap, against Young's modulus E, varying in a suitable range the parameters F_b, F_m, κ_c, $k_{off,slip}$, k_{ont}, n_c, v_u, n_c kept equal to n_m, $k_{off,catch}$, F_{catch}, as in Table A.1.

case, in most of the graphs, for each row i.e. fixing the parameter, after reaching the maximum value of the cell traction P, it decreases very sharply. Conversely, in the catch case, P always follows a symmetric biphasic graph. As mentioned before, this can be justified by the definition of catch bond lifetime, as the average force F_c over bound binders increases for stiffer substrates.

A.2 Clutch model with talin reinforcement

Now, for the clutch model with talin reinforcement, we vary the parameters over suitable ranges, to see their influence on the main variables of our problem. In Table A.2 we give the values used inside the parametric analysis of Figure A.4. The defaults are the fixed values while varying another parameter, and the minima and maxima are the range limits. For all parameters, 16 values are taken inside each range, equispaced or with exponential distribution. The default parameters are taken from literature

Parameters	**Catch**		
	Default (Elosegui-Artola *et al.*, 2016)	Min	Max
E (kPa)	-	0.1	100
a (nm)	1700	-	-
n_c	1200	50	2320
κ_c (pN/nm)	1000	0.001	1000
k_{ont} ($\mu m^2/s$)	2.11×10^{-4}	3.5×10^{-6}	8.3×10^{-4}
d^0_{int} (int /μm^2)	300	10	1000
$k_{off,slip}$ (s^{-1})	7.9938×10^{-4}	1×10^{-5}	0.01
$F_{b,slip}$ (pN)	8.1633	0.1	20
$k_{off,catch}$ (s^{-1})	10.143	0.1	30
$F_{b,catch}$ (pN)	6.2461	0.1	20
F_m (pN)	2	0.1	5
n_m	800	50	2320
v_u (nm/s)	110	20	250
k_{onv} (s^{-1})	1×10^8	1	1×10^8
int_{add} (int /μm^2)	24	5	300
m_r (int /μm^2)	15000	-	-

Table A.2: For the model with talin reinforcement, default values and ranges for the parameters used in Figure A.4. Linear or exponential distribution are adopted inside the ranges.

(Elosegui-Artola *et al.*, 2016). We use the same ranges for the parameters as in Section A.1. We also vary the initial density of integrins d^0_{int}. Regarding the new parameters, we do not to vary the maximum integrin density m_r, as the value is very high and it never happens to reach it. Finally, for the binding rate of vinculin k_{onv} we take a range to the left of the default value, being the default bigger than experimental binding rates (Hu *et al.*, 2016, Tapia-Rojo *et al.*, 2020).

In Figure A.4 we show the graphs of the cell traction P against Young's modulus, with variations of the parameters. The first big difference that we can point out comparing

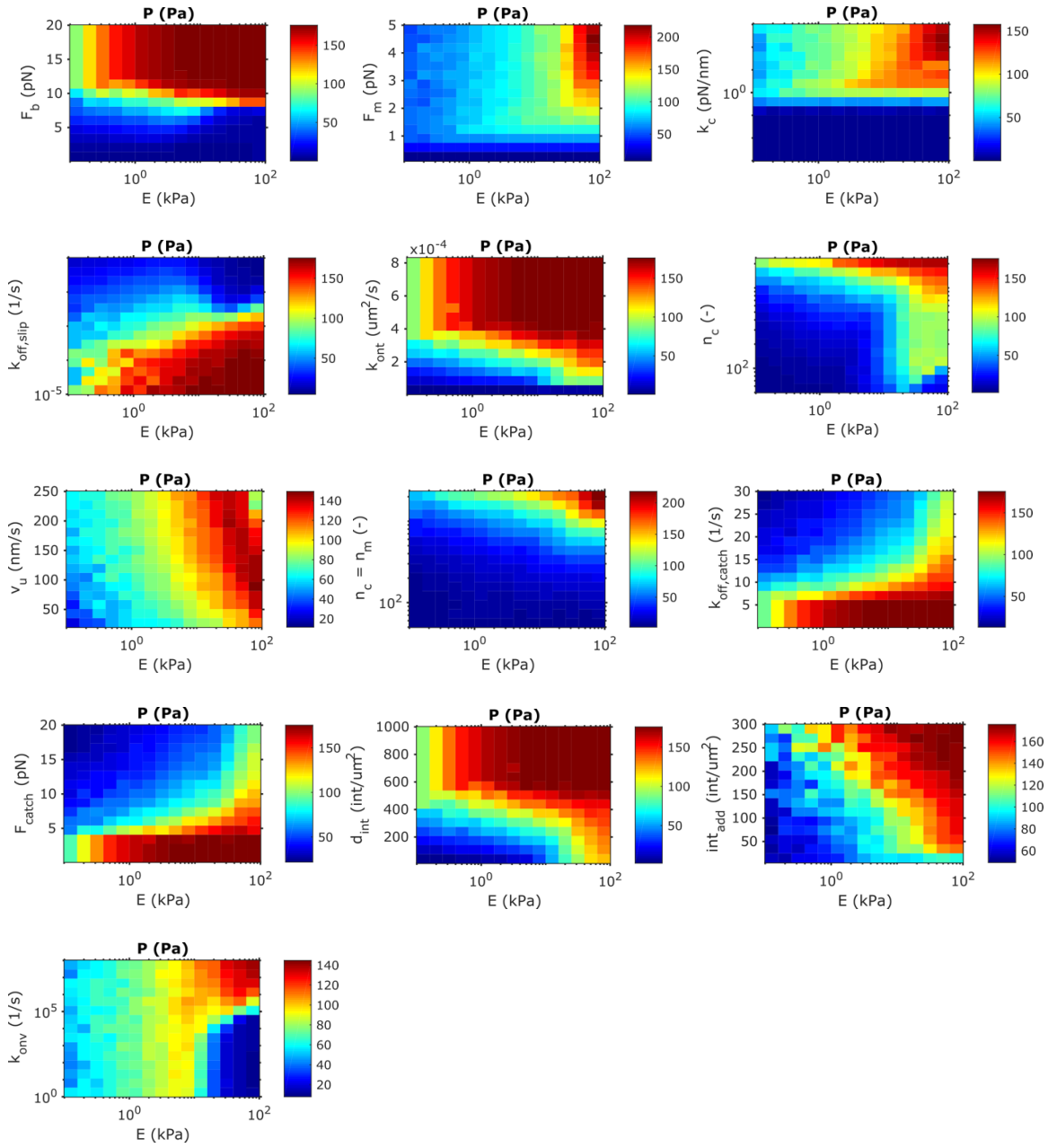

Figure A.4: For the model with talin reinforcement, values of the cell traction P following colormap, against Young's modulus E, varying in a suitable range the parameters F_b, F_m, κ_c, $k_{off,slip}$, k_{ont}, n_c, v_u, n_c kept equal to n_m, $k_{off,catch}$, F_{catch}, d^0_{int}, int_{add}, k_{onv}, as in Table A.2.

these results with the catch case without talin reinforcement (Figure A.3), is that in the variation of almost all the parameters, the maximum cell traction P is reached for the stiffest Young's modulus E. For values of the vinculin binding rate k_{onv} lower than 1×10^5, the optimal stiffness is in the middle of the range, while for values higher than 1×10^5, P is monotonically increasing. This fact explains the choice of a high default value for k_{onv}, as it is needed to show talin reinforcement. Apart from this difference, each parameter keeps a behaviour similar to the catch case without talin reinforcement. As for the new parameters introduced, by increasing d_{int}^0, int_{add} or k_{onv}, we get an increase in the cell traction P corresponding to the optimal stiffness. This can be explained biologically, as increasing the initial integrin density d_{int}^0 will increase the on-rate according to Eq. 2.1, and therefore will give more bound binders and higher cell traction. Similarly, increasing the integrin density added at each recruitment step int_{add} will increase the total integrin density, which will increase the on-rate, according to Eq. 2.1. Finally, increasing the on-rate of vinculin k_{onv} will increase the number of binders with vinculin bound, binders that recruit more integrins, and, following the same argument as above, this will give higher cell traction. Moreover, similarly to the other parameters strengthening the clutches, an increase in k_{onv} shifts the optimum to higher stiffnesses.

In light of these findings, the optimal stiffness is influenced by the individual and joint variation of parameters. This can clarify why different cell types have a cell traction P which increases or decreases for stiffer substrates. Indeed, each cell type has a different parameter set, including the number of motors and clutches and the binding and unbinding rates, which result in different stiffness optima (Bangasser *et al.*, 2017). Thanks to talin unfolding, in many cases cells grow FAs above a threshold in rigidity. Large adhesions increase integrin clustering and the effective binding rate of the system, preventing the entry into the frictional slippage regime and maintaining high force transmission (Elosegui-Artola *et al.*, 2018). The clutch model with talin reinforcement considering the catch behaviour of $\alpha_5\beta_1$ integrins, manages to reproduce the monotonic behaviour of the cell traction in mouse embryonic fibroblasts (Elosegui-Artola *et al.*, 2016). The model without talin reinforcement considering the slip behaviour of the binders manages to reproduce the biphasic behaviour of the cell traction in embryonic chick forebrain neurons (Chan and Odde, 2008). Therefore our inference is that these cells do not exhibit talin reinforcement.

B Time and space discretization

B.1 Transport equations

We describe the discretization in time and space of a parabolic equation that defines every transport equation involved in the models presented in Chapter 3,

$$\begin{cases} \rho_t + (v\rho - D\rho_x)_x = s - \sigma\rho & \text{in } \Omega \times [0, T] \\ v\rho - D\rho_x = 0 & \text{on } \Gamma_N, \end{cases} \tag{B.1}$$

where ρ is the density of interest, v is a convection velocity, D a diffusion constant and σ and s constants. The specific forms for the actin and myosin densities are particular cases of this equation.

B.1.1 Time Discretization

We use a second-order implicit, Crank-Nicolson method,

$$\frac{\Delta(\bullet)}{\Delta t} - \frac{1}{2}\Delta(\bullet)_t = (\bullet)^n_t, \tag{B.2}$$

to discretize the problem in time. We define $\Delta(\bullet) = (\bullet)^{n+1} - (\bullet)^n$ and we use the subscript notation $(\bullet)_t$ for the time derivative. We set a time interval $\mathcal{T}$ and a number of subintervals n, $\mathcal{T} = \bigcup_0^{n-1}[t^n, t^{n+1}]$, where the time increment is $\Delta t = t^{n+1} - t^n \geq 0$. Once discretized in time, the parabolic equation reads

$$\frac{\rho}{\Delta t} + \frac{1}{2}\mathcal{L}(\rho) = \frac{\rho^n}{\Delta t} - \frac{1}{2}\mathcal{L}(\rho^n) + s, \tag{B.3}$$

where $\mathcal{L}(\bullet) = \partial_x(v(\bullet) - D\partial_x(\bullet)) + \sigma(\bullet)$ acts on ρ. The time increment superindex $n+1$ has been dropped for sake of simplicity.

B.1.2 Weak Form and spatial discretization of the semi-discretized transport equation

To discretize in space the weak form of the semi-discretized Eq. B.3, we follow a standard Galerkin formulation. We first define a collection of trial functions, $\mathcal{S}_t$, that fulfill the Dirichlet condition in Γ_D, and a collection of test functions, $\mathcal{V}$, that are square integrable, have square integrable first derivatives in Ω and vanish in Γ_D, i.e:

$$\begin{aligned} \mathcal{S}_t &= \{\rho | \rho(\cdot, t) \in \mathcal{H}^1(\Omega),\ t \in [0, T] \text{ and } \rho(x, t) = \rho^D \text{ on } \Gamma_D\} \\ \mathcal{V} &= \{\omega \in \mathcal{H}^1(\Omega) \mid \omega = 0 \text{ on } \Gamma_D\} \end{aligned} \tag{B.4}$$

The weak form of the transport problem in Eq. B.3 reads: find $\rho \in \mathcal{S}_t$, for any $t \in [0, T]$ such that

$$\int_\Omega \omega \frac{\rho}{\Delta t} d\Omega + \frac{1}{2}\int_\Omega \omega \mathcal{L}(\rho) d\Omega = \int_\Omega \omega \frac{\rho^n}{\Delta t} d\Omega - \frac{1}{2}\int_\Omega \omega \mathcal{L}(\rho^n) d\Omega + \int_\Omega \omega s d\Omega \quad \forall \omega \in \mathcal{V}. \tag{B.5}$$

We apply the Gauss theorem on the total flux term and apply $v\rho - D\rho_x = 0$ on Γ_N, so that the problem reduces to find $\rho \in \mathcal{S}_t$, for any $t \in [0, T]$ such that

$$\begin{aligned} \left(\omega, \frac{\rho}{\Delta t}\right) + \frac{1}{2}[a(\omega, \rho) + c(v; \omega, \rho) + (\omega, \sigma\rho)] = \\ \left(\omega, \frac{\rho^n}{\Delta t}\right) - \frac{1}{2}[a(\omega, \rho^n) + c(v; \omega, \rho^n) + (\omega, \sigma\rho^n)] + (\omega, s) \; \forall \omega \in \mathcal{V} \end{aligned} \tag{B.6}$$

where

$$(\omega, \rho) = \int_\Omega \omega\rho d\Omega, \qquad c(v; \omega, \rho) = \int_\Omega \partial_x \omega v \rho d\Omega \quad \text{and} \quad a(\omega, \rho) = \int_\Omega \partial_x \omega (D\partial_x \rho) d\Omega. \tag{B.7}$$

We define

$$\hat{\mathcal{L}}(\bullet) = \int_\Omega \partial_x \omega v(\bullet) d\Omega + \int_\Omega \partial_x \omega D \partial_x(\bullet) d\Omega + \int_\Omega \omega\sigma(\bullet) d\Omega \tag{B.8}$$

so that we can rewrite the weak form as

$$\left(\omega, \frac{\rho}{\Delta t}\right) + \frac{1}{2}\hat{\mathcal{L}}(\rho) = \left(\omega, \frac{\rho^n}{\Delta t}\right) - \frac{1}{2}\hat{\mathcal{L}}(\rho^n) + (\omega, s). \tag{B.9}$$

We discretized in space the semi-discrete weak form following a Galerkin finite element approximation. The finite dimensional subset of spaces $\mathcal{S}^h$ and $\mathcal{V}^h$ are:

$$\begin{aligned} \mathcal{S}^h = \{\rho \mid \rho(\cdot, t) \in \mathcal{H}^1(\Omega), \rho(\cdot, t)_{|\Omega_e} \in \mathcal{P}_m(\Omega_e), \; t \in [0, T] \; \forall e \text{ and } \rho = \rho^D \text{ on } \Gamma_D\} \\ \mathcal{V}^h = \{\omega \in \mathcal{H}^1(\Omega) \, , \omega_{|\Omega_e} \in \mathcal{P}_m(\Omega_e) \; \forall e \text{ and } \omega = 0 \text{ on } \Gamma_D\}, \end{aligned} \tag{B.10}$$

where $\mathcal{P}_m$ is the finite element interpolating space.
Finally, the problem reduces to find $\rho^h \in \mathcal{S}^h$ for any $t \in [0, T]$, and for all $\omega^h \in \mathcal{V}^h$ such that

$$\left(\omega^h, \frac{\rho^h}{\Delta t}\right) + \frac{1}{2}\hat{\mathcal{L}}^h(\rho^h) = \left(\omega^h, \frac{\rho^n}{\Delta t}\right) - \frac{1}{2}\hat{\mathcal{L}}^h(\rho^n) + (\omega^h, s). \tag{B.11}$$

The domain Ω is discretized in n_{el} elements Ω_e and we use an isoparametric interpolation with linear shape functions N_I. We use elements of the same size $h = L(t)/n_{el}$. The standard Galerkin solution presents non-physical oscillations for convective dominant problems, i.e. if the Peclet number is larger than one (Codina, 2000, Jean Donea and Huerta, 2003). We define n_{el} large enough to avoid numerical oscillations.
We define $\mathbb{B} = \{I \,|\, I = 1, n_{np}\}$ the full set of n_{np} global node points in the finite element discretization, that can be related to all the sets of element nodes, $\mathbb{B}^e = \{i \,|\, i = 1, n_{en}\}$, as $\mathbb{B} = \bigcup_{e=1}^{n_{en}} \mathbb{B}^e$. The geometry is then approximated as

$$\mathbf{x}^h = \sum_{i=1}^{n_{en}} N_i \, \mathbf{x}_i \tag{B.12}$$

where the nodal positions are $\mathbf{x}_i$, $i = 1..n_{en}$ and

$$\omega^h = N_i \in \mathcal{V}^h \quad \text{and} \quad \rho^h = \sum_{j=1}^{n_{en}} N_j \rho_j \in \mathcal{S}^h. \tag{B.13}$$

The full discretized transport equation is:

$$\left[\frac{\mathbf{M}}{\Delta t}\right] \rho + \frac{1}{2}(\boldsymbol{\mathcal{L}})\rho = \left[\frac{\mathbf{M}}{\Delta t}\right] \rho^n - \frac{1}{2}[\boldsymbol{\mathcal{L}}]\rho^n + [\mathbf{m}] \tag{B.14}$$

where $\boldsymbol{\mathcal{L}} = \mathbf{m_c} + \mathbf{K} + \sigma\mathbf{M}$ and

$$\mathbf{M} = \mathop{\mathbf{A}}_{e=1}^{n_{el}} \int_{\Omega_e} N_i N_j \mathrm{d}\Omega, \;\; \mathbf{m} = \mathop{\mathbf{A}}_{e=1}^{n_{el}} \int_{\Omega_e} N_i \mathrm{d}\Omega, \;\; \mathbf{m_c} = \mathop{\mathbf{A}}_{e=1}^{n_{el}} \int_{\Omega_e} N_i' v N_j \mathrm{d}\Omega \text{ and } \mathbf{K} = \mathop{\mathbf{A}}_{e=1}^{n_{el}} \int_{\Omega_e} N_i' D N_j' \mathrm{d}\Omega. \tag{B.15}$$

$\mathop{\mathbf{A}}_{e=1}^{n_{el}} \int_{\Omega_e}$ is the assembly operator of the local element matrix and vectors.

B.2 Momentum-balance equation

To solve the balance of linear momentum,

$$\partial_x \left[\mu \partial_x v + \zeta \rho\right] = \eta v \quad \text{in } \Omega \tag{B.16}$$

$$\mu \partial_x v + \zeta \rho \;\; = \;\; \tau(l_f(t)) \qquad \text{on} \quad \Gamma_N, \tag{B.17}$$

we also use the finite element method. Recall that μ is the viscous coefficient, ζ is the contractility constant and η is the friction parameter. We use the same trial and test function spaces to derive the weak form of the problem as

$$-\int_\Omega \mu w_x v_x \, dx - \int_\Omega \eta w v \, dx = \int_\Omega \zeta w_x \rho \, dx - \tau \qquad \forall w \in \mathcal{V}, \tag{B.18}$$

where we have applied Neumann boundary conditions such that $\tau = (\mu \partial_x v + \zeta \rho)|_{\Gamma_N}$. We use again the Galerkin discretization described above and obtain the final discretized algebraic system of equations,

$$[-\mu \mathbf{K} - \eta \mathbf{M}] v = \mathbf{f} \tag{B.19}$$

where

$$K_{ij} = \int_\Omega N_i' N_j' \, dx, \quad M_{ij} = \int_\Omega N_i N_j \, dx \quad \text{and} \quad f_i = \int_\Omega \zeta N_i' \, dx - \tau_i. \tag{B.20}$$

Bibliography

K. J. Amann and T. D. Pollard. The Arp2/3 complex nucleates actin filament branches from the sides of pre-existing filaments. *Nature cell biology* **3**, 306 (2001).

M. Arnold, E. A. Cavalcanti-Adam, R. Glass, and W. Eck. Activation of integrin function by nanopatterned adhesive interfaces. *ChemPhysChem* **5**, 383 (2004). https://chemistry-europe.onlinelibrary.wiley.com/doi/pdf/10.1002/cphc.200301014 .

P. Atherton, F. Lausecker, A. Carisey, A. Gilmore, D. Critchley, I. Barsukov, and C. Ballestrem. Relief of talin autoinhibition triggers a force-independent association with vinculin. *Journal of Cell Biology* **219** (2020).

P. Atherton, B. Stutchbury, D.-Y. Wang, D. Jethwa, R. Tsang, E. Meiler-Rodriguez, P. Wang, N. Bate, R. Zent, I. L. Barsukov, *et al.*. Vinculin controls talin engagement with the actomyosin machinery. *Nature Communications* **6**, 1 (2015).

K. Austen, P. Ringer, A. Mehlich, A. Chrostek-Grashoff, C. Kluger, C. Klingner, B. Sabass, R. Zent, M. Rief, and C. Grashoff. Extracellular rigidity sensing by talin isoform-specific mechanical linkages. *Nature cell biology* **17**, 1597 (2015).

L. Azizi, A. R. Cowell, V. V. Mykuliak, B. T. Goult, P. Turkki, and V. P. Hytönen. Cancer associated talin point mutations disorganise cell adhesion and migration. *Scientific reports* **11**, 1 (2021).

L. Bačáková, E. Filova, F. Rypáček, V. Švorčík, and V. Starỳ. Cell adhesion on artificial materials for tissue engineering. *Physiol Res* **53**, S35 (2004).

N. Q. Balaban, U. S. Schwarz, D. Riveline, P. Goichberg, G. Tzur, I. Sabanay, D. Mahalu, S. Safran, A. Bershadsky, L. Addadi, *et al.*. Force and focal adhesion assembly: a close relationship studied using elastic micropatterned substrates. *Nature cell biology* **3**, 466 (2001).

D. Banerjee, V. Vitelli, F. Jülicher, and P. Surówka. Active viscoelasticity of odd materials. *Physical Review Letters* **126**, 138001 (2021).

B. L. Bangasser, S. S. Rosenfeld, and D. J. Odde. Determinants of maximal force transmission in a motor-clutch model of cell traction in a compliant microenvironment. *Biophysical Journal* **105**, 581 (2013).

B. L. Bangasser and D. J. Odde. Master equation-based analysis of a motor-clutch model for cell traction force. *Cellular and molecular bioengineering* **6**, 449 (2013).

B. L. Bangasser, G. A. Shamsan, C. E. Chan, K. N. Opoku, E. Tüzel, B. W. Schlichtmann, J. A. Kasim, B. J. Fuller, B. R. McCullough, S. S. Rosenfeld, *et al.*. Shifting the optimal stiffness for cell migration. *Nature Communications* **8**, 1 (2017).

E. Barnhart, K.-C. Lee, G. M. Allen, J. A. Theriot, and A. Mogilner. Balance between cell- substrate adhesion and myosin contraction determines the frequency of motility initiation in fish keratocytes. *Proceedings of the National Academy of Sciences* **112**, 5045 (2015).

E. L. Barnhart, K. C. Lee, K. Keren, A. Mogilner, and J. A. Theriot. An adhesion-dependent switch between mechanisms that determine motile cell shape. *PLoS Biology* **9** (2011). 10.1371/journal.pbio.1001059.

V. Barsegov. Resolving two-dimensional kinetics of the integrin IIb 3-fibrinogen interactions using binding-unbinding correlation spectroscopy. *The Journal of Biological Chemistry* **287**, 35275 (2012).

E. L. Batchelder, G. Hollopeter, C. Campillo, X. Mezanges, E. M. Jorgensen, P. Nassoy, P. Sens, and J. Plastino. Membrane tension regulates motility by controlling lamellipodium organization. *Proceedings of the National Academy of Sciences of the United States of America* **108**, 11429 (2011).

J. E. Bear and J. M. Haugh. Directed migration of mesenchymal cells: Where signaling and the cytoskeleton meet. *Current Opinion in Cell Biology* **30**, 74 (2014).

G. I. Bell. Models for the specific adhesion of cells to cells. *Science* **200**, 618 (1978). https://www.science.org/doi/pdf/10.1126/science.347575 .

G. Bendas and L. Borsig. Cancer cell adhesion and metastasis: selectins, integrins, and the inhibitory potential of heparins. *International journal of cell biology* **2012** (2012).

M. Bennett, M. Cantini, J. Reboud, J. M. Cooper, P. Roca-Cusachs, and M. Salmeron-Sanchez. Molecular clutch drives cell response to surface viscosity. *Proceedings of the National Academy of Sciences* **115**, 1192 (2018).

M. Bergert, A. Erzberger, R. A. Desai, I. M. Aspalter, A. C. Oates, G. Charras, G. Salbreux, and E. K. Paluch. Force transmission during adhesion-independent migration. *Nature Cell Biology* **17**, 524 (2015).

K. Bhadriraju, W. F. Liu, D. S. Gray, and C. S. Chen. Engineering Cell Adhesion. in *BioMEMS and Biomedical Nanotechnology* (Springer, 2006) pp. 325–343.

M. A. Bodescu, M. Grison, J. Aretz, M. Rief, and R. Fassler. Single-molecule mechanics of the talin-integrin bond. *Biophysical Journal* **118**, 397a (2020).

T. Bogenrieder and M. Herlyn. Axis of evil: molecular mechanisms of cancer metastasis. *Oncogene* **22**, 6524 (2003).

P. R. Bois, B. P. O'Hara, D. Nietlispach, J. Kirkpatrick, and T. Izard. The vinculin binding sites of talin and α-actinin are sufficient to activate vinculin. *Journal of Biological Chemistry* **281**, 7228 (2006).

L. Bollmann, D. E. Koser, R. Shahapure, H. O. Gautier, G. A. Holzapfel, G. Scarcelli, M. C. Gather, E. Ulbricht, and K. Franze. Microglia mechanics: Immune activation alters traction forces and durotaxis. *Frontiers in Cellular Neuroscience* **9**, 1 (2015).

C. Borau, T. Kim, T. C. Bidone, J. M. García-Aznar, and R. D. Kamm. Dynamic mechanisms of cell rigidity sensing: insights from a computational model of actomyosin networks. *PloS one* **7**, 1 (2012).

D. Bray and J. G. White. Cortical flow in animal cells. *Science* **239**, 883 (1988).

A. Brugués, E. Anon, V. Conte, J. H. Veldhuis, M. Gupta, J. Colombelli, J. J. Muñoz, G. W. Brodland, B. Ladoux, and X. Trepat. Forces driving epithelial wound healing. *Nature physics* **10**, 683 (2014).

K. Burridge and E. S. Wittchen. The tension mounts : Stress fibers as force-generating mechanotransducers. *Journal of Cell Biology* **200**, 9 (2013).

K. Burridge, E. Monaghan-Benson, and D. M. Graham. Mechanotransduction: from the cell surface to the nucleus via RhoA. *Philosophical Transactions of the Royal Society B* **374**, 20180229 (2019).

D. T. Butcher, T. Alliston, and V. M. Weaver. A tense situation: forcing tumour progression. *Nat Rev Cancer* **9**, 108 (2009).

Y. Cai, N. Biais, G. Giannone, M. Tanase, G. Jiang, J. Hofman, C. H. Wiggins, P. Silberzan, A. Buguin, B. Ladoux, and M. P. Sheetz. Nonmuscle myosin IIA-dependent force inhibits cell spreading and drives F-actin flow. *Biophysical Journal* **91 10**, 3907 (2006).

D. A. Calderwood. Talin controls integrin activation. *Biochemical Society Transactions* **32**, 434 (2004).

K. G. Campellone and M. D. Welch. A nucleator arms race: cellular control of actin assembly. *Nature reviews. Molecular cell biology* **11**, 237 (2010).

M.-f. Carlier, V. Laurent, J. Santolini, R. Melki, D. Didry, G.-x. Xia, Y. Hong, N.-h. Chua, and D. Pantaloni. Actin Depolymerizing Factor (ADF/Cofilin) Enhances the Rate of Filament Turnover: Implication in Actin-based Motility. *J. Cell Biol.* **136**, 1307 (1997).

L. Casares, R. Vincent, D. Zalvidea, N. Campillo, D. Navajas, M. Arroyo, and X. Trepat. Hydraulic fracture during epithelial stretching. *Nature materials* **14**, 343 (2015).

L. B. Case and C. M. Waterman. Integration of actin dynamics and cell adhesion by a three-dimensional, mechanosensitive molecular clutch. *Nature Cell Biology* **17**, 955 (2015).

E. A. Cavalcanti-Adam, T. Volberg, A. Micoulet, H. Kessler, B. Geiger, and J. P. Spatz. Cell spreading and focal adhesion dynamics are regulated by spacing of integrin ligands. *Biophysical Journal* **92**, 2964 (2007).

E. A. Cavalcanti-Adam, A. Micoulet, J. Blümmel, J. Auernheimer, H. Kessler, and J. P. Spatz. Lateral spacing of integrin ligands influences cell spreading and focal adhesion assembly. *European Journal of Cell Biology* **85**, 219 (2006).

C. E. Chan and D. J. Odde. Traction dynamics of filopodia on compliant substrates. *Science* **322**, 1687 (2008). http://science.sciencemag.org/content/322/5908/1687.full.pdf .

R. Changede, X. Xu, F. Margadant, and M. P. Sheetz. Nascent integrin adhesions form on all matrix rigidities after integrin activation. *Developmental Cell* **35**, 614 (2015).

P. h. G. Chao, S. C. Sheng, and W. R. Chang. Micro-composite substrates for the study of cell-matrix mechanical interactions. *Journal of the Mechanical Behavior of Biomedical Materials* **38**, 232 (2014).

G. Charras and E. Sahai. Physical influences of the extracellular environment on cell migration. *Nature Reviews Molecular Cell Biology* **15**, 813 (2014).

O. Chaudhuri, L. Gu, M. Darnell, D. Klumpers, S. A. Bencherif, J. C. Weaver, N. Huebsch, and D. J. Mooney. Substrate stress relaxation regulates cell spreading. *Nature Communications* **6**, 1 (2015).

B. Chen, B. Ji, and H. Gao. Modeling Active Mechanosensing in Cell–Matrix Interactions. *Annual Review of Biophysics* **44**, 1 (2015a).

W. Chen, J. Lou, and C. Zhu. Forcing switch from short-to intermediate-and long-lived states of the αA domain generates LFA-1/ICAM-1 catch bonds. *Journal of Biological Chemistry* **285**, 35967 (2010).

X. Chen, Z. Mao, and B. Chen. Probing time-dependent mechanical behaviors of catch bonds based on two-state models. *Scientific reports* **5**, 1 (2015b).

Y. Z. Chen and K. Y. Lee. Analysis of the M-Integral in Plane Elasticity. *Journal of Applied Mechanics* **71**, 572 (2004).

Y. Chen, H. Lee, H. Tong, M. Schwartz, and C. Zhu. Force regulated conformational change of integrin αVβ3. *Matrix biology* **60**, 70 (2017).

B. Cheng, M. Lin, Y. Li, G. Huang, H. Yang, G. M. Genin, V. S. Deshpande, T. J. Lu, and F. Xu. An integrated stochastic model of matrix-stiffness-dependent filopodial dynamics. *Biophysical Journal* **111**, 2051 (2016).

B. Cheng, W. Wan, G. Huang, Y. Li, G. M. Genin, M. R. Mofrad, T. J. Lu, F. Xu, and M. Lin. Nanoscale integrin cluster dynamics controls cellular mechanosensing via FAKY397 phosphorylation. *Science Advances* **6**, eaax1909 (2020).

C. K. Choi, M. Vicente-Manzanares, J. Zareno, L. A. Whitmore, A. Mogilner, and A. R. Horwitz. Actin and α -actinin orchestrate the assembly and maturation of nascent adhesions in a myosin II motor-independent manner. *Nature Cell Biology* **10** (2008). 10.1038/ncb1763.

D. Choquet, D. P. Felsenfeld, and M. P. Sheetz. Extracellular matrix rigidity causes strengthening of integrin–cytoskeleton linkages. *Cell* **88**, 39 (1997).

C. Chothia and E. Y. Jones. The molecular structure of cell adhesion molecules. *Annual review of biochemistry* **66**, 823 (1997).

R. Codina. On stabilized finite element methods for linear systems of convection–diffusion-reaction equations. *Computer Methods in Applied Mechanics and Engineering* **188**, 61 (2000).

G. P. Coló, P. Hernández-Varas, J. Lock, R. A. Bartolomé, N. Arellano-Sánchez, S. Strömblad, and J. Teixidó. Focal adhesion disassembly is regulated by a RIAM to MEK-1 pathway. *Journal of cell science* **125**, 5338 (2012).

B. Cortese, I. E. Palamà, S. D'Amone, and G. Gigli. Influence of electrotaxis on cell behaviour. *Integrative Biology (United Kingdom)* **6**, 817 (2014).

M. F. Coughlin and D. Stamenović. A prestressed cable network model of the adherent cell cytoskeleton. *Biophysical Journal* **84**, 1328 (2003).

E. M. Craig, J. Stricker, M. Gardel, and A. Mogilner. Model for adhesion clutch explains biphasic relationship between actin flow and traction at the cell leading edge. *Physical Biology* **12**, 035002 (2015).

D. Critchley. Biochemical and structural properties of the integrin-associated cytoskeletal protein talin. *Annual Review of Biophysics* **38**, 235 (2009). https://doi.org/10.1146/annurev.biophys.050708.133744 .

G. Cuda, E. Pate, R. Cooke, and J. R. Sellers. In vitro actin filament sliding velocities produced by mixtures of different types of myosin. *Biophysical Journal* **72**, 1767 (1997).

D. Cuvelier, M. Théry, Y. S. Chu, S. Dufour, J. P. Thiéry, M. Bornens, P. Nassoy, and L. Mahadevan. The Universal Dynamics of Cell Spreading. *Current Biology* **17**, 694 (2007).

A. Dai, F. Ye, D. Taylor, G. Hu, M. Ginsberg, and K. Taylor. The structure of a full-length membrane-embedded integrin bound to a physiological ligand. *The Journal of Biological Chemistry* **290** (2015).

G. Danuser, J. Allard, and A. Mogilner. Mathematical Modeling of Eukaryotic Cell Migration: Insights Beyond Experiments. *Annual Review of Cell and Developmental Biology* **29**, 501 (2013).

D. Dedden, S. Schumacher, C. F. Kelley, M. Zacharias, C. Biertümpfel, R. Fässler, and N. Mizuno. The architecture of talin1 reveals an autoinhibition mechanism. *Cell* **179**, 120 (2019).

A. del Rio, R. Perez-Jimenez, R. Liu, P. Roca-Cusachs, J. M. Fernandez, and M. P. Sheetz. Stretching single talin rod molecules activates vinculin binding. *Science* **323**, 638 (2009).

V. S. Deshpande, M. Mrksich, R. M. McMeeking, and A. G. Evans. A bio-mechanical model for coupling cell contractility with focal adhesion formation. *Journal of the Mechanics and Physics of Solids* **56**, 1484 (2008).

P. G. Detilleux, B. L. Deyoe, and N. F. Cheville. Penetration and intracellular growth of Brucella abortus in nonphagocytic cells in vitro. *Infection and immunity* **58**, 2320 (1990).

C. D. Devillard and C. A. Marquette. Vascular Tissue Engineering: Challenges and Requirements for an Ideal Large Scale Blood Vessel. *Frontiers in Bioengineering and Biotechnology* **9** (2021). 10.3389/fbioe.2021.721843.

C. Diaz, S. Neubauer, F. Rechenmacher, H. Kessler, and D. Missirlis. Recruitment of $\alpha v\beta 3$ integrin to $\alpha 5\beta 1$ integrin-induced clusters enables focal adhesion maturation and cell spreading. *Journal of cell science* **133**, jcs232702 (2020).

A. Diz-Muñoz, D. A. Fletcher, and O. D. Weiner. Use the force: Membrane tension as an organizer of cell shape and motility. *Trends in Cell Biology* **23**, 47 (2013).

R. S. D'Souza, J. Y. Lim, A. Turgut, K. Servage, J. Zhang, K. Orth, N. G. Sosale, M. J. Lazzara, J. Allegood, and J. E. Casanova. Calcium-stimulated disassembly of focal adhesions mediated by an ORP3/IQSec1 complex. *Elife* **9**, e54113 (2020).

B. J. Dubin-Thaler, J. M. Hofman, Y. Cai, H. Xenias, I. Spielman, A. V. Shneidman, L. A. David, H. G. Döbereiner, C. H. Wiggins, and M. P. Sheetz. Quantification of cell edge velocities and traction forces reveals distinct motility modules during cell spreading. *PLoS ONE* **3** (2008). 10.1371/journal.pone.0003735.

B. J. DuChez, A. D. Doyle, E. K. Dimitriadis, and K. M. Yamada. Durotaxis by Human Cancer Cells. *Biophysical Journal* **116**, 670 (2019).

L. Edelstein-Keshet, W. R. Holmes, M. Zajac, and M. Dutot. From simple to detailed models for cell polarization. *Philosophical Transactions of the Royal Society B: Biological Sciences* **368** (2013). 10.1098/rstb.2013.0003.

A. Elosegui-Artola, E. Bazellières, M. Allen, I. Andreu, R. Oria, R. Sunyer, J. Gomm, J. Marshall, L. J. Jones, X. Trepat, and P. Roca-Cusachs. Rigidity sensing and adaptation through regulation of integrin types. *Nature Materials* **13**, 631 (2014).

A. Elosegui-Artola, R. Oria, Y. Chen, A. Kosmalska, and C. Pérez-González. Mechanical regulation of a molecular clutch defines force transmission and transduction in response to matrix rigidity. *Nature Cell Biology* **18**, 540 (2016).

A. Elosegui-Artola, X. Trepat, and P. Roca-Cusachs. Control of mechanotransduction by molecular clutch dynamics. *Trends in Cell Biology* **28**, 356 (2018).

A. Elosegui-Artola, I. Andreu, A. E. Beedle, A. Lezamiz, M. Uroz, A. J. Kosmalska, R. Oria, J. Z. Kechagia, P. Rico-Lastres, A. L. Le Roux, C. M. Shanahan, X. Trepat, D. Navajas, S. Garcia-Manyes, and P. Roca-Cusachs. Force Triggers YAP Nuclear Entry by Regulating Transport across Nuclear Pores. *Cell* **171**, 1397 (2017).

E. Eng, B. Smagghe, T. Walz, and T. Springer. Intact $\alpha_{IIb}\beta_3$ integrin is extended after activation as measured by solution X-ray scattering and electron microscopy. *The Journal of Biological Chemistry* **286**, 35218 (2011).

A. J. Engler, S. Sen, H. L. Sweeney, and D. E. Discher. Matrix elasticity directs stem cell lineage specification. *Cell* **126**, 677 (2006).

T. Erdmann and U. S. Schwarz. Stochastic dynamics of adhesion clusters under shared constant force and with rebinding. *The Journal of Chemical Physics* **121**, 8997 (2004). https://doi.org/10.1063/1.1805496 .

H. P. Erickson, N. Carrell, and J. McDonagh. Fibronectin molecule visualized in electron microscopy: a long, thin, flexible strand. *The Journal of Cell Biology* **91**, 673 (1981).

J. A. Espina, C. L. Marchant, and E. H. Barriga. Durotaxis: the mechanical control of directed cell migration. *FEBS Journal* (2021). 10.1111/febs.15862.

S. Etienne-Manneville and A. Hall. Integrin-mediated activation of Cdc42 controls cell polarity in migrating astrocytes through PKCζ. *Cell* **106**, 489 (2001).

A. Etzioni. Adhesion molecules-their role in health and disease. *Pediatric Research* **39**, 191 (1996).

E. Evans. Probing the relation between force, lifetime and chemistry in single molecular bonds. *Annual Review of Biophysics and Biomolecular Structure* **30**, 105 (2001).

E. A. Evans and K. Ritchie. Dynamic strength of molecular adhesion bonds. *Biophysical Journal* **72**, 1541 (1997).

E. B. Evans, S. W. Brady, A. Tripathi, and D. Hoffman-Kim. Schwann cell durotaxis can be guided by physiologically relevant stiffness gradients. *Biomaterials Research* **22**, 1 (2018).

R. D. Fields. Cell adhesion molecules: Implications for neurological disease. *The Neuroscientist* **4**, 4 (1998).

L. a. Flanagan, Y.-E. Ju, B. Marg, M. Osterfield, and P. a. Janmey. Neurite branching on deformable substrates. *Neuroreport* **13**, 2411 (2002). arXiv:NIHMS150003 .

M. J. Footer, J. W. Kerssemakers, J. A. Theriot, and M. Dogterom. Direct measurement of force generation by actin filament polymerization using an optical trap. *Proceedings of the National Academy of Sciences of the United States of America* **104**, 2181 (2007).

J. Fouchard, C. Bimbard, N. Bufi, P. Durand-Smet, A. Proag, A. Richert, O. Cardoso, and A. Asnacios. Three-dimensional cell body shape dictates the onset of traction force generation and growth of focal adhesions. *Proceedings of the National Academy of Sciences of the United States of America* **111**, 13075 (2014).

P. Friedl and D. Gilmour. Collective cell migration in morphogenesis, regeneration and cancer. *Nature reviews. Molecular cell biology* **10**, 445 (2009a).

P. Friedl and D. Gilmour. Collective cell migration in morphogenesis, regeneration and cancer. *Nature Reviews Molecular Cell Biology* **10**, 445 (2009b).

P. Friedl and K. Wolf. Tumour-cell invasion and migration: diversity and escape mechanisms. *Nature Reviews Cancer* **3**, 362 (2003).

M. Fukata, M. Nakagawa, and K. Kaibuchi. Roles of Rho-family GTPases in cell polarisation and directional migration. *Current Opinion in Cell Biology* **15**, 590 (2003).

K. Galior, Y. Liu, K. Yehl, S. Vivek, and K. Salaita. Titin-based nanoparticle tension sensors map high-magnitude integrin forces within focal adhesions. *Nano letters* **16**, 341 (2016).

H. Gao, J. Qian, and B. Chen. Probing mechanical principles of focal contacts in cell-matrix adhesion with a coupled stochastic-elastic modelling framework. *Journal of the Royal Society Interface* **8**, 1217 (2011).

N. C. Gauthier, M. A. Fardin, P. Roca-Cusachs, and M. P. Sheetz. Temporary increase in plasma membrane tension coordinates the activation of exocytosis and contraction during cell spreading. *Proceedings of the National Academy of Sciences of the United States of America* **108**, 14467 (2011).

N. C. Gauthier, T. A. Masters, and M. P. Sheetz. Mechanical feedback between membrane tension and dynamics. *Trends in Cell Biology* **22**, 527 (2012).

B. Geiger, J. P. Spatz, and A. D. Bershadsky. Environmental sensing through focal adhesions. *Nature Reviews Molecular Cell Biology* **10**, 21 (2009).

B. Geiger, A. Bershadsky, R. Pankov, and K. M. Yamada. Transmembrane crosstalk between the extracellular matrix and the cytoskeleton. *Nature reviews Molecular cell biology* **2**, 793 (2001).

M. Ghibaudo, A. Saez, L. Trichet, A. Xayaphoummine, J. Browaeys, P. Silberzan, A. Buguin, and B. Ladoux. Traction forces and rigidity sensing regulate cell functions. *Soft Matter* **4**, 1836 (2008).

M. Ghosh, X. Song, G. Mouneimne, M. Sidani, D. S. Lawrence, and J. S. Condeelis. Cofilin promotes actin polymerization and defines the direction of cell motility. *Science (New York, N.Y.)* **304**, 743 (2004).

G. Giannone, R. M. Mège, and O. Thoumine. Multi-level molecular clutches in motile cell processes. *Trends in Cell Biology* **19**, 475 (2009).

D. T. Gillespie. A general method for numerically simulating the stochastic time evolution of coupled chemical reactions. *Journal of computational physics* **22**, 403 (1976).

D. T. Gillespie. Exact stochastic simulation of coupled chemical reactions. *The journal of physical chemistry* **81**, 2340 (1977).

D. T. Gillespie. Stochastic simulation of chemical kinetics. *Annu. Rev. Phys. Chem.* **58**, 35 (2007).

A. R. Gingras, N. Bate, B. T. Goult, L. Hazelwood, I. Canestrelli, J. G. Grossmann, H. Liu, N. S. Putz, G. C. Roberts, N. Volkmann, *et al.*. The structure of the C-terminal actin-binding domain of talin. *The EMBO journal* **27**, 458 (2008).

A. R. Gingras, W. H. Ziegler, A. A. Bobkov, M. G. Joyce, D. Fasci, M. Himmel, S. Rothemund, A. Ritter, J. G. Grossmann, B. Patel, *et al.*. Structural determinants of integrin binding to the talin rod. *Journal of Biological Chemistry* **284**, 8866 (2009).

A. R. Gingras, W. H. Ziegler, R. Frank, I. L. Barsukov, G. C. Roberts, D. R. Critchley, and J. Emsley. Mapping and consensus sequence identification for multiple vinculin binding sites within the talin rod. *Journal of Biological Chemistry* **280**, 37217 (2005).

S. L. Goodman, G. Risse, and K. von der Mark. The E8 subfragment of laminin promotes locomotion of myoblasts over extracellular matrix. *Journal of Cell Biology* **109**, 799 (1989).

R. E. Gough and B. T. Goult. The tale of two talins–two isoforms to fine-tune integrin signalling. *FEBS letters* **592**, 2108 (2018).

B. T. Goult, X.-P. Xu, A. R. Gingras, M. F. Swift, B. Patel, N. Bate, P. M. Kopp, I. L. Barsukov, D. R. Critchley, N. Volkmann, and D. Hanein. Structural studies on full-length talin1 reveal a compact auto-inhibited dimer: implications for talin activation. *Journal of Structural Biology* **184 1**, 21 (2013a).

B. T. Goult, J. Yan, and M. A. Schwartz. Talin as a mechanosensitive signaling hub. *Journal of Cell Biology* **217**, 3776 (2018). https://rupress.org/jcb/article-pdf/217/11/3776/1377357/jcb_201808061.pdf .

B. T. Goult, T. Zacharchenko, N. Bate, R. Tsang, F. Hey, A. R. Gingras, P. R. Elliott, G. C. Roberts, C. Ballestrem, D. R. Critchley, *et al.*. RIAM and vinculin binding to talin are mutually exclusive and regulate adhesion assembly and turnover. *Journal of Biological Chemistry* **288**, 8238 (2013b).

C. Grashoff, B. D. Hoffman, M. D. Brenner, R. Zhou, M. Parsons, M. T. Yang, M. A. McLean, S. G. Sligar, C. S. Chen, T. Ha, and M. A. Schwartz. Measuring mechanical tension across vinculin reveals regulation of focal adhesion dynamics. *Nature* **466**, 263 (2010).

C. Guillot and T. Lecuit. Mechanics of epithelial tissue homeostasis and morphogenesis. *Science* **340**, 1185 (2013).

B. M. Gumbiner. Cell adhesion: the molecular basis of tissue architecture and morphogenesis. *Cell* **84**, 345 (1996).

B. Guo and W. Guilford. Mechanics of actomyosin bonds in different nucleotide states are tuned to muscle contraction. *Proceedings of the National Academy of Sciences of the United States of America* **103**, 9844 (2006).

M. Guthold, W. Liu, E. Sparks, L. Jawerth, L. Peng, M. Falvo, R. Superfine, R. Hantgan, and S. Lord. A comparison of the mechanical and structural properties of fibrin fibers with other protein fibers. *Cell Biochemistry and Biophysics* **49**, 165 (2007).

W. J. Hadden, J. L. Young, A. W. Holle, M. L. McFetridge, D. Y. Kim, P. Wijesinghe, H. Taylor-Weiner, J. H. Wen, A. R. Lee, K. Bieback, B. N. Vo, D. D. Sampson, B. F. Kennedy, J. P. Spatz, A. J. Engler, and Y. S. Cho. Stem cell migration and mechanotransduction on linear stiffness gradient hydrogels. *Proceedings of the National Academy of Sciences of the United States of America* **114**, 5647 (2017).

S. J. Han, K. S. Bielawski, L. H. Ting, M. L. Rodriguez, and N. J. Sniadecki. Decoupling substrate stiffness, spread area, and micropost density: A close spatial relationship between traction forces and focal adhesions. *Biophysical Journal* **103**, 640 (2012).

B. Henning Stumpf, A. Ambriović-Ristov, A. Radenovic, and A.-S. Smith. Recent advances and prospects in the research of nascent adhesions. *Frontiers in Physiology* , 1562 (2020).

J. H. Hetmanski, H. de Belly, I. Busnelli, T. Waring, R. V. Nair, V. Sokleva, O. Dobre, A. Cameron, N. Gauthier, C. Lamaze, J. Swift, A. del Campo, T. Starborg, T. Zech, J. G. Goetz, E. K. Paluch, J. M. Schwartz, and P. T. Caswell. Membrane Tension Orchestrates Rear Retraction in Matrix-Directed Cell Migration. *Developmental Cell* **51**, 460 (2019).

R. J. Hickey and A. E. Pelling. Cellulose Biomaterials for Tissue Engineering. *Frontiers in Bioengineering and Biotechnology* **7** (2019). 10.3389/fbioe.2019.00045.

G. S. Hillis and A. D. Flapan. Cell adhesion molecules in cardiovascular disease: a clinical perspective. *Heart* **79**, 429 (1998).

H. Hirata, M. Sokabe, and C. T. Lim. Molecular mechanisms underlying the force-dependent regulation of actin-to-ECM linkage at the focal adhesions. *Progress in Molecular Biology and Translational Science* **126**, 135 (2014a).

H. Hirata, H. Tatsumi, C. T. Lim, and M. Sokabe. Force-dependent vinculin binding to talin in live cells: a crucial step in anchoring the actin cytoskeleton to focal adhesions. *American Journal of Physiology-Cell Physiology* **306**, C607 (2014b).

H. Honda, H. Nagashima, and S. Asakura. Directional movement of F-actin in vitro. *Journal of Molecular Biology* **191**, 131 (1986).

U. Horzum, B. Ozdil, and D. Pesen-Okvur. Step-by-step quantitative analysis of focal adhesions. *MethodsX* **1**, 56 (2014).

P. Hotulainen and P. Lappalainen. Stress fibers are generated by two distinct actin assembly mechanisms in motile cells. *The Journal of cell biology* **173**, 383 (2006).

A. R. Houk, A. Jilkine, C. O. Mejean, R. Boltyanskiy, E. R. Dufresne, S. B. Angenent, S. J. Altschuler, L. F. Wu, and O. D. Weiner. Membrane tension maintains cell polarity by confining signals to the leading edge during neutrophil migration. *Cell* **148**, 175 (2012).

K. Hu, L. Ji, K. T. Applegate, G. Danuser, and C. M. Waterman-Storer. Differential transmission of actin motion within focal adhesions. *Science* **315**, 111 (2007).

X. Hu, C. Jing, X. Xu, N. Nakazawa, V. W. Cornish, F. M. Margadant, and M. P. Sheetz. Cooperative vinculin binding to talin mapped by time-resolved super resolution microscopy. *Nano Letters* **16**, 4062 (2016).

D. L. Huang, N. A. Bax, C. D. Buckley, W. I. Weis, and A. R. Dunn. Vinculin forms a directionally asymmetric catch bond with F-actin. *Science* **357**, 703 (2017).

A. Huttenlocher. Cell polarization mechanisms during directed cell migration. *Nature Cell Biology* **7**, 336 (2005).

N. Ibata and E. M. Terentjev. Development of nascent focal adhesions in spreading cells. *Biophysical journal* **119**, 2063 (2020).

B. C. Isenberg, P. A. DiMilla, M. Walker, S. Kim, and J. Y. Wong. Vascular smooth muscle cell durotaxis depends on substrate stiffness gradient strength. *Biophysical Journal* **97**, 1313 (2009).

A. Isomursu, K.-Y. Park, J. Hou, C. Bo, G. Shamsan, B. Fuller, J. Kasim, M. M. Mahmoodi, T. J. Lu, G. M. Genin, *et al.*. Negative durotaxis: cell movement toward softer environments. *BioRxiv* (2020).

D. V. Iwamoto and D. A. Calderwood. Regulation of integrin-mediated adhesions. *Current opinion in cell biology* **36**, 41 (2015).

M. Janiszewska, M. C. Primi, and T. Izard. Cell adhesion in cancer: Beyond the migration of single cells. *Journal of Biological Chemistry* **295**, 2495 (2020).

Jean Donea and A. Huerta. *Finite Element Methods for Flow Problems* (Wiley, 2003) p. 362.

G. Jiang, G. Giannone, D. R. Critchley, E. Fukumoto, and M. P. Sheetz. Two-piconewton slip bond between fibronectin and the cytoskeleton depends on talin. *Nature* **424**, 334 (2003).

D. Joaquin, M. Grigola, G. Kwon, C. Blasius, Y. Han, D. Perlitz, J. Jiang, Y. Ziegler, A. Nardulli, and K. J. Hsia. Cell migration and organization in three-dimensional in vitro culture driven by stiffness gradient. *Biotechnology and Bioengineering* **113**, 2496 (2016).

A. M. Johansen, L. Evers, and N. Whiteley. Monte carlo methods. *Lecture notes* **200** (2010).

P. Kanchanawong, G. Shtengel, A. M. Pasapera, E. B. Ramko, M. W. Davidson, H. F. Hess, and C. M. Waterman. Nanoscale architecture of integrin-based cell adhesions. *Nature* **468**, 580 (2010).

E. Kassianidou and S. Kumar. A biomechanical perspective on stress fiber structure and function. *Biochimica et Biophysica Acta (BBA)-Molecular Cell Research* **1853**, 3065 (2015).

A. Katsumi, J. Milanini, W. B. Kiosses, M. A. Del Pozo, R. Kaunas, S. Chien, K. M. Hahn, and M. A. Schwartz. Effects of cell tension on the small GTPase Rac. *Journal of Cell Biology* **158**, 153 (2002).

T. Kawano and S. Kidoaki. Elasticity boundary conditions required for cell mechanotaxis on microelastically-patterned gels. *Biomaterials* **32**, 2725 (2011).

R. R. Kay, P. Langridge, D. Traynor, and O. Hoeller. Changing directions in the study of chemotaxis. *Nature Reviews Molecular Cell Biology* **9**, 455 (2008).

J. Z. Kechagia, J. Ivaska, and P. Roca-Cusachs. Integrins as biomechanical sensors of the microenvironment. *Nature Reviews Molecular Cell Biology* **20**, 457 (2019).

K. Keren. Cell motility : the integrating role of the plasma membrane. *Eur Biophys J* **40**, 1013 (2011).

K. Keren, Z. Pincus, G. M. Allen, E. L. Barnhart, G. Marriott, A. Mogilner, and J. A. Theriot. Mechanism of shape determination in motile cells. *Nature* **453**, 475 (2008).

B. Klapholz and N. H. Brown. Talin–the master of integrin adhesions. *Journal of cell science* **130**, 2435 (2017).

B. Klapholz, S. L. Herbert, J. Wellmann, R. Johnson, M. Parsons, and N. H. Brown. Alternative mechanisms for talin to mediate integrin function. *Current biology* **25**, 847 (2015).

E. Klotzsch, M. L. Smith, K. E. Kubow, S. Muntwyler, W. C. Little, F. Beyeler, D. Gourdon, B. J. Nelson, and V. Vogel. Fibronectin forms the most extensible biological fibers displaying switchable force-exposed cryptic binding sites. *Proceedings of the National Academy of Sciences* **106**, 18267 (2009).

G. H. Koenderink and E. K. Paluch. Architecture shapes contractility in actomyosin networks. *Current opinion in cell biology* **50**, 79 (2018).

K. S. Kollepara, P. D. Mulye, and P. Saez. Fully coupled numerical model of actin treadmilling in the lamellipodium of the cell. *International Journal for Numerical Methods in Biomedical Engineering* **34**, 1 (2018).

F. Kong, Z. Li, W. M. Parks, D. Dumbauld, A. García, A. Mould, M. Humphries, and C. Zhu. Cyclic mechanical reinforcement of integrin-ligand interactions. *Molecular Cell* **49**, 1176 (2013).

F. Kong, A. J. García, A. P. Mould, M. J. Humphries, and C. Zhu. Demonstration of catch bonds between an integrin and its ligand. *Journal of Cell Biology* **185**, 1275 (2009).

D. E. Koser, A. J. Thompson, S. K. Foster, A. Dwivedy, E. K. Pillai, G. K. Sheridan, H. Svoboda, M. Viana, L. da F Costa, J. Guck, *et al.*. Mechanosensing is critical for axon growth in the developing brain. *Nature neuroscience* **19**, 1592 (2016).

C. Kothapalli, G. Mahajan, and K. Farrell. Substrate stiffness induced mechanotransduction regulates temporal evolution of human fetal neural progenitor cell phenotype, differentiation, and biomechanics. *Biomaterials science* **8**, 5452 (2020).

M. Kovacs, F. Wang, A. Hu, Y. Zhang, and J. R. Sellers. Functional divergence of human cytoplasmic myosin II: kinetic characterization of the non-muscle IIA isoform. *Journal of Biological Chemistry* **278**, 38132 (2003).

M. M. Kozlov and A. Mogilner. Model of polarization and bistability of cell fragments. *Biophysical Journal* **93**, 3811 (2007).

D. P. Kroese, T. Brereton, T. Taimre, and Z. I. Botev. Why the Monte Carlo method is so important today. *Wiley Interdisciplinary Reviews: Computational Statistics* **6**, 386 (2014).

S. J. Kron and J. A. Spudich. Fluorescent actin filaments move on myosin fixed to a glass surface. *Proceedings of the National Academy of Sciences of the United States of America* **83**, 6272 (1986).

A. Kumar, M. Ouyang, K. Van den Dries, E. J. McGhee, K. Tanaka, M. D. Anderson, A. Groisman, B. T. Goult, K. I. Anderson, and M. A. Schwartz. Talin tension sensor reveals novel features of focal adhesion force transmission and mechanosensitivity. *Journal of Cell Biology* **213**, 371 (2016).

B. Ladoux and R. M. Mège. Mechanobiology of collective cell behaviours. *Nature Reviews Molecular Cell Biology* **18**, 743 (2017).

K. Lam Hui, C. Wang, B. Grooman, J. Wayt, and A. Upadhyaya. Membrane dynamics correlate with formation of signaling clusters during cell spreading. *Biophysical Journal* **102**, 1524 (2012).

R. Langer and D. A. Tirrell. Designing materials for biology and medicine. *Nature* **428**, 487 (2004).

K. Larripa and A. Mogilner. Transport of a 1D viscoelastic actin-myosin strip of gel as a model of a crawling cell. *Physica A: Statistical Mechanics and its Applications* **372**, 113 (2006).

H.-S. Lee, P. Anekal, C. J. Lim, C.-C. Liu, and M. H. Ginsberg. Two modes of integrin activation form a binary molecular switch in adhesion maturation. *Molecular biology of the cell* **24**, 1354 (2013).

S. E. Lee, R. D. Kamm, and M. R. Mofrad. Force-induced activation of talin and its possible role in focal adhesion mechanotransduction. *Journal of biomechanics* **40**, 2096 (2007).

J. I. Lehtimäki, E. K. Rajakylä, S. Tojkander, and P. Lappalainen. Generation of stress fibers through myosin-driven reorganization of the actin cortex. *Elife* **10**, e60710 (2021).

E. C. Lessey, C. Guilluy, and K. Burridge. From mechanical force to RhoA activation. *Biochemistry* **51**, 7420 (2012).

G. Letort, H. Ennomani, L. Gressin, M. Théry, and L. Blanchoin. Dynamic reorganization of the actin cytoskeleton. *F1000Research* **4** (2015).

D. J. Lew. Formin' actin filament bundles. *Nature Cell Biology* **4**, E29 (2002).

J. Li and T. A. Springer. Integrin extension enables ultrasensitive regulation by cytoskeletal force. *Proceedings of the National Academy of Sciences* **114**, 4685 (2017).

J. Li, D. Han, and Y. P. Zhao. Kinetic behaviour of the cells touching substrate: The interfacial stiffness guides cell spreading. *Scientific Reports* **4**, 1 (2014).

Z. Li, F. Kong, and C. Zhu. A model for cyclic mechanical reinforcement. *Scientific reports* **6**, 1 (2016).

C. Lin, E. Espreafico, M. Mooseker, and P. Forscher. Myosin Drives Retrograde F-Actin Flow in Neuronal Growth Cones. *Neuron* **16**, 769 (1996).

J. Liu, Y. Wang, W. I. Goh, H. Goh, M. A. Baird, S. Ruehland, S. Teo, N. Bate, D. R. Critchley, M. W. Davidson, and P. Kanchanawong. Talin determines the nanoscale architecture of focal adhesions. *Proceedings of the National Academy of Sciences* **112**, E4864 (2015a).

Y. J. Liu, M. Le Berre, F. Lautenschlaeger, P. Maiuri, A. Callan-Jones, M. Heuzé, T. Takaki, R. Voituriez, and M. Piel. Confinement and low adhesion induce fast amoeboid migration of slow mesenchymal cells. *Cell* **160**, 659 (2015b). arXiv:1407.3510 .

C. M. Lo, H. B. Wang, M. Dembo, and Y. L. Wang. Cell movement is guided by the rigidity of the substrate. *Biophysical journal* **79**, 144 (2000). arXiv:NIHMS150003 .

M. Lotfi, M. Nejib, and M. Naceur. Cell Adhesion to Biomaterials: Concept of Biocompatibility. in *Advances in Biomaterials Science and Biomedical Applications*. edited by R. Pignatello (IntechOpen, Rijeka, 2013) Chap. 8.

M. MacHacek, L. Hodgson, C. Welch, H. Elliott, O. Pertz, P. Nalbant, A. Abell, G. L. Johnson, K. M. Hahn, and G. Danuser. Coordination of Rho GTPase activities during cell protrusion. *Nature* **461**, 99 (2009).

S. G. Martin. Spontaneous cell polarization: Feedback control of Cdc42 GTPase breaks cellular symmetry. *BioEssays* **37**, 1193 (2015).

R. Mayor and S. Etienne-Manneville. The front and rear of collective cell migration. *Nature Publishing Group* **17**, 97 (2016).

C. D. McCaig, A. M. Rajnicek, B. Song, and M. Zhao. Controlling cell behavior electrically: current views and future potential. *Physiological reviews* **85**, 943 (2005).

A. J. McKenzie, S. R. Hicks, K. V. Svec, H. Naughton, Z. L. Edmunds, and A. K. Howe. The mechanical microenvironment regulates ovarian cancer cell morphology, migration, and spheroid disaggregation. *Scientific Reports* **8**, 1 (2018).

N. Metropolis and S. Ulam. The monte carlo method. *Journal of the American statistical association* **44**, 335 (1949).

T. J. Mitchison and L. P. Cramer. Actin-based cell motility and cell locomotion. (1996).

T. Mitchison and M. Kirschner. Cytoskeletal dynamics and nerve growth. *Neuron* **1**, 761 (1988).

A. Mogilner. Mechanics of motor proteins and the cytoskeleton. *Physics Today* **55**, 63 (2002).

A. Mogilner. Mathematics of cell motility: Have we got its number? *Journal of Mathematical Biology* **58**, 105 (2009).

A. Mogilner and A. Manhart. Intracellular Fluid Mechanics: Coupling Cytoplasmic Flow with Active Cytoskeletal Gel. *Annual Review of Fluid Mechanics* **50**, 347 (2018).

A. Mogilner and G. Oster. Force generation by actin polymerization II: The elastic ratchet and tethered filaments. *Biophysical Journal* **84**, 1591 (2003).

J. Molloy, J. Burns, J. Kendrick-Jones, R. Tregear, and D. White. Movement and force produced by a single myosin head. *Nature* **378**, 209 (1995).

Y. Mori, A. Jilkine, and L. Edelstein-Keshet. Wave-pinning and cell polarity from a bistable reaction-diffusion system. *Biophysical Journal* **94**, 3684 (2008).

M. Morimatsu, A. H. Mekhdjian, A. S. Adhikari, and A. R. Dunn. Molecular tension sensors report forces generated by single integrin molecules in living cells. *Nano Letters* **13**, 3985 (2013).

M. Morimatsu, A. H. Mekhdjian, A. C. Chang, S. J. Tan, and A. R. Dunn. Visualizing the interior architecture of focal adhesions with high-resolution traction maps. *Nano letters* **15**, 2220 (2015).

M. Murrell, P. W. Oakes, M. Lenz, and M. L. Gardel. Forcing cells into shape: the mechanics of actomyosin contractility. *Nature reviews Molecular cell biology* **16**, 486 (2015).

M. Nagano, D. Hoshino, N. Koshikawa, T. Akizawa, and M. Seiki. Turnover of focal adhesions and cancer cell migration. *International journal of cell biology* **2012** (2012).

J. Neumann and K.-E. Gottschalk. The integrin–talin complex under force. *Protein Engineering, Design and Selection* **29**, 503 (2016).

R. Niederman and T. D. Pollard. Human platelet myosin II. In vitro assembly and structure of myosin filaments. *The Journal of Cell Biology* **67**, 72 (1975).

E. A. Novikova, M. Raab, D. E. Discher, and C. Storm. Persistence-Driven Durotaxis: Generic, Directed Motility in Rigidity Gradients. *Physical Review Letters* **118**, 1 (2017). arXiv:1512.06024 .

A. F. Oberhauser, C. Badilla-Fernandez, M. Carrion-Vazquez, and J. M. Fernandez. The mechanical hierarchies of fibronectin observed with single-molecule AFM. *Journal of molecular biology* **319**, 433 (2002).

C. B. O'Connell, M. J. Tyska, and M. S. Mooseker. Myosin at work: motor adaptations for a variety of cellular functions. *Biochimica et Biophysica Acta (BBA) - Molecular Cell Research* **1773**, 615 (2007).

R. Oria, T. Wiegand, J. Escribano, A. Elosegui-Artola, J. Uriarte, C. Moreno-Pulido, I. Platzman, P. Delcanale, L. Albertazzi, D. Navajas, X. Trepat, J. Garcia-Aznar, E. Cavalcanti-Adam, and P. Roca-Cusachs. Force loading explains spatial sensing of ligands by cells. *Nature* **552** (2017).

D. Pantaloni, C. Le Clainche, and M. F. Carlier. Mechanism of actin-based motility. *Science* **292**, 1502 (2001).

J. T. Parsons, A. R. Horwitz, and M. A. Schwartz. Cell adhesion: integrating cytoskeletal dynamics and cellular tension. *Nature reviews Molecular cell biology* **11**, 633 (2010).

A. Pathak, V. S. Deshpande, R. M. McMeeking, and A. G. Evans. The simulation of stress fibre and focal adhesion development in cells on patterned substrates. *Journal of The Royal Society Interface* **5**, 507 (2008).

M. D. Pato, J. R. Sellers, Y. A. Preston, E. V. Harvey, and A. R. S.. Baculovirus expression of chicken nonmuscle heavy meromyosin II-B. Characterization of alternatively spliced isoforms. *Journal of Biological Chemistry* **271**, 2689 (1996).

R. Paul, P. Heil, J. P. Spatz, and U. S. Schwarz. Propagation of mechanical stress through the actin cytoskeleton toward focal adhesions: model and experiment. *Biophysical Journal* **94**, 1470 (2008).

R. J. Pelham and Y. L. Wang. Cell locomotion and focal adhesions are regulated by substrate flexibility. *Proceedings of the National Academy of Sciences of the United States of America* **94**, 13661 (1997).

S. Pellegrin and H. Mellor. Actin stress fibres. *Journal of Cell Science* **120**, 3491 (2007).

Y. V. Pereverzev, O. V. Prezhdo, M. Forero, E. V. Sokurenko, and W. E. Thomas. The two-pathway model for the catch-slip transition in biological adhesion. *Biophysical journal* **89**, 1446 (2005).

S. V. Plotnikov, A. M. Pasapera, B. Sabass, and C. M. Waterman. Force fluctuations within focal adhesions mediate ECM-rigidity sensing to guide directed cell migration. *Cell* **151**, 1513 (2012).

T. D. Pollard and J. A. Cooper. Actin, a Central Player in Cell Shape and Movement. *Science (New York, N.Y.)* **326**, 1208 (2009a).

T. D. Pollard. Actin and actin-binding proteins. *Cold Spring Harbor Perspectives in Biology* **8** (2016). 10.1101/cshperspect.a018226.

T. D. Pollard, L. Blanchoin, and R. D. Mullins. Molecular mechanisms controlling actin filament dynamics in nonmuscle cells. *Annu. Rev. Biophys. Biomol. Struct.* **29**, 545 (2000).

T. D. Pollard and G. G. Borisy. Cellular motility driven by assembly and disassembly of actin filaments. (2003).

T. D. Pollard and J. A. Cooper. Actin, a central player in cell shape and movement. *Science (New York, N.Y.)* **326**, 1208 (2009b).

B. Pontes, P. Monzo, L. Gole, A. L. Le Roux, A. J. Kosmalska, Z. Y. Tam, W. Luo, S. Kan, V. Viasnoff, P. Roca-Cusachs, L. Tucker-Kellogg, and N. C. Gauthier. Membrane tension controls adhesion positioning at the leading edge of cells. *Journal of Cell Biology* **216**, 2959 (2017).

A. Ponti, M. Machacek, S. L. Gupton, C. M. Waterman-Storer, and G. Danuser. Two Distinct Actin Networks Drive the Protrusion of Migrating Cells. *Science* **305**, 1782 (2004a). arXiv:1002.1037 .

A. Ponti, M. Machacek, S. L. Gupton, C. M. Waterman-Storer, and G. Danuser. Two Distinct Actin Networks Drive the Protrusion of Migrating Cells. *Science* **305**, 1782 (2004b). arXiv:1002.1037 .

G. Popescu, T. Ikeda, K. Goda, C. A. Best-Popescu, M. Laposata, S. Manley, R. R. Dasari, K. Badizadegan, and M. S. Feld. Optical measurement of cell membrane tension. *Physical Review Letters* **97**, 1 (2006).

J. Prost, F. Jülicher, and J. F. Joanny. Active gel physics. *Nature Physics* **11**, 111 (2015).

T. Putelat, P. Recho, and L. Truskinovsky. Mechanical stress as a regulator of cell motility. *Physical Review E* **97**, 1 (2018). arXiv:1801.07477 .

J. Qian and H. Gao. Soft matrices suppress cooperative behaviors among receptor-ligand bonds in cell adhesion. *PLoS ONE* **5** (2010). 10.1371/journal.pone.0012342.

M. Raab, J. Swift, P. C. P. Dingal, P. Shah, J. W. Shin, and D. E. Discher. Crawling from soft to stiff matrix polarizes the cytoskeleton and phosphoregulates myosin-II heavy chain. *Journal of Cell Biology* **199**, 669 (2012).

R. Rahikainen, T. Öhman, P. Turkki, M. Varjosalo, and V. P. Hytönen. Talin-mediated force transmission and talin rod domain unfolding independently regulate adhesion signaling. *Journal of cell science* **132**, jcs226514 (2019).

D. Raucher and M. P. Sheetz. Cell spreading and lamellipodial extension rate is regulated by membrane tension. *Journal of Cell Biology* **148**, 127 (2000).

D. Raz-Ben Aroush, N. Ofer, E. Abu-Shah, J. Allard, O. Krichevsky, A. Mogilner, and K. Keren. Actin Turnover in Lamellipodial Fragments. *Current Biology* **27**, 2963 (2017).

X.-D. Ren, W. B. Kiosses, D. J. Sieg, C. A. Otey, D. D. Schlaepfer, and M. A. Schwartz. Focal adhesion kinase suppresses Rho activity to promote focal adhesion turnover. *Journal of cell science* **113**, 3673 (2000).

A. J. Ridley. Rho GTPases and cell migration. *Journal of Cell Science* **114**, 2713 (2001).

A. J. Ridley. Rho GTPase signalling in cell migration. *Current Opinion in Cell Biology* **36**, 103 (2015).

A. J. Ridley, M. A. Schwartz, K. Burridge, R. A. Firtel, M. H. Ginsberg, G. Borisy, J. T. Parsons, and A. R. Horwitz. Cell Migration: Integrating Signals from Front to Back. *Science (New York, N.Y.)* **302**, 1704 (2003).

D. Riveline, E. Zamir, N. Q. Balaban, U. S. Schwarz, T. Ishizaki, S. Narumiya, Z. Kam, B. Geiger, and A. D. Bershadsky. Focal contacts as mechanosensors: externally applied local mechanical force induces growth of focal contacts by an Mdia1-dependent and Rock-independent mechanism. *Journal of Cell Biology* **153**, 1175 (2001).

P. Roca-Cusachs, N. C. Gauthier, A. Del Rio, and M. P. Sheetz. Clustering of $\alpha 5 \beta 1$ integrins determines adhesion strength whereas $\alpha v \beta 3$ and talin enable mechanotransduction. *Proceedings of the National Academy of Sciences* **106**, 16245 (2009).

W. Ronan, V. S. Deshpande, R. M. McMeeking, and J. P. McGarry. Cellular contractility and substrate elasticity: A numerical investigation of the actin cytoskeleton and cell adhesion. *Biomechanics and Modeling in Mechanobiology* **13**, 417 (2014).

K. A. Rosowski, R. Boltyanskiy, Y. Xiang, and K. V. D. Dries. Vinculin and the mechanical response of adherent fibroblasts to matrix deformation. *Scientific Reports* , 1 (2018).

O. Rossier, V. Octeau, J.-B. Sibarita, C. Leduc, B. Tessier, D. Nair, V. Gatterdam, O. Destaing, C. Albigès-Rizo, R. Tampé, L. Cognet, D. Choquet, B. Lounis, and G. Giannone. Integrins $\beta 1$ and $\beta 3$ exhibit distinct dynamic nanoscale organizations inside focal adhesions. *Nature Cell Biology* **14**, 1057 (2012).

B. Rubinstein, M. F. Fournier, K. Jacobson, A. B. Verkhovsky, and A. Mogilner. Actin-myosin viscoelastic flow in the keratocyte lamellipod. *Biophysical Journal* **97**, 1853 (2009).

Z. M. Ruggeri and G. L. Mendolicchio. Adhesion mechanisms in platelet function. *Circulation research* **100**, 1673 (2007).

I. Saiki. Cell adhesion molecules and cancer metastasis. *The Japanese Journal of Pharmacology* **75**, 215 (1997).

G. Salbreux, G. Charras, and E. Paluch. Actin cortex mechanics and cellular morphogenesis. *Trends in Cell Biology* **22**, 536 (2012).

W. M. Saltzman and S. Chien. Introductory Biomechanics: from Cells to Organisms. *Langtoninfo Com* (2007).

K. K. Sarangapani, J. Qian, W. Chen, V. I. Zarnitsyna, P. Mehta, T. Yago, R. P. McEver, and C. Zhu. Regulation of catch bonds by rate of force application. *The Journal of Biological Chemistry* **286, 37**, 32749 (2011).

V. Schaufler, H. Czichos-Medda, V. Hirschfeld-Warnecken, S. Neubauer, F. Rechenmacher, R. Medda, H. Kessler, B. Geiger, J. P. Spatz, and E. A. Cavalcanti-Adam. Selective binding and lateral clustering of α 5 β 1 and α v β 3 integrins: Unraveling the spatial requirements for cell spreading and focal adhesion assembly. *Cell adhesion & migration* **10**, 505 (2016).

C. H. Schreiber, M. Stewart, and T. Duke. Simulation of cell motility that reproduces the force-velocity relationship. *Proceedings of the National Academy of Sciences of the United States of America* **107**, 9141 (2010).

U. S. Schwarz and S. A. Safran. Physics of adherent cells. *Reviews of Modern Physics* **85**, 1327 (2013).

A. Shellard and R. Mayor. Durotaxis: The Hard Path from In Vitro to In Vivo. *Developmental Cell* **56**, 227 (2021).

Z. Shi, Z. T. Graber, T. Baumgart, H. A. Stone, and A. E. Cohen. Cell Membranes Resist Flow. *Cell* **175**, 1769 (2018).

B. Short. Stress fibers guide focal adhesions to maturity. (2012).

G. Shtengel, J. A. Galbraith, C. G. Galbraith, J. Lippincott-Schwartz, J. M. Gillette, S. Manley, R. Sougrat, C. M. Waterman, P. Kanchanawong, M. W. Davidson, *et al.*. Interferometric fluorescent super-resolution microscopy resolves 3D cellular ultrastructure. *Proceedings of the National Academy of Sciences* **106**, 3125 (2009).

M. S. Shutova and T. M. Svitkina. Common and Specific Functions of Nonmuscle Myosin II Paralogs in Cells. *Biochemistry (Moscow)* **83**, 1459 (2018).

S. P. Singh, M. P. Schwartz, J. Y. Lee, B. D. Fairbanks, and K. S. Anseth. A peptide functionalized poly(ethylene glycol) (PEG) hydrogel for investigating the influence of biochemical and biophysical matrix properties on tumor cell migration. *Biomater. Sci.* **2**, 1024 (2014).

E. Sitarska and A. Diz-Muñoz. Pay attention to membrane tension: Mechanobiology of the cell surface. *Current Opinion in Cell Biology* **66**, 11 (2020).

J. Srivastava, G. Barreiro, S. Groscurth, A. Gingras, B. T. Goult, D. Critchley, M. Kelly, M. Jacobson, and D. Barber. Structural model and functional significance of pH-dependent talin–actin binding for focal adhesion remodeling. *Proceedings of the National Academy of Sciences* **105**, 14436 (2008).

S. Stam, J. Alberts, M. L. Gardel, and E. Munro. Isoforms confer characteristic force generation and mechanosensation by myosin II filaments. *Biophysical Journal* **108**, 1997 (2015).

J. Stricker, Y. Beckham, M. W. Davidson, and M. L. Gardel. Myosin II-mediated focal adhesion maturation is tension insensitive. *PloS one* **8**, e70652 (2013).

B. H. Stumpf, A. Ambriović-Ristov, A. Radenovic, and A.-S. Smith. Recent advances and prospects in the research of nascent adhesions. *Frontiers in Physiology* **11** (2020).

S. Suei, R. Seyan, P. Noguera, J. Manzi, J. Plastino, and L. Kreplak. The mechanical role of VASP in an Arp2/3-complex-based motility assay. *Journal of molecular biology* **413**, 573 (2011).

B. Suki and R. Hubmayr. Epithelial and endothelial damage induced by mechanical ventilation modes. *Current opinion in critical care* **20**, 17 (2014).

Z. Sun, M. Costell, and R. Faessler. Integrin activation by talin, kindlin and mechanical forces. *Nature Cell Biology* **21** (2019).

Z. Sun, S. S. Guo, and R. Fässler. Integrin-mediated mechanotransduction. *The Journal of Cell Biology* **215**, 445 (2016).

R. Sunyer, V. Conte, J. Escribano, A. Elosegui-Artola, A. Labernadie, L. Valon, D. Navajas, J. M. García-Aznar, J. J. Muñoz, P. Roca-Cusachs, and X. Trepat. Collective cell durotaxis emerges from long-range intercellular force transmission. *Science* **353**, 1157 (2016).

R. Sunyer and X. Trepat. Durotaxis. *Current Biology* **30**, R383 (2020).

T. Svitkina. The actin cytoskeleton and actin-based motility. *Cold Spring Harbor Perspectives in Biology* **10**, 1 (2018).

T. M. Svitkina, A. B. Verkhovsky, K. M. McQuade, and G. G. Borisy. Analysis of the actin-myosin II system in fish epidermal keratocytes: Mechanism of cell body translocation. *Journal of Cell Biology* **139**, 397 (1997).

V. Swaminathan and C. M. Waterman. The molecular clutch model for mechanotransduction evolves. *Nature Cell Biology* **18**, 459 (2016).

T. H. Tan, M. Malik-Garbi, E. Abu-Shah, J. Li, A. Sharma, F. C. MacKintosh, K. Keren, C. F. Schmidt, and N. Fakhri. Self-organized stress patterns drive state transitions in actin cortices. *Science advances* **4**, eaar2847 (2018).

R. Tapia-Rojo, A. Alonso-Caballero, and J. M. Fernandez. Direct observation of a coil-to-helix contraction triggered by vinculin binding to talin. *Science Advances* **6**, eaaz4707 (2020).

S. Y. Tee, J. Fu, C. S. Chen, and P. A. Janmey. Cell shape and substrate rigidity both regulate cell stiffness. *Biophysical Journal* **100**, L25 (2011).

W. Thomas. Catch bonds in adhesion. *Annual Review of Biomedical Engineering* **10**, 39 (2008).

S. Tojkander, G. Gateva, and P. Lappalainen. Actin stress fibers-assembly, dynamics and biological roles. *Journal of Cell Science* **125**, 1855 (2012).

A. Torres-Sánchez, D. Millán, and M. Arroyo. Modelling fluid deformable surfaces with an emphasis on biological interfaces. *Journal of fluid mechanics* **872**, 218 (2019).

L. Trichet, J. Le Digabel, R. J. Hawkins, S. R. K. Vedula, M. Gupta, C. Ribrault, P. Hersen, R. Voituriez, and B. Ladoux. Evidence of a large-scale mechanosensing mechanism for cellular adaptation to substrate stiffness. *Proceedings of the National Academy of Sciences of the United States of America* **109**, 6933 (2012).

T. A. Ulrich, E. M. de Juan Pardo, and S. Kumar. The Mechanical Rigidity of the Extracellular Matrix Regulates the Structure, Motility, and Proliferation of Glioma Cells. *Cancer Research* **69**, 4167 (2009).

P. J. M. Van Haastert and P. N. Devreotes. Chemotaxis: signalling the way forward. *Nature reviews. Molecular cell biology* **5**, 626 (2004).

S. Van Helvert, C. Storm, and P. Friedl. Mechanoreciprocity in cell migration. *Nature Cell Biology* **20**, 8 (2018).

C. Veigel, J. Molloy, S. Schmitz, and J. Kendrick-Jones. Load-dependent kinetics of force production by smooth muscle myosin measured with optical tweezers. *Nature Cell Biology* **5**, 980 (2003).

G. Vertelov, E. Gutierrez, S. A. Lee, E. Ronan, A. Groisman, and E. Tkachenko. Rigidity of silicone substrates controls cell spreading and stem cell differentiation. *Scientific Reports* **6**, 1 (2016).

M. Vicente-Manzanares, C. K. Choi, and A. R. Horwitz. Integrins in cell migration – the actin connection. *Journal of Cell Science* **1473**, 199 (2009a).

M. Vicente-Manzanares and A. R. Horwitz. Adhesion dynamics at a glance. *Journal of Cell Science* **124**, 3923 (2011).

M. Vicente-Manzanares, X. Ma, R. S. Adelstein, and A. Horwitz. Non-muscle myosin II takes centre stage in cell adhesion and migration. *Nature Reviews. Molecular Cell Biology* **10**, 778 (2009b).

M. Vicente-manzanares and A. R. Horwitz. Adhesion dynamics at a. (2011). 10.1242/jcs.095653.

C. Vigouroux, V. Henriot, and C. Le Clainche. Talin dissociates from RIAM and associates to vinculin sequentially in response to the actomyosin force. *Nature communications* **11**, 1 (2020).

J. von der Ecken, M. Müller, W. Lehman, D. J. Manstein, P. A. Penczek, and S. Raunser. Structure of the F-actin–tropomyosin complex. *Nature* **519**, 114 (2015).

S. Walcott and S. X. Sun. A mechanical model of actin stress fiber formation and substrate elasticity sensing in adherent cells. *Biophysical Journal* **98**, 365a (2010).

S. Walcott, D.-H. Kim, D. Wirtz, and S. X. Sun. Nucleation and decay initiation are the stiffness-sensitive phases of focal adhesion maturation. *Biophysical journal* **101**, 2919 (2011).

F. Wang, E. V. Harvey, M. A. Conti, D. Wei, and J. R. Sellers. A conserved negatively charged amino acid modulates function in human nonmuscle myosin IIA. *Biochemistry* **39**, 5555 (2000).

F. Wang, M. Kovacs, A. Hu, J. Limouze, E. V. Harvey, and J. R. Sellers. Kinetic mechanism of non-muscle myosin IIB: functional adaptations for tension generation and maintenance. *Journal of Biological Chemistry* **278**, 27439 (2003).

H. B. Wang, M. Dembo, S. K. Hanks, and Y. L. Wang. Focal adhesion kinase is involved in mechanosensing during fibroblast migration. *Proceedings of the National Academy of Sciences of the United States of America* **98**, 11295 (2001).

J. Wang and H. Gao. Clustering instability in adhesive contact between elastic solids via diffusive molecular bonds. *Journal of the Mechanics and Physics of Solids* **56**, 251 (2008).

X. Wang and T. Ha. Defining single molecular forces required to activate integrin and notch signaling. *Science* **340**, 991 (2013).

R. Wedlich-Soldner, S. Altschuler, L. Wu, and R. Li. Spontaneous cell polarization through actomyosin-based delivery of the Cdc42 GTPase. *Science (New York, N.Y.)* **299**, 1231 (2003).

U. G. K. Wegst, H. Bai, E. Saiz, A. P. Tomsia, and R. O. Ritchie. Bioinspired structural materials. *Nature Materials* **14**, 23 (2014).

G.-w. Wei and Z. Chen. for Charge Transport . **54**, 699 (2012).

C. Weinberger, W. Cai, and D. Barnett. Lecture Notes - Elasticity of Microscopic Structures. (2021).

E. S. Welf, U. P. Naik, and B. A. Ogunnaike. A spatial model for integrin clustering as a result of feedback between integrin activation and integrin binding. *Biophysical journal* **103**, 1379 (2012).

C. A. Wilson, M. A. Tsuchida, G. M. Allen, E. L. Barnhart, K. T. Applegate, P. T. Yam, L. Ji, K. Keren, G. Danuser, and J. A. Theriot. Myosin II contributes to cell-scale actin network treadmilling through network disassembly. *Nature* **465**, 373 (2010).

H. Wolfenson, A. Bershadsky, Y. I. Henis, and B. Geiger. Actomyosin-generated tension controls the molecular kinetics of focal adhesions. *Journal of Cell Science* **124**, 1425 (2011).

H. Wolfenson, T. Iskratsch, and M. P. Sheetz. Early events in cell spreading as a model for quantitative analysis of biomechanical events. *Biophysical Journal* **107**, 2508 (2014).

J. Y. Wong, A. Velasco, P. Rajagopalan, and Q. Pham. Directed Movement of Vascular Smooth Muscle Cells on Gradient-Compliant Hydrogels. *Langmuir* **19**, 1908 (2003).

S. Wong, W. H. Guo, and Y. L. Wang. Fibroblasts probe substrate rigidity with filopodia extensions before occupying an area. *Proceedings of the National Academy of Sciences of the United States of America* **111**, 17176 (2014).

B. Woods and D. J. Lew. Polarity establishment by Cdc42: Key roles for positive feedback and differential mobility. *Small GTPases* **10**, 130 (2019).

D. B. Wormer, K. A. Davis, J. H. Henderson, and C. E. Turner. The focal adhesion-localized CdGAP regulates matrix rigidity sensing and durotaxis. *PLoS ONE* **9** (2014). 10.1371/journal.pone.0091815.

P. T. Yam, C. A. Wilson, L. Ji, B. Hebert, E. L. Barnhart, N. A. Dye, P. W. Wiseman, G. Danuser, and J. A. Theriot. Actin-myosin network reorganization breaks symmetry at the cell rear to spontaneously initiate polarized cell motility. *Journal of Cell Biology* **178**, 1207 (2007).

K. M. Yamada and M. Sixt. Mechanisms of 3D cell migration. *Nature Reviews Molecular Cell Biology* **20**, 738 (2019).

H. Yamaguchi, J. Wyckoff, and J. Condeelis. Cell migration in tumors. *Current Opinion in Cell Biology* **17**, 559 (2005).

M. Yao, B. Goult, B. Klapholz, X. Hu, C. P. Toseland, Y. Guo, P. Cong, M. P. Sheetz, and J. Yan. The mechanical response of talin. *Nature Communications* **7**, 1 (2016).

M. Yao, B. T. Goult, H. Chen, P. Cong, M. P. Sheetz, and J. Yan. Mechanical activation of vinculin binding to talin locks talin in an unfolded conformation. *Scientific reports* **4**, 1 (2014).

T. Yeung, P. C. Georges, L. A. Flanagan, B. Marg, M. Ortiz, M. Funaki, N. Zahir, W. Ming, V. Weaver, and P. A. Janmey. Effects of substrate stiffness on cell morphology, cytoskeletal structure, and adhesion. *Cell Motility and the Cytoskeleton* **60**, 24 (2005).

J. Yu, J. Huang, J. A. Jansen, C. Xiong, and X. F. Walboomers. Journal of the Mechanical Behavior of Biomedical Materials Mechanochemical mechanism of integrin clustering modulated by nanoscale ligand spacing and rigidity of extracellular substrates. *Journal of the Mechanical Behavior of Biomedical Materials* **72**, 29 (2017).

H. Yuan and H. Gao. On the mechanics of integrin clustering during cell-substrate adhesion. *Acta Mechanica Solida Sinica* **25**, 467 (2012).

Y. Yuan, L. Li, Y. Zhu, L. Qi, L. Azizi, V. P. Hytönen, C.-G. Zhan, and C. Huang. The molecular basis of talin2's high affinity toward β1-integrin. *Scientific reports* **7**, 1 (2017).

X. Zhang, G. Jiang, Y. Cai, S. J. Monkley, D. R. Critchley, and M. P. Sheetz. Talin depletion reveals independence of initial cell spreading from integrin activation and traction. *Nature cell biology* **10**, 1062 (2008).

O. C. Zienkiewicz and R. L. Taylor. The Finite Element Method (Fluid Dynamics). *Methods* **3**, 347 (2000).